October 2019

A SYNTHETIC HUMAN BRAIN ECM HYDROGEL FOR TIGHT CONTROL OF ASTROCYTE ACTIVATION

Sualyneth Galarza

Recommended Citation

Galarza, Sualyneth, "A SYNTHETIC HUMAN BRAIN ECM HYDROGEL FOR TIGHT CONTROL OF ASTROCYTE ACTIVATION" (2019). *Doctoral Dissertations*. 1723.
https://scholarworks.umass.edu/dissertations_2/1723

A SYNTHETIC HUMAN BRAIN ECM HYDROGEL FOR TIGHT CONTROL OF ASTROCYTE ACTIVATION

A Dissertation Presented

by

SUALYNETH GALARZA

Submitted to the Graduate School of the
University of Massachusetts Amherst in partial fulfillment
of the requirements for the degree of

DOCTOR OF PHILOSOPHY

September 2019

Department of Chemical Engineering

A SYNTHETIC HUMAN BRAIN ECM HYDROGEL FOR TIGHT CONTROL OF ASTROCYTE ACTIVATION

A Dissertation Presented

by

SUALYNETH GALARZA

Approved as to style and content by:

Shelly R. Peyton, Chair

Alfred J. Crosby, Member

Jungwoo Lee, Member

Michele Markstein, Member

John Klier, Department Head
Department of Chemical Engineering

DEDICATION

To my grandma Hilda Luz Sanchez-Rivera and my aunt Milta Sanchez-Rivera, patients of Alzheimer's and Glioblastoma. May this work help provide a platform to tackle brain diseases.

ACKNOWLEDGEMENTS

First, I would like to thank Dr. Shelly Peyton for giving me the chance to be part of her lab. Although I had no prior experience in cell culture or tissue engineering related work, when I heard about the project of building a brain, I knew I wanted in. Throughout the years Dr. Shelly Peyton has been an inspiring mentor pushing my scientific boundaries outside of comfort zones and guiding me to be the best scientist I could be. I admire her driven attitude towards science but also towards mentoring students. Thank you for your support and allowing me to meet and engage with colleagues and professors in the tissue engineering field through conferences extending from Phoenix to Canada. Thank you for bringing a positive mindset to all of our work. Thank for allowing your lab to be diverse and integrating diversity in science.

Next, I think one of the most important mentors I have had, and I would like to thank is Dr. Sandra Petersen. I met both Dr. Shelly Peyton and Dr. Sandra Petersen back in Puerto Rico when they went to introduce NEAGEP to my school in UPRM. Upon arriving at UMass Amherst Dr. Sandra Petersen made sure to make us feel like home. She would always say hello with a warm hug and smile and even if it was a tough moment in graduate school that interaction would make it feel like everything was going to be alright. Additionally, by participating in monthly dinners organized by her I came to meet other graduate students that have become like family to me. Dr. Anesia Auguste and Orfely Auguste were my family away from home that I met through NEAGEP. Anesia was my mentor during my first year of graduate school and since then we have always been close. Thank you both for all of your support throughout all of these years. I am very grateful to have met you and have you been part of my life as you continue being.

Next, I would like to thank my academic support. First, Dr. Alfred Crosby thank you for your guidance during my first years of graduate school where I started material characterization in your lab. It was really helpful to have meetings in which I could discuss and understand findings and also be included in meetings with other members of your lab. Participating in those meetings helped

me grow as a scientist in a cross-functional environment. I would also like to thank the members of my committee Dr. Michele Markstein and Dr. Jungwoo Lee. Thank you for being open to meet with me and providing such helpful feedback about my work. I believe your insight and advice towards my research project helped shape what it is today. I would also like to thank Dr. Stephen Eyles for providing experimental help and insightful conversations for the mass spectrometry used in this work. Thank you for always being able and available to meet and discuss ideas and sharing your knowledge in the field. Dr. Sarah Perry, thank you for teaching all I know about peptide synthesis which was an integral part of this work. I really appreciate all of your time, advice and providing the tools to synthetize the peptides in your lab.

Next, I would like to also thank my support away from home. The network of friends that although being far away from me physically were there to support me in good and bad times. Amanda and Oleg Korneitchouk, thank you for dropping me off my first day of graduate school, I literally would have not arrived in Amherst without you. Thank you for letting me stay with you in New York when I needed and for all the good times we have shared. I am very proud of you both. I would also like to thank Wendy Gomez and Joel Ortiz. You both have always been there for me regardless of the distance, either China or Puerto Rico. You mean the world to me. Next, I cannot forget to thank Jeannette Rivera. Thank you for being one of my best friends throughout college and still supporting me through graduate school. Our conversations have been invaluable to me and I am lucky to have you as my friend.

I would also like to acknowledge that I am very grateful for the friends I have made throughout graduate school. First, Dr. Lauren Jansen, Dr. Kris Kolewe, Dr. Benjamin Cherniawski, Dr. Coralie Backlund, Dr. Edmund Burnett and Dr. Charlie Swofford thank you for being my roommates, confidants, and board games companion among scientific conversations throughout most of my time in Amherst. My experience would have not been the same without you. It was an amazing experience to enjoy softball, grow my knowledge about beer but also always be amongst driven and successful scientists.

I would also like to thank all of my friends I have made through graduate school. There are so many but particularly I would like to acknowledge my friends Vishnu Raman and Edwin Murenzi for being there to be sources of happiness and insightful conversations. I would like to also thank all my friends that have made this a great graduate school experience, Dr. Kara Martin, Dr. Jack Ly, Dr. Ryan Seihort, Christian Steinmitz and Dr. Stephen Strassburg for being roommates, friends, colleagues and sources of happiness in this journey.

Finally, I would like to thank my lab members Carey Dougan, Aritra Kundu, Hyuna Kim, Ning Tseng, Yen Tran, Katie Bittner and Inha Baek for conversations and great lab get togethers. I cannot forget to thank previous peyton lab members Dr. Lauren Barney, Dr. Thuy Nguyen, Dr. Lauren Jansen, Dr. Alyssa Schwartz and Dr. Elizabeth Brooks for being sources of inspiration and hard work. Also, for being great companions during scientific conferences.

Last, but not least, I would like to particularly thank Ned Burnett, my life would not be the same without you. Thank you for your patience and your support throughout thick and thin. I would not be the person and scientist I am today without you. Thank you for making me part of your life and for making me be part of your family. I cannot wait to see what is next.

ABSTRACT

A SYNTHETIC HUMAN BRAIN ECM HYDROGEL FOR TIGHT CONTROL OF ASTROCYTE ACTIVATION

SEPTEMBER 2019

SUALYNETH GALARZA

B.S., UNIVERSITY OF PUERTO RICO MAYAGUEZ

Ph.D., UNIVERSITY OF MASSACHUSETTS AMHERST

Directed by: Professor Shelly R. Peyton

Bioengineers have aimed to design instructive extracellular matrix (ECM) models that can tailor the protein composition and biomechanics of the brain *in vitro* in order to study how astrocytes remodel the brain during trauma and inflammation. However, these parameters cannot be independently controlled in protein-based models, and although tunable in synthetic systems, current astrocyte cultures fail to retain their characteristic stellate morphology without becoming activated. To this date there is no biomaterial model that can retain astrocyte quiescence *in vitro*. This dissertation sought to develop such an *in vitro* model that would enable the study of specific ECM factors that control astrocyte activation while retaining quiescent astrocytes *in vitro*. Here we introduce a synthetic hydrogel, that for the first time shows maintenance of astrocyte quiescence, and control over activation on demand. We first characterized the human brain ECM via proteomics, and the brain biomechanics via needle-induced cavitation rheology and volume-controlled cavity expansion and incorporated the top ECM components responsible for integrin-mediated and MMP-mediated degradation alongside matched mechanical properties into a fully synthetic hydrogel. Using this hydrogel, composed of just PEG and peptides, we demonstrate control over astrocyte activation via tuning of the integrin-binding and MMP-degradable profile or via cytokine molecules, in contrast to other protein-based models like collagen where astrocytes remain in a reactive state. Finally, to aid with the implementation of biomaterials as *in vitro* platforms to predict *in vivo* physiology, the correlation between current 2D, 3D and *in vivo* studies of glioblastoma motility was explored, and how an effect size can help standardize comparison across labs and culture dimensions. An additional study highlighted the importance of adopting growth rate in drug metric responses and how these can be implemented in current biomaterial platforms. Overall, this work can help integrate biomaterials as models to predict *in vivo* physiology. This brain hydrogel system can be used as a new platform to model the physiological state of quiescent astrocytes and their reactivity upon injury, for the first time, *in vitro.*

TABLE OF CONTENTS

Page

CHAPTER

APPENDICES

LIST OF TABLES

LIST OF FIGURES

CHAPTER 1

BIOMATERIALS TO MIMIC THE BRAIN EXTRACELLULAR MATRIX

1.1 The Extracellular Matrix (ECM) composes the tissue microenvironment

1.1.1 The brain extracellular matrix (ECM)

The brain is covered by layers of membranes, the meninges, and submerged in cerebrospinal fluid[1]. This organ can be grossly divided into different neuroanatomical functional regions such as the frontal, parietal, temporal, occipital lobes and central gray matter structures[1]. Anatomically and histologically, the brain can be further stratified into the cerebral cortex representing the outermost gray matter overlying white matter and innermost deep gray matter components (fig. 1.1a). The cerebral cortex incorporates neurons and glial cells, whereas the white matters hosts oligodendrocytes and axons from cortical and subcortical projection neurons[2-4].

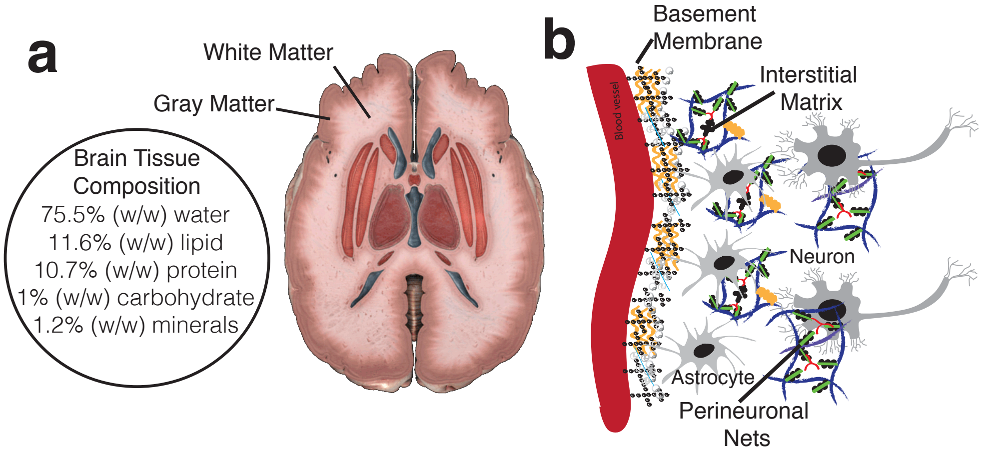

Figure 1.1: The brain extracellular matrix (ECM). a) The brain cerebral cortex accounts for 80% of the organ volume and is macroscopically divided into white and gray matter structures. These tissues are mainly composed of water, lipids and protein. b) Microscopically, the extracellular space accounts for 20% of the total volume of the mature brain and is filled with an organized extracellular matrix (ECM). Histology has identified three main ECM structures in the brain: the basement membrane near vasculature, interstitial matrix between cells, and perineuronal nets surrounding neuron axons.

Immunohistochemical studies that have characterized the brain extracellular space, which accounts for 20% of the total volume of the mature brain, have identified three prominent structures that compose the brain extracellular matrix compartments: the blood-brain barrier (BBB), the perineuronal nets (ECM structure most prominent around neurons) and the interstitial matrix (figure 1.1b)[5-8]. Cells are the main source of these extracellular proteins that compose and give rise to differences in tissues. In the brain, astrocytes are the big synthesizers of proteins in the cortex[9].

The components of the extracellular matrix can be divided into core proteins, core associated proteins and ECM regulators like small molecules that interact with the ECM[10-12]. Core ECM proteins include collagens, proteoglycans and glycoproteins[11]. Collagens and glycoproteins, like fibronectin and laminin, are mostly found around the vasculature in the basement membrane[8]. A mixture of collagen, glycoproteins and proteoglycans can be found in interstitial ECM giving rise to the microenvironment that surrounds the cells[10]. Matrix affiliated proteins and ECM regulators include those proteins and small molecules that are colocalized in the extracellular space but do not readily assemble to form the matrix that gives rise to tissue[10]. The interaction of cell with ECM components provide the cues give rise to biological cascades[13].

Integrin molecule pairs, consisting of α and β heterodimers, are the main surface receptors from which cells interact with ECM proteins[14-17]. These transmembrane receptors can bind to both ECM proteins and the cellular cytoskeleton providing mechanical and biochemical signaling that regulates cell response[17]. Additionally, in order to degrade and remodel the ECM, cell release enzymes that allow them to spread and migrate in the native microenvironment. Matrix metalloproteinases (MMP) are a family of enzymes that cleave various proteins of the ECM[18]. Together these interactions of cells and their ECM microenvironment have been shown to play a role in development[19, 20], differentiation[21] and disease[17, 18, 20].

1.1.2 The composition of the brain ECM changes during health and disease

The extracellular matrix has been found to undergo dynamic changes during development, health and disease[13, 22, 23]. For example, ECM molecules are already present in the developing embryo where they play important roles in the development of the central nervous system[7]. The composition of the brain ECM has been shown to change during different developmental stages[7]. Similarly, studies have found changes in the ECM composition during disease progression that have been in instances used as biomarkers. As an example, proteins like serpins have been shown to be present in brain metastases samples via histology approaches while these proteins are not present in the normal brain (figure 1.2a)[24]. Similarly, during transitioning stages of glioblastoma there is an increase in the deposition of tenascin C in the human cortex (figure 1.2b)[25].

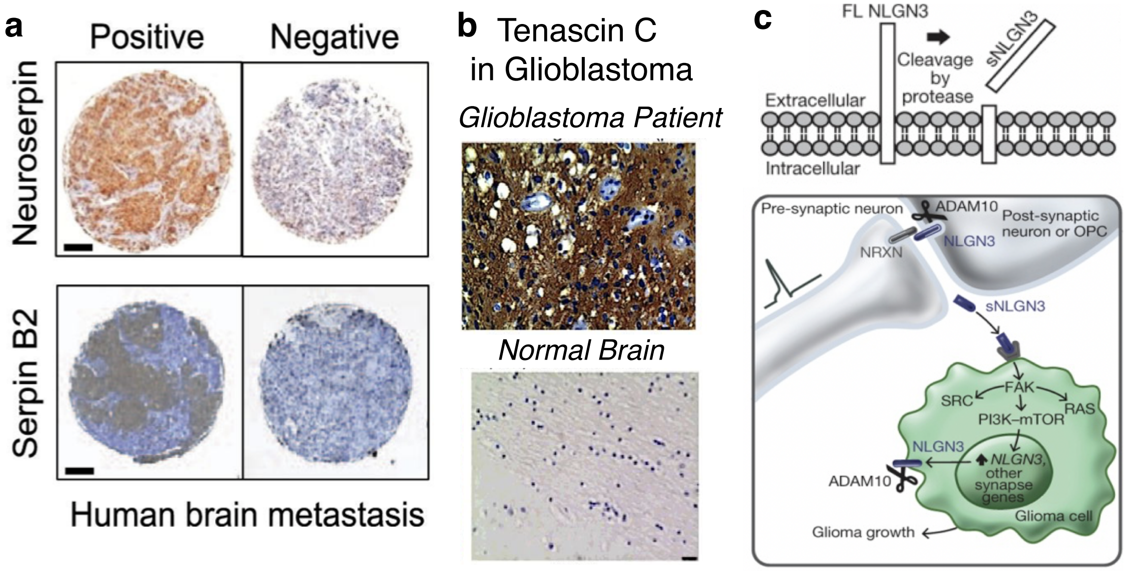

Figure 1.2: Changes of the brain ECM in brain tumors. a) Alterations in ECM protein deposition in the brain after brain metastasis progress. Representative brain metastasis tissue microarray cores stained with neuroserpin or serpin B2 antibodies. Figure adapted from [24]with permission from Elsevier. b) The ECM protein tenascin C is highly abundant in the brain of a glioblastoma patient in contrast to a healthy donor. Figure adapted from[25] with permission from American Association of Cancer Research. c) Glioblastoma progression is influenced by the microenvironment of the normal brain. Venkatesh et al., showed neuron secretion of neuroligin-3 and cleavage by extracellular protease ADAM10 stimulates oncogenic signaling in glioma cells inducing transcriptional changes that lead to glioma growth. Figure adapted from[26] with permission from Springer Nature.

While this is a glycoprotein normally expressed in very low levels in the healthy brain[8], an increase in the abundance of tenascin c receptors have been shown to increase cell proliferation and initiation of brain tumor cells[25]. Recently, work by Venkatesh et al.,[26] illustrated how targeting the brain microenvironment could be a potential avenue to eradicate glioblastoma. In their work they found that the progression of glioblastoma is influenced by the microenvironment of the normal brain where neurons secrete the protein neuroligin-3 which upon cleavage by proteases in the brain extracellular space stimulates and oncogenic signaling in glioma cells that induces glioma cell growth (figure 1.2c)[26, 27]. Authors found that by inhibiting the cleavage of this protein by the protease

Adam10 glioblastoma progression could be inhibited. However, current understanding of the interaction between cancer cells and the brain microenvironment is limited. These examples highlight the need to consider the unique physiology of the brain microenvironment and how it would offer a new approach to treating cancer cells by focusing on the surrounding cells. The idea of interrupting the molecular support that cancer cells receive from the brain microenvironment raises the possibility of blocking the progression of a diverse range of cancers.

1.1.3 Extracellular matrix remodeling give rise to differences in brain mechanical properties

The extracellular matrix changes during health and disease have a critical effect in the mechanical properties of the tissue[19, 22, 28-32]. For example, the ECM is known to stiffen during cancer progression [31, 33]. Research has shown that the stiffening of the microenvironment in tissues like the breast, comes from increases in pressure forces caused from cell increased proliferation and due to the increase in collagen deposition at the site of the tumor by local cells like fibroblasts and stem cells[34-37]. In the case of the brain, comparison of the Young's modulus measured via indentation of normal brain and glioma samples showed that glioma samples undergo stiffening as the compression is increased (figure 1.3a)[31]. Similarly, dynamic changes in the stiffness and viscoelastic properties of brain tissue have been also correlated with Alzheimer's disease[38], traumatic axonal injuries[39], cortical contusions[40], and brain tumors[41]. One study showed the elastic modulus (G_d) of normal brain tissue was higher in comparison to areas where a tumor or breast cancer metastases had formed (figure 1.3b)[41].

These macroscale mechanical properties also matter at the microscale, since central nervous system cells have been shown to respond to mechanical cues[29, 31] and undergo differentiation changes depending on local stiffness[22]. Both neurons and glia, as major cellular constituents of the brain, contribute to mechanical properties of the tissue[42]. Measurements at the cellular level have reported glial cells to be softer than neurons, and both single cells show a frequency dependent Young's modulus similar to bulk brain tissue and elastic moduli magnitude at a macroscopic level[22]. Inspection of cell responses to changes in the substrate shear modulus have shown that neurons reduce their number of branches as substrates reach a higher modulus, while astrocytes increase in the surface area in more rigid substrates (figure 1.3c)[22]. Similarly, protein arrangement within this cell types can change dependent on the mechanical properties of the substrate (figure 1.3d)[31]. However, while there have been many studies on the elastic, viscoelastic, and poroelastic properties of the brain, there has not been a consensus on the magnitude of several key mechanical properties of this tissue. Reports of Young's elastic modulus of the brain range from 100s of Pa to 10s of kPa and vary considerably among experimental techniques[22, 29, 32, 43]. This highlights the need for studies that can characterize location dependent mechanical properties of the brain.

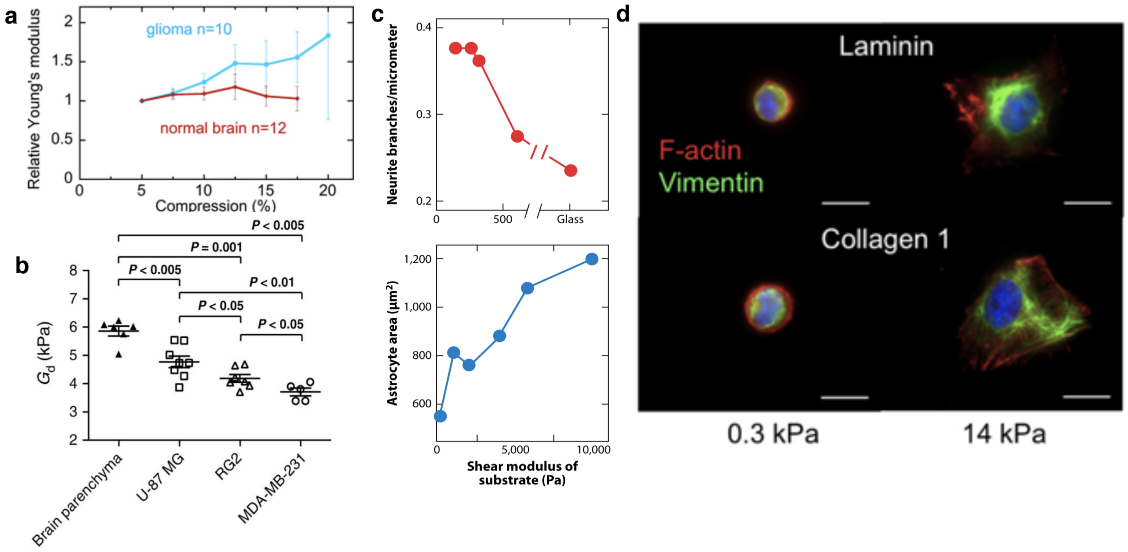

Figure 1.3: Disease alters brain mechanical properties and cells are sensitive to modulus changes. a) Relative Young's modulus comparison obtained via indentation of normal mouse brain and glioma samples show glioma brain follows compression stiffening. Figure adapted from[31] with permission from IOP Science. b) Jamin et al., showed the elastic modulus (G_d) of normal brain parenchyma is higher compared to metastases produced by U-87-MG, RG2 and MDA-MB-231 cell lines and as measured by magnetic resonance elastography. Mechanical properties were dependent on the cell line. Figure adapted from[41] with permission from American Association for Cancer Research. c) Neuron and astrocytes show morphological changes in branch length and cell area respectively upon increasing substrate shear modulus. Figure adapted from[22] with permission from annual review of biomedical engineering. d) Pogoda et al., showed substrate stiffness effect on glioma cell morphology and cytoskeleton protein arrangement.[31]

1.1.4 Astrocytes are a key cellular component of the brain microenvironment

Major drivers of the changes in the brain ECM during health and disease are the cellular constituents of the tissue. Astrocytes constitute approximately 30% of the cells in the mammalian brain characterized by their star-shaped morphology and cellular cytoplasmic processes reaching both synapses and capillary walls[9, 44, 45]. These cells populate gray and white matter tissue and the spinal cord of the CNS and function as key mediators of the brain ECM homeostasis[44].

During brain trauma and inflammation, astrocytes adopt a reactive phenotype where they are termed as reactive astrocytes[45, 46]. These post-injury astrocytes are identified by upregulation of intermediate filament proteins like glial fibrillary acidic protein (GFAP), vimentin and nestin, alongside aberrant morphological changes spanning from moderate astrogliosis to severe astrogliosis (figure 1.4a)[47-49]. In contrast to healthy tissue astrocytes, whose processes do not overlap, reactive astrocytes are characterized by a high expression or GFAP and overlapping processes[47, 50]. Others have shown, via time-lapse microscopy and immunostaining, that these cells are first responders to extravasation of cancer cells in the brain microenvironment (figure 1.4b)[51-53] and remain activated many days post injury (figure 1.4c)[50].

Studies aimed to understand molecular mechanisms driving reactive astrocyte interactions have identify ECM components like the protein collagen I induces astrocyte activation mediated by integrin-N-cadherin signaling[50]. Similarly, others have found that reactive astrocytes exhibit pro- or anti-inflammatory functions dependent on the type of injury. A1 neuroinflammatory astrocytes upregulate many genes destructive to synapses and are suggested to be harmful[54-56]. Alternatively, ischemia-induced A2 astrocytes upregulate many neurotrophic factors that promote survival, growth of neurons, and have been suggested to be helpful[57-60]. As an example of helpful astrocytes, during breast cancer metastasis to the brain, reactive astrocytes have been shown to produce the plasminogen activators (PA) tPA and uPA to convert plasminogen into plasmin since this creates a mechanism to eliminate extravasated cancer cells[24]. Yet, blocking of plasminogen by cancer cells via serpins has been shown to prevent their death. (figure 1.4d)[61]. However, these helpful astrocytes can become harmful as remaining cancer cells induce signaling changes. These cancer cells that remain in the brain vasculature induce changes in reactive astrocytes by producing calcium and cGAMP signals that result in astrocyte production of inflammation cytokines TNF and IFN-alpha that induce cancer cell proliferation (figure 1.4e)[51, 61]. Together, these examples show

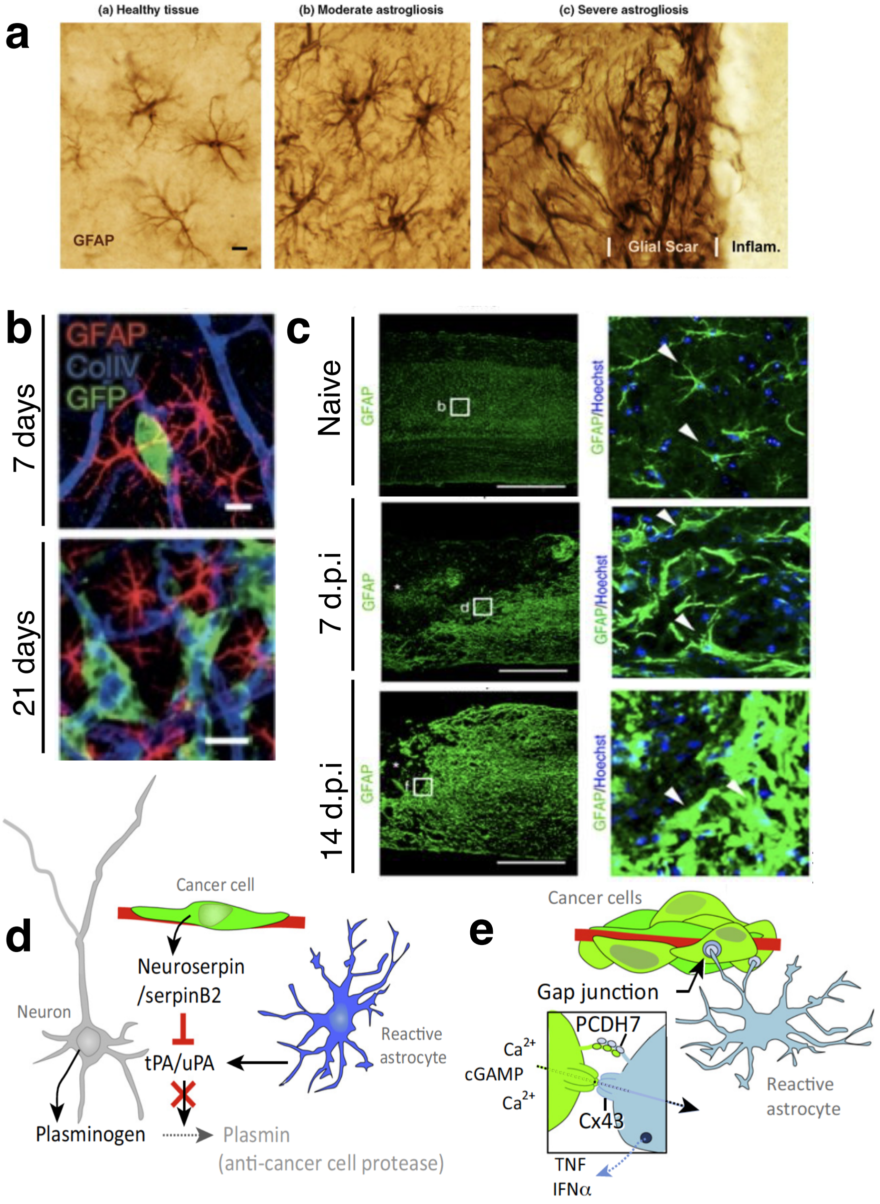

Figure 1.4: Astrocytes are key components of the brain microenvironment. a) Glial fibrillary acidic protein (GFAP) staining of astrocytes in wild type mice shows morphology in healthy tissue, moderate astrogliosis and severe astrogliosis events. Astrocyte processes do not overlap in healthy tissue. Figure adapted from [47] with permission from Elsevier. b) Astrocytes are the first responders upon cancer cell invasion in the brain. GFP+ H2030-BrM3(green) are surrounded by GFAP+ activated astrocytes (red) in the brain parenchyma at early (day 7) and later (day 21) time points after intracardiac inoculation in mice. Blue, collagen IV (ColIV) staining in vessels. Scale bars, 10 μm. Adapted from [51] with permission from Springer Nature. c) Example images depicting GFAP staining (green) of naïve spinal cord and injured spinal cords at day 7 and day 14 post injury (d.p.i.) Scale bars 50 μm. Figure adapted from[50] with permission from Springer Nature. d) Reactive astrocytes defend the brain microenvironment by producing the plasminogen activators (PA) tPA and uPA that activate plasminogen to plasmin which eliminates extravasated cancer cells. Cancer cells block this response through anti-PA serpins (neuroserpin/serpinB2) that inhibit plasmin generation and prevent cancer cell death. e) Surviving cancer cells continue to interact with reactive

astrocytes during brain colonization and establishing gap junctions with reactive astrocytes where they send calcium and cGAMP to astrocytes via Cx43 junction, and activate a signaling pathway in astrocytes leading to secretion of TNF and IFN-alpha that induces cancer cell proliferation. Figure adapted from[61] with permission from Elsevier.

how astrocytes are a key component of the brain microenvironment and extracellular cues can affect their response. However, although some of these molecular mechanisms have been identified in physiologically relevant animal models like rodents[62], the large number of cell types involved in inflammatory responses in CNS injury and disease[45], as well as the complex cell-cell interactions among these and other neural cell types has hampered mechanistic understanding of environment driven astrocyte reactivity.

1.2 Better models are needed to understand brain cell-ECM interactions *in vitro*

1.2.1 Limitations in studying astrocytes *in vivo*

Current *in vivo* astrocyte studies in rodents face the challenge of isolating single cell-ECM interactions that lead to activation due to the poor control on the microenvironmental cues of this system[45, 52, 63]. As such, what relevant extracellular and intracellular signaling pathways induce astrocyte activation remain to be understood. Similarly, studies have highlighted major differences between human astrocytes to those from different species. For example, Oberheim et al.,[44] highlighted how protoplasmic astrocytes in the human neocortex are 2.6-fold larger in diameter and extend 10-fold more GFAP positive primary processes than rodent astrocytes. Similarly, the deposition of calcium by human astrocytes is significantly faster than in rodent counterparts. Lastly, the human neocortex contains several subclasses of astrocytes not represented in rodent models[44]. Those astrocytes that are present in both species, like is the case of fibrous astrocytes are larger in diameter in the human brain[44]. Thus, human cortical astrocytes are larger and structurally more complex and diverse then those in the rodent brain[9, 44]. In addition, rodent models are expensive, time-consuming, and difficult to control and manipulate[64]. These examples highlight the need for more humanized models in which to study astrocytes *in vitro.*

1.2.2 Biomaterials to understand astrocyte activation *in vitro*

Within the context of the brain, cell culture platforms derived from tissue such as tissue slices, decellularized scaffolds and organoids have been used as more complex *in vitro* models of the brain[65, 66]. Astrocytes grown in three-dimensional (3D) organoids pose recent cell culture platforms that provide aspects of the brain architecture, but their inherent complexity limits the identification of individual drivers of astrocyte activation[67-70]. Alternatively, protein-based 3D hydrogels, mostly composed of collagen[71], hyaluronic acid[72-74], and mixtures of these proteins[75, 76], have been popularized as brain *in vitro* platforms, as they constitute native brain ECM proteins, exert biocompatibility, and in certain cases, lower upregulation of GFAP as compared to astrocytes grown in a two-dimensional monolayer[75] (figure 1.5 a-d). However, previous studies have identified certain combinations of proteins, cytokines, and stiffnesses can influence astrocyte activation, and these parameters cannot be independently controlled in these materials[77]. For example, a study that explored astrocyte response in a wound assay found different ECM proteins influenced astrocyte migration speeds[77]. Similarly, the simultaneous tuning of mechanical and biochemical properties in commercially available protein system impedes identifying what specific parameters control for astrocyte activation. As an example, a combination of collagen, hyaluronic acid and Matrigel resulted in quiescent astrocyte culture, but it remains poorly understood what particular protein composition led to that response as the exact composition of these materials is lot-dependent and in the case of Matrigel is not completely understood (figure 1.5d)[75].

Synthetic hydrogels, in contrast, provide a tremendous opportunity to design tissue specific scaffolds with tight control of parameters, but bioactive moieties need to be incorporated to represent the microenvironment of interest (figure 1.5e)[78, 79]. Yet, currently there is no *in vitro* model that can simultaneously culture quiescent astrocytes with their characteristic star-shape morphology and allow for controlled activation *in vitro*. For example, a recent platform developed by Papadimitriou et al.,[80] to culture fetal primary astrocytes in a poly-ethylene-glycol (PEG) heparin hydrogel, produced cells with high level of GFAP expression similar to that in 2D cultures (figure 1.5f)[81]. Other studies have focused on the development of hyaluronic acid (HA) containing PEG hydrogels, due to the presence of HA in the brain but cultures take a very long time (around 48-70 days) to differentiate from neural stem progenitor cells (NS/PC) to astrocytes (figure 1.5g)[82]. In work by Seidlits et al.,[82] NS/PC were differentiated into astrocytes with low levels of GFAP but further staining for other astrocyte markers suggest these cells differentiated into oligodendrocytes instead (figure 1.5h). Similarly, other work that has looked into the elimination of serum-based cultures since these are known to induce activation of astrocytes *in vitro* and replace it for Heparin-binding EGF-like growth factor (HBEGF) cultures have also resulted in reactive astrocytes cultures regardless of dimensionality[83]. Overall most of these studies are also conducted with primary murine astrocytes which also impedes direct comparison to the human specific astrocyte phenotypes identified by Oberheim et al.[44] Lastly, a vast number of astrocytes with low expression of GFAP show rounded morphologies in biomaterial platforms[82, 84]. Taken together these examples highlight the need for better models to control for astrocyte activation *in vitro.*

1.2.3 Translation of biomaterial models to predict physiological responses & means to standardize *in vitro* models to identify druggable targets

Reactive astrocytes are an integral part of brain cancers as they have been shown to become reactive near metastases from lung[24], breast[24] and melanoma[85] origin (figure 1.6a). Yet, the percentage of patients with brain metastases that are susceptible to targeted therapy is very low[61](fig. 1.6b). Similarly, mechanisms that could be targeted in these reactive astrocytes remain poorly understood. Perhaps, the current lack of appropriate model systems is a potential limiting factor in uncovering molecular mechanisms underlying brain cell-ECM interactions. These examples highlight the need for better biomaterials to predict physiological responses that could lead to druggable target identification.

Bioengineers have aimed to develop better models to better translate *in vitro* responses to *in vivo* physiology (figure 1.6c)[66, 86, 87]. However, as materials increase in complexity additional interpretation challenges arise with them. For example, one of the foreseeable applications for biomaterials is as platforms to study cell-drug responses. Currently, a number of studies comparing across reported responses have highlighted the heterogeneity of responses to similar compounds[88] that is mostly attributed to differences in experimental design from different groups. Yet, these

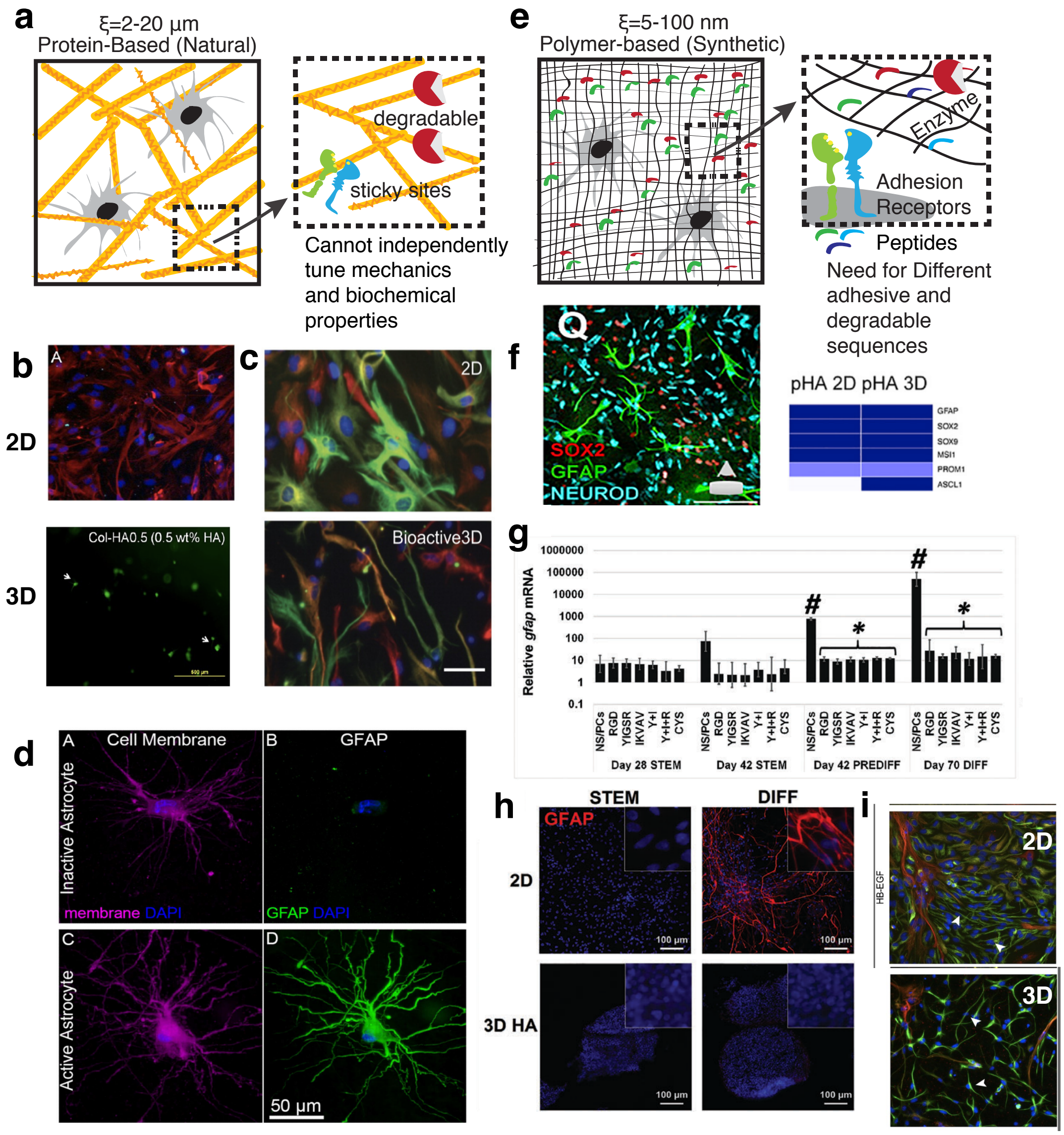

Figure 1.5: Hydrogels as biomaterials to study astrocytes *in vitro:* current activation control and morphology limitations. a) Protein based hydrogels have been employed as biomaterials for *in vitro* cell culture due to their inherent biochemical signals to cells, but their mechanical and biochemical properties cannot be independently tuned. b) Normal astrocyte culture in 2D plastic show adherent morphology and high expression of GFAP (red). Hoechst stain labels the nucleus blue, whereas rhodamine-GFAP labels cytoskeleton red. Astrocyte culture in 3D collagen hydrogel with 0.5wt% Hyaluronic acid (HA) shows rounded morphology of cells with GFP positive (green). Figure from[84] with permission from American Chemical Society. c) Puschmann et al., show astrocyte culture in 2D and a 3D bioactive laminin coated nanofiber-based culture system. Figure shows immunocytochemical detection of intermediate filament proteins GFAP (green) and nestin (red). Figure adapted from[76] with permission from Wiley. d) Examples of inactive and active astrocytes in 3D culture in a gel composed of 2 mg/mL collagen, 1mg/mL Hyaluronic acid, and 1mg/mL Matrigel. Immunofluorescence images of DAPI (blue, and membrane (purple) or GFAP (green). Figure from[75] with permission from Elsevier. e) Synthetic hydrogels allow for controlled modification of mechanical and biochemical properties but, need incorporation of bioactive moieties to allow for cell mediated interactions. f) Immunocytochemical images of fetal primary human

astrocytes cultured in a starPEG-Heparin 3D hydrogel with neural stem cell markers GFAP (green), SOX2 (red) and neural fate determinant NEUROD1 (blue). Heatmap for expression levels of neural stem/progenitor cell markers show high levels of astrocyte activation with GFAP similar to 2D. Figure from[81] with permission from Elsevier. g) GFAP expression by Neural Stem/progenitor cells evaluated with RT-PCR in 2D and 3D hydrogels with different integrin binding peptides. Cells showed a statistically significant decrease in GFAP expression compared to NS/PCs cultured in the same media conditions in 2D after 42 and 70 days of differentiation. Representative images in h) show cells present high staining for GFAP (red) while in a 3D with YIGSR, IKVAV, and RGD peptides did not differentiate to astrocytes as seen with lack of GFAP. Authors show the cells differentiated to oligodendrocyte type astrocytes. Figures from [82] with permission from Wiley. i) Astrocytes intermediate filament morphology visualized by immunocytochemical staining for nestin (green) and vimentin (red) and nuclei with DAPI (blue) in 2D and 3D cultures in bioactive 3D nanofiber cultures with HB-EGF treatment. Figures from [83] with permission from Wiley.

cases were from traditional culture polystyrene (TCPS) which easy to use and hence allows for standardization. As these drug screening assays move to more complex biomaterials other parameters need to be taken into consideration like, for example, how fast cells grow in these systems[89], the incorporation of multicellular components[90], and cell line responses versus patient derived cells[91].

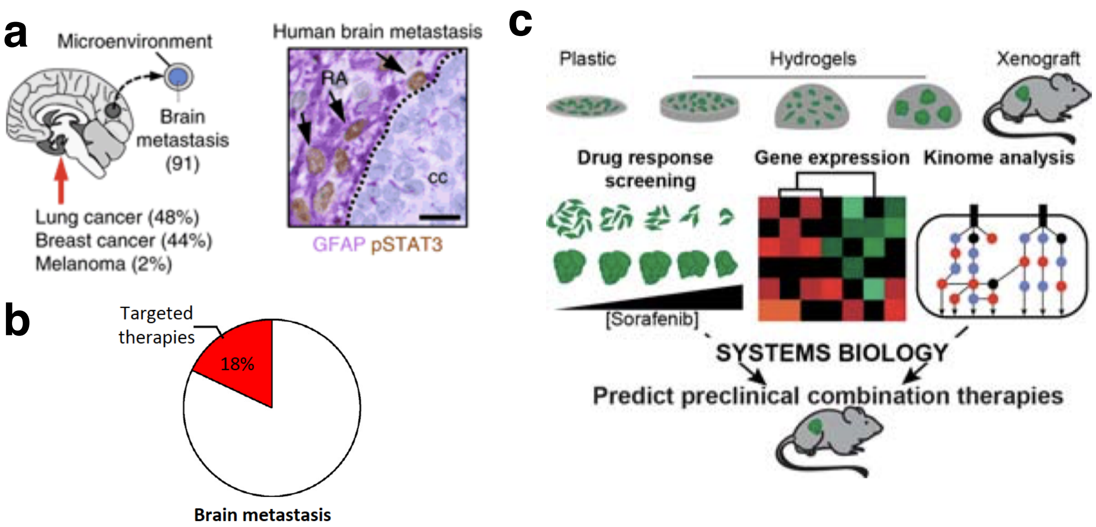

Figure 1.6: Better models can be used to predict preclinical combination therapies in brain cancer. a) Priego et al., showed brain metastases acquired from human donors from lung, breast cancer and melanoma had reactive astrocytes surrounding the tumors. Figures adapted from [85] with permission from Springer Nature. b) Currently, the percentage of patients harboring brain metastases that are susceptible to targeted therapy is very low. Figure from [61] with permission from Elsevier. c) As showed by Schwartz et al., the combination of more physiologically relevant biomaterial platforms could help identify new targets and ECM-mediated drug resistance. Figure from [86] from Biorxiv.

Work by Jansen et al.,[92] show how cell culture media supplement needed to be incorporated in order to rescue the viability of different cell lines cultured in 3D. Similarly, a high-profile study illustrated how growth rate needs to be accounted for in drug response metrics[89, 93]. In order to implement biomaterials as platforms to identify druggable targets, standardization[94, 95] of 3D cultures should be implemented that allow for comparison across studies and better translation between models.

1.3 Hypothesis

Current models to recreate the brain extracellular matrix are very limited in their ability to mimic human astrocyte reactivity *in vitro*. Here, I hypothesize the design and implementation of a tissue specific hydrogel would provide a tool to control for astrocyte activation *in vitro*. While current brain hydrogels can mimic some of the mechanical properties of the tissue, they are too simplistic in the array of bioactive cues they provide for cell interaction. Considering the unique brain physiology and protein content will help pinpoint what drivers of the ECM can control for astrocyte reactivity. I foresee that the development of such a platform would help advance biomaterial applications in hypothesis driven and drug testing methodologies of the brain.

1.4 Objectives

The following were the objectives for this dissertation:

1. Mechanical and proteomic characterization of human brain tissue
2. Design of a brain specific hydrogel to control for astrocyte activation *in vitro*
3. Standardization of *in vitro* biomaterials and their correlation with *in vivo* physiology in glioma motility via effect size
4. Assessment of biomaterials as platforms for drug screening and growth rate drug response

1.5 Significance

I have conducted a throughout characterization of human brain tissue providing detail information on its ECM composition and biomechanical responses. I have designed a fully synthetic brain hydrogel filtering integrin binding and matrix metalloproteinase degradable proteins incorporated as peptides in a PEG based hydrogel. This approach resulted in a brain-specific ECM microenvironment that provided an optimal niche for quiescent astrocyte culture achieved for the very first time *in vitro*. I explored external cues to induce astrocyte activation and how the phenotype of these cells is changed upon cytokine-induced activation *in vitro*. I explored possible avenues to standardize cell responses obtained from biomaterials to allow for comparison across reports and expand drug screening applications. Overall this is the first *in vitro* system to allow for quiescent astrocyte culture that will open avenues in the exploration of astrocyte role in traumatic brain injury, cancer and other neurological diseases not possible in current systems.

CHAPTER 2

BULK, LOCAL AND IN SITU MECHANICAL PROPERTIES OF BRAIN TISSUE

2.1 Introduction

In order to characterize the extracellular matrix (ECM) properties of brain tissue we start first with the biomechanics of the organ. Work by others has shown that the dynamic changes in the stiffness and viscoelastic properties of brain tissue correlate with Alzheimer's disease[38], traumatic axonal injuries[39], cortical contusions[40] and brain tumors[41], and it is the ECM, which occupies an estimated 20% of the brain organ, that is considered to give rise to these mechanical changes[6]. In the brain, during neurulation, mechanical changes at the tissue level can alter cytoskeletal contractility[28] and the ability of cells to bind to ECM components, leading to an increase in cell ECM and enzyme production[96] This crosslinking can further alter tissue-level mechanics[97]. Similarly, the changes in ECM composition during brain development give rise to differences in the mechanical properties of normal tissue[19]. Transitions of mature brain from a healthy to a disease state during glioblastoma have also shown to result in mechanical property changes due to the increase in ECM proteins like Tenascin-C[25, 31]. Together, these studies highlight the importance of understanding brain mechanical properties and their relation to disease progression. To fully understand the dysfunctions inherent to brain disorders, it is important to consider the mechanical properties of the brain and the signaling changes they induce in cells. Thus, the response of brain tissue to deformation would be of interest for tissue engineering, modeling of TBI, and the design of brain specific biomaterials like is the motivation of this work.

However, while there have been many studies on the elastic, and viscoelastic properties of brain, there are discrepancies in the reported mechanical properties of the tissue. Reports of the Young's elastic modulus, *E*, of brain range from 100s of Pa to 10s of kPa,[22, 29, 32] and are reported to vary significantly among experimental techniques[32, 43, 98] (figure. 2.1). Previous studies probing different compartments of the brain have identified that brain tissue exhibits location-dependent mechanical properties like intraregional anisotropy for white matter in contrast to gray matter[98-100], intraregional variations in different compartments of the brain[101-103], and regional inhomogeneities between corpus callosum, corona radiata, brain stem and gray matter structures[99, 104]. These elastic and viscoelastic properties of brain tissue have been measured most commonly by rheology[31, 98, 103, 105], shear relaxation[99, 105-107], and unconfined uniaxial compression or tension[100, 105, 108]. At the microscale, measurements have been conducted via macroscale instrumented indentation[101, 103, 109-111], and atomic force microscopy (AFM)-enabled instrumented indentation[104, 112, 113]. The macro and micrometer length scales of these techniques are limited in their spatial resolution and the need for sectioning of the sample limits the capabilities to test intra- and inter regional variations *in situ*.

To overcome these limitations, we have complemented, alongside shear rheology and indentation, two relatively new mechanical techniques: needle-induced cavitation rheology (NICR) and volume-controlled cavity expansion (VCCE) as techniques to measure elastic modulus *in situ* at an arbitrary location. This approach allows to explore the continuity among diverse mechanical techniques and sample preparations effect on the characterization of porcine and murine brain mechanical properties. NICR and VCCE provide the capabilities of testing local deformation, *in situ* at a spatial resolution within 100μm to 10 mm not possible with indentation or rheology[114-117]. NICR has recently been used to explore mechanical properties of polymers and tissues like the eye[114], bone marrow[117], lung[118] and skin[119]. Similarly, VCCE incorporates the same methodology of NICR with an incompressible working fluid[120], providing additional information about the cavity volume which cannot be visually extracted in biological samples due to the inherent opaque nature of most tissues. Here the mechanical properties of porcine brain were measured via these four techniques to characterize brain mechanical properties at a specific location and to introduce NICR and VCCE as an alternative, inexpensive technique to characterize localized modulus of brain tissue. Results show brain modulus remains constant after freezing and is dependent on strain rates. Indentation, rheology and VCCE find brain modulus is approximately 1kPa while NICR and VCCE show modulus stiffens at higher stretches where NICR provides a significantly higher modulus due to its relation to a critical pressure. A finite element modeling (FEM) simulation was used to investigate this critical pressure event with two constitutive models upon introducing a cavity in brain.

2.2 Results

2.2.1 Wide range of variation in brain modulus reports across the literature

Figure 2.1 illustrates the wide range of modulus reported for brain tissue via two of the most widely used techniques: shear rheology and indentation. Differences in this set of values could be attributed to parameters like technique[43], post-mortem time[121, 122], location[103], temperature[122, 123], species[124] and strain rates[125]. Figure 2.1 a-c illustrates the elastic (G') and loss (G") modulus obtained via oscillatory shear rheology for bovine, porcine and human brain. From these reports, most of the measurements were conducted within 6 hours post-mortem, however, a large range of moduli is reported for porcine brain mostly due to the lack of availability of human brain (fig. 2.1a). Given the capability of the rheology set up to control for temperature, this parameter has been used and shown to impact the modulus reported. From our search from a pool of 10 publications, we found that these reports had a wide range of temperatures to measure brain under shear, ranging from 4 to 37 ^{o}C (fig. 2.1b). Similarly, the frequency under which shear was performed ranged widely across these reports (fig. 2.1c). Although these reports show a somewhat similar range for G' and G" for these range of frequencies, this can be a limitation for the design of cell instructive biomaterials as these values range from 0.1 to 10 of kPas and biomaterials, particularly hydrogels[126], have been shown to induce differences in cell responses out of the modulation of this property alone. For this reason, it is difficult to compare brain modulus across species or the effect of temperature or post-mortem time in brain tissue and how a single value could be used to design a biomaterial. Additionally, the need to section samples in shear rheology could also impact the modulus reported[110].

To overcome these challenges, there has been an increasing interest in acquiring the localized mechanical properties of brain tissue. This is the case of indentation, where local properties can be measured, however, a limited set of publications have focused on the mechanical properties of brain with this technique. Figure 2.1 shows a comparison of the Young's modulus reported for bovine, porcine and rat brain for white and gray matter locations via indentation. Comparison within the same species does not show significant discrepancies for white and gray modulus (fig. 2.1d-e). However, there seems to be discrepancies between species as rat brain reported a lower modulus compared to bovine brain measured *in vitro* (fig. 2.1d-e). Only one report has conducted indentation in the porcine brain *in vivo* while the animal was alive and under anesthesia[109]. The modulus reported for this work seem higher that that obtained for porcine brain *in vitro* (fig. 2.1d). Among the work compared in figure 2.1d and e, the major difference was the post-mortem time of testing, as temperature was not controlled or reported in these

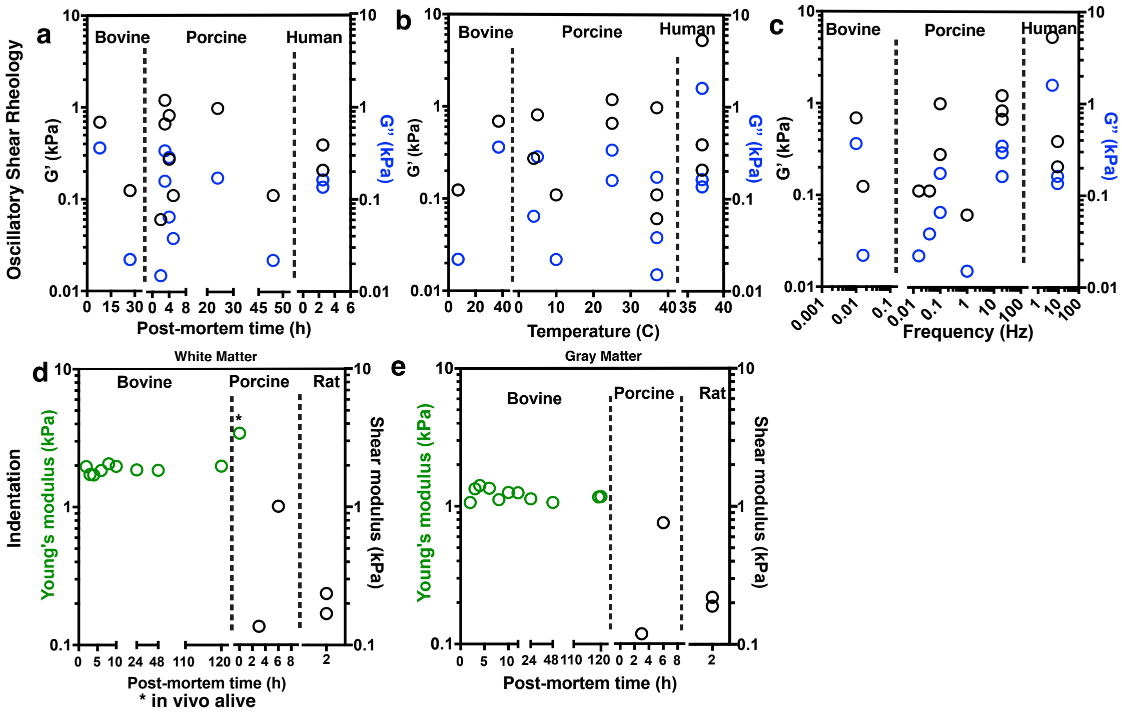

Figure 2.1: Wide range of modulus reported for brain tissue. a) Storage (G') and loss (G") modulus reported in literature for bovine, porcine and human brain data from[122] as measured via oscillatory shear rheology and presented as a function of post-mortem time, b) temperature and c) frequency. In shear rheology most measurements were conducted within 6 hours post mortem but wide range of modulus reported could be attributed at differences in temperature (b) during testing and frequency tested (c). a) Young's modulus reported in the literature for bovine (78kHz), porcine (20kHz) and rat (20kHz) brain white and b) gray matter as measured via indentation (flat probe bovine and rat; spherical probe porcine) presented as a function of post-mortem time at the moment of testing. Modulus obtained via indentation for porcine and rat brain was reported converted to shear modulus in the publication to allow for comparison to shear rheology reports. Modulus remained constant within the time-lapse tested for bovine brain. There are apparent differences between species modulus. Limited amount of work for brain tissue measurements via indentation. Bovine data from [111] Porcine data from [109](*in vivo),* [103] and [104]. Rat data from [127].

publications (fig. 2.1d-e). However, post-mortem time comparison for bovine brain shows the modulus follows a constant trend. Other parameters that can vary in this technique include probe geometry and dimensions[111] and loading rates[128]. The methodology across these reports was similar. Rates were within 20-78 kHz, all work was with flat punch probe outside of *in vivo* porcine brain that used an spherical punch. No indentation reports for human brain were found.

2.2.2 Four complementary techniques to characterize brain bulk, local, and *in situ* properties

To overcome the large range of values reported in literature (figure 2.1), intact brain tissue was harvested, with minimal post mortem time, from 6-month old pigs and 12-weeks old mice. Porcine brain was chosen as a model organism because they are anatomically similar to humans[129], while murine brain was chosen for their widespread use as subjects for *in vivo* studies of the brain[64]. Figure 2.2 summarizes the four techniques used to measure the localized and bulk mechanical properties: shear rheology (fig 2.2a), indentation (fig. 2.2b), needle-induced cavitation rheology (NICR) (fig. 2.2c) and volume-controlled cavity expansion (VCCE) (fig.2.2d). Shear rheology and indentation are two conventional techniques most commonly used to characterize brain tissue. Shear rheology allows for measurements of the bulk elastic or viscoelastic properties of a biopsy punched sample by analyzing the material response to an applied frequency deformation (fig. 2.2a). Indentation provides the advantage of testing local mechanical properties of a material upon applying a load within an indentation depth resulting in a load-unload curve that can be related to the effective modulus of the material (fig. 2.2b). Both shear rheology and indentation techniques require the sample to be manipulated to fit specific dimensions. Rheology samples were punched to an 8mm diameter in the white matter region of cortical slices, while brain slices of 1mm height were used for indentation in white and gray matter regions.

Needle-induced cavitation rheology (NICR) and volume-controlled cavity expansion (VCCE), in contrast, do not require sample manipulation as they provide the advantage of testing at an arbitrary location (fig. 2.2c-d). Both of these techniques rely on the insertion of a needle at a specific location where fluid is pressurized into the system. For NICR, this fluid can be air (compressible) or water (incompressible) and multiple needle radii are used to obtain a critical pressure (Pc) (fig. 2.2c). By obtaining a critical pressure as a function of needle radii an effective young's modulus can be obtained following the relation Pc = 5/6E + 2λ/r[115]. VCCE, in contrast, monitors the pressure as a function of volume while an incompressible fluid (silicone oil) is pressurized in the system[120]. The volume measurements are transformed into an effective cavity radius (a) and the pressure-effective radius results are used to find the elastic properties of the material in accordance with a chosen constitutive model (fig 2.2d).

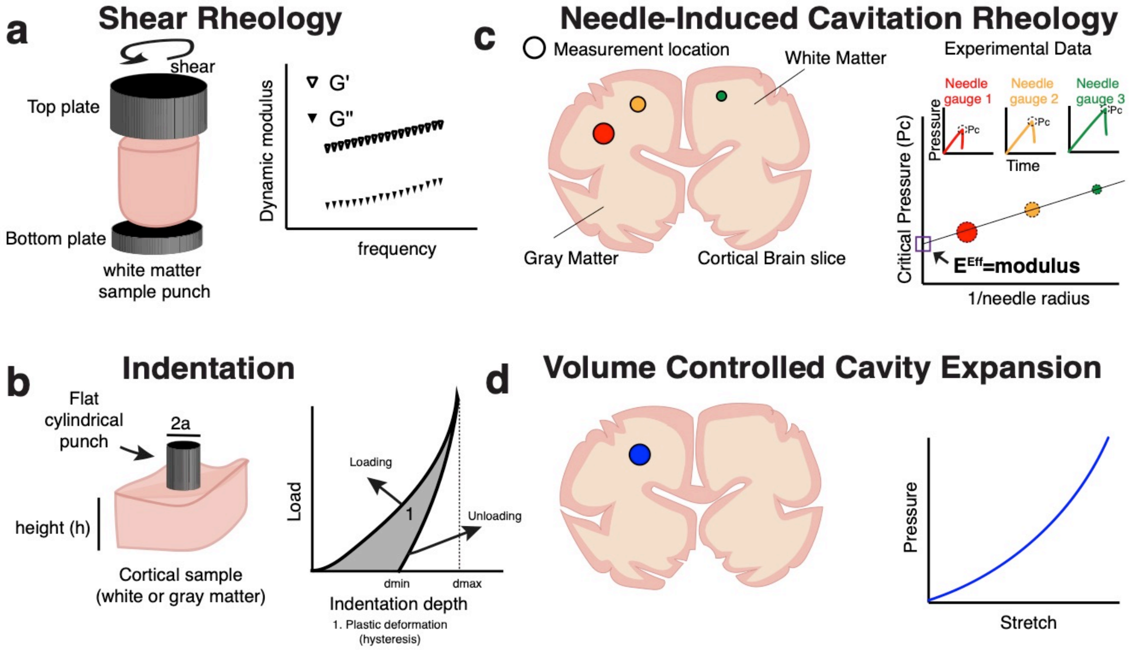

Figure 2.2: Measurement of brain mechanical properties via four techniques. a) White matter was excised from porcine brain slices with a sample punch of diameter of 8 mm. Samples were placed between two parallel plates and oscillatory shear was performed to obtain a dynamic modulus. Open and closed triangles represent elastic and loss modulus, respectively. b) A custom-built indentation instrument was used to measure localized properties of brain tissue. A flat cylindrical punch with diameter of 1.5 mm came into contact with a cortical sample containing white and gray matter regions of height (h). Loading force was tracked as a function of indentation depth and a modulus was extracted from the loading curve. Cartoon depicts loading curve histogram (1) representative of hysteresis exhibited by brain samples. c) Needle-induced cavitation rheology was performed to assess local deformation of brain *in situ.* Porcine brain coronal slices were tested at white or gray matter regions. Cartoon circle depicts location of measurement. Multiple measurements are conducted with needles of varying small radius size to account for the role of surface tension. Single measurements tracked pressure increase in the system as a working fluid (compressible or incompressible) is pressurized in the sample. A critical pressure (Pc) is obtained and plotted as a function of 1/needle radius. An effective Young's modulus (E^{eff}) can be extracted

from the y-intercept of this curve following the relation Pc = 5/6E + 2λ/r. d) Volume controlled cavity expansion is an extension of needle-induced cavitation rheology in which a needle of larger diameter is placed in the location of measurement and an incompressible fluid is pressurized in the system. Throughout the experiment the pressure inside a cavity is measured as well as the volume of the cavity which is then transformed into an effective cavity radius. The pressure-effective radius curve is used to find the elastic properties of a material in accordance with a chosen constitutive model.

2.2.3 Conventional techniques show brain tissue has a low Young's modulus and these differ per species

Figure 2.3 shows the modulus comparison for rheology and indentation of porcine and murine tissue. We found indentation and rheology values of white matter were similar in the case of porcine brain and showed no significant discrepancies in the modulus reported for the same brain (fig. 2.3a). In the case of murine individual brains, the brain was too small and did not allow for different technique measurements of the same brain. We found that comparison of modulus measurements between different animals showed no significant difference between the two techniques (fig. 2.3b). Comparison of the bulk modulus of both techniques, average of all brains, show no significant difference in the case of porcine brain (fig. 2.3 c). We found, however, indentation gave a higher modulus for murine brain as compared to rheology (fig. 2.3d). Similarly, indentation provided a wider range of values in contrast to shear rheology. Together, these results show minimal variation in the modulus across individual animals as compared via two conventional techniques that measure bulk mechanical properties. For measurements conducted within the same brain via two distinct techniques, modulus obtained was very similar. Comparison across species via indentation shows murine brain had a larger moduli.

2.2.4 Young's modulus of brain tissue remains constant after freezing

Post-mortem tissues can be used for a myriad of applications ranging from cell culture to genetic and molecular profiling. Conservation of these samples, if required for RNA and protein work, is mostly undergoing freezing at very low temperatures. For this reason, it would be of interest to investigate how mechanical properties of the tissue change overtime after harvest and if freezing manipulation would change the mechanical properties of the brain. We found, via indentation, that the Young's modulus of porcine and murine brain remained constant within 6 hours post-harvest (fig. 2.4 a). Similarly, comparison of post-harvest and post-thawed brain tissue showed similar modulus via shear rheology measurements (fig. 2.4 b-c). Given that one of the major motivators to characterize brain mechanical properties in species such as porcine is due to the challenges in obtaining fresh human brain tissue, we decided to test the mechanical properties of post-thawed human brain tissue. We acquired three human brains with minimal post mortem time as indicated by the NIH neurobiobank report and tested the Young's modulus via indentation of the white and gray matter structures. We found that the Young's modulus was very similar to that of post-harvest porcine brain when probed at white and gray matter structures (fig. 2.4 d).

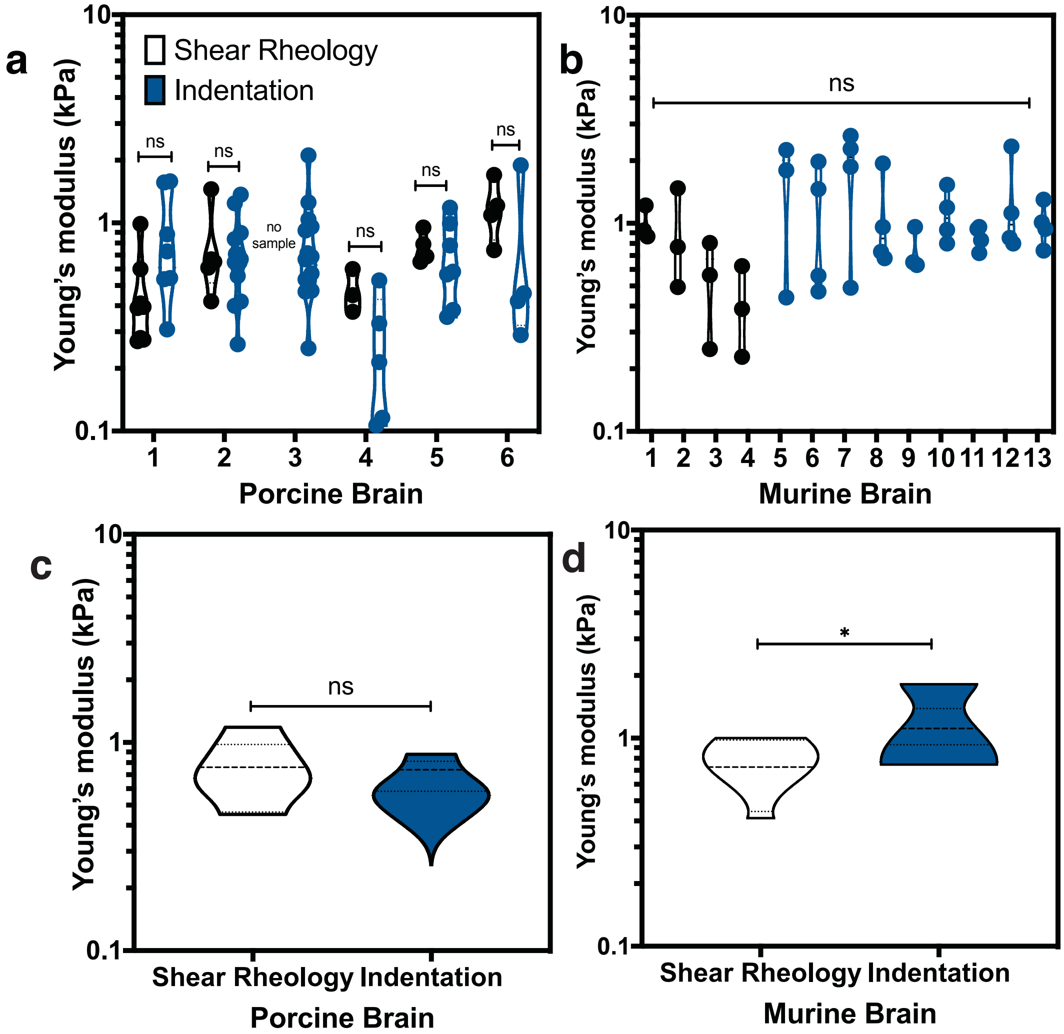

Figure 2.3: Porcine and murine brain Young's modulus as measured via indentation and shear rheology techniques. a) Six porcine brains were tested via shear rheology (black) and indentation (blue). White matter samples were extracted from the same porcine brain and prepared

for each technique. Indentation measurements illustrate a wider distribution of moduli measurements within the same brain. Comparison of average modulus between both techniques shows no significant difference between measurements. Each data point represents an independent measurement. b) Thirteen murine brains were acquired, and measurements were conducted on individual brains due to their small size. Comparison across modulus obtained for all murine brain showed no significant difference between independent brains. c) Comparison of bulk measurements obtained via shear rheology and indentation for all porcine brains show no significant difference between the modulus reported by each technique. Porcine brain reported a modulus of approximately 1 kPa. d) Comparison of bulk measurements for all murine brains shows indentation reported a modulus higher than that obtain via shear rheology. Shear rheology data was acquired in collaboration with Dr. Nathan Birch and Dr. Jessica Schiffman. Statistical analyses were performed using Prism (GraphPad). Data in a, c and d was analyzed using a t-test. Data in b was analyzed using a one-way analysis of variance (ANOVA). * indicates $P<0.05$; N.S., not significant.

We similarly found that modulus had a weak dependence with temperature. Shear rheology measurements of porcine brain complex modulus (G*) show a slightly lower modulus obtained at 37 ^{0}C as compared to 25 ^{0}C (fig. 2.5 a). This was also the case for viscous properties of brain as the viscosity showed very weak dependence with temperature (fig. 2.5 b). Together, these data show that the Young's modulus measured for brain tissue after flash freezing conservation is similar to that of post-harvest brain.

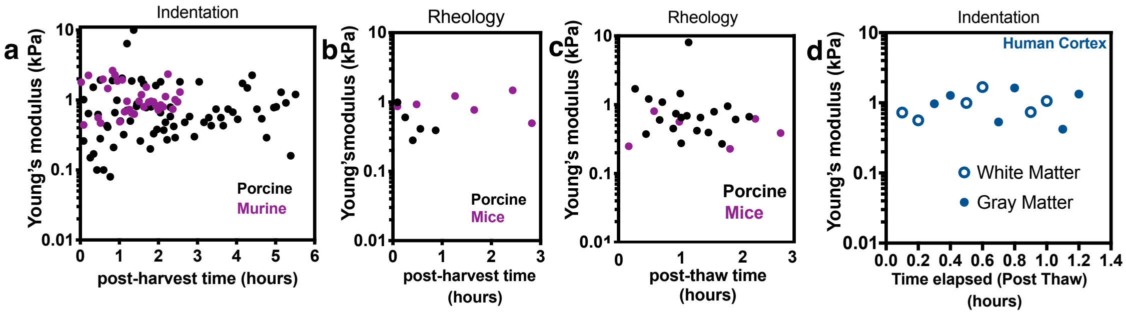

Figure 2.4: Similar Young's modulus between post-harvest and post-thaw brain samples. a) Young's modulus measurements for porcine (black) and murine (purple) brains as measured via indentation over a period of 6 hours post-harvest shows a constant trend. b) Comparison between post-harvest and c) post-thaw Young's modulus measurements obtained via shear rheology show a similar modulus within a period of 3 hours of testing. Shear rheology data gathered in collaboration with Dr. Nathan Birch and Dr. Jessica Schiffman. d) Post-thaw human Young's modulus as measured via indentation at white (blue open circles) and gray (blue closed circles) matter locations exhibits similar Young's modulus to that of fresh porcine and murine brain. Data depicts data gathered for three human brains in order of testing.

However, we also found that the method of freezing impacts the load-unload curves obtained via indentation. Figure 2.6 compares loading cycles across post-harvest samples (fig. 2.6a), flash frozen-then thawed (fig, 2.6b), and slowly frozen at -80 ^{o}C (fig. 2.6c). Post-harvest samples exhibited large hysteresis at every cycle performed (fig. 2.6a). We did observe an increase in modulus with increasing cycle at the same location after samples were allowed to recover for 50 seconds in each cycle. Post-thaw samples tested that were previously flash frozen exhibited a large hysteresis in the first cycle that was decreased with subsequent loading (fig. 2.6b). This change was more dramatic for post-thaw samples that were previously frozen slowly at -80 °C as the hysteresis area was smaller (fig. 2.6c). A significant increase in the loading slope was seen after the first cycle, however, subsequent cycles had a very similar slope (fig, 2.6c). Together, these data show that the method of freezing impacts the mechanical properties of brain tissue.

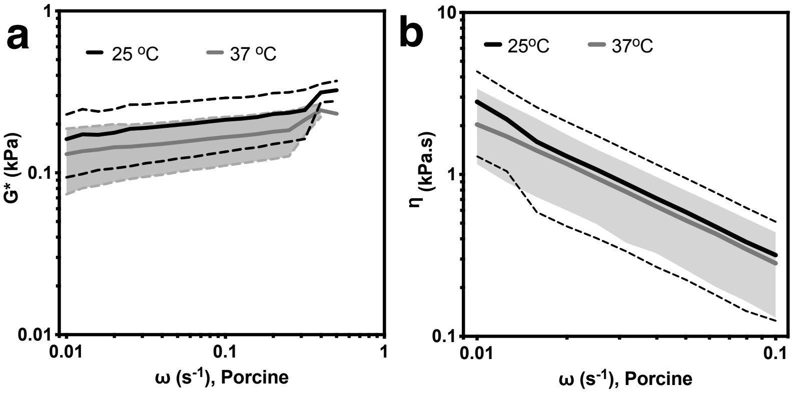

Figure 2.5: Porcine brain complex modulus and viscosity relation with temperature and frequency. a) Complex modulus (G*) obtained for six porcine brain samples at 25 °C (black) and 37 °C (gray) shows slight decrease. Measurements at both temperatures show a weak dependence on frequency. Data are mean (solid line) and standard deviation (dashed line for 25 °C and shaded area for 37 °C). b) Measurements of viscosity at 25 °C and 37 °C show very weak dependence on temperature as measured via shear rheology. Shear rheology data gathered in collaboration with Dr. Nathan Birch and Dr. Jessica Schiffman.

2.2.5 Young's modulus of brain tissue exhibits strain rate dependence and strain hardening more dramatic at higher strains

Both shear rheology and indentation techniques apply a frequency dependent strain to the material. Work by others has shown that brain tissue exhibits a strain rate dependent response in techniques like uniaxial compression (fig. 2.7 a-c) and indentation (fig. 2.7 d-e). This has also been observed in different species like porcine (fig 2.7 a, d), bovine (fig 2.7 b,e), and human brain (fig. 2.7c). We next decided to explore how brain tissue strain rate dependent properties affect the modulus obtained from these measurements. To obtain linear elastic properties of brain shear rheology is conducted in the quasistatic regime[43]. However, moving beyond to faster strain rates brain tissue exhibits higher modulus values (fig. 2.7).

Figure 2.8a shows that the modulus reported in literature for porcine brain, as well as that conducted in this work, shows a clear dependence on the strain rate. We found that regardless of freezing, post-thaw human brain still exhibited a strain rate dependence in the modulus obtained via indentation (fig. 2.8b). Similarly, we found a strong correlation moving beyond the quasistatic region to those values reported at very high strain rates (fig. 2.8c). Together, these results highlight the strong dependence of modulus on strain rate and how this could be one of the reasons why there is a wide variation in brain tissue modulus reports in the literature (fig. 2.1). It is important to mention, however, that literature values that reported very high modulus at high strain rates were also conducted at high strains (50%, indentation) (fig.2.8c).

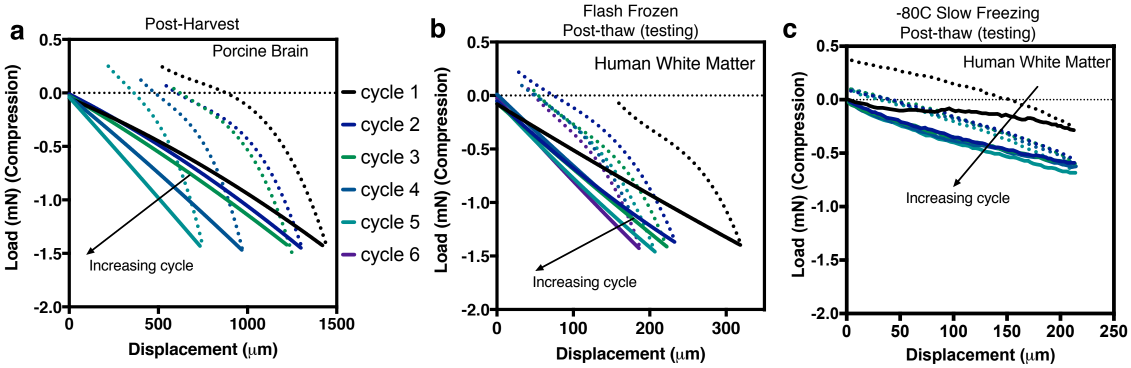

Figure 2.6: Method of freezing impacts mechanical properties of brain. a) Load-unload curve for porcine brain as measured post-harvest. Each cycle exhibits large hysteresis and the loading curve increased with each subsequent cycle. b) Load-unload cycles for human brain tissue flash frozen after low post-mortem time. Initial cycle exhibits large hysteresis and slope increases with each cycle. c) Load-unload curves of human brain re-frozen upon thaw and subsequently tested via indentation. Curves show less hysteresis in comparison with flash-frozen sample. Loading curve increased with subsequent cycle. All cycles were performed within 50 seconds from each other to allow for tissue recovery after each cycle.

2.2.6 NICR and VCCE show brain tissue stiffens at larger stretches and results in modulus variation

Because of the large local variation reported by others, we wanted to introduce a technique that would allow for location specific measurements. Needle induced cavitation rheology (NICR) has recently been used by others to measure mechanical properties of biological samples and has been validated as a robust technique to measure mechanical properties alongside more conventional techniques like indentation and rheology[114, 115, 130-132]. This technique allows us to induce a localized increase in pressure *in situ* that can be related to the Young's modulus of a material by a single measurement if we know the surface tension between the solvent and the material following the relation Pc = 1.5E [130]. Alternatively, when the surface tension of the material is not known, several measurements can be conducted with multiple needle radii and the Young's modulus can be estimated by the intercept of the relation shown in section 2.1.1. The technique, which relies on a hyperelastic neo-Hookean material model[133], has the capability of measuring local elastic properties on the length scale of microns to millimeters not possible with rheology or indentation. Similarly, VCCE is a novel technique to measure nonlinear elastic properties of compliant materials such as soft PDMS[120]. Since VCCE is an extension of NICR methodology, it has the same capabilities of *in situ*, localized measurements as NICR; however, since VCCE also allows measurement of both pressure and volume of injected incompressible fluid, it allows for fitting of any incompressible hyperelastic constitutive equation with a single measurement. Here we expanded the use of this technique to characterize the elastic behavior of the brain tissue with an incompressible two-term Ogden model, which has been previously shown to capture the strain stiffening response of the brain tissue[100].

Figure 2.9a shows representative data gathered for three porcine brains via VCCE where similar pressure-stretch curves can be observed for measurements at low stretches (below 1.1) while significant differences across brains are observed at larger stretches. Analysis of the localized modulus of white and gray matter via VCCE resulted in small Young's modulus within the smaller stretch regime (fig. 2.9b). From this analysis we found white matter had a significantly higher Young's modulus as compared to gray matter in the porcine cortex (fig. 2.9b). In the case of NICR, because the surface tension of the material is not known, we most conduct multiple measurements with needles of different radii as shown in figure 2.9c. The brain modulus calculated from this approach depends on the formation of an instability event that results in a critical pressure (Pc). From this Pc-needle relation we can obtain an effective Young's modulus from the intercept (fig.

2.2c and fig.2.8c). For the twelve brains tested via NICR, we found large variation in the modulus and very high values (fig. 2.9d). We will discuss these results further in section 2.1.7.

In the case of indentation, where we can also test white and gray matter structures of the cortex, we found no significant difference in the modulus reported for individual white and gray matter structures of porcine brain (fig. 2.9 e). This is in contrast to VCCE, were we consistently found a higher modulus in white matter (fig. 2.9b). Comparison of the four techniques illustrates that VCCE shows a similar modulus as those obtained via rheology and indentation since we consider the smaller stretch regime (fig. 2.9 f).

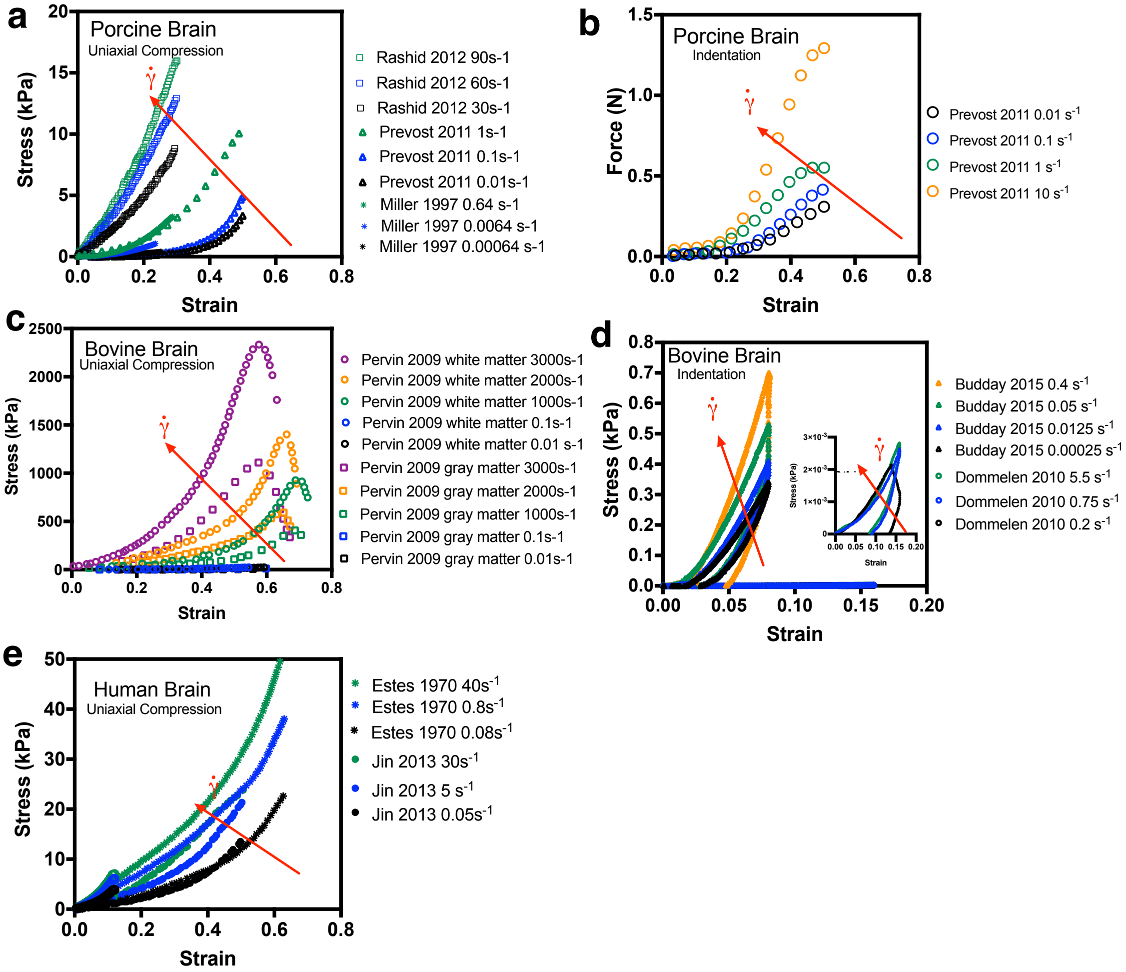

Figure 2.7: Literature reports show brain tissue exhibits strain rate dependence. a) Stress-strain curves for porcine brain b) bovine brain and c) human brain as measured via uniaxial compression show strain rate dependence in literature reports. d) Stress-strain curves for porcine and e) bovine brain show loading rate dependence as measured via indentation. f) Load and

displacement curves for post-harvest murine brain also show loading rate dependence as measured via indentation.

NICR reported significantly higher modulus as compared to the other techniques since it relies on a critical pressure, but we still observed a higher modulus for white matter as compared to gray matter. Hence, we next sought to understand why NICR would provide significant higher modulus for the same porcine brain samples in which indentation and rheology were conducted.

2.2.7 Analytical and finite element modeling predict that cavitation instability is unlikely in strain-hardening tissues like brain

We used analytical and finite element (FE) models of cavity growth to simulate the pressure-stretch relationship in absence of surface tension (fig. 2.10a) and in the presence of surface tension (Fig. 2.10b) for the Neo-Hookean and Ogden material models. The analytical model of a spherical cavity plots pressure vs. hoop stretch at the surface, while the FE model plots pressure vs. areal stretch, consistent with the work of Hutchens and Crosby[130]. FE model uses a geometry with the needle retracted from its initial position, as shown in figure 2.10c. From figure 2.10a, we see that the FE model gives a similar P/E – stretch relationship to the analytical model, and that the retracted needle geometry (of an initially cylindrical cavity (i)) shows a near-spherical geometry, at low stretches (ii) and especially at larger stretches (iii).

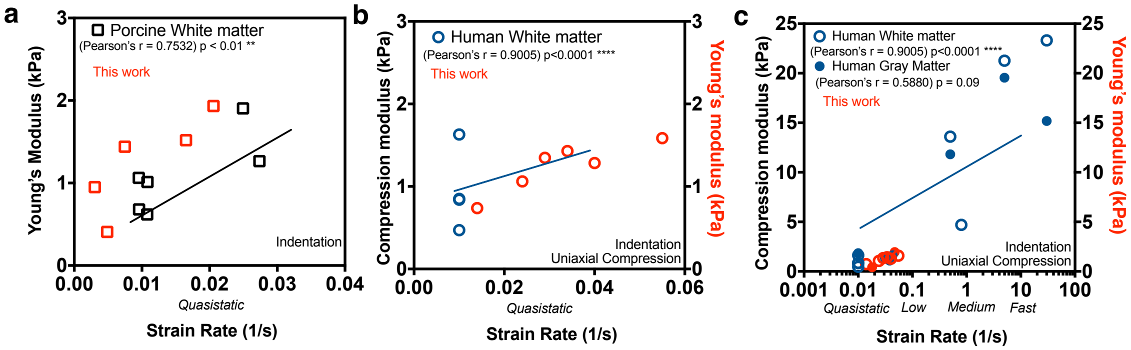

Figure 2.8: Modulus correlates with strain rate. a) Porcine brain Young's modulus as measured via indentation shows correlation with strain rate with Pearson's r r=0.75 (p<0.01). Literature porcine brain data (black) from [104] and [103] .b) Compression modulus reported from uniaxial compression test for human white matter and post-thaw human brain measured in this work shows correlation with strain rate with a Pearson's r r=0.9 (p<0.0001). Literature data from [122] c) Modulus correlation at larger strain rates reported in literature shows Pearson's r=0.59 (p=0.09) and r=0.9 (p<0.0001), respectively. Modulus of post-thaw human tissue collected in this work (red circles) also shows correlation with strain rate. Pearson's correlation was performed using Prism (GraphPad). **, **** indicate P<0.01 and P<0.0001.

Since cavitation instabilities occur when there is either a plateau or maximum in the pressure-stretch curve, our FE and analytical models do not predict cavitation in the two-term Ogden model used here (same as Hutchens and Crosby) due to appreciable strain stiffening. The Ogden model shows a pressure-stretch curve that continues to increase with increasing stretch, unlike the Neo-Hookean model, where P/E asymptotically approaches 5/6 at increasing stretch (fig. 2.10a). When the effect of surface tension between air and tissue is superimposed with elastic resistance to deformation, the surface tension provides a larger driving force for cavitation instability because it has a decreasing stress-stretch relationship for lambda > 1.5. However, even when surface tension is incorporated in the model with conservative values (low E ~ 1 kPa, low needle radius r ~100 um), there is no maximum in the pressure-stretch curve, indicating that cavitation is not expected due to strain stiffening. Together this data indicate that a cavitation instability is unlikely in brain tissue due to its strain hardening properties.

Because others have shown that the critical pressure obtained via NICR can be associated to elastic events or plastic deformations[115, 116] we performed pressurization cycles in post-harvest murine brain to track the critical pressure in subsequent cycles. Here, we hypothesized based on previous work[116], that if the critical pressure were to change over time (decrease) another event outside of cavitation is occurring in brain tissue, which could be indicative of fracture. Figure 2.11 shows pressurization cycle results in which we see a decrease in the critical pressure after the first NICR cycle. Work by others has illustrated that brain undergoes softening when loaded after a certain threshold until material failure is observed[100]. It is possible this decrease in critical pressure in brain tissue via NICR is associated to a fracture event.

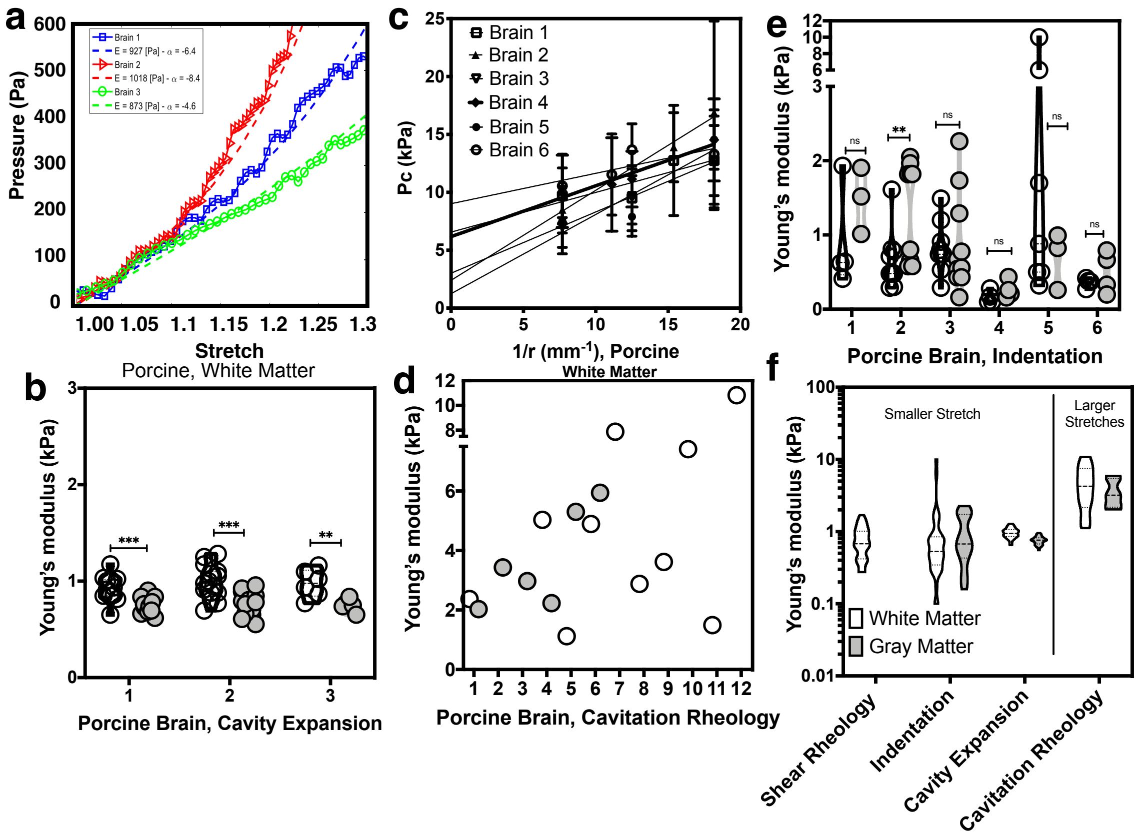

Figure 2.9: Needle-induced cavitation rheology and cavity expansion show brain tissue stiffens at larger stretches. a) Representative data for three porcine brains obtained via cavity expansion. Pressure-stretch curves show similar slope at smaller stretches. At higher stretches pressure increases significantly and higher variation between brain tissue can be observed. b) Localized measurements of porcine brain via cavity expansion at low stretches show white matter modulus is significantly higher than gray matter. Each circle represents a single measurement. c) Representative cavitation rheology data for white matter. Multiple needles of varying diameter are used to obtain a critical pressure (Pc). The y-intercept of a linear regression between the critical pressure and 1/needle radius is used to obtain the modulus following the equation $Pc = 5/6E + 2\boldsymbol{\gamma}/r$. d) Young's modulus obtained via cavitation rheology shows a wider range of moduli for white matter (white circles) and gray matter (gray circles). Each data point represents the y-intercept obtained from cavitation rheology measurements in a single brain. e) Violin plots of white matter (white circles) and gray matter (gray circles) modulus obtained via indentation show no significant difference between these two structures. Each circle represents a single measurement. f) Young's modulus obtained for porcine white (white) and gray (gray) matter for rheology, indentation, cavity expansion and needle-induced cavitation rheology. Cavitation rheology show significantly higher values for brain potentially for measurements conducted at larger stretches. Cavitation rheology and cavity expansion data gathered in collaboration with Aleksander Mijailovic, Dr. Krystyn Van Vliet, Shabnam Raayai-Ardakani, Dr. Tal Cohen and Dr. Alfred Crosby. Statistical analyses were performed using Prism (GraphPad). Data in b and d was analyzed using a T-test. **, *** indicate $P<0.01$ and $P<0.0001$; NS, not significant.

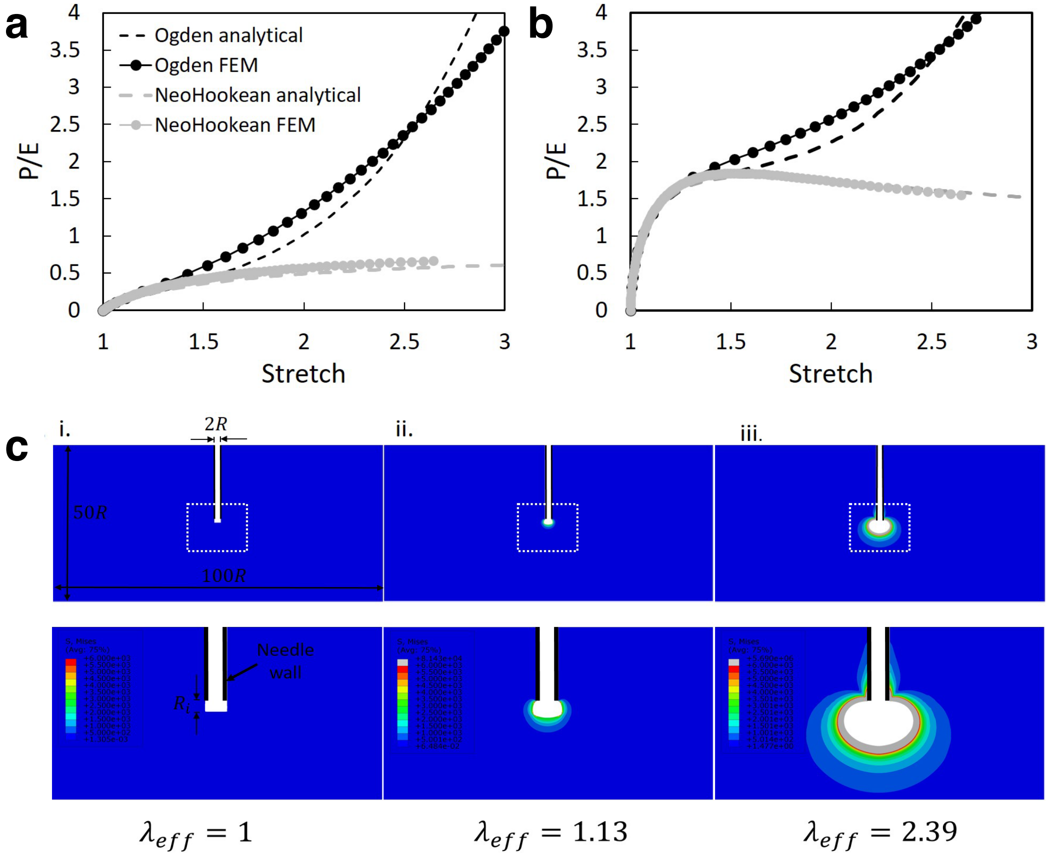

Figure 2.10: Finite element modeling shows the strain stiffening behavior of brain does not allow for maximum pressure-stretch values. a) Pressure-stretch curves normalized by Young's modulus (E) for a Neo-Hookean model (gray) and an Ogden model of brain tissue reproduced from Hutchens and Crosby, 2014 (black), with $\boldsymbol{\alpha}_1$=4, $\boldsymbol{\alpha}_4$=8, $\boldsymbol{\mu}_1=\boldsymbol{\mu}_2$. Dotted lines represent analytical results for a pressurized sphere, and circles represent finite element models of a needle geometry. The Neo-Hookean model approaches the asymptotic value P/E=5/6, indicating expected cavitation, whereas the Ogden model shows extensive strain stiffening behavior without an asymptotic plateau, suggesting cavitation instabilities cannot occur. b) Pressure-stress curves from part (a) with surface tension included, using a needle with radius of 100 $\boldsymbol{\mu}$m, a surface tension value of 72 mN/m, and Young's modulus of 1 kPa. Under these conditions, a Neo-Hookean material is expected to cavitate as shown by a peak in the pressure. However, even in this conservative model where the effect of surface tension is most pronounced (i.e., small needle radius, low Young's modulus), the strain stiffening behavior of the Ogden model does not allow for a maximum value in the pressure-stretch curve, and thus cavitation should not occur. c) Axisymmetric finite element modeling of the needle geometry for the brain shown in figure (a) with areal stretches of i. λ_{eff} = 1, ii. λ_{eff} = 1.13, and iii. λ_{eff} = 2.39. The top panel represents the full geometry (with a needle radius *R*, a width of 100*R* and height of 50*R*) and the bottom panel represents a zoom of the full geometry. In the underformed configuration (i.), the initial unpressurized cylindrical void has a radius *R* and height *R.* As the void is pressurized, the deformation approaches a spherical geometry as stretch increases (ii. and iii.) Data obtained in collaboration with Aleksander Mijailovic and Dr. Krystyn Van Vliet.

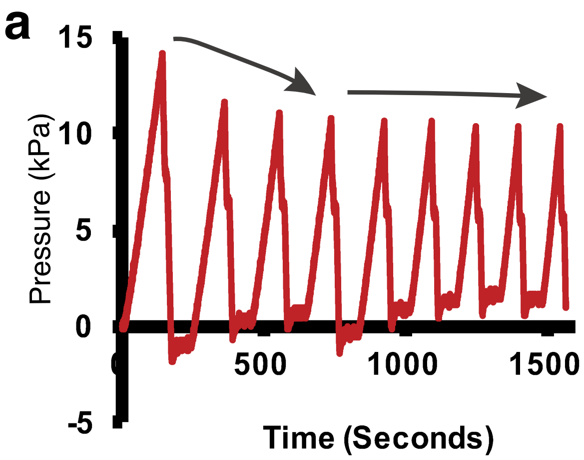

Murine, Cavitation Rheology

Figure 2.11: Pressurization cycles via NICR in murine brain result in decrease in pressure. Air as a working fluid was pressurized into a mouse brain in order to evaluate if the critical pressure achieved would remain constant over time which is indicative of an elastic event. In this case we observed a decrease in the critical pressure after subsequent cycles. Softening in brain tissue has been shown to happen by others after a failure event [100] which could be indicative of fracture in NICR.

2.3 Materials and Methods

2.3.1 Sample preparation

Brains from 6-month old pigs were collected from Baystate Medical Center Springfield MA. Brains from B6 albino mice, 12 weeks old, were received from the Tremblay lab at the University of Massachusetts, Amherst. The six porcine brains were dissected two hours post-mortem as four mm-thick horizontal slices and used for indentation, and cavitation rheology. Mice brain were kept whole for indentation and cavitation rheology and tested 30 minutes post-mortem. Brain tissue punches from both animals were 8 mm wide and 1 mm thick for shear rheology. To prevent tissue dehydration, all samples were placed in phosphate-buffered saline (pH 7.4) and kept on ice until mechanical testing was performed. To assure tissue integrity, most test were performed within 6 hours post mortem[43], and all tests were performed within 48 hours. To test the effect of freezing tissue, some samples were flash frozen overnight and kept at -80C and tested within a period of 4 hours post-thaw.

2.3.2 Shear rheology

Small-amplitude oscillatory-shear tests were performed on murine and porcine brain punches. Samples were placed in the lower plate of a Kinexus Pro rheometer (Malvern Instrument, UK) while the top plate was lowered into the sample and any excess was removed. The configuration was parallel-plate geometry, with a diameter of 8 mm. The temperature was maintained at 25^{0}C and the oscillatory frequency sweeps were conducted between 0.1 and 1 Hz. Temperature variation was captured by heating samples to 35^{0}C. Finally, the effective Young's modulus, E^{eff}, was calculated at a frequency of 0.1 Hz assuming an isotropic material of Poisson's ratio, v of 0.5.

$$E^{eff} = 2G * (1 + v)$$

Four mice brain samples were subjected to rheology at 25^{0}C and then temperature was raised to 37^{0}C. A total of 6 porcine brains were tested at 25^{0}C. Samples were tested after frozen to address rheological changes after thaw and rheology was performed at 25^{0}C.

2.3.3 Indentation

For indentation measurements, a cylindrical flat punch (High-Speed M2 Tool Steel Hardened Undersized Rod, 1.5-mm diameter) came into contact with brain tissue samples with a fixed displacement rate (20 μm/s) and a maximum load (1.5 mN). A force transducer (Honeywell Sensotec, Columbus, OH) monitored the loading force, P, while a nanoposition manipulator (Burleigh instruments Inchworm Model IW-820) controlled the displacement, δ. A material compliance factor, C, calculated as the ratio between change in displacement over change in force

$$C = \frac{d\delta}{dP}$$

was recorded by a National Instruments LabVIEW code. For the case of a contact radius, r, much smaller than the dimensions of the elastic sample, *a*, with a correction confinement described by 0.5 <a/h < 2 where h is the sample height, the effective Young's modulus (E^{eff}) can be calculated given the relation, [117]

$$E^{eff} = \frac{3}{8C\{1+1.33\left(\frac{a}{h}\right)+1.33(\frac{a}{h})^3\}a}$$

Nine mice brains were subjected to testing, a total of 6 porcine brains and 3 individual human brains. For the loading cycles, each cycle was performed within 50 seconds of each other to allow for tissue recovery as shown by others.

2.3.4 Needle-induced Cavitation rheology (NICR)

Needle-induced cavitation rheology (NICR) measurements were taken in a custom-built instrument consisting of a syringe pump (New Era Syringe Pump NE1000), pressure sensor (Omega Engineering PX26-001GV), and a syringe needle connected to a DAQ card that can record the pressure overtime. A needle was inserted into the tissue sample (1.8 mm) and air was injected at a rate 400 μL/min. The pressure increases steadily balanced by the sample elasticity and surface tension until a critical pressure is reached that gives rise to a sudden and abrupt pressure collapse. This pressure change was recorded overtime using a custom-developed LabVIEW code for different needles with gauges between (22-32 gauge). The critical pressure achieved is a function of the needle radius, and an effective Young's modulus can be calculated with the following equation assuming an isotropic material on the size scale of the needle[130]

$$P_c = 1.05E + \frac{2.1\gamma}{r}$$

Were P_c is the critical pressure, γ is the surface tension, and r is the inner radius of the needle.

2.3.5 Volume Controlled Cavity expansion (VCCE)

Volume Controlled Cavity Expansion (VCCE) technique has been previously discussed in detail by Raayai-Ardakani et al. [120] In summary, using a needle-syringe system connected to an Instron Universal Testing Machine, a cavity filled with incompressible liquid (silicone oil) is expanded (in a volume controlled manner – rate of $2.7\ \mu L/s$) inside the material of interest. Silicone oil was chosen to ensure immiscibility with the surrounding material. Throughout the experiment, the pressure inside the cavity is measured using a load cell connected to the syringe piston and is calibrated (by subtracting the frictional forces in the system and normalizing by the cross-sectional area of the piston) as previously discussed[120]. The volume measurements at every instance of the experiment are then transformed into an effective cavity radius (a) and the pressure-effective radius results are used to find the elastic properties of the material in accordance with a chosen constitutive model.

Since brain has been previously identified as a strain-stiffening material[100], here, we employ an incompressible, one-term Ogden model with the strain energy density defined as

$$W(\lambda_1, \lambda_2, \lambda_3) = \frac{2E}{3\alpha^2}(\lambda_1^\alpha + \lambda_2^\alpha + \lambda_3^\alpha - 3)$$

where E is the Young's Modulus of the material and α is an exponent capturing the strain-stiffening response of the material, and $\lambda_i (i = 1,2,3)$ are the principal stretches. In the case of the problem of the expansion of a cavity then $\lambda_2 = \lambda_3 = \lambda_\theta$ and $\lambda_1 = \lambda_\theta^{-2}$ where λ_θ is the circumferential stretch in the bulk material encapsulating the cavity. Employing the above strain energy density, it can be theoretically shown that the pressure inside the cavity (inside a body of material much larger than the radius of the cavity) can be found as

$$p(\lambda)= \frac{4E}{3\alpha}\int_\lambda^1 \frac{(1-\lambda_\theta^{3\alpha})}{(1-\lambda_\theta^3)} \frac{d\lambda_\theta}{\lambda_\theta^{2\alpha+1}}$$

where λ is the circumferential stretch at the cavity wall which can be written as the ratio of the cavity radius at every time instance (a) normalized by the initial cavity radius (a_0).

From the experimental measurements, values of a and p are known for the duration of the expansion process, while the initial radius of the cavity is an unknown that cannot be measured using the conventional techniques available. Therefore, to be able to use this theoretical model against the experimental results to identify the elastic properties (E, α) of the material[120], one can consider a_0 as an additional unknown in the problem and fit the result for the three unknowns.

Under three circumstances the test results were considered as physically un-acceptable (not successful) and have been removed from the analysis: (1) the pressure measurement captures negative or zero values, or (2) the measurements captures a pressure of more than 200 Pa at $\lambda = 1$ (pre-stress), or (3) if the measured $a_0$is larger than the average radius of the needle (average of the inner and outer radii; a gauge 22 needle has been used for these experiments). Under the third condition, the measurements are believed to be dominated by damages incurred on the brain tissue rather than by elastic processes.

2.4 Discussion

Changes in the elastic properties of brain tissue have been correlated with progression of neurodegenerative disorders[134], traumatic brain injury[39, 40] and brain cancers[41]. Previous studies probing different compartments of the brain have identified that brain tissue exhibits location-dependent mechanical properties like intraregional anisotropy[98, 100, 135], intraregional variations[136-138], and regional inhomogeneities between different compartments[104, 135]. Yet, although most of the investigations carried in brain tissue explore bulk mechanical properties at distinct locations via rheology[99, 139, 140] and indentation[111, 138, 141] the macro and micrometer length scales of these techniques are limited in their spatial resolution and the need for sectioning of the sample limits the capabilities to test intra- and inter regional variations *in situ*.

Needle-induced cavitation rheology (NICR)[133] and volume-controlled cavity expansion (VCCE)[120] are two relatively novel techniques that provide the capabilities to test local deformation, *in situ* at a spatial resolution within 100μm to 10 mm not possible with indentation or rheology. NICR has recently been used to explore mechanical properties of polymers and tissues like the eye[116], bone marrow[117], lung[118] and skin[142], highlighting its capabilities of testing local mechanical properties *in situ*. Similarly, VCCE incorporates the same methodology of NICR with an incompressible working fluid[120], providing additional information about the cavity volume which cannot be visually extracted in biological samples due to the inherent opaque nature of most tissues. Here we measured mechanical properties of porcine brain via NICR and VCCE alongside rheology and indentation to validate their applicability in obtaining modulus at a specific location.

From our modulus comparison with conventional techniques shown in figure 2.3, we found rheology and indentation values of 0.9 + 0.1kPa and 1.0 + 0.2kPa, respectively for porcine brain, which show agreement with those reported in work by others[111, 143]. Indentation allows for localized measurements at the surface of the sample at a micrometer length scale and we observed a wide range of stiffness for porcine (0.1-10 kPa) and murine (0.4 – 11 kPa) tested at different locations. Comparison of the average of these measurements, in contrast, showed no significant difference among individual brains, but murine cortex resulted in a higher modulus compared to porcine cortex via indentation (fig 2.2). This result would agree with recent work from MacManus et al.,[144] where indentation of murine and porcine brain in the same cortex location yielded different moduli. Similarly, others have used more localized techniques to investigate the mechanical properties of white and gray matter. In our case, white matter was found to be slightly stiffer then gray matter (fig. 2.9) similar to studies from[99, 111, 138, 145] and in contrast to studies from[139, 146]. However, NICR reported values of 4.75±0.9 kPa and 3.65± 0.7 kPa for white and gray matter respectively which are significantly higher compared to conventional techniques. VCCE, in contrast, obtained an average modulus of 1 kPa similar to that found via indentation and rheology. Previous NICR modulus values for synthetic soft materials, like hydrogels, have shown agreement with shear rheology and contact mechanics techniques[115, 133]. In the case of biological tissues, like in this work, some have reported a slightly higher value via NICR in contrast to other techniques[117, 118] while others have shown good agreement[116]. Hence, we next sought to understand why NICR of brain tissue would yield a significantly higher modulus in comparison to other techniques.

We begin with the assumptions in VCCE and NICR analysis. In both techniques, we assume hyperelastic material behavior and a spherical cavity forms with increasing pressure; the main difference is that, in NICR, the maximum pressure value is used to measure E, whereas in VCCE, the pressure-volume relationship before the maximum pressure is fit to measure E. In NICR, we specifically assume that the material behaves in a Neo-Hookean manner, which leads to an elastic cavitation instability at a high enough pressure[133]. Assuming the effect of surface tension is modelled from equation shown in section 2.1.1, we find the modulus by extrapolating the critical pressure to an infinite needle radius (where surface tension contribution is zero) (fig. 2.2). In VCCE, we assume that a cavity of initially unknown volume and shape is expanded spherically. With a large enough needle such that surface tension is negligible, we can fit a hyperelastic constitutive model to the measured pressure vs inserted incompressible fluid volume. In both techniques, we assume that the material does not fracture in the modelled part of the deformation (but can fracture after, for example after the cavitation pressure Pc is reached in NICR), that the deformation rate is sufficiently slow such that viscoelastic effects are negligible, and that the tissue behaves hyperelastically. We emphasize that, while the deformation mechanism is essentially the same in both techniques (except for the pressurizing fluid, which must be incompressible in VCCE and can be either incompressible or compressible in NICR), the main difference is the assumption of elastic cavitation in NICR, which is not necessary in VCCE because a pressure-stretch curve may be fit.

The discrepancy in the measurement of Young's modulus by NICR vs. that of rheology, indentation and VCCE is likely due to the inadequate assumption of a Neo-Hookean material. While we cannot confirm this experimentally by imaging due to brain tissue's opacity, theoretical evidence suggests that cavitation is unlikely in brain due to its strain stiffening behavior as seen in figure 2.8. From figure 2.9a, we see that an Ogden model of brain tissue reported by Franceschini et al.,[100] has appreciable strain stiffening and will not have a maximum or plateau in the pressure-stretch curve, unlike the Neo-Hookean model which becomes increasingly compliant at higher stretch. Figure 2.9b suggests that, even with the conservative assumptions of low surface tension/E ratio and low needle radius (i.e., conditions that increase the driving force for cavitation due to a decreasing –pressure stretch relationship), the Ogden model of brain tissue does not predict cavitation. Thus, brain tissue's appreciable strain stiffening makes the assumption of cavitation unsatisfactory. Hence, the modulus cannot be accurately measured from the critical pressure Pc from equation ($P_c = 5/6E + 2\lambda/r$), and Pc may instead be correlated to fracture events. In the case of VCCE, we note that the surface tension effect should be negligible in these experiments due to the large needle radius, so figure 2.9a is governed by only the brain tissue's elastic response, and we hypothesize that damage or fracture govern the response at higher stretches. While the cavitation assumption is likely invalid in NICR for strain stiffening materials, we sought to evaluate validity of the assumption of spherical deformation in VCCE, which is critical in the technique's analysis.

To verify the assumption of nearly spherical cavity geometry in VCCE, we performed finite element modelling of the VCCE experiment, and we compared the pressure-stretch curve from our analytic model to that of the FE model. In our experiments, needles are typically retracted after insertion into the material, leaving a cavity in the original volume pierced by the needle, so in our modelling, we replicate this setup with an initially cylindrically shaped cavity. During pressurization, the cavity approaches spherical at relatively low surface hoop stretch (lambda = 1.1) (fig. 2.9c), and the pressure-stretch behavior is similar in magnitude and trend to the analytical solution (fig. 2.9a). However, given that NICR like VCCE is a needle-based technique that relies on the pressurization of the system and we see larger variations in the modulus at larger stretches in VCCE (fig. 2.8a) it is possible NICR measurements are occurring at a larger stretch regime. Hence it would be of great interest to understand the event that leads to a critical pressure in NICR.

From pressurization cycles performed by others via NICR, the shape of the cavity formed can be indicative if the event occurring is an elastic instability or fracture[115, 116]. This is also related to the critical pressure obtained in subsequent cycles. From the pressurization cycles performed in murine brain in figure 2.11 we see a decrease in the critical pressure after the first pressurization cycle event. Work by others have associated the brain softening event to take place after the material has reached failure at large stretches. Loading cycles performed by Franceschini et al.,[100] identified brain underwent softening beyond the failure point. It is possible the event leading to a critical pressure in NICR for brain is associated with fracture in this case, but additional studies should be conducted to confirm this. However, fracture events have been shown to happen at very large stretches and strain rate events[100, 147]. Given that brain exhibits strain rate dependent responses and strain hardening behavior, NICR would be an effective technique to study local deformation of brain *in situ* and what parameters induce fracture in brain. This could be beneficial for studies related to traumatic brain injury or blast induce cavitation which rely in similar mechanisms as NICR to induce the formation of an instability event.

As for NICR for brain tissue explored here, constitutive relation assumptions can verge advantages or limitations dependent on the technique. For example, assumptions in rheology in which brain exhibits linear elastic deformations at low strains and more viscoelastic deformation at higher strains are very good. However, the assumption of a homogeneous deformation can pose as a limitation since other work as shown the heterogeneity present in brain tissue[99]. In the case of indentation which also assumes homogenous deformation, this is dependent on the technique parameters like probe size or distance to different areas of the tissue. In contrast to rheology, however, indentation assumptions of linear elastic deformations at low strains are dependent on strain rates. This pose limitations in frequency dependent materials like the brain (fig. 2.6). In our VCCE (and NICR) analysis, we assume that the deformation length-scales and deformation rates are in a sufficient range such that brain behaves as an incompressible, hyper-elastic solid, and does not have significant viscoelastic, poro-elastic, or fracture behavior.

Similarly, we aimed to conduct our measurements within the first six hours of acquiring the tissue samples due to previous work highlighting the effect of post-mortem time in measured modulus[43, 106, 121, 148]. We observed no significant change in brain modulus when tested within the 6 hours post-mortem via indentation and shear rheology (fig. 2.4). Similarly, to address contradicting literature on the effect of freezing of brain tissue[149-151] we performed shear rheology in post-thaw samples. Although we observed an increase in the spread of the moduli range obtained via shear rheology, no major moduli differences were found under post-thaw measurements conducted via these two techniques (fig 2.4). This result agrees with observations from[149] with moduli remaining constant during a large period of time. This also extended to post-thaw human brain tissue which we saw exhibited similar modulus to post-harvest brain and values remained constant within the time window tested. Similarly, others have recently shown the importance of controlled storage conditions of brain for mechanical property tests[123, 152]. We saw that for the case of measurements conducted with 25 ^{0}C and 37 ^{0}C modulus did not change significantly and exhibited similar viscous responses (fig. 2.5).

Together we present two techniques to probe local measurements *in situ*: NICR and VCCE that not only provide mechanical information but also response to deformation events at length scales beyond traditional techniques like rheology and contact mechanics. We foresee the use of this technique in additional biological materials and the expansion of constitutive models beyond Neo-Hookean to better describe materials following strain hardening and viscoelastic responses like brain tissue. Future work could help expand brain deformation with incompressible fluids in NICR. Similarly, future work evaluating the fracture events within NICR and how these can translate to other brain related diseases like TBI and blast wave induced cavitation. We think this would help expand the range of biological tissues that can be probed *in situ* given the inherent advantage of both cavitation rheology and cavity expansion techniques.

2.5 Conclusion

In this study we complemented four distinct techniques to characterize local and *in situ* modulus of brain tissue and to compare continuity among mechanical techniques. We find that brain tissue has a low Young's modulus as measured via bulk, localized and *in situ* mechanical techniques and white matter tissue reported a higher modulus via VCCE. Brain tissue was found to exhibit similar Young's modulus after freezing and modulus remained constant within a window of 6 hours of testing. Modulus was found to correlate with strain rate and percent of strain applied. Additionally, loading cycles showed that brain tissue exhibits strain hardening. While VCCE can be used to understand the material response via a constitute relation applied to a pressure-stretch curve, NICR can help explore events associated with higher stretches where we expect fracture can occur as our FE experiments indicate cavitation is unlikely in strain hardening tissues like the brain. We foresee the use of this technique in additional biological materials and the expansion of constitutive models beyond Neo-Hookean to better describe materials following strain hardening and viscoelastic responses like brain tissue. Future work could help expand brain deformation with incompressible fluids in NICR. Similarly, future work evaluating the fracture events within NICR and how these can translate to other brain related diseases like TBI and blast wave induced cavitation. We think this would help expand the range of biological tissues that can be probed *in situ* given the inherent advantage of both cavitation rheology and cavity expansion technique.

CHAPTER 3

PROTEOMICS OF HUMAN BRAIN AND THYMUS ECM PROTEINS

3.1 Introduction

The brain extracellular space, accounts for 20% of the total volume of the mature brain, and consists of three prominent structures that compose the brain extracellular matrix compartments: the blood-brain barrier (BBB), the perineuronal nets (ECM structure most prominent around neurons) and the interstitial matrix[5-8]. Cells are the main source of these ECM proteins that compose and give rise to differences in tissues. In the brain, astrocytes are the big synthesizers of proteins in the cortex[9].

Others have shown that the components of the ECM can be divided into core proteins, core associated proteins and ECM regulators like small molecules that interact with the ECM[10-12]. Core ECM proteins include collagens, proteoglycans and glycoproteins[11]. Collagens and glycoproteins, like fibronectin and laminin, are mostly found around the vasculature in the basement membrane[8]. A mixture of collagen, glycoproteins and proteoglycans can be found in interstitial ECM giving rise to the microenvironment that surrounds the cells[10]. Matrix affiliated proteins and ECM regulators include those proteins and small molecules that are colocalized in the extracellular space but do not readily assemble to form the matrix that gives rise to tissue[10]. The interaction of cell with ECM components provide the cues give rise to biological cascades[13].

Integrin molecule pairs, consisting of α and β heterodimers, are the main surface receptors from which cells interact with ECM proteins[14-17]. These transmembrane receptors can bind to both ECM proteins and the cellular cytoskeleton providing mechanical and biochemical signaling that regulates cell response[17]. Additionally, in order to degrade and remodel the ECM, cell release enzymes that allow them to spread and migrate in the native microenvironment. Matrix metalloproteinases (MMP) are a family of enzymes that cleave various proteins of the ECM[18]. Together these interactions of cells and their ECM microenvironment have been shown to play a role in development[19, 20], differentiation[153] and disease[17, 18, 20].

In order to understand the ECM dynamic changes during development, health and disease[13, 22, 23], as for example, ECM molecules are already present in the developing embryo where they play important roles in the development of the central nervous system[7] and the composition of these brain ECM proteins has been shown to change during different developmental stages[7], others have aimed to characterize the ECM composition of tissues via proteomics. Proteomic work by others has illustrated the ECM diversity in tissues[10, 154], as for example, comparisons between lung and colon tissues ECM highlighted there are a subset of proteins unique to each tissue and could give rise to the macroscopic differences that are observed in different organs. However, proteomic work has been limited to a subset of tissues as it has become a new approach and although there is a vast range of work with histological approaches, like the publicly accessible Protein atlas, these are not focused on the ECM composition. A limited number of existing reports, however, focused on the deposition of ECM proteins has been limited to those produced from *in vitro* cell culture or have been performed in tissue from origin other than human and hence are limited in the information they can provide from the native human microenvironment. These are examples that illustrate how additional work in needed in order to characterize the ECM profile of human brain tissue. Hence, to expand on this set of proteomic characterization, this work aimed to characterize the ECM composition of tissues of human origin, particularly brain, at a defined age and healthy state and complemented with histology to assess protein location. The proteomics performed in this work could be used for the design of tissue specific instructive materials of the ECM *in vitro.*

3.2 Results and Discussion

3.2.1 Characterization of the Human Brain ECM

We acquired four healthy human frontal cortex samples (fig. 3.1a) given that the cerebral cortex accounts for 77% of the brain volume in order to characterize the unique brain ECM-profile.[155] These samples were decellularized and enriched for ECM proteins following an ECM enrichment protocol recently introduced by Naba et al,[154] which resulted in an insoluble pellet of 1-2 (w/w) %

analyzed via Liquid-Chromatography Mass-spectrometry (LC-MS/MS) (fig. 3.1a).[154] Protein hits were compared to the Human Matrisome Database and classified into ECM core or related proteins

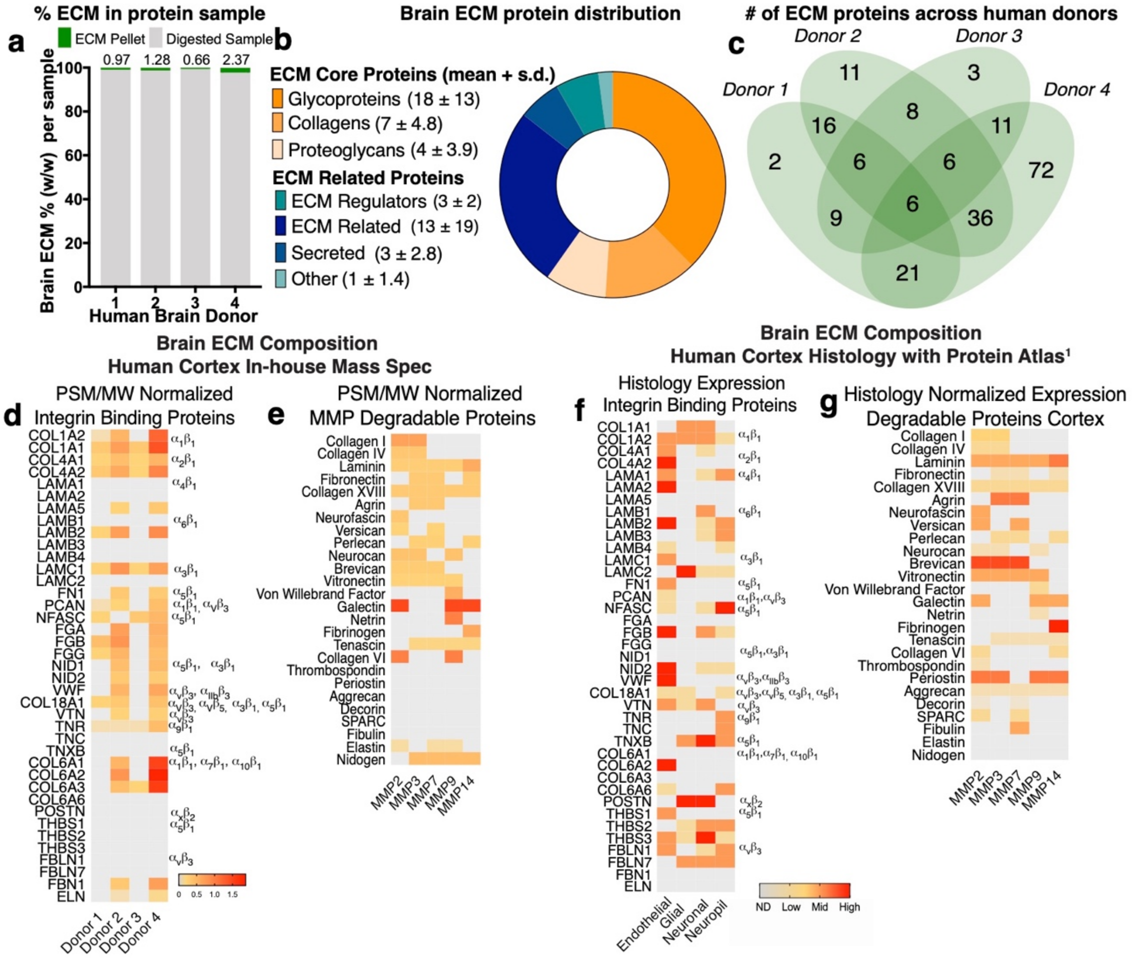

Figure 3.1: Characterization of the Human Brain Cortex Extracellular Matrix. a) Right frontal cortex samples from four healthy human donors were decellularized and enriched for extracellular matrix (ECM) proteins resulting in an insoluble pellet that was solubilized, reduced, and digested into peptides identified via Liquid Chromatography-Mass Spectrometry (LC-MS). b) Protein hits were compared to the Human Matrisome Database and classified into ECM core or related proteins. Data shown is average number of proteins found in four donors + s.d. c) Distribution of Brain ECM signature proteins among donors d) Proteins present in at least two donors were screened for affinity to integrin binding and e) enzymatic degradation via matrix metalloproteinases (MMP). Heat map depicts protein abundance based on peptide spectrum match (PSM) normalized to protein molecular weight (MW) for Integrin binding- and MMP-degradable proteins. f) The Human Protein Atlas was screened for ECM proteins in the human brain cortex as identified via histology images. Heat map depicts protein abundance via histology expression of integrin binding and g) MMP-degradable proteins in the human brain cortex. Degree of expression denoted as ND (not detected), low, medium or high.

(fig. 3.1b). Glycoproteins, collagens and proteoglycans, which are known to interact with integrin heterodimers, compose the core ECM proteins (fig. 3.1b).[12] From this list, and including hits found in at least two donors, proteins were further stratified by affinity to integrin binding and enzymatic degradation via matrix metalloproteinases (fig. 3.1c-e, Table A.1, A.3, and A.4). Peptide spectrum match (PSM) and the protein molecular weight were used to quantify a relative abundance of selected proteins (fig. 3.1d-e). In sum, we found 116 ECM proteins, 18 with known integrin interactions and 21 known to be degraded by matrix metalloproteinases (fig. 3.1d-e, Table A.1, A.3, A.4).

To address protein localization, we complemented our LC-MS/MS findings with a published histological screen of brain proteins by the Human Protein Atlas[156], where we found 147 brain ECM proteins in the cortex (Table A.2). These were similarly screened by core proteins known from the Matrisome database, resulting in 17 proteins with known integrin binding and 24 that undergo MMP degradation (fig. 3.1f-g, Table A.2). Spatial location of proteins within the brain cortex was assessed via the protein atlas histology to differentiate proteins located at the basement membrane (endothelial cells) or at the intercellular space (astrocytes, neurons, neuropil) (fig. 3.1f-g).[7] The grade of histology reported by the Protein Atlas (ND, high, medium, or low) was used to assess abundance of proteins alongside location (Table A.5, A.6). Tables A.1, A.2, A.5 and A.6 show the complete list of human brain ECM proteins as categorized for Core or matrisome related proteins. These are further stratified into integrin-binding and MMP-degradable proteins in tables A.3, A.4 and A.7

3.2.2 Proteomics of pediatric and fetal thymus

In order to expand this proteomic characterization to other tissues, we explored the ECM composition of fetal and pediatric thymus with the aim to understand what set of ECM proteins help in T-cell maturation in collaboration with the Maehr group at UMass Medical School. The use of proteomics could help characterize the unique features of the thymus ECM and could also help us validate how sensitive is this technique to the protein composition of the same tissue at different stages of development. Figure 3.2 shows differences in the thymus ECM composition between fetal to pediatric stages of development. We found that the fetal thymus is rich in ECM proteins that are usually present in the vasculature like fibronectins, fibrillins, and thrombospondins, while these proteins were not present in the pediatric thymus (fig. 3.2a). This composition was very conserved across the two fetal thymus samples tested (fig. 3.2b). We also found that regardless of the developmental stage, the ECM was rich in glycoproteins and a low number of proteoglycans was detected although more where present at the fetal stage (fig. 3.2a, and b). Comparison of the set of samples identified 11 unique proteins for the fetal thymus that were not present at the pediatric stage, however, both share a set of 19 proteins that compose the thymus tissue (fig.3.2c).

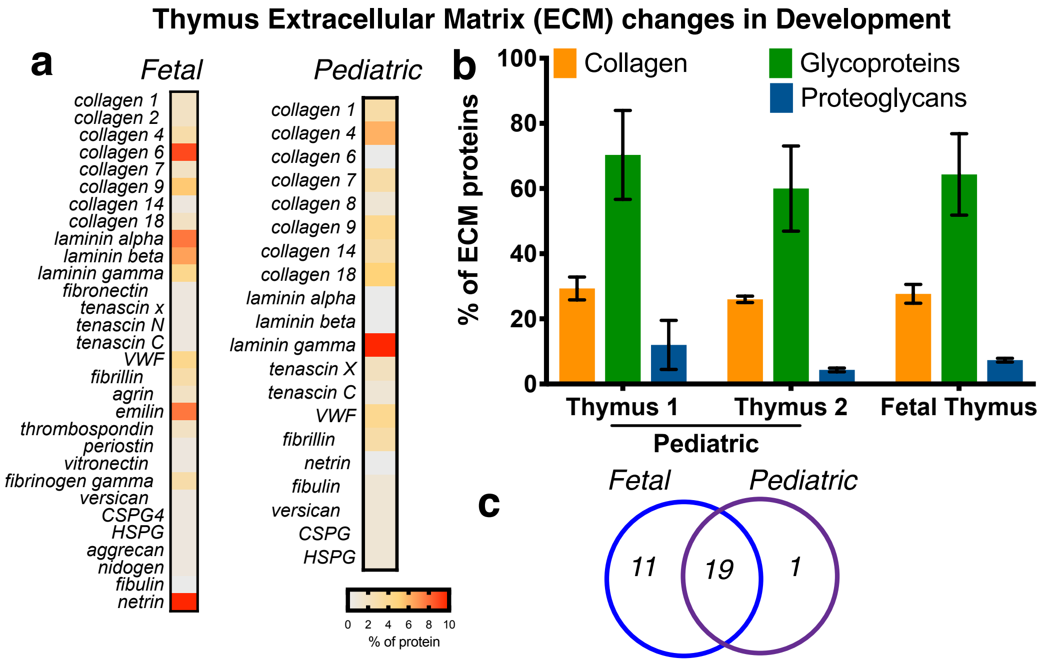

Figure 3.2: Proteomics to identify ECM changes in development. a) ECM proteins identified via proteomics workflow in fetal and pediatric thymus. Heat map depicts percent of protein as normalized via peptide spectrum match and molecular weight of protein. b) Distribution of core ECM proteins across two samples for pediatric thymus and one fetal thymus sample. All samples contain three technical replicates. Data shown is mean with s.e.m. for collagens (orange), glycoproteins (green) and proteoglycans (blue). c) Venn diagram depicts ECM proteins found in both samples and proteins found in individual thymus.

3.2.3 Screening of integrin-binding and MMP-degradable proteins of tissue specific proteomes

The proteomic information acquired with this approach allows for the design of tissue specific instructive materials that could be used to understand ECM signals that regulate cell behavior *in* *vitro.* In order to accomplish this, literature mining was performed to identify ECM proteins that have been shown by others to interact with cells via integrin-heterodimers. By further identifying amino acid sequences present in these proteins with literature mining, these specific sequences of interactions are known and can be synthesized at small scales via solid phase peptide synthesis. Together, the combination of these approaches illustrates a simple way to extract the ECM composition of tissues via proteomics in order to design tissue specific instructive biomaterials (fig 3.3). We foresee the information presented here being used by others aiming to understand the proteomic composition of human brain and thymus tissue.

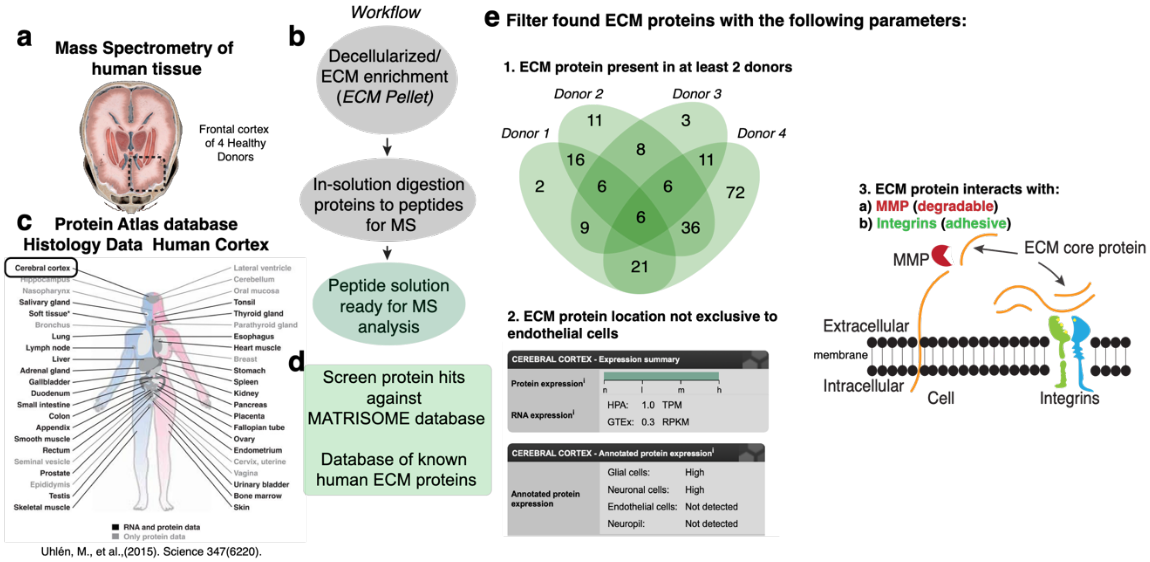

CEREBRAL CORTEX - Expression summary

Protein expression

RNA expression
HPA: 1.0 TPM
GTEx: 0.3 RPKM

CEREBRAL CORTEX - Annotated protein expression

Annotated protein expression
Glial cells: High
Neuronal cells: High
Endothelial cells: Not detected
Neuropil: Not detected

Uhlén, M., et al.,(2015). Science 347(6220).

Figure 3.3: Proteomics and histology complemented workflow. a) Healthy human brain was acquired and b) decellularized and enriched for ECM proteins prepared for mass spectrometry via digestion. c) Publicly accessible histology data on the same organ of interest (e.g. brain) was used to assess protein localization in the extracellular space. d) Both approaches used were screened against the human MATRISOME database to identify proteins that belong to the human Core of Matrisome associated ECM. e) For the design of tissue specific ECM instructive biomaterials, the list of ECM proteins can be further stratified into integrin-binding and MMP-degradable proteins that would allow for cell-ECM interaction *in vitro.*

3.3 Materials and Methods

3.3.1 Acquisition of human brain tissue

Human tissues were obtained from the NIH NeuroBioBank at Harvard Medical School. Frozen post-mortem tissues from four neurologically normal individuals from the ages of 30-68 where obtained flash frozen.

3.3.2 Decellularization and Enrichment of tissue

The CNMCS Compartment Protein Extraction Kit (Millipore, Sigma) was used to decellularize all human brain tissue samples. Briefly, intracellular soluble proteins were extracted with sequential incubation in the appropriate buffers according to manufacturer's instructions. This resulted in an insoluble ECM-rich pellet.

3.3.3 In-solution digestion of proteins for LC-MS/MS

The ECM-rich pellet of four brain tissue samples was solubilized and reduced in 8 M Urea, 100 mM ammonium bicarbonate, and 10 mM dithiothreitol (DTT) (Thermo) for 30 minutes at pH 8 and 37C. Samples were then alkylated with 25mM iodoacetamide (Sigma-Aldrich) in the dark at RT for 30 minutes. Samples were subsequently quenched with 5mM DTT and the solution was diluted to 2 M urea with 100 mM ammonium bicarbonate (pH 8). Proteins were digested via trypsin (Thermo) and Lys-C endoproteinase (Promega, Madison, WI) at a ratio of 1:50 enzyme to protein overnight (12-16 hours) at 37 C. Finally, samples were cleaned and concentrated using a C18 column (Thermo).

3.3.4 LC-MS/MS protein analysis

Digested peptides were separated by reverse phase LC gradient prior to mass analysis. Mass spectrometry analysis was performed in an Orbitrap Fusion Tribid (Thermo). Identified peptides were aligned against the Matrisome using the Thermo Proteome Discoverer 1.41.x. Parameters for analysis used trypsin as a protease, with 4 missed cleavages per peptide, a precursor mass tolerance of 10 ppm, and fragment tolerance of 0.6 Da.

3.3.5 Identification of integrin-binding and MMP-degradable proteins in brain

Using a top-down approach, we screened the human cerebral cortex for ECM tissue features that could be incorporated into a synthetic poly(ethylene)glycol (PEG)-based hydrogel to capture biochemical properties of the brain. The cerebral cortex accounts for 77% of the brain volume[155], and we assessed the brain cortex ECM composition via histology-based bioinformatics and proteomics. Histology data from the Human Protein Atlas[156] was used to identify cortex enriched proteins, their expression, and local distribution. Human brain samples analyzed by LC-MS identified relative protein abundance. From the list of ECM proteins, those with integrin-binding capabilities and susceptibility to matrix metalloproteinase (MMP) cleavage were chosen to allow for cell adhesion and hydrogel degradation. Bioactive motifs of the selected proteins previously identified in literature were synthesized and incorporated in the hydrogel as 9 cell-adhesive ligand peptides and 5 MMP-degradable sequences representative of the brain ECM.

3.3.6 Thymus ECM protein enrichment

Three tissue samples from healthy patients were obtained from the UMass Medical School (Worcester, MA). ECM proteins were extracted from 300mg, 600mg, and 90mg samples using the CNMCS compartmental protein extraction kit according to the manufacturer's instructions (Millipore, Billerica, MA). This resulted in an insoluble ECM pellet.

3.3.7 Thymus Mass Spectrometry LC/MS

Three biological replicates were analyzed for two individual pediatric thymus and one fetal thymus tissue. The ECM-rich pellet prepared from the CNMCS kit was solubilized and reduced in 8M urea 100mM of ammonium bicarbonate, and 10mM dithiothreitol (DTT) (Thermo) for 30 minutes at pH 8 and 37C. Samples were alkylated with 25mM iodoacetamide (Sigma-Aldrich) in the dark at RT for 30minutes and subsequently quenched with 5mM DTT. This solution was then diluted to 2 M urea with 100 mM ammonium bicarbonate at pH 8 and cleaved via trypsin (Thermo) and Lys-C endoproteinase (Promega Madison, WI), at a ratio of 1:50 enzyme to substrate overnight (12-18hrs) at 37C. Samples were desalted and concentrated using a C18 column (Thermo). A reverse phase LC gradient was used to separate peptides prior to mass analysis. Mass spectrometry analysis was performed in an Orbitrap Fusion Tribid (Thermo). Resulting peptides were aligned against the Matrisome using the Thermo Proteome Discoverer 1.41.14. Parameters used trypsin as a protease, with 4 missed cleavage per peptides, a precursor mass tolerance of 10 ppm, and fragment tolerance of 0.6 Da

3.3.8 Identifying integrin-binding and MMP-degradable proteins in Pediatric and Fetal Thymus

Manual data mining was used to identify 14 integrin-binding and 20 MMP-degradable proteins in pediatric thymus. For the fetal thymus 21 proteins were integrin-binding and 27 were MMP-degradable. This list was used to identify which proteins would be represented by integrin-binding or degradable peptide sequences. The proteins were relatively quantified with the peptide-spectrum match (PSM) from the mass spectrometry data and normalized to the molecular weight of the protein. The ratio was annotated for each protein and a relative percent abundance was obtained from the ratio of each protein over a sum of the total ratio identified per sample. This value was averaged across all the patient scores and was used to determine the percentage of each integrin-binding peptide and MMP-degradable crosslinker to use for proteins in the thymus ECM cocktail represented in supplementary tables 1 and 2, respectively.

CHAPTER 4

TIGHT CONTROL OF ASTROCYTE ACTIVATION IN A SYNTHETIC BRAIN HYDROGEL

4.1 Introduction

In order to understand how ECM signals are instructive to cells, we aimed to design a tissue specific brain hydrogel based on the proteomic information gathered from Chapter 3. To test this design, we focused on a particular cell type that has been known to remodel and produce the brain ECM, astrocytes. Astrocytes constitute approximately 30% of the cells in the mammalian brain and function as key mediators of the brain ECM homeostasis.[9, 44, 45] During brain trauma[157] and inflammation[45, 46], astrocytes adopt a reactive phenotype characterized by upregulation of the intermediate filament proteins glial fibrillary acidic protein (GFAP)[9, 44, 45], vimentin[158], and nestin[158], alongside morphological changes[48]. It is these reactive astrocytes that have been shown to help mediate brain metastasis[24, 51, 159, 160], and form glial scarring following an injury that impedes recovery[50, 157]. Yet, mechanisms that control for astrocyte activation remain poorly understood. A potential limitation to address this question is that current *in vivo* studies of astrocyte activation cannot isolate how single cell-ECM events lead to astrocyte reactivity. As such, what relevant extracellular signaling pathways control astrocyte activation remain to be understood. There is an imminent need for *in vitro* models in which to complete mechanistic investigations of astrocyte activation.

In order to pinpoint what single cell-ECM interactions regulate the activation of these cells we need better controlled environments. For this reason, bioengineers have aimed to develop more tunable systems in which to study astrocytes *in vitro.* Astrocytes grown as three-dimensional (3D) organoids[67, 68, 70] provide aspects of the brain architecture, like stellate morphology, and astrocyte heterogeneity, yet their use of Matrigel and the culture of astrocytes in close proximity limit the isolation of cell-cell and cell-ECM interactions. This is of particular importance since astrocyte processes only overlap *in vivo* when they are reactive.[9, 47] Similarly, protein-based 3D hydrogels, typically Type I collagen[71, 75], hyaluronic acid[73], or mixtures of these proteins[71, 75], have been popularized as brain *in vitro* platforms, as they are ECM proteins that exert biocompatibility, and in certain cases, lower upregulation of GFAP[75] as compared to astrocytes grown in a 2D monolayer. Yet, the combination of proteins[50, 75, 77, 161], cytokines[55], and mechanical[77] cues that have been shown to influence astrocyte activation, cannot be independently controlled in these materials.

Synthetic hydrogels, in contrast, provide a tremendous opportunity to design tissue-specific scaffolds with tight control over parameters, like stiffness and ligand density, but bioactive moieties need to be incorporated to represent the microenvironment of interest.[76, 80, 81] Yet, these models are characterized by astrocytes that adopt a rounded morphology or express high levels of GFAP when in an stellate form. Currently there is no cell culture environment that can retain inactive or quiescent astrocytes *in vitro.*

We sought to develop such an *in vitro* model that would enable us and others to study the specific extracellular factors that control astrocyte activation while starting from a quiescent state. To accomplish this, we first characterized the human brain ECM via mass spectrometry and Protein Atlas histology[156] as shown in Chapter 3, and incorporated the top ECM components responsible for integrin-mediated adhesion and MMP-mediated degradation of the brain into a fully synthetic hydrogel, like will be discussed further in this chapter. Using this biomaterial, composed of solely of poly(ethylene)glycol (PEG) and peptides, we overcome the current challenge of retaining primary human astrocyte quiescence *in vitro* and we can control and induce activation. Here we demonstrate control over astrocyte activation via tuning of the integrin-binding and MMP-degradable profile or via cytokine molecules*,* in contrast to other protein-based models like collagen where astrocytes remain in a state of activation.

4.2 Results and discussion

4.2.1 Design of a synthetic Brain ECM hydrogel

Astrocytes have been shown to be responsive to ECM proteins *in vitro.* For example, work by Johnson et al,[77] demonstrated that the ECM composition determined astrocyte responses to the substrate stiffness and inflammatory stimuli. In this work, astrocyte migration was arrested when cultured on fibronectin while fast migration was observed when cultured on tenascin or laminin.

Others have shown, astrocyte attachment to fibronectin, laminin and fibrillin-1 regulates IL-1 induced activation in an integrin-dependent manner.[162] We thus hypothesized that a brain-specific ECM would allow for control of astrocyte activation *in vitro.* Integrin heterodimers are the transmembrane receptors that mediate tissue-specific cell binding to the ECM. We therefore narrowed our ECM Matrisome screening, from Chapter 3, to proteins with known interactions with integrin heterodimers.[163, 164] From the pool of proteins present in both Figs. 3.1d and f, (both approaches were used to determine the relative amounts of proteins present in the brain cortex) (fig. 4.1a; Table A.7) integrin-binding sequences were matched via literature mining to their integrin pairs (Table A.3, A.5, A.7). Proteins identified were screened to those present in at least two donors, not present only near endothelial cells, and with known amino acid sequences (fig. 4.1a and 4.2b). This resulted in 15 proteins that were further grouped based on the adhesive sequence. Seven proteins had the RGD interactive site while eight proteins had a unique site of interaction, these are represented by a total of 9-integrin binding peptides that compose the adhesive landscape of the synthetic brain ECM (fig. 4.1a and 4.1b).

Matrix metalloproteinases (MMP) are a family of enzymes that cleave ECM proteins.[18] Since synthetic hydrogels are characterized by their small mesh size, cells need to be able to degrade the biomaterial in order to migrate[165]. Thus, to allow for hydrogel degradation, we screened ECM proteins with the same parameters used for integrins as described above (fig. 4.1a) and we further screened ECM proteins with susceptibility to MMP degradation. These were grouped based on the MMP of interaction as found via literature mining (Table A.3 and A.6, fig. 4.1a and 4.1c) and resulted in nineteen proteins. From this group, sequences known to be degraded by the MMPs of interest [166](fig. 4.1c) were used to represent the degradable profile of each group of proteins. (fig. 4.1a and 4.1c). This screen resulted in 5-degradable peptides that compose the degradable landscape of the synthetic brain ECM. Both integrin-binding and MMP-degradable peptides can be easily incorporated in the hydrogel following a Michael addition reaction.[167] Integrin-binding peptides are incorporated via a single cysteine functionalization while MMP-degradable peptides have a double-

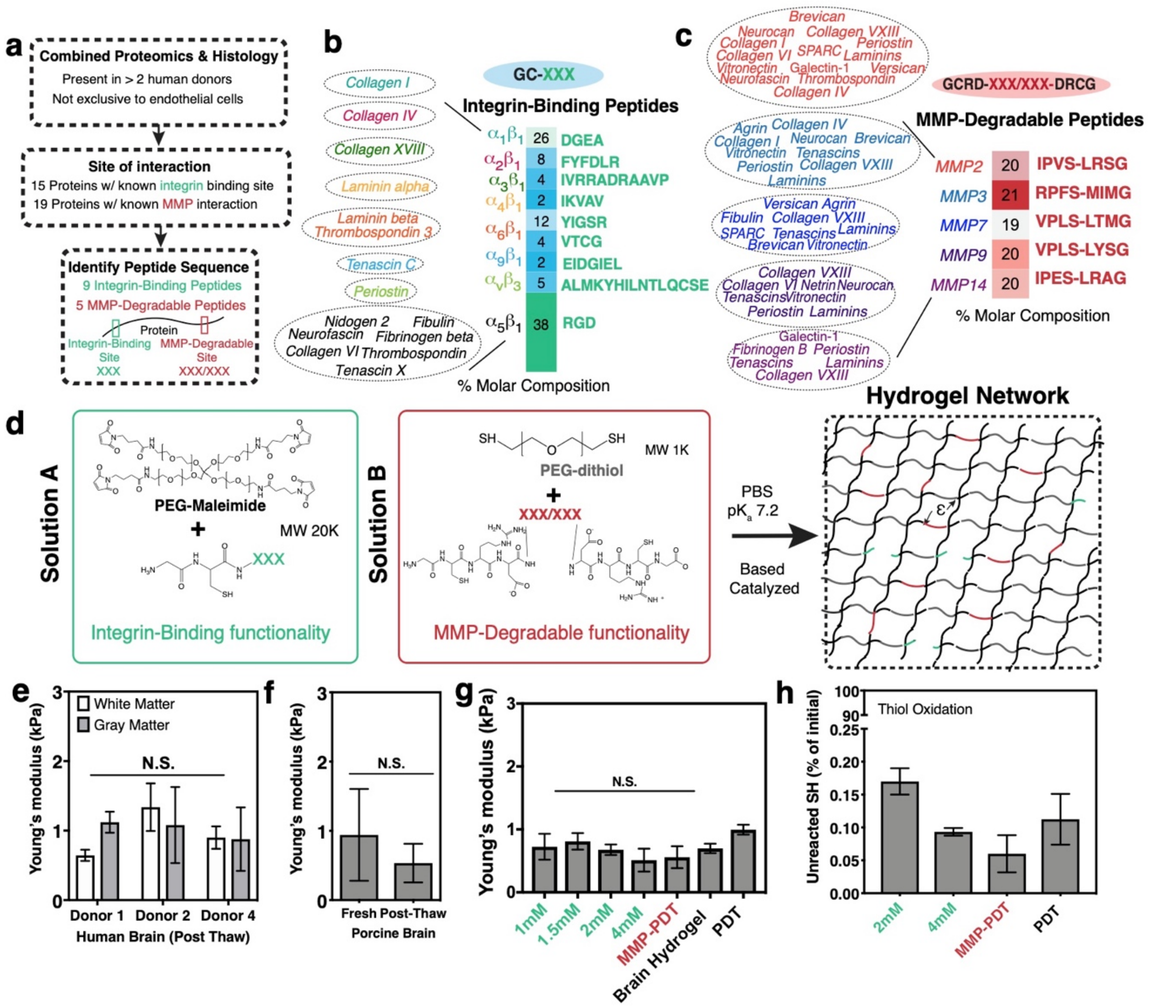

Figure 4.1: Design of a Synthetic Brain Extracellular Matrix Hydrogel. a) Proteins identified via *in-house* proteomics (present in >2 donors) and histology from the protein atlas (not only expressed by endothelial cells) were screened by integrin-binding (ITG) and matrix metalloproteinase (MMP) degradable sequences, later synthesized into peptides. b) ITG peptides represent the adhesive landscape of brain via fifteen proteins, incorporated into the hydrogel via single cysteine functionality. Heat map depicts peptide molar distribution in the cocktail. c) MMP peptides represent the proteolytic landscape of brain as filtered by a group of 19 degradable proteins and incorporated into the hydrogel by two cysteines one at each end. Heat map depicts peptide molar distribution in the cocktail. d) Michael addition reaction for the hydrogel formulation and schematic of the hydrogel network. Hydrogel is formed by mixing two solutions, solution A with integrin-binding functionality and solution B with MMP-degradable functionality with non-degradable crosslinker. e) Young's modulus of post-thawed human brain f) fresh and post-thawed porcine brain *n=6* and g) hydrogel tuned to the same Young's modulus as brain tissue as measured via indentation. Modulus is maintained after incorporation of integrin-binding (green) or MMP-degradable (red) peptides. *n=8.* h) Percent of unreacted thiols after hydrogel reduction with $NaBH_4$. High polymerization efficiency is maintained. *n=8.* All data are mean with s.d. Statistical analyses were performed using Prism (GraphPad). Data in e-g was analyzed using a one-way analysis of variance followed by a Tukey's multiple comparison test with 95% confidence interval. N.S. is not significant.

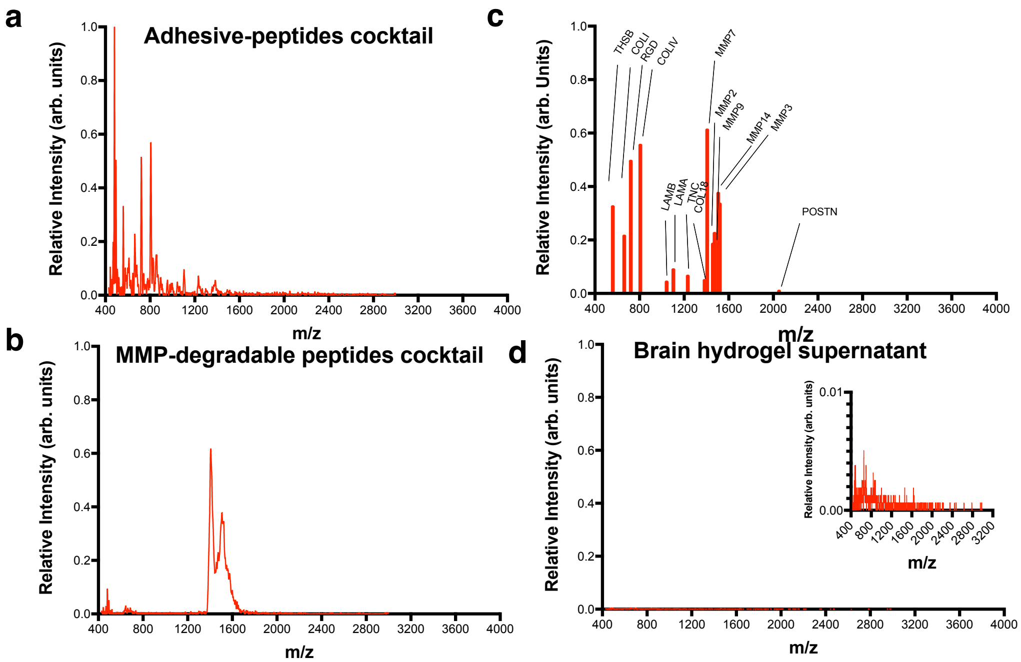

Figure 4.2: Identification of Synthetic Peptides via MALDI-TOF. a) Spectra of adhesive and b) degradable peptides as identified via MALDI-TOF analysis. c) Peaks corresponding to the different amino acid sequences in the mixture. d) Analysis of brain hydrogel supernatant after polymerization was performed for 10 minutes shows no peaks.

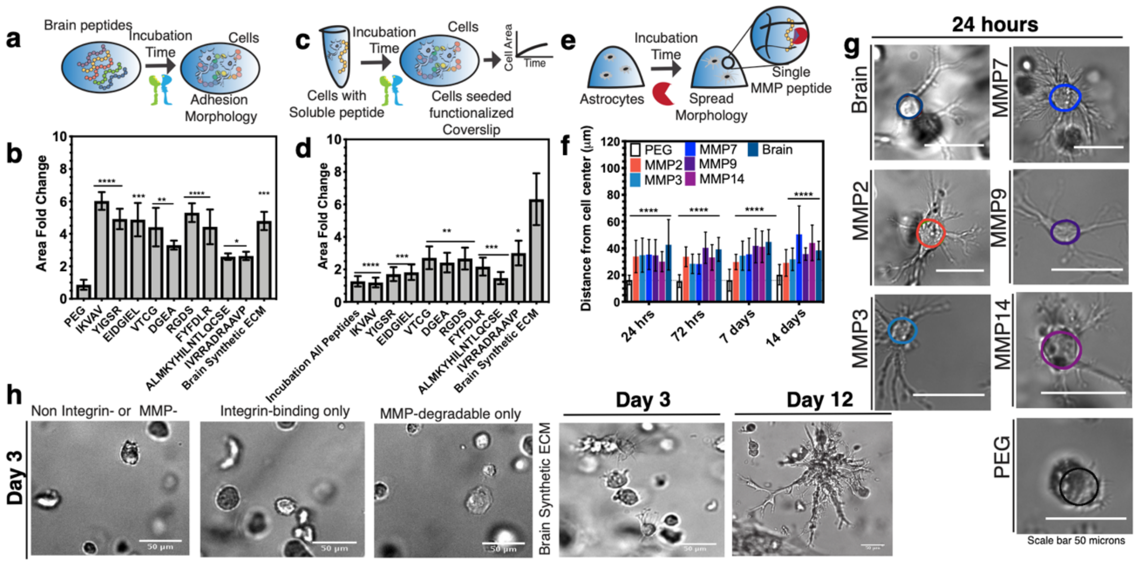

Figure 4.3: 2D Adhesion and 3D degradation of integrin-binding and MMP-degradable peptides. a) Schematic depicting coverslip functionalization with integrin-binding peptides and cell seeding. b) Area fold change after incubation. Cells can adhere to surfaces functionalized with integrin-binding peptides better than PEG and similar to RGD. N=2, *n=3.* c) Schematic depicting a competitive binding assay of individual integrin-binding peptides. d) Change in cell area after incubation in surfaces. Cell area is significantly decreased in previously treated conditions compared to cells allowed to adhere to cocktail of integrin-binding peptides without previous

treatment. N=2, *n=3*. e) Schematic depicting encapsulation of cells in 3D hydrogels functionalized with MMP-degradable peptides. f) Distance of process length originating from the cell center. Astrocytes elongate processes at each MMP-degradable peptide condition better than PEG alone after 24 hours of encapsulation. N=2, *n=4*. g) Distance of process length originating from cell center at different timepoints. Cells elongate processes overtime and can be encapsulated in the brain hydrogel for a period of 14 days. N=2, *n=4.* h) Representative human primary astrocyte morphology in the different hydrogel conditions. i. Images of astrocytes in hydrogel without interactive sites, with integrin-binding only, MMP-degradable only and both integrin-binding and MMP- degradable peptides over 24 hours; After 12 days astrocytes show elongated processes. All data are mean + s.d. Statistical analyses were performed using Prism (GraphPad). Data in b, d, and f was analyzed using a one-way analysis of variance followed by a Dunnett's multiple comparison test with 95% confidence interval. *, **, ***, and **** indicate $P<0.05$, $P<0.01$, $P<0.001$ and $P<0.0001$.

end cysteine modification to allow for crosslinking of the hydrogel with degradable backbone (fig. 4.1d). The formation of the hydrogel consists of two solutions that contain adhesive and degradable components, respectively, and which polymerize under a minute (fig. 4.1d). The speed of the reaction can be tuned with the strength of the buffer as shown previously.[92]

Given the current advances in recombinant protein production and engineering, one attractive avenue is the recombinant production[168] of ECM proteins used to design this hydrogel system. Since proteins also have cysteine sites, they would be able to undergo incorporation into the brain hydrogel chemistry. Yet, although it sounds very appealing at first, one important limitation from this approach is that this would not limit the interaction between the cells and the protein site to be exclusively at integrin binding and MMP degradable sequence domains, as proteins have many other sites of interaction. However, if the interest is still to have the whole protein sequence, there are multiple challenges that would need to be overcome in order to produce all of these proteins successfully. First, posttranslational modifications which are very important for protein production, as a most common example glycosylation[169], can lead to differences in protein stability[170], solubility[171], antigenicity[172], folding[173], localization[174] and biological activity[175] if it is not modified properly. This is a challenge since glycosylation[169] is a very complex posttranslational modification that requires several consecutive steps and involves tens of enzymes and substrates, and this process is protein-[176], tissue-[177] and animal-specific[178]. Other posttranslational modifications such as phosphorylation[179], methylation[180], C-terminal amination[181], etc., although less common that glycosylation, may also be important to other recombinant proteins and these depend on the host[182] utilized since they are only available in higher eukaryotic cells. Finally, overcoming the protein localization production is challenging since recombinant proteins may be directed to different cellular compartments by signal peptides[183, 184] or through fusion proteins[184] and it is difficult to predict if these would be intracellular[184] or secreted[184]. These different sites of protein localization can have advantages or disadvantages, as for example, intracellular[185] accumulation often leads to high protein amounts and allows for an easy recovery but purification of the product from the protein-rich cell extract may be difficult. On the other hand, secreted proteins[184] facilitate its purification and allow for easy recovery but are often highly diluted. Additionally, challenges in the secretion pathway[184] can further reduce their accumulation in the culture medium. Protein localization is particularly important when producing proteins with a specific native sequence[168], as for example, if they are produced in the cytoplasm, they are highly susceptible to proteolysis and would hence lose the desired sequence. Together these are examples of the time-consuming, expensive and complex process of producing all ECM proteins in the brain hydrogel recombinantly instead of just synthesizing the peptides of interest, which is a cheap, fast-turnaround controllable alternative adopted in this work.

Next, since microenvironment biomechanical forces can dictate cell behavior, we aimed to replicate the modulus of brain tissue *in vitro.*[29] However, reported Young's modulus of the brain ranged from 100s of Pa to 10s of kPa and were found to vary considerably among experimental techniques.[43] In order to narrow the modulus within the cortex, as discussed in Chapter 2 in more detail, we characterized the mechanical properties of human brain, via an indentation technique previously published by our group[117], and we found the Young's modulus to be approximately 1kPa (fig. 4.1e).[117]

Due to limitations in the ability to find fresh human brain tissue, and to confirm there was no difference in modulus of fresh tissue, we also characterized the bulk modulus of fresh and post-thawed porcine brain cortex given the anatomy and gray to white matter ratio is similar to that of human brain.[111] Via indentation, we found a surprisingly similar Young's modulus to that of post-thaw human brain and a slightly lower post-thaw modulus that was not significantly different (fig. 4.1e and 4.1f).

To match these mechanical properties into our brain hydrogel, and taking a similar approach to work by others[186] that have modulated the biomaterial's Young's modulus due to the elastic properties of hydrogels, we adjusted the macromer concentration until reaching a similar Young's modulus to that of brain (fig. 4.1g). Given that at very low strains, the brain behaves as an elastic material, as shown in work from chapter 2, we find the Young's modulus is sufficient to modulate the mechanical properties of the hydrogel as cells will apply forces at very low strains in the biomaterial as well. Similarly, at these low strains, brain tissue does not exhibit strain rate dependence has illustrated by shear rheology results in chapter 2 and hence we do not foresee these properties as critical in the brain hydrogel design. We also found the Young's modulus was not affected with the incorporation of adhesive or degradable motifs and these peptides can be incorporated efficiently into the PEG-maleimide system (fig. 4.1g and 4.1h, fig. 4.2).

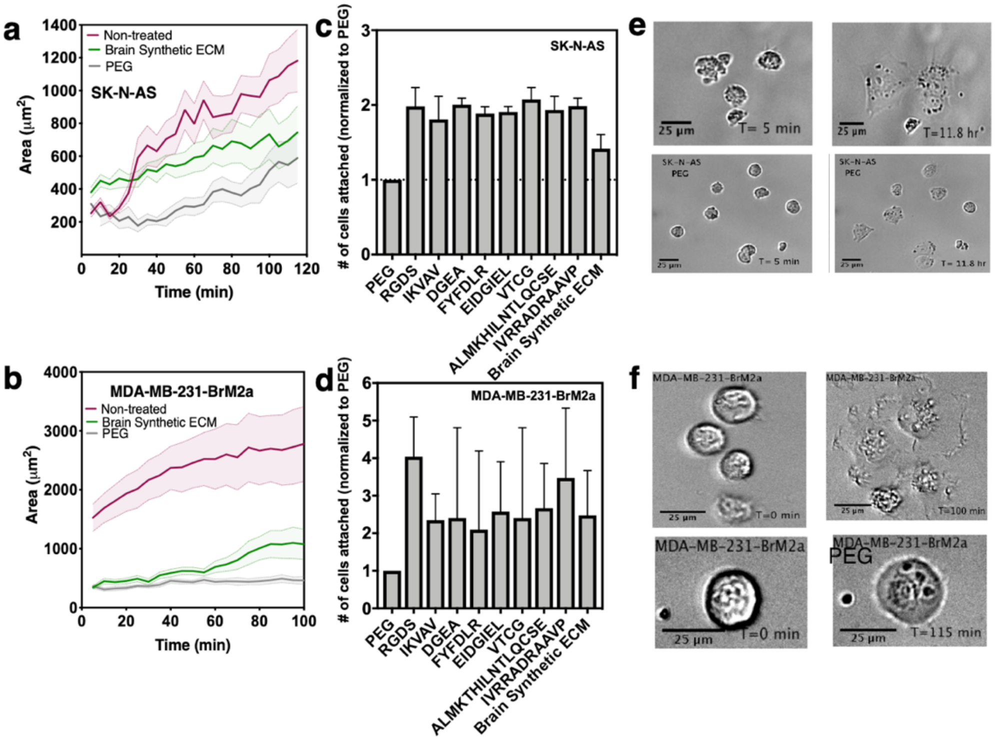

Figure 4.4: Adhesion of integrin-binding peptides to human cell lines. Cell lines a) SK-N-AS and b) MDA-MB-231-BrM2a were seeded in surfaces functionalized with poly(ethylene)glycol (PEG) (gray), brain synthetic adhesive peptides (maroon), or previously treated with adhesive

cocktail (green) and then seeded into a coverslip functionalized with the integrin-specific peptide mixture. Cell area was traced every five minutes for a period of 120- and 100-minutes respectively. Cell area increased significantly in the non-treated (maroon) cells that were seeded directly onto coverslips with the adhesive peptide mixture, while the cell area remained small in the PEG condition. Cells treated with the adhesive peptide mixture for five minutes prior to seeding onto coverslips took longer to increase the cell area. Data shown is mean (solid line) + s.d. (shade region). N=2, *n=30.* c) SK-N-AS and d) MDA-MB-231-BrM2a cells were seeded into coverslips functionalized with each integrin-binding peptide for a period of 2 hours. Cells were washed, fixed and stained with Dapi and counted with ImageJ software. Data shown is the number of cells attached normalized to PEG as mean + s.d. N=2, *n=3.* e) Representative images of SK-N-AS and f) MDA-MB-231-BrM2a cells adhering overtime to coverslips functionalized with the integrin-binding peptide mixture or PEG. Cells show a larger area when cultured on coverslips functionalized with the adhesive peptide mixture in contrast to PEG alone.

4.2.2 Design and validation of brain-specific integrin-binding peptides

In order to validate that cells can adhere to the integrin-binding peptides we intended to include in the brain-specific hydrogel, we performed a 2D adhesion assay with a human neuroblastoma cell line SK-N-AS. We found that cell area increased significantly for cells seeded on surfaces functionalized with integrin-binding peptides compared to negative control surfaces (fig. 4.3a-b, fig.

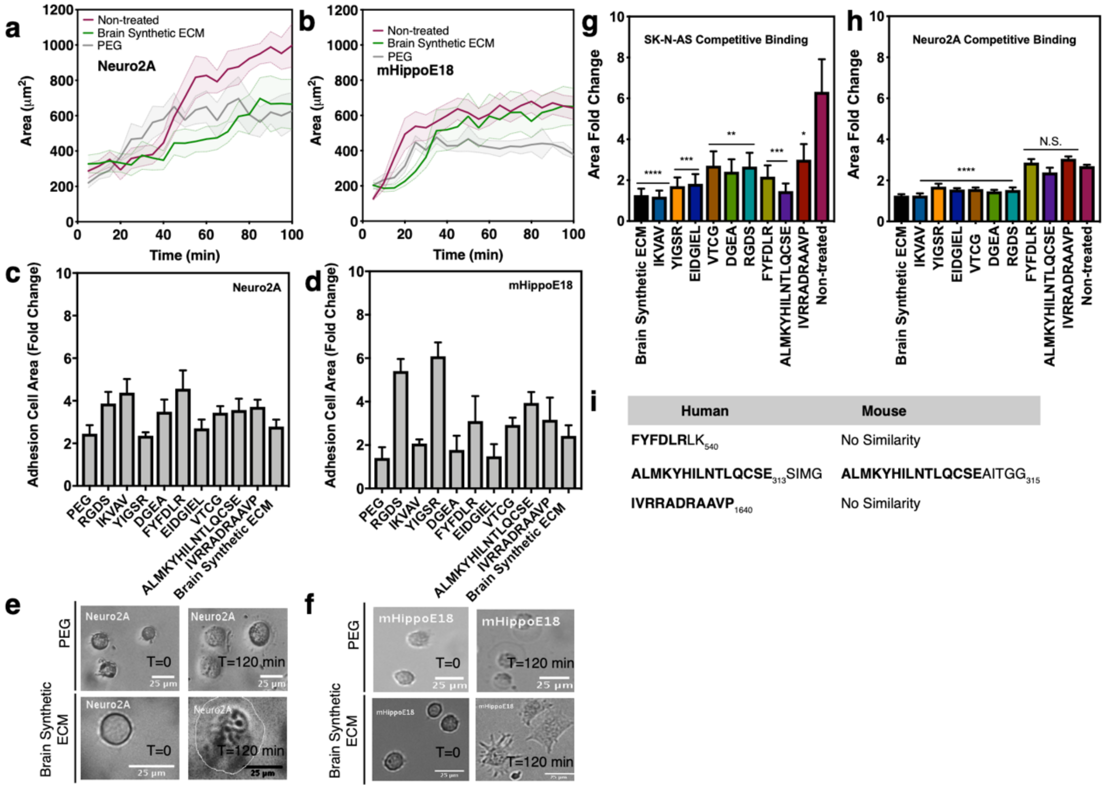

Human	Mouse
FYFDLRLK$_{540}$	No Similarity
ALMKYHILNTLQCSE$_{313}$SIMG	**ALMKYHILNTLQCSE**AITGG$_{315}$
IVRRADRAAVP$_{1640}$	No Similarity

Figure 4.5: Peptides are specific to human cell adhesion. a) Quantification of cell area traces overtime for the murine cell lines Neuro2A and b) mHippoE18. Cells were seeded into coverslips functionalized with poly(ethylene)glycol (PEG) (gray), adhesive brain synthetic ECM (maroon) or

incubated for five minutes in adhesive brain synthetic ECM mixture followed by seeding into coverslip functionalized with adhesive brain synthetic ECM (green). Data shown is mean (solid line) + s.d. (shaded area). N=2, *n=30.* c) Cells lines Neuro2A and d) mHippoE18 were seeded into coverslips functionalized with each integrin-binding peptide and allowed to adhere for 2 hours. Change in cell area from time=zero to time=2 hours are shown for each integrin-binding peptide, PEG and the adhesive brain synthetic ECM mixture. e) Neuro2A and f) mHippoE18 representative images of cell spreading in coverslips functionalized with PEG or the adhesive brain synthetic ECM mixture for a period of 120 minutes. g) Competitive binding of the human cell line SK-N-AS and h) murine cell line Neuro2A. Cells were previously incubated for five minutes in the peptide of interest in soluble form and subsequently seeded into a coverslip functionalized with the integrin-binding peptide mixture. Data shown is mean + s.e.m. N=2, *n=30.* i) Sequences that did not inhibit cell adhesion of the Neuro2A cell line to the adhesive peptide mixture functionalized coverslip are not found in the protein sequence of the mouse.

4.4).[16] Experiments with the commonly used breast cancer cell line MDA-MB-231 in adhesion assays showed similar results (fig. 4.4, Tables A.3, A.5).[187, 188]

We conversely performed a competitive binding assay where cells were pre-incubated with integrin-binding peptides in solution before being exposed to a surface with the full cocktail of brain-specific integrin-binding peptides (fig. 4.3c). Compared to those cells incubated with peptide, non-treated cells fully spread and adhered to the brain peptide cocktail surfaces (fig. 4.3d, fig. 4.5). We also found that sequence homology mattered. Exposing a murine cell line to peptides sequences whose sequence differed from that of human resulted in non-attachment to the full cocktail surface (collagen type IV, periostin, and collagen type XVIII, fig. 4.5).

We encapsulated human primary astrocytes in hydrogels containing a single integrin-binding peptide for a period of 5 minutes prior to fixing and staining for the integrin heterodimers receptors expected to bind the peptide ligand, based on an assay developed by Li *et al.* (Table A.5)[189]. We positively identified integrin heterodimers via immunofluorescence for the predicted integrin ligand-receptor pairs in contrast to culture in PEG alone (fig. 4.6). Together this data illustrates the human specific design of this brain hydrogel and the specificity of the integrin-binding peptides.

4.2.3 Human Astrocytes cleave MMP-degradable peptides to extend processes

We encapsulated human primary astrocytes in hydrogels containing a single integrin-binding peptide for a period of 5 minutes prior to fixing and staining for the integrin heterodimers receptors expected to bind the peptide ligand, based on an assay developed by Li *et al.* (Tables A.3, A.5)[189].

Astrocytes have a morphology characterized by their ramification and long processes, and we expected that gels that do not contain MMP-degradable peptides would yield rounded astrocytes or small processes.[9, 44] Human primary astrocytes were encapsulated in 3D hydrogels with conditions testing blank and functionalized hydrogel with integrin-binding peptides only or with both integrin- and MMP-degradable group of peptides (fig. 4.3e). We optimized astrocyte cell density in the brain hydrogel to prevent cell clustering over long culture periods (fig. 4.7). We found that astrocytes were able to extend processes in conditions that incorporated both integrin-binding and MMP-degradable moieties and remained viable in the brain hydrogel for a period of 12 days (fig. 4.3e, fig. 4.8). In order to verify that each degradable peptide was in fact susceptible to degradation

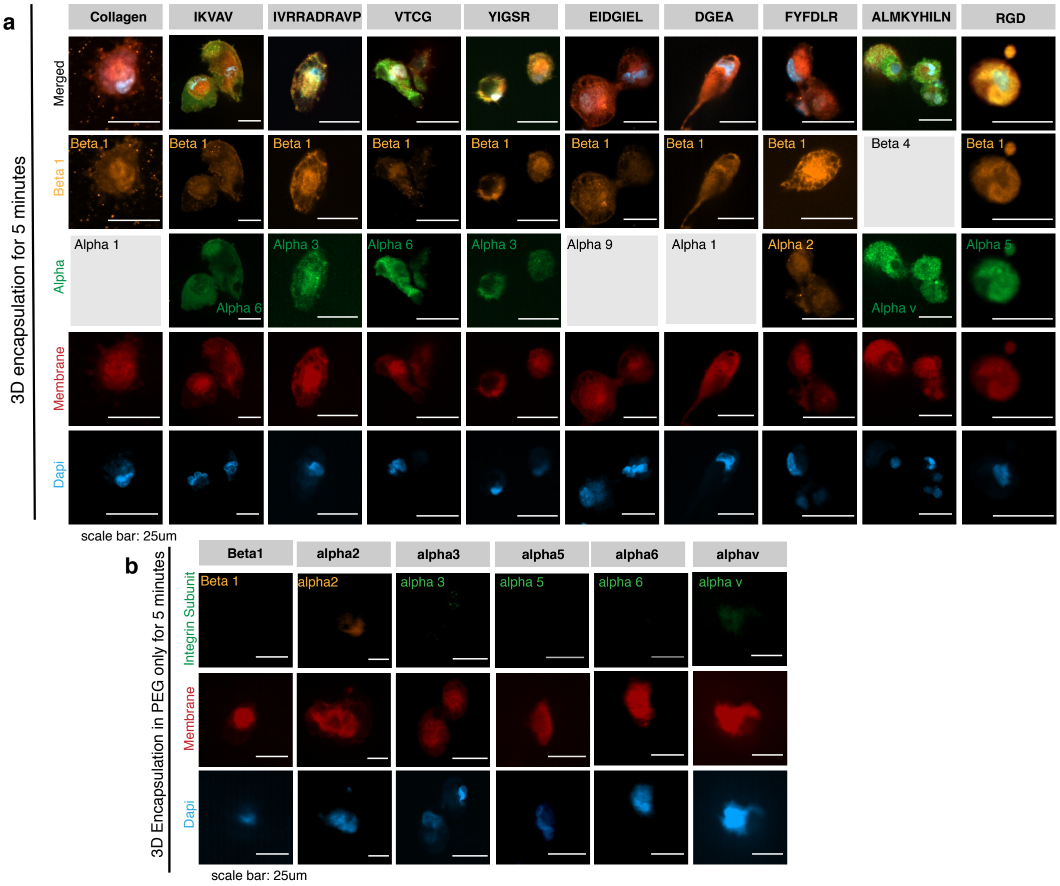

Figure 4.6: Adhesive peptides elicit integrin expression via immunofluorescence. a) Human primary astrocytes were encapsulated for five minutes in collagen or hydrogels modified with a single integrin-binding peptide at the same concentration as in the brain adhesive peptide mixture. b) Or non-functionalized poly(ethylene)glycol hydrogels. Hydrogels were fixed and stained for the

expected integrin-heterodimers known to bind the amino acid sequences selected (Table A3-A5). Membrane stain (red) and Dapi (blue) were used for cell co-localization.

by astrocytes, as shown by others[166] for other cell types, cells were encapsulated in hydrogels containing integrin-binding peptides and individual MMP-degradable crosslinks. Further quantification of astrocyte process length from the cell center over time, shows that cells were able to extend their processes, over a period of 14 days, better than in PEG alone (fig. 4.3e-i, fig. 4.9). Together these results demonstrate that the hydrogel can be degraded and retain cell viability for 2 weeks.

4.2.4 Astrocyte activation can be controlled with hydrogel composition

Recent work by Placone et al.,[75] illustrated that modifying the concentration of components in a protein-based hydrogel composed of Type I Collagen, hyaluronic acid, and Matrigel reduced the expression of GFAP, an astrocyte specific marker correlated with activation, in primary fetal human

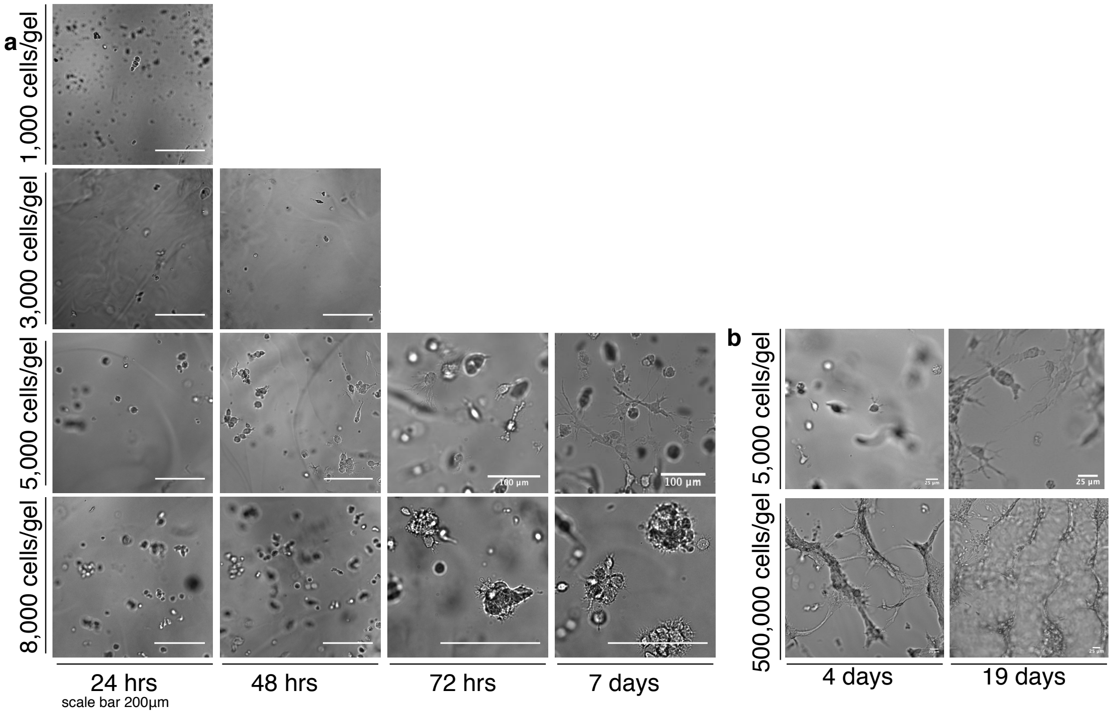

Figure 4.7: Optimization of human primary astrocytes seeding density in the brain hydrogel. a) Human primary astrocytes were encapsulated at a density of 1,000-, 3,000-, 5,000-, and 8,000 cells/gel in the brain hydrogel and cultured for a period of 7 days. b) Cells can also be encapsulated at greater densities (e.g. 500,000 cell/gel) and form networks over time.

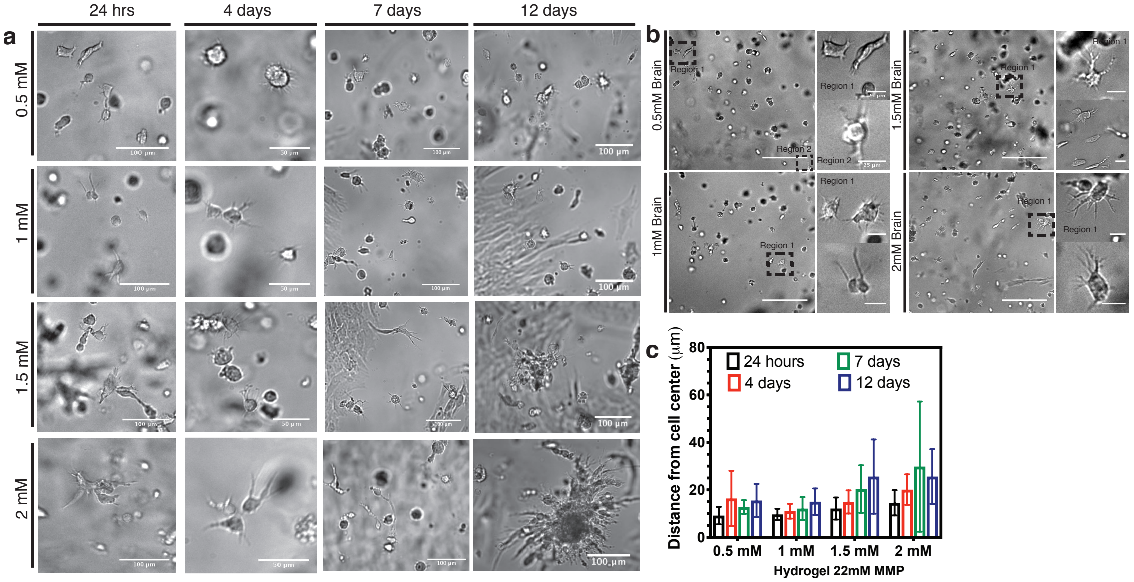

Figure 4.8: Human Astrocytes spreading increases with integrin-binding peptide concentration. a) Human astrocytes were encapsulated in brain hydrogel with 0.5mM, 1mM, 1.5mM and 2mM integrin-specific binding mixture and a constant 25mol% MMP-peptide mixture for a period of 12 days. b) Cells elongated their processes significantly after 24 hours of encapsulation in the 2mM integrin-binding hydrogel. c) Quantification of the distance from the cell center for astrocytes culture over a period of 12 days in the hydrogel at the specified condition. Data shown is mean + s.d. N=2, *n=4.*

astrocytes as compared to culture in 3D collagen alone. Similarly, work by Hara et al.,[50] demonstrated that astrocytes become reactive when cultured in a collagen coated substrate as mediated by the integrin-n-cadherin pathway. We thus hypothesized that tuning the composition of the brain hydrogel would have an impact in astrocyte GFAP expression and this could be compared to culture in a collagen gel.

To test the brain hydrogel effect on astrocyte reactivity, we explored integrin-binding peptide concentrations around the range that allowed for cell spreading in a 3D geometry (fig. 4.10). We found that increasing the concentration of adhesive peptides beyond a concentration of 2mM resulted in astrocytes with long processes similar to those in a collagen-based gel, but beyond a 3mM concentration yielded astrocytes with high levels of GFAP fluorescence similar to that in collagen (fig. 4.11a-c).[75] We thus decided to test if modifying the concentration of MMP-degradable peptides would also have an effect in activation. We found that combining a 4mM concentration of integrin-binding peptides with a 13mol% concentration of MMP-degradable peptides yielded significantly low activation in astrocytes cultured *in vitro* compared to collagen (fig. 4.11d-f, fig. 4.10). This result agrees with the astrocyte activation observed by others upon ECM deposition *in vivo,* where, for example, increase in the production of protein has correlated with observed astrocyte activation.[24, 50]

Figure 4.11g shows representative morphologies and levels of GFAP fluorescence in primary astrocytes encapsulated in the different conditions. We found a particular brain hydrogel formulation that resulted in low levels of GFAP and stellate morphology. Together these data show that astrocyte activation can be controlled in a fully synthetic brain hydrogel by tuning of integrin-binding and degradable motifs.

4.2.5 Quiescence is not achievable in protein-based hydrogels

Recent work by Liddelow et al.[55] described astrocyte activation via three cytokines produced by microglia: interleukin 1 alpha (IL-1alpha), tumor necrosis factor alpha (TNF-alpha) and complement component 1, subcomponent q (C1q) were activation was defined by high expression of GFAP.[55] Similarly, work by Hara et al.,[50] identified *gfap* and *vimentin* as genes highly expressed by spinal cord injured activated astrocytes. To confirm quiescent astrocytes can undergo activation in the brain hydrogel, we triggered activation by dosing with the three cytokines identified by Liddelow[55] after 24 hours of culture in the brain hydrogel (fig. 4.12a). We found that under standard culture medium conditions, astrocytes express low levels of activation markers GFAP and Vimentin compared to collagen-cultured astrocytes (fig. 4.12b-c).[50]

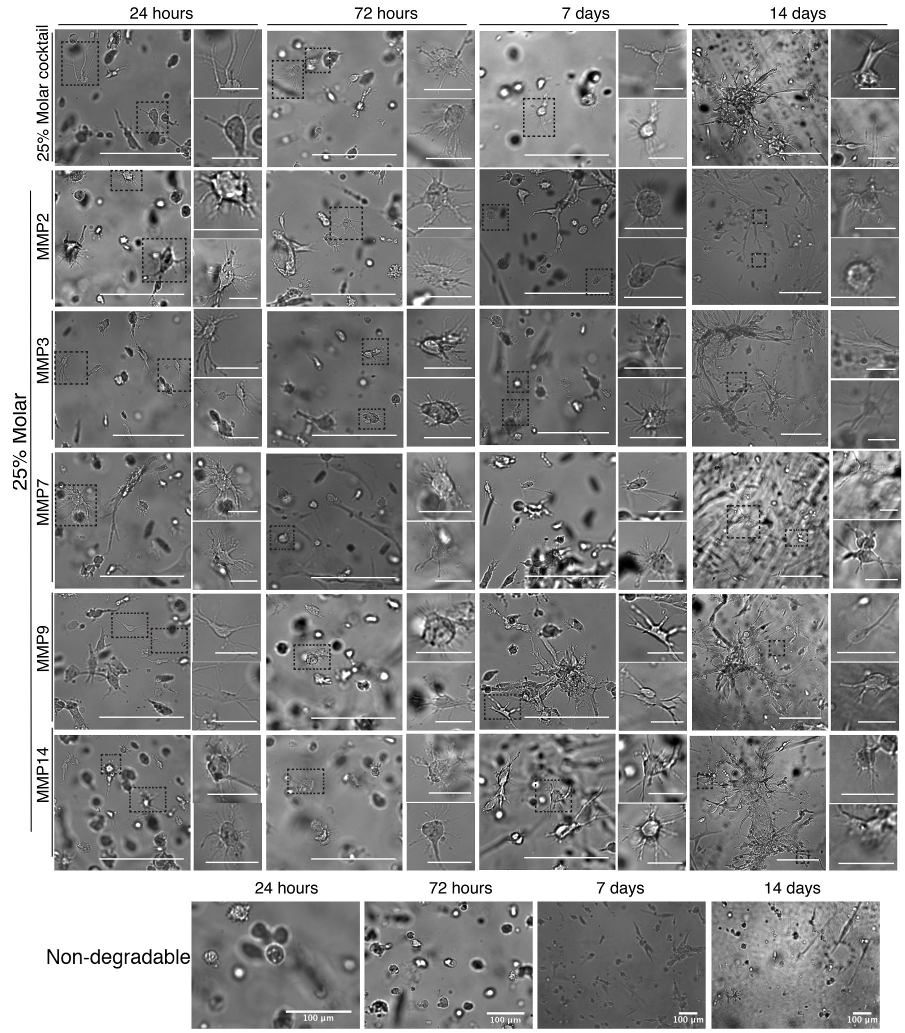

Figure 4.9: Human primary astrocytes can remodel the synthetic brain hydrogel. Representative images of human astrocytes encapsulated in a functionalized brain hydrogel, hydrogels with a single MMP-specific peptide and an adhesive peptide concentration of 2mM, or a non-degradable PEG hydrogel for a period of 14 days.

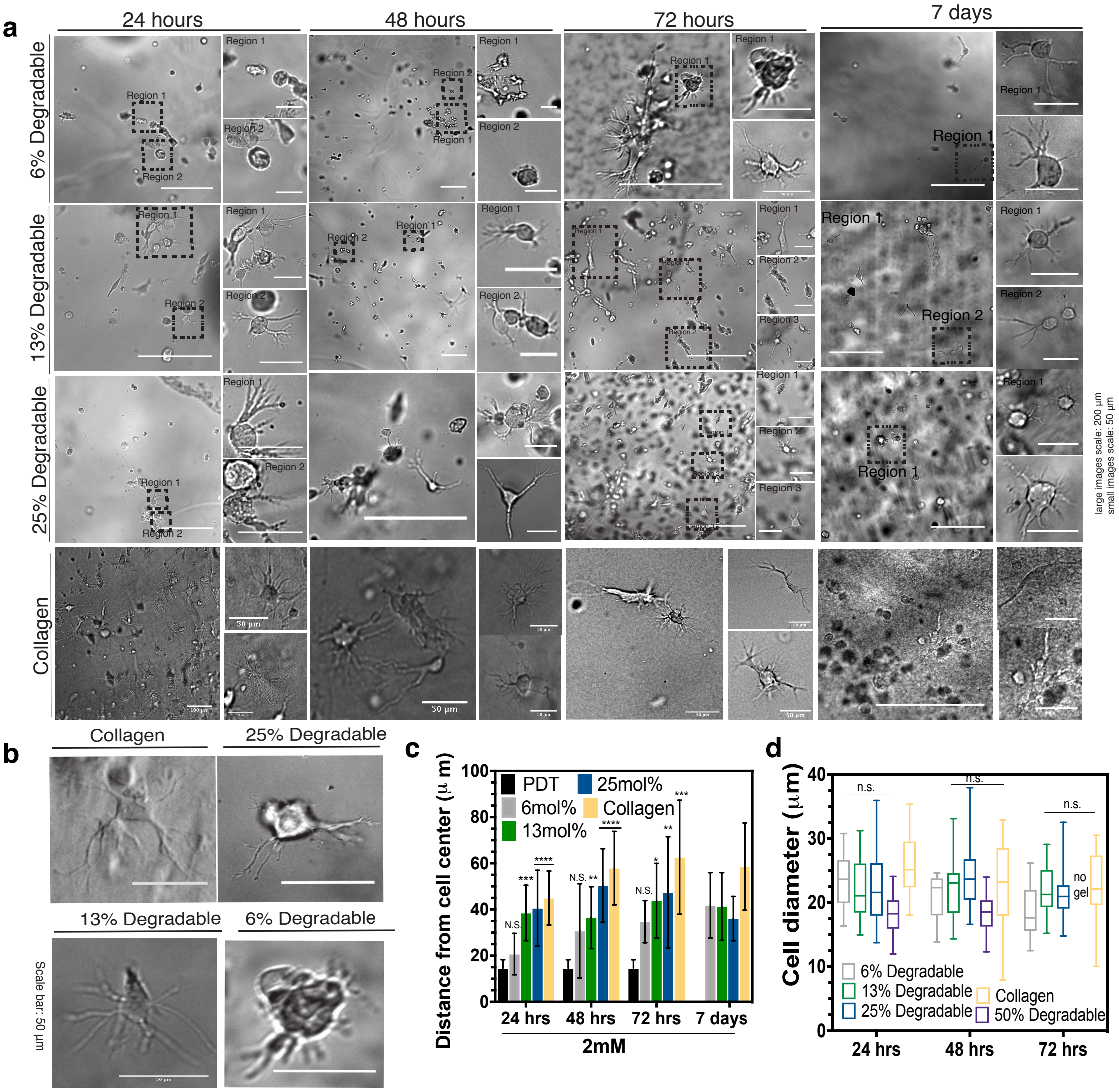

Figure 4.10: Optimization of MMP-peptide concentration in the Brain Hydrogel. a) Human astrocytes were encapsulated in collagen and brain hydrogels functionalized with 6mol%, 13mol%, and 25mol% MMP-specific peptide mixture at a constant 2mM integrin-specific peptide concentration. Representative images of cell morphology and dynamic remodeling of the hydrogel for a period of 7 days. b) Representative images of astrocyte cell morphology after 72 hours of encapsulation. c) Quantification of the distance from the cell center over time for hydrogels at different conditions as compared to a non-degradable poly(ethylene)dithiol (PDT) hydrogel. Astrocytes encapsulated in a brain hydrogel with 13mol% and 25mol% MMP-specific peptide mixture achieve a longer extension similar to collagen cultured astrocytes. d) Cell diameter of astrocytes cultured in brain hydrogels at different conditions and collagen for 72 hours. There was no significant difference in the cell diameter. Data shown is mean + s.d. N=3, *n=4.*

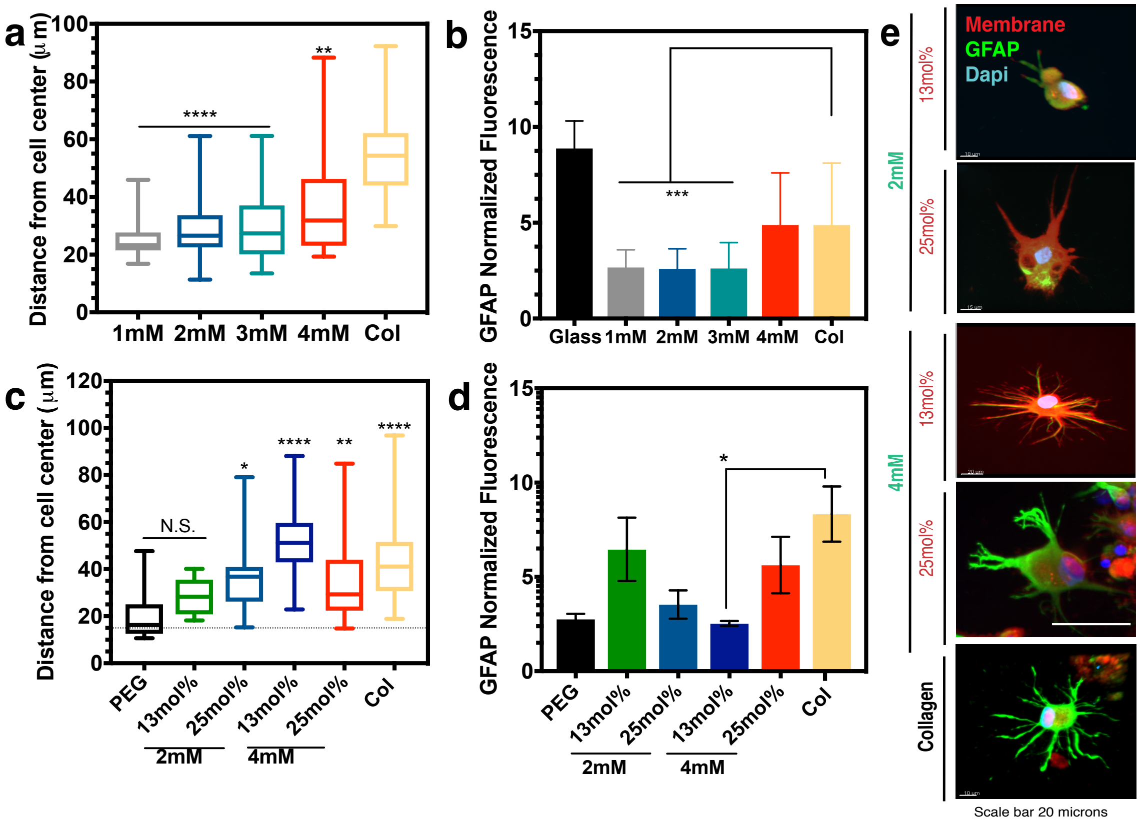

Figure 4.11: Human Primary Astrocytes Activation can be Controlled via Integrin-binding and MMP-degradable Peptides in the Brain Hydrogel. a) Box and whisker plot show distance of process length from the cell center increases with integrin-specific peptide concentration. N=2, *n=3.* b) Normalized fluorescence intensity of glial fibrillary acidic protein (GFAP) as a function of integrin-specific peptide concentration. Low concentrations of integrin-specific peptides retain low activation of astrocytes and short process length. c) Box and whisker plot illustrating length of astrocyte process originating from cell center at different hydrogel conditions and time points. Astrocyte process length varies with hydrogel degradability which can be tuned with MMP-degradable peptide concentration. N=2, *n=4.* d) Normalized GFAP fluorescence as a function of hydrogel integrin-binding and MMP-degradable peptide concentration after 72 hours of encapsulation. N=2, *n=4.* e) Representative images of astrocytes encapsulated in different hydrogel conditions at 72 hours. GFAP expression is lowest at the 4mM integrin-binding and 13mol% MMP-degradable hydrogel condition. Data in b,c and e are mean + s.d. Data in f is mean + s.e.m. Statistical analyses were performed using Prism (GraphPad). Data in b, c, e and f were analyzed using a one-way analysis of variance followed by a Dunnett's multiple comparison test with 95% confidence interval. *, **, ***, and **** indicate $P<0.05$, $P<0.01$, $P<0.001$ and $P<0.0001$. N.S. is not significant.

Similarly, using a serum-free media with the trophic support of Heparin-Binding EGF-like growth factor (HBEGF) denoted as quiescent medium in the publication by Liddelow et al.,[55] we obtained a quiescent astrocyte population low on activation markers, while in collagen, the population remained highly activated with positive expression of GFAP and Vimentin (fig. 4.12b-c, fig. 4.13).

Additional dosing with cytokines resulted in astrocyte population changes that became significantly activated with increasing dosages after 24 hours of culture (fig. 4.12b-c). In contrast, astrocytes cultured in collagen, with or without serum, retained a similar population of activation markers across conditions. These results illustrate that activation can be observed in the brain hydrogel, but collagen cultured astrocytes are already in an activated state.

To further confirm a reactive phenotype, we quantified changes in astrocyte morphology. Work by others have demonstrated that activated astrocytes become significantly smaller compared to non-activated astrocytes *in vivo.*[55] In the case of astrocytes expressing high levels of *gfap* marker during activation, cells exhibit aberrant different morphologies resulting in a heterogenous population.[48] We found that astrocytes retain predominantly a stellate morphology when cultured in the brain hydrogel in standard and quiescent conditions while the population changes to that of rounded, polarized and stellate cells in cytokine induced conditions (fig. 4.12d-e). In collagen, we found astrocytes exhibited a heterogeneous range of morphologies as expected in activated populations (fig. 4.12d-e).[48] Similar to A1 activated astrocytes in the work by Liddelow et al., we found astrocytes process length, volume and surface area was decreased significantly in the highest treated cytokine concentration in the brain hydrogel while there was no significant difference across collagen cultured conditions (fig. 4.12f-h).[55] Together these results confirm a reactive astrocyte phenotype of rounded and smaller sized astrocytes compared to quiescent populations that could only be captured in a synthetic hydrogel with additional integrin-binding and MMP-degradable sites, and not in collagen culture alone.

4.2.6 Reactive astrocytes are highly migratory *in vitro*

Astrocytes have been shown to become highly migratory upon activation *in vivo*[46, 190]. To confirm their reactive phenotype we explored astrocyte migration speeds upon dosing with cytokines in the fully synthetic brain hydrogel. As compared to highly migratory astrocytes on 2D TCPS, we found that cells migrated significantly more in cytokine dose brain hydrogel conditions as compared to the standard culture in the control brain hydrogel (fig. 4.12i).[191] Together these data demonstrate

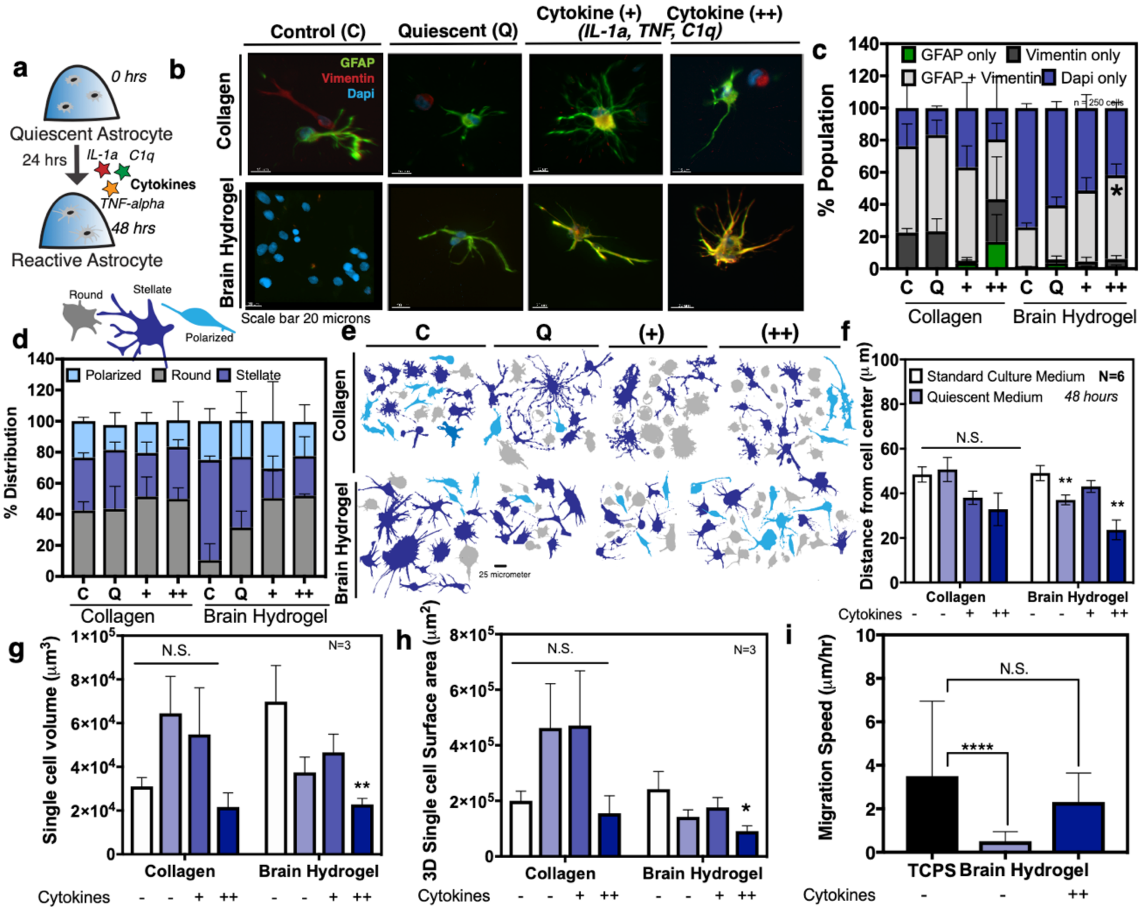

Figure 4.12: Dynamic astrocyte activation can be recapitulated in the brain hydrogel. a) Human primary astrocytes were encapsulated in biomaterials for 24 hours and dosed with cytokines IL-1alpha, TNF and C1q after 24 hours. b) Representative images of astrocytes after 48 hours in biomaterials and incubated with standard culture medium (control), defined quiescent medium, and dosed with cytokines. Scale bar 20 microns. c) Cell population distribution across conditions stained for *gfap, vimentin* activation markers and dapi for nuclear stain. N=2, *n=250 cells per condition.* d) Distribution of cell morphology and e) representative cell morphologies in the different populations identified as round (gray), stellate (blue) or polarized (light blue). N=3, *n = 100 cells per condition.* f) Quantification of distance from cell center of astrocytes N=6, *n=3.* g) Single cell volume and h. Single cell surface area for astrocytes encapsulated for 48 hours at different conditions. Process length, cell volume and area decreased significantly in cytokine dosed astrocytes, indicative of activated phenotype. N=3, *n=3*). i) Comparison of migration speed astrocytes seeded in 2D TCPS, 3D brain hydrogel with and without cytokines shows astrocytes migrate significantly more in activated conditions. N = 2. All plots represent mean + s.e.m. Statistical analyses were performed using Prism (GraphPad). Data in c was analyzed using a one-way analysis of variance (ANOVA). Data in f-h were analyzed using a two-way ANOVA followed by a Tukey's multiple comparison test with 95% confidence interval. Data in i was analyzed using a one-way ANOVA followed by a Dunnett's multiple comparison test with 95% confidence interval. *, ** and **** indicate P<0.05, P<0.01 and P<0.0001; NS, not significant.

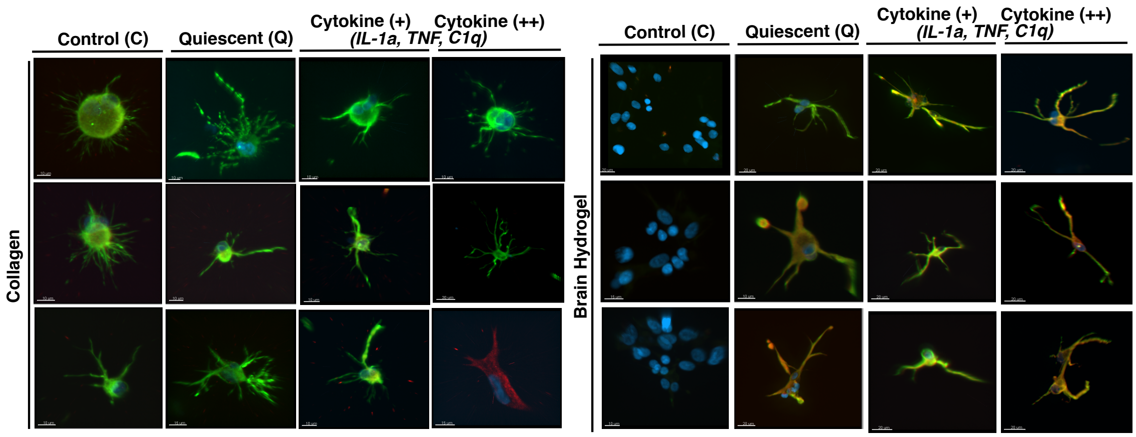

Figure 4.13: Astrocytes undergo cytokine mediated activation in the brain hydrogel. Representative images of astrocytes encapsulated in collagen or brain hydrogel at control (c), quiescent medium (Q), or cytokine dosed conditions with increasing concentrations (+) and (++).

that astrocytes cultured in the brain hydrogel remain quiescent *in vitro* and can undergo cytokine mediated activation as shown by changes in morphology, activation markers and a migratory phenotype. Similarly, together this data illustrates the heterogeneity in the cell population of reactive astrocytes as expected from work by others *in vivo*[48]. However, it would be of interest to understand why there is a clustering to three major group of cells based on their morphology and if there is a genetic predisposition that allows certain cells to become reactive as stellate or as rounded cells. For example, given that this group of cells is of primary origin from a human brain, it is possible there are different genetic profiles when looking at each individual cell type. Future work could help pinpoint what are the major differences in these three different groups of activated astrocytes by resorting to tools like single cell sequencing techniques. As discussed by Liddelow et al.,[45] only two types of reactive astrocytes have been identified so far (e.g. A1 and A2) however, it is possible that astrocytes are reactive in more than just two states. Single cell genomics could be applied to the population of astrocytes in the brain hydrogel and these profiles could be compared to results published by Zamanian et al.,[54] on the genetic profile of reactive astrocytes immunopanned in 2D. Another alternative to control for this population, however, could be sorting of cells via flowcytometry to then culture a pure astrocyte population and completely divide them based on their genetic profile.

4.2.7 Incorporation of Hyaluronic acid (HA) in the brain gel induces activation

Because HA is a polysaccharide present in brain tissue that has been commonly incorporated in *in vitro* ECM models of the brain and, correlation between concentrations and disease have been shown by others,[72, 73, 192, 193] we decided to test how HA would affect astrocyte activation in the brain hydrogel. We incorporated thiolated HA in the brain hydrogel system and stained for GFAP after 48 hours of encapsulation (fig. 4.14). We found that astrocytes GFAP expression increased in a dose dependent manner, with 0.1mM HA being the lowest dose at which astrocytes remained quiescent (fig. 4.14). This finding agrees with that shown by others in which low and high molecular weight HA induce activation of glial cells.[193] Others have also shown increase in malignant phenotype of glioma cells in a dose dependent manner.[192]

To further test if astrocyte activation could be induced with cytokine dosage like shown previously, astrocytes encapsulated in HA-modified brain hydrogels were dosed with cytokines and stained for *gfap* markers (fig. 4.15).

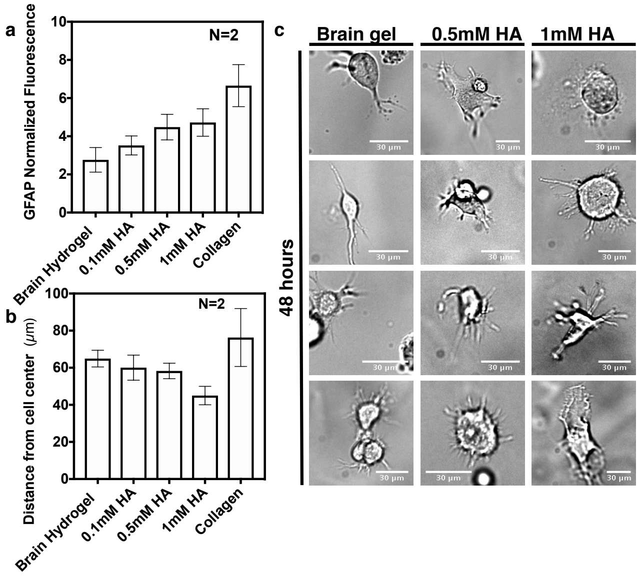

Figure 4.14: Human primary astrocytes become activated to hyaluronic acid in a dose dependent manner. a) Normalized GFAP fluorescence increases with increasing concentration of hyaluronate thiol in the brain hydrogel. Data shown are mean and s.e.m. N=2, *n=3.* b) Distance from the cell center for astrocytes encapsulated in hyaluronate thiol modified brain hydrogels for 48 hours. Process length decreases with increasing concentration of HA. Data shown are mean and s.e.m. N=2, *n=3.* c) Representative bright field images of astrocytes encapsulated in hyaluronate thiol modified brain hydrogels for a period of 48 hours.

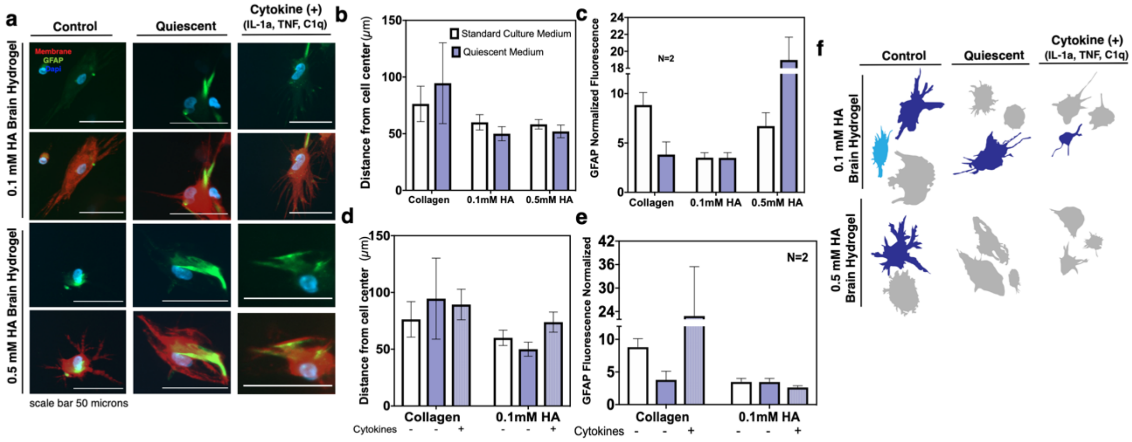

Figure 4.15: Hyaluronate thiol (HA) in the brain hydrogel masks effect of cytokine induced activation. a) Representative images of primary astrocytes in HA modified brain hydrogels with standard culture medium (control), defined quiescent medium, or dosed with cytokine medium. Cells were stained for *gfap* (green), membrane (red) and dapi (blue). b) Distance from the cell center for astrocytes encapsulated in collagen and HA modified brain hydrogels. Morphology did not change based on culture medium. Data shown mean and s.e.m. N=2, *n=3*. c) Normalized GFAP expression for astrocytes in HA modified brain hydrogel after 48 hours of encapsulation with standard culture medium or defined quiescent medium. *Gfap* increased significantly in HA concentrations beyond 0.5mM. Data shown are mean + s.e.m. N=2, *n=3.* d) Distance from cell center for cytokine dosed conditions including the best HA dosed conditions. There was no change in cell morphology for collagen or HA containing brain hydrogel after cytokine dosing. Data shown is mean + s.e.m. N=1, *n=3.* e) Normalized *gfap* fluorescence for cytokine dosed conditions. There was no significant change in *gfap* after cytokine dosing. Data are mean + s.e.m. N=2, *n=3.* f) Representative cell morphology for astrocytes cultured in brain hydrogel modified with HA. Cell morphology becomes rounded with the presence of HA.

We found that astrocyte activation was inhibited in the presence of HA in the brain hydrogel and cells exhibited predominantly a rounded morphology. Together these results show that astrocytes become reactive in a HA dose dependent manner and at high concentrations of HA cells do not undergo cytokine activation *in vitro.*

4.3 Materials and methods

4.3.1 Cell Culture

Normal human astrocytes of cortical origin were purchased from ScienCell Research Laboratories (San Diego, CA USA) and maintained in Astrocyte medium (ScienCell, San Diego, CA USA). Primary cells were used at passage 1 to 5. MDA-MB-231-BrM2a and MDA-MB-231 cell lines (from where) were cultured on 10% serum DMEM while neuronal cells N2A and SK-N-AS were culture on 10% serum DMEM supplemented with 0.1mM NEAA, 1% L-glutamine and 1mM sodium pyruvate.

4.3.2 Identification of integrin-binding and MMP-degradable proteins in brain

Using a top-down approach, we screened the human cerebral cortex for ECM tissue features that could be incorporated into a synthetic poly(ethylene)glycol (PEG)-based hydrogel to capture biochemical properties of the brain. The cerebral cortex accounts for 77% of the brain volume[155], and we assessed the brain cortex ECM composition via histology-based bioinformatics and proteomics. Histology data from the Human Protein Atlas[156] was used to identify cortex enriched proteins, their expression, and local distribution. Human brain samples analyzed by LC-MS identified relative protein abundance. From the list of ECM proteins, those with integrin-binding capabilities and susceptibility to matrix metalloproteinase (MMP) cleavage were chosen to allow for cell adhesion and hydrogel degradation. Bioactive motifs of the selected proteins previously identified in literature were synthesized and incorporated in the hydrogel as 9 cell-adhesive ligand peptides and 5 MMP-degradable sequences representative of the brain ECM.

4.3.3 PEG-Maleimide hydrogel bulk modulus optimization

To modulate the physical properties of the brain hydrogel, we characterized porcine and murine brain tissue and tuned the hydrogel to the same modulus. To assess the hydrogel modulus, PEG-Maleimide hydrogels were formed and swollen in PBS buffer overnight. The effective Young's modulus was measured using an indentation custom built instrument used as previously described.[92] Briefly, a flat cylindrical punch was brought into contact with the hydrogel at a fixed displacement rate of 15 um/s, for a maximum load of 1.5mN. The linear curve of the low regime section was analyzed using a Hertzian model accounting for dimensional confinement between the contact radius (a) and the sample height (h) ($0.5 < a/h < 2$) as described previously[117].

4.3.4 Solid-phase peptide synthesis

All the peptides were synthesized on a CEM's Liberty Blue automated solid phase peptide synthesizer (CEM, Mathews, NC) using Fmoc protected amino acids (Iris Biotech GMBH, Germany). The peptide was cleaved from the resin by sparging-nitrogen gas through a solution of trifluoroacetic acid (TFA), triisopropylsilane (TIPS), 2,2'(Ethylenedioxy)diethanethiol (DODT) and water at a ratio of 92.5:2.5:2.5:2.5 % by volume, respectively (Sigma-Aldrich, St. Louis, MO) for 2-3 hours at room temperature in a reactor vessel (ChemGlass, Vineland, NJ). After reaction, the solution was filtered, and the peptide was precipitated using ethyl ether at -80C (Thermo). The molecular weight of the peptide was validated using a MicroFlex MALDI-TOF (Bruker, Billerica, MA) using alpha-cyano-4-hydroxycinnamic acid as the matrix (Sigma-Aldrich). Peptides were analyzed and purified to >95% on a VYDAC reversed-phase C18 column attached to a Waters 2487 dual (lambda) adsorbable detector and 1525 binary HPLC pump (Waters, Milford, MA).

The following sequences were synthesized: GRGDSPCG, GCALMKYHILNTLQCSE, GCDPGIVRRADRAAVP, GCDPGIKVAV, GCDPGYISGR, GCGDGEA, GCGFYFDLR, CSVTCG, CGGAEIDGIEL, GCRDIPVSLRSGDRCG, GCRDRPFSMIMGDRCG, GCRDVPLSLTMGDRCG, GCRDVPLSLYSGDRCG, GCRDIPESLRAGDRCG

4.3.5 Collagen Hydrogel Preparation

Type I collagen extracted from rat tails was used to construct an in vitro 3D hydrogel. Collagen gels were formed by neutralizing collagen I with NaOH, according to the manufacturer's instructions. 10X DMEM (Sigma) and cells in cold, serum-free media were then added to the neutralized collagen and allowed to polymerize at 37C for 30 minutes.

4.3.6 3D Brain-customized Hydrogel Preparation

A 20K 4-arm PEG-maleimide (Jenkem Technology, Plano, TX) was reacted with 2mM of the brain-ECM integrin-binding peptide cocktail for 10 minutes in serum free medium at pH 7.4. This solution was crosslinked at a 1:1 molar ratio of thiol to Maleimide in TEA at pH 7.4, and the crosslinker solution was composed of 75 molar % of 1K linear PEG-dithiol (Jenkem) and 25 molar % of the MMP-degradable peptide cocktail. Gels were allowed to polymerize in 10uL volumes with 5,000 cells/ul and cell culture media was added after 10 minutes to swell the hydrogel. Other hydrogel combinations to optimize the system for brain astrocytes were made with 3mM, 4mM integrin-binding peptides and crosslinked at a 1:1 molar ratio of thiol to Maleimide with 45mM, 22mM, 12mM and 6mM MMP-degradable peptide cocktail.

4.3.7 Immobilization of integrin-binding peptides on glass surfaces

Peptides were immobilized into glass coverslips as previously described. [194] Briefly, 15mm coverslips were oxygen plasma treated (Harrick Plasma, Ithaca, NY, USA), and silanized through vapor phase deposition of (3-aminopropyl)triethoxysilane (Sigma-Aldrich, St. Louis, MO, USA) at 900C for a minimum of 18 hours. The coverslips were sequentially rinsed in toluene (Fischer Scientific), 95% ethanol (Pharmco-AAPER, Brookfield, CT, USA), and water, and dried at 90 C for one hour. These were subsequently functionalized with 10 g/L N,N,-disuccinimidyl carbonate (Sigma-Aldrich) and 5% v/v diisopropylethylamine (Sigma-Aldrich) in acetone (Fischer Scientific) for two hours. Finally, coverslips were rinse three times in acetone and air-dried. Peptides were then covalently bound to the glass coverslips via the reactive amines using the same molar concentrations as in the integrin-binding cocktail of fig. 5.2b.

4.3.8 Brain hydrogel platform

Glass surfaces were UV/ozone treated for 10 minutes and functionalized with 2 % volume solution of 3-mercaptopropyl-trimethoxysilane (MPT, Thermo) in 95% ethanol (adjusted to pH 5.0 with glacial acetic acid) for 1 hour. The wells were rinsed 3 times with 100% ethanol and let to air dry for 10 minutes before functionalized brain customized hydrogels on the respective surfaces.

4.3.9 Cell adhesion assay

Cells were seeded at 10,000 cells per cm^2 to functionalized glass coverslip surfaces in serum free DMEM and imaged by a controlled Zeiss Axio Observer Z1 microscope (Carl Zeiss, Oberkochen, Germany) using an AxioCam MRm camera and an EC Plan-Neofluar 20X 04 NA air objective. Images were taken every five-minutes for an incubation period of 1-, 2- and 12-hours. Cell area was assessed over time and traced in ImageJ (NIH, Bethesda, MD).

4.3.10 Competitive binding assay

Cells were seeded at 10,000 cells per cm^2 in their normal cell culture media after 30 minutes of pretreatment with individual peptides or the complete brain-ECM cocktail. Cells were imaged beginning at 5 minutes after seeding in an environment-controlled Zeiss Axio Observer Z1 microscope (Carl Zeiss, Oberkochen, Germany) using an AxioCam MRm camera and an EC Plan-

Neofluar 20X 04 NA air objective. Images were taken using Zeiss Axio Observer Z1 (Carl Zeiss) at five-minute intervals for 2 hours or every fifteen-minutes for 12 hours and cell areas were traced in ImageJ (NIH, Bethesda, MD).

4.3.11 Validation of peptide incorporation

The Measure-iT thiol kit was used to quantify unreacted thiols (Thermo) as previously described. (use lenny's paper citation). Buffers were prepared according to manufacturing instructions. Single-cysteine peptides were incorporated at the same concentration they are found in the brain hydrogel in a 100 uL volume of PEG-maleimide for 10 minutes before reacting with 100uL of the kit working solution. Bi-cysteine peptides were reacted with the PEG-maleimide in 10ul aliquots for 10 minutes before reacting with 100uL of the kit working solution. To assess reduction, the hydrogel was incubated in sodium borohydrige (NaBH4, Sigma-Aldrich) in water at a molat ratio of 4:1 NaBH4 to thiol for 4 hours before adding the thiol kit working solution. Hydrogel supernatant and solutions were acquired and read at an excitation of 494nm and emission of 517nm within 5 minutes of the reaction taking place. To assess peptides that did not react, hydrogel supernatants were acquired and diluted to a theoretical concentration of 100pmole/ul. This solution was analyzed using MicroFlex MALDI-TOF (Buker) with alpha-cyano-4-hydroxy cinnamic acid (Sigma-Aldrich) as the matrix.

4.3.12 HA spreading and variation of integrin-binding peptide concentration

Human astrocytes were encapsulated into the brain customized hydrogel with integrin-binding peptide concentrations varying from 0 to 4 mM. After 24 hours, hydrogels were fixed in 4% formaldehyde for 10 minutes and stained with GFAP, CellMask Membrane stain and Dapi. Cell were imaged on a Zeiss Spinning Disc Observer Z1 microscope (Carl Zeiss) using an HRm AxioCam and an (specifications of objectives here 10X. Images were taken using Zen (Carl Zeiss) and cell areas were traced in ImageJ (NIH).

4.3.13 Immunohistochemistry

Hydrogels were fixed in 4% paraformaldehyde solution for 10 minutes at room temperature then washed 3X with ice-cold PBS. To assess morphology cells were blocked with 5% Bovine Serum albumin (BSA) for 30 minutes followed by incubation with the CellMask membrane stain (Thermo-Fischer Scientifc) for 1 hour in the dark at room temperature. Gels were then washed 3X with PBS. To assess GFAP expression, gels were permeabilized with 0.25% Triton X-100 solutions for 10 minutes. Hydrogels were then washed with PBS 3X for 5 minutes and blocked with 5% BSA at room temperature for 30 minutes. Finally, gels were incubated with primary antibody solutions overnight at 4C, washed and incubated in secondary antibody solutions for 1 hour at room temperature. Cells were imaged on a Zeiss Spinning Disc Observer Z1 microscope (Carl Zeiss) using an HRm AxioCam and an (insert detail of objectives) 20x, 25xW, and 40xW objectives. Images were taken using Zen (Carl Zeiss) and cell morphology was analyzed in ImageJ (NIH) and Imaris (BitPlane).

4.3.14 Imaging and image processing

Three dimensional reconstructions of the astrocyte cell morphology were generated from confocal Z-stacks using Imaris (Bitplane) to obtain quantitative morphological data. Filament tracing was done from the CellMask membrane stain channel to obtain information about the morphology of the whole cell. Sholl analysis was performed to access the amount of astrocyte process and length (citation of Sholl). Total additive process length, degree of branching (# process ends / # primary processes, and cell diameter were calculated for each cell analyzed.

4.3.15 FAK phosphorylation by integrin-binding peptides

Cells were seeded in the brain customized hydrogel and collagen gel at 10,000 cells in 10uL volume gel. Cells were culture for 5, 15, 30, 60 minutes and 24 hours then washed once with ice cold PBS and lysed in RIPA buffer (Triton X-100, NaCl, Tris-HCl base, Deoxycholic acid, SDS and water) supplemented with protease (EDTA-free protease inhibitor cocktail tablets, 1 tablet in 10 mL, Roche, Indianapolis, IN) and phosphatase (1x phosphatase inhibitors cocktail-II, Boston Bioproducts, Boston, MA) inhibitors, 1mM phenylmethylsulfonyl fluoride (Thermo Fisher Scientic), 5 ug/ml pepstatin A (Thermo Fisher Scientic), 10 ug/ml of leupeptin (Thermo Fischer Scientific), 1 mM sodium pyrophosphate (Thermo Fisher Scientific), 25 mM beta-glycerophosphate (Santa Cruz, Dallas, TX). Protein concentrations were determined with a BCA assay (Sigma-Aldrich). PEG-maleimide gels were manually dissociated with a pipet tip for 30 seconds after addition of lysis buffer and lysate concentrations were adjusted to 1000 ug/ml. Each sample was prepared with 8X loading buffer and 40 ug of total protein was loaded into a graduated 8% acrylamide gel (Biorad). After western, the protein was transferred onto a xx membrane (Thermo Scientific). Blots were blocked in 5% BSA and then incubated overnight in primary antibody. Primary antibodies included: pFAK (1:1000, Abcam), FAK (1:500, Abcam), beta-actin (1:1000). Secondary antibodies were LiCor anti-rabbit and anti-mouse. Films were developed, imaged and quantified relative to beta-actin loading for each sample.

4.3.16 Statistical Analysis

Statistical analysis was performed with GraphPad Prism (7.0d) (GraphPad Software, Inc., La Jolla, CA). Statistical significance was evaluated using a one-way analysis of variance (ANOVA) followed by a Tukey's post-test for pairwise comparisons. For the analysis, p-values <0.05 are considered significant, where $p < 0.05$ is denoted with *, < 0.01 with **, < 0.001 with ***, and < 0.0001 with ****.

4.4 Conclusions

Reactive astrocytes play a key role in brain injury and inflammation, yet molecular mechanisms that induce activation remain poorly understood.[45] Bioengineers have aimed to design brain *in vitro* models that can recapitulate the brain ECM since components like protein composition, cytokines and biomechanics have been shown to affect astrocyte activation. [50, 55, 75, 77, 161] However, to date there is no *in vitro* model that can control astrocyte activation. Our work shows the first hydrogel to control astrocyte reactivity as demonstrated by the maintained physiological cell morphology and quiescence. Activation can be controlled via tuning of the hydrogel integrin-binding and MMP-degradable profile or induced via cytokine molecules *in vitro* in contrast to other protein-based models like collagen and hyaluronic acid where they remain reactive. We foresee the use of this biomaterial to understand extracellular mechanisms of astrocyte induction, as well as to allow to probe interactions of reactive astrocyte with other central nervous system cells.

CHAPTER 5

CAN BIOMATERIALS PREDICT IN VIVO INVASION OUTCOMES IN 2D OR 3D MODELS? CORRELATION BETWEEN 2D, 3D AND IN VIVO MOTILITY

5.1 Introduction

Outside of understanding mechanistic interactions of cells with the ECM, engineers have also aimed to identify and understand drivers from the microenvironment that regulate cell migration. Cell migration is one of the hallmarks of cancer that mediates cell invasion and metastasis.[195] Metastasis, the spread of cancer cells from the primary tumor to secondary sites, accounts for 90% of cancer related deaths since increased invasion of tumor cells is correlated with poor patient prognosis.[196, 197] In cancers characterized by dramatic tissue invasion, like glioblastoma (GBM) the deadliest form of brain cancer[198], identifying therapeutic targets that address cancer invasion would have dramatic effects in patient survival[199]. To this end, intrinsic efforts have focused on predicting cell invasion *in vivo* in order to discover druggable targets that could halt malignant cells from invading and metastasizing by controlling for cell-extracellular matrix (ECM) interactions[200], substrate rigidity[201] and physical influences of the ECM[202], in 2D and 3D tissue model systems in which to study cell motility *in vitro*.[165, 203-207]

Mechanistic invasion and motility assays aim to determine the response to particular stimuli or inhibitors and determine if that difference is statistically significant from some internal control. Currently, motility studies performed *in vivo* are limited by imaging tools that make it difficult to track single cell migration. Although some have adopted the use of intravital imaging and fluorescently label of cells[208, 209], the use of *in vitro* systems is still highly preferred due to their tunable control, ease of implementation, and reduced cost.

Across the literature, cellular motility is examined not only via different metrics and assays, but also with varying experimental setups as reviewed most recently by Decaestecker et al.[210] and Ridley et al.[211] This diverse set of assays, metrics, and analyses of motility in different biomaterial-based systems makes it difficult to correlate results across platforms, stimuli, and publish reports. Most of the metrics used to analyze cellular invasion and motility have been developed in 2D and translated to 3D studies[210]. Yet, to date, there has been no systematic study to explicitly relate and compare cell motility measurements between these geometries and systems.

To address this, we performed a study to understand if there is correlation between 2D, 3D and *in vivo* cell motility metrics focused on glioblastoma cell lines as a case study. In this analysis, we found that the diversity of invasion and motility assay measurements, approaches, reporting tools, and responses all vary across published lab reports. For *in house* studies of glioblastoma cell lines, we found 2D motility correlation with 3D motility, however, there was no obvious relationship between assay duration, cell density and cell migration outcome from literature data. Interestingly, *in vivo* invasion in glioma negatively correlated with 3D chemotactic index.

From this data we identify that standardized metrics are needed to allow for direct comparison between 2D, 3D, and *in vivo* models. Effect size can allow us to better compare the effects of different stimuli on motility metrics and perhaps draw conclusions independent of dimension and environment[94]. Given the rise of more physiological *in vitro* models that result in more complicated responses, this could be a first step to implement comparison of metrics across the field. Standardizing motility metric outcomes could help bridge the gap between 2D, 3D *in vitro* systems and their translation to *in vivo* physiology. We foresee this study would highlight the need to move towards standardization of motility metrics that will allow for direct comparison across biomaterial experiments within different research groups.

5.2 Results

In order to understand how cellular motility metrics may interrelate, we analyzed the correlations between outcomes for multiple glioma cell lines. These are summarized in Table B.1, which include percent invading cells, percent migrating cells, chemotactic index, speed, total, and net displacement. Excluding percent invasion, which is a chamber-based endpoint assay, all other metrics mentioned are obtained from live, continuous microscopy. The correlations with percent invasion are particularly interesting as the invasion of cells *in vitro* is often assumed to be predictive of invasiveness *in vivo*. Overall, these correlations indicate that it may be possible to infer some cellular motility behaviors from a single assay/measurement. This may be important when making decisions regarding experimental design and analysis of data.

5.2.1 No obvious relationship between measurement time or cell density and cell migration quantification in literature

Across the literature, cellular motility is examined not only via different metrics and assays, but also with varying experimental setup. Thus, we aimed to examine the variability in assay set up and its potential effects on outcomes through a careful literature search focused on several of the most widely examined cell lines in motility assays. We compiled data from a list of publications measuring motility in 2D and 3D platforms (fig. 5.1, and Tables B.1-B.7) among widely used cell lines to extrapolate our findings to that beyond our own labs. We focused on studies of cell motility in 3D that reported % invasion (fig. 5.1a, b) and % migrating (fig. 5.1c, d), and studies that reported % wound closure in 2D (fig. 5.1e). We saw no significant correlation for the 3D motility outcomes with the two consistent experimental conditions reported (assay duration and cell density). In the case of wound healing assays, however, there was an unsurprising correlation between assay duration and percent of wound closure ($r=0.87$, $p<0.01$) (fig. 5.1c).

We found that biomaterial properties like pore size and composition were similar across studies, although concentrations of basement membrane extract (*i.e.* Matrigel^{R}) used were often not reported (Tables B.2-3). Cell invasion outcomes from tissue culture insert assays were reported differently across publications and included total cell number, self-defined "invasion value", fold change, percent invasion, or images without quantitative metrics (Table B.4). Assay readouts varied significantly between crystal violet, H&E staining, trypsinization prior to counting, or simply imaging counting, all at different time points (Tables B.4-5). In the case of invasion, attractants used in invasion assays were unique to each study (Table B.7). Thus, we could not determine a correlation between the assay experimental setup and the cell migration-related outcomes. We were also unable to quantitatively evaluate all experimental design components (such as matrix concentration) within this small sample size of publications.

5.2.2 In vivo invasion in glioma negatively correlates with 3D chemotactic index

The ultimate goal of *in vitro* assays is to predict the behavior of cells in a host organism. For glioblastoma (GBM), the deadliest form of brain cancer, invasion is a hallmark of its behavior and is responsible for recurrence after treatment. Unlike other cancers, in GBM, invasive cells remain within the primary organ, which allows for straightforward quantification of invasion at an endpoint using immunohistochemistry. We hypothesized that this invasion would positively correlate with outcomes of cellular motility *in vitro*. Using data from five models of GBM (our four glioma stem cell lines and the rat glioma line RT2) implanted into mouse cortex, we quantified cells that had invaded beyond the tumor border and correlated these numbers to our assays *in vitro* (fig.

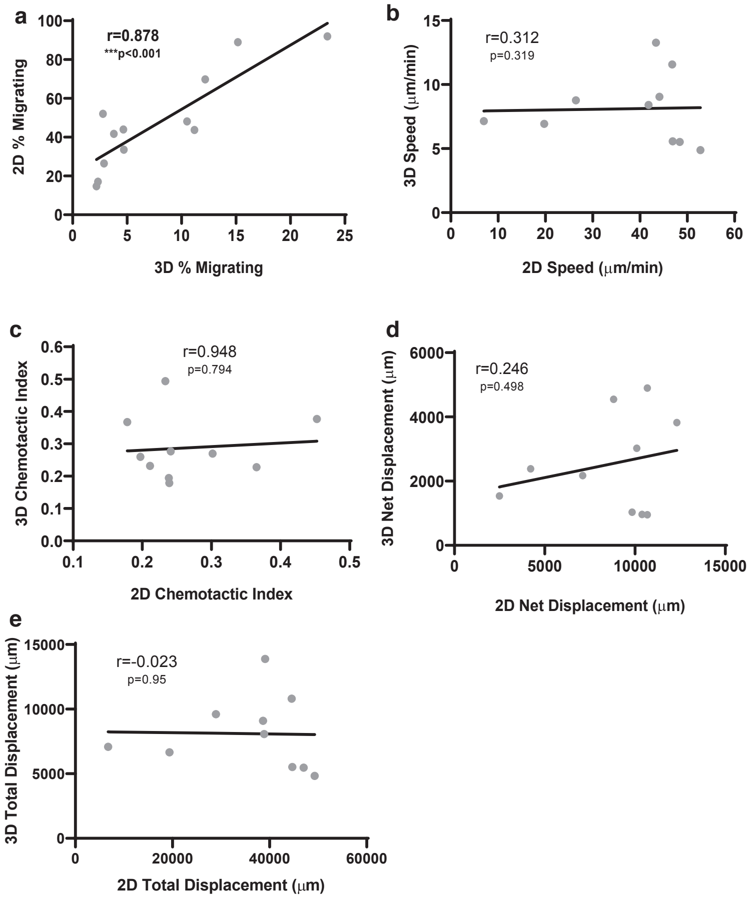

Figure 5.1: Motility metrics compared in 2D and 3D environments for glioma cells. Averaged motility outcomes determined from live imaging and tracking are shown for individual experimental runs and correlated by glioma cell line. a) Percent of cells migrating greater than two cell lengths. b) Speed of cells c) Chemotactic index d) Net displacement and e) Total displacement as determined from individual tracks. Pearson r correlation with p values listed on each graph. Data gathered in collaboration with Dr. Jennifer Munson, Naciye Atay and Hyuna Kim.

5.2a). Results from at least five mice were averaged (data from [212]) and plotted against averaged values from at least four *in vitro* experiments. For cells in 3D, we did not see a statistically significant correlation between any motility metric *in vitro* and our *in vivo* results. However, we did see large negative effects when correlating 3D chemotactic index and net displacement with *in vivo* invasion. Interestingly, the opposite was true with 2D chemotactic index (fig. 5.3). In 2D, we saw large negative relationships of speed and displacement with the invasion metric *in vivo* (fig. 5.4). Due to our low number of cell lines to compare *in vitro* and *in vivo*, it is difficult to conclude anything concrete between invasion *in vitro* and *in vivo*, though we see interesting negative trends that are contrary to our current assumptions about translating *in vitro* invasion outcomes to *in vivo* results.

5.2.3 Effect size as a statistical tool to measure motility changes across dimensions

Mechanistic invasion and motility assays aim to determine the response to particular stimuli or inhibitor (and determine if that difference is statistically significant from some internal control). It is often assumed, though not directly tested, that if a stimulus increases 2D motility it will do the same in 3D. To directly test this assumption, we revisited our data and calculated effect sizes (Cohen's d) in 2D and 3D to determine if 1) dimensionality altered the effect of stimuli and 2) we can use effect size to better analyze and compare cell motility in response to stimuli across dimensions. Effect size is a statistical concept that defines the strength of a relationship between two variables or conditions on the same numeric scale[94]. Thus, one can easily compare the effect of one treatment to another regardless of laboratory, experimental setup, or outcome measure to determine how universal findings are.

5.2.3.1 Glioma motility in response to CXCL12.

We examined motility of multiple patient-derived glioma stem cell lines in the presence of 100nM of CXCL12 in 2D and 3D (fig. 5.6b) by reanalyzing our previously published data [212]. CXCL12 is a pro-migratory chemokine that has been implicated in glioma motility and invasion[213]. We quantified multiple outcomes with live cell tracking and found that the effect size varied based on the dimensionality. For some cell lines (G62) the effect size was nearly equal for percent motile cells when cells were stimulated in 2D or 3D and indicated that there was low effect (<0.2) of the stimulation. For G2 and G528, the effect size varied but remained large (>0.8) for both cell lines in both dimensions. Interestingly though, for G34, the effect in 2D was medium, but large in 3D, indicating that dimensionality may affect this cell line-specific response to CXCL12.

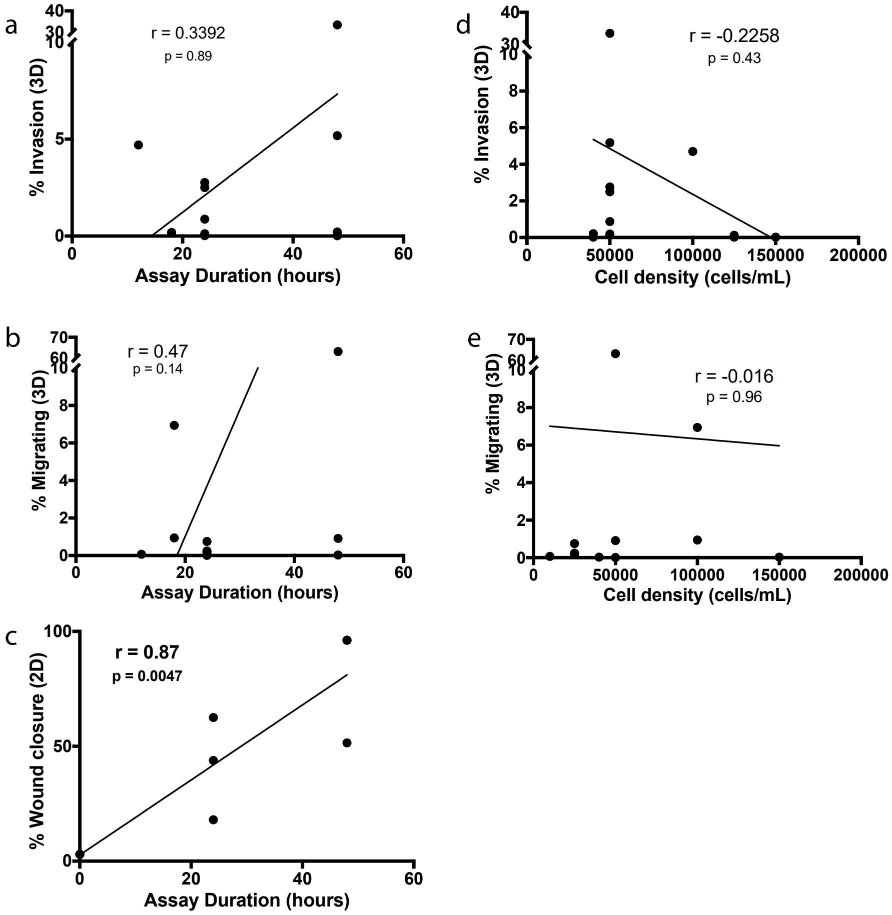

Figure 5.2: Correlation of experimental set up and outcomes from literature for tumor cells. Compiled data outcomes from existing experiments in the literature that examine tumor cell motility as compared to assay parameters. a) Percent invasion in a tissue culture insert-Matrigel assay vs. duration of the experiment and b) initial cell seeding density. c) Percent of cells migrating through tissue culture inserts (without Matrigel) vs. the duration of the experiment and d) initial cell seeding density. e) Percent of wound closure in traditional 2D scratch assay vs the duration of the experiment. Pearson r correlation with p values listed on each graph.

5.2.3.2 Breast cancer motility in response to EGF and integrin inhibitors.

To broaden the utility of effect size beyond glioma to breast cancer cell behavior, figure 5.6c shows SkBr3 cells that were seeded on a bone-ECM functionalized surface and stimulated with EGF or inhibitors for integrin subunits β_1 and α_2[214]. Comparison of effect sizes, as we saw for glioma, the effect size for 2D and 3D for all types of stimulation had roughly the same effect. EGF stimulation had a small effect, β_1 integrin inhibition had a medium effect, and α_2 integrin inhibition had a large effect regardless of geometry. Our analysis highlights the utility of using the statistical tool effect size to determine its importance given its ability to span dimensionality and cell sources.

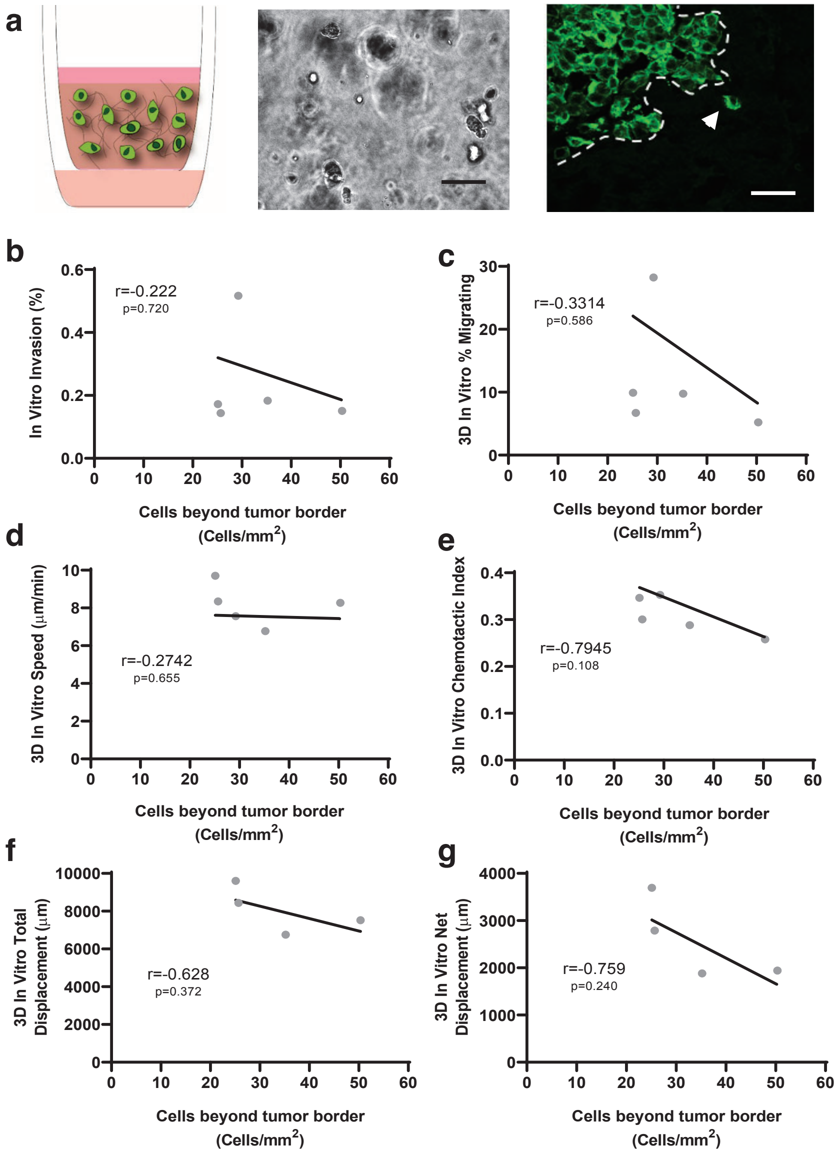

Figure 5.3: Motility metrics for glioma cells in 3D *in vitro* compared to *in vivo* invasion. a) From left to right the images represent the *in vitro* invasion assay, live imaging micrograph from cells in a 3D hyaluronan matrix *in vitro* and glioma cells implanted in mouse brain with border (dotted line) and invasion beyond the border (arrowhead). b) *In vitro* percent invasion c) Percent cells migrating, d) Speed, e) Chemotactic Index, f) Total Displacement, and g) Net displacement graphed by glioma cell line vs. the number of invaded cells beyond the tumor border *in vivo* per

mm2 of tissue. Pearson r correlation with p values listed on each graph. Data gathered in collaboration with Dr. Jennifer Munson and Naciye Atay.

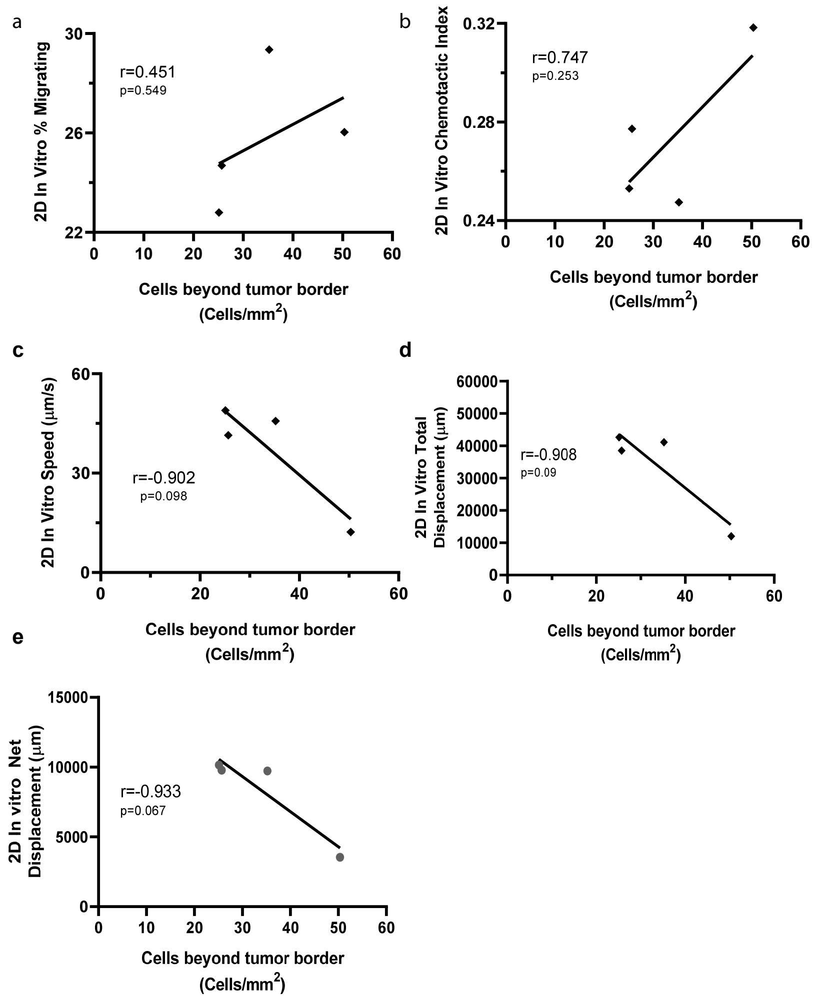

Figure 5.4: Motility metrics for glioma cells in 2D *in vitro* compared to *in vivo* invasion. a) Percent of cells migrating, b) chemotactic index, c) speed, d) total displacement, and e) net displacement graphed by glioma cell line vs. the number of invaded cells beyond the tumor border *in vivo* per mm2 of tissue. Pearson r correlation with p values listed on each graph. Data gathered in collaboration with Dr. Jennifer Munson and Naciye Atay.

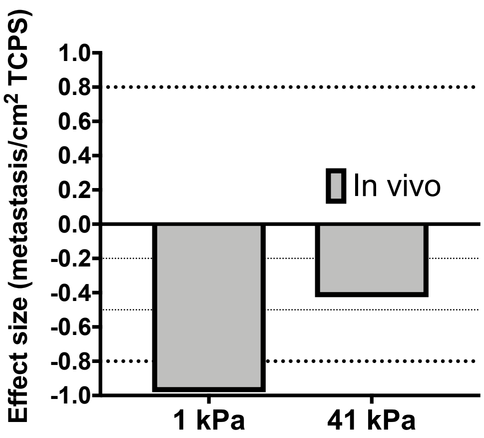

Figure 5.5: Invasion of MDA-MB-231 cell line correlates with metastasis. *In vivo* effect sizes compared to tissue culture polystyrene (TCPS) for cells cultured in soft (1kPa) or stiff (41kPa) hydrogels prior to implantation. Data gathered in collaboration with Dr. Alyssa Schwartz.

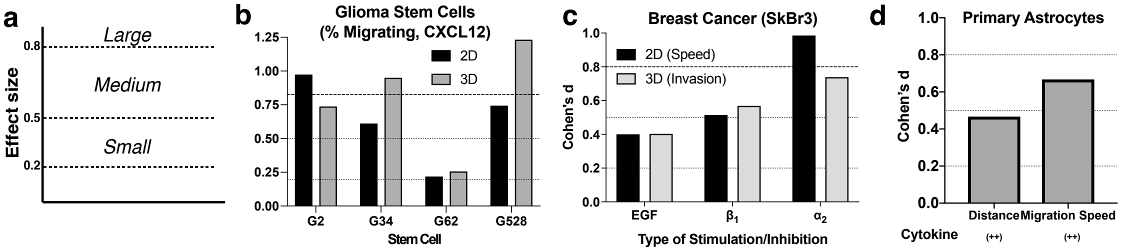

Figure 5.6: Motility effect sizes for tumor cells in 2D or 3D. a) Cohen's d (effect size) delineations for small, medium and large effect sizes. b) Cohen's d calculated for percent migrating cells when stimulated with CXCL12 vs. vehicle control of patient-derived glioma stem cell lines in 2D and 3D. c) Cohen's d for SkBr3 breast cancer cells when stimulated with epidermal growth factor or treated with inhibitors of Integrinβ_1 or Integrinα_2 in 2D (for speed of cell migration) or 3D (for invasion into collagen gels). d) Cohen's d calculated for distance migrated and speed of astrocytes cultured in 3D and dosed with cytokines in contrast to astrocytes in a quiescent state. Data gathered in collaboration with Dr. Jennifer Munson, Naciye Atay and Hyuna Kim.

5.3 Materials and Methods

5.3.1 Cell culture

All cell culture supplies were purchased from Thermo Fisher Scientific (Waltham, MA) unless otherwise noted. The SkBr3 cell line was purchased from ATCC (Manassas, VA), and cells were grown in DMEM, supplemented with 10% fetal bovine serum (FBS) and 1% penicillin/streptomycin (pen/strep). The G2, G34, G62, and G528 glioblastoma stem cells (GSCs) were originally gifted to Dr. Benjamin Purow by Dr. Jakub Godlewski. These cells are primary derived and have been reported and characterized previously by Lee *et al*[215]. The cells were cultured in Neurobasal media with human recombinant EGF and bFGF (50 ng/mL), N2 and B27 without vitamin A supplements, pen/strep in low-adhesion tissue culture flasks (Grenier), and Glutamax.

5.3.2 Preparation of ECMs for SkBr3 migration experiments

Glass coverslips (15 mm and 18 mm diameter, Fisher Scientific, Agawam, MA, USA) were functionalized with 10 g/L N,N-disuccinimidyl carbonate (Sigma-Aldrich) and 5% v/v diisopropylethylamine (Sigma-Aldrich), and ECM protein cocktails were then covalently bound to the glass coverslips through reactive amines: 5 µg/cm^2 of 99% collagen I and 1% osteopontin[214]. Coverslips were incubated with proteins at room temperature for three hours, rinsed three times with PBS, and then incubated with 10 µg/cm^2 MA(PEG)24 (Thermo Scientific, Rockford, IL, USA) for two hours. Coverslips were rinsed three times with PBS, epoxied to the plate (Devcon 5 minute epoxy) and UV-sterilized prior to cell seeding. For invasion studies from coverslips, cells were seeded on coverslips and then overlaid with a collagen gel as previous described[214].

5.3.3 3D Invasion Assays

Invasion assay data for glioma cells was acquired from our previous publications where it was conducted as described[212, 216]. Briefly, cells were seeded in a 1.2 mg/ml thiolated hyaluronan (ESI)/0.8 mg/ml rat tail collagen I (Corning) matrix at a concentration of 1E6 cells/ml. 100μl of this gel was applied to a 8-μm pore tissue culture insert (Millipore). Serum free media was applied to the top and bottom of the well and the system was incubated for 18h after which gels were removed and membranes fixed and stained with DAPI. Membranes were imaged at five non-overlapping locations and %invasion was calculated as an extrapolated cell count divided by the seeded cell count x 100.

5.3.4 Live Imaging and Analysis

Glioma Motility: The motility metrics were determined via live imaging and single-cell tracking of glioma cells in either the hydrogel system (above) or on tissue culture plastic. The EVOS FL Auto (ThermoFisher) microscope and the EVOS Onstage Incubator (ThermoFisher) were used for imaging in 15 minute intervals for 14-18 hours. The incubator was set to the following conditions:

5% CO2, 20% air, and 80% humidity. Images were taken in 20 minute intervals for 18-24 hours. The manual tracking feature on Celleste 4.1 was used to record the location of the visually identified center of the cell of interest in each image of the sequence. An average of 15 cells were tracked per image. The recorded X and Y coordinates were analyzed in Matlab 2018b with the following outcomes: average speed, net and total displacements, and chemotactic index of each cell. Two to nine image sequences were analyzed per cell type (G528, G62, G34, and G2) and experimental condition (2D, 3D) combination per experiment. The averaged values per experiment are reported here.

SkBr3 Motility: Cells were seeded at 4000 cells/cm^2 on ECM protein treated surfaces. They were then treated with a live-cell fluorescent dye (CMFDA, Life Technologies), and fresh medium or medium supplemented with EGF and/or integrin antibodies were provided 4 hours prior to microscopy. Brightfield and fluorescent images were taken at 15-minute intervals for 12 hours using an EC Plan-Neofluar 10x 0.3 NA air objective (Carl Zeiss). Cells were tracked using Imaris (Bitplane, St. Paul, MN, USA) to generate individual cell paths, and individual cell speeds were determined by calculating a speed at every 15-minute time interval, then averaging these over the entire 12 hours.

5.3.5 Tumor Inoculation

Eight to ten week old male non-obese diabetic severe combined immunodeficiency (NOD SCID) mice were stereotactically injected with 15,000 G2 (n = 3), G34 (n = 5), G62 (n = 4), or 400,000 G528 (n = 4). The cells were injected 2.7 mm within the tissue at a 2 mm distance lateral and posterior to bregma, which is the anatomical site at which the coronal and sagittal sutures of the skull intersect. The University of Virginia Institutional Animal Care and Use committee approved all animal experiments as stated in protocol 4021.

5.3.6 Tissue post-processing

Evans blue dye injections were administered intravenously to the animals ten to eleven days after tumor inoculation. Intracardial saline perfusion was performed the following day to euthanize the animals. The brains were harvested, cryoembedded, and sectioned at 12 μm. Immunostaining for 4',6-Diamidino-2-Phenylindole, Dihydrochloride (DAPI, Sigma) and mouse anti-human nuclei (clone 235-1, Millipore) was performed on sections at differing depths of the tumor. EVOS FL Auto 2.0 was used to scan whole sections. After importing raw images into ImageJ, integrated density was used to quantify Evans blue intensity in four to five 0.49 mm^2 regions of the image. Integrated density of each region was normalized to tumor maximum.

5.3.7 Invasion calculations from published data

Percent of invasion, and migration data were extracted with the WebPlotDigitizer v4.1 from the published work cited in figure 4.3 and Tables B1-4. Re-plotted data was used to calculate the percent of invasion based on the initial number of seeded cells.

5.3.8 Effect size calculations

Effect size measures were performed between two independent groups following Cohen's d calculation.

$$\boldsymbol{d = M_1 - M_2 / s_{pooled}}$$

$$\boldsymbol{s_{pooled} = \sqrt{(s_1^2 + s_2^2)/2}}$$

Using the online calculator from Dr. Lee A. Becker at the University of Colorado, Colorado Springs at https://www.uccs.edu/lbecker/

5.4 Discussion

In this analysis, we found that the diversity of invasion and motility assay measurement approaches, reporting tools, and responses all vary across labs (fig. 5.1 and Tables B2-7). Though motility metrics have been studied in multiple contexts for decades, there is still not a consensus nor clarity in terms of the importance of each and the impact of each on outcomes *in vivo*. In cancer, this is particularly striking as there is already a high level of heterogeneity in the disease itself, which is amplified as we move into complex *in vitro* models. One major impediment to the field's progress is the variability from lab to lab in the implementation and analysis of these experiments.

First, we identified high variability in the assay setup. As illustrated in Tables B1-5, concentrations of Matrigel used for invasion assays differed, and in some publications, were not reported. We know that the source and lot of basement membrane extracts (like Matrigel) can influence experiments alone, let alone the concentration[217]. Similarly, assay durations and cell densities differed across most publications using breast cancer cell lines. Unsurprisingly, the assay duration correlated positively with degree of wound closure (fig. 5.1c). When we looked through how different publications quantified their assay outcomes, we noticed variable methods to count invasive cells from the bottoms of tissue culture inserts, including selection of immunocytological stain and/or fixation vs. cellular detachment and counting. Regardless, publications generally reported some final number, though this could be a percent, fold change, or total number of cells that prevented us from directly comparing their results as were able to do for our own experiments. A standardized metric that best conveys the raw data would allow to compare outcomes in a meaningful way across labs.

We propose effect size as a useful metric to understand how and if stimuli and inhibitors affect cell motility across geometries and labs. For example, as seen on figure 5.6b and 5.6c, comparing each Cohen's d value illustrates the effect of each ECM substrate or each stimulus for two different cell types. Within each cell line, we can see the significant effect of the stimulus on cell response, across geometries, and independent of the cell's genetic background. Additionally, comparing the value of the effect size (>0.2, >0.5, or >0.8) allows us to better understand how large an effect is, without the need for a p-value (which has been recently put into question[95]).

The desire to understand how 2D cell migration relates to that in 3D is not unique to our study. Meyer *et al.* quantified breast cancer cell line motility and showed that the degree of initial cell protrusion in 2D was predictive of 3D invasion across many different stimuli[218]. In agreement with or analysis of glioma cells, Meyer *et al.* found no other obvious correlations between 2D and 3D cell migration measurements. Similarly, when studying the role of focal adhesion proteins in cellular motility, Fraley *et al.* compared speed, persistence, protrusion length/number/time, etc. in 2D and 3D and found no correlation between any of the metrics in the two environments.[219] Next generation biomaterials are being developed that provide possible explanations of the key differences between 3D and 2D environments that drive the unique motility phenotypes, such as confinement [220, 221] and porosity[222].

Ultimately, we are attempting to predict cell invasion *in vivo* so that we can potentially discover druggable targets to halt malignant cells from invading and metastasizing. In our limited dataset we show that there is a negative correlation between migration in 3D collagen gels with invasion *in vivo*. Live imaging data may reveal more information, but with at least our endpoint assay, we cannot predict *in vivo* "invasiveness" with *in vitro* invasion in glioma. It's possible that our *in vitro* systems, even when 3D, do not hold enough complexity to capture true *in vivo* behavior.

Taken together, standardized metrics are needed that allow for direct comparison between 2D, 3D, and *in vivo* models. Effect size can allow us to better compare the effects of different stimuli on motility metrics and perhaps draw conclusions independent of dimension and environment. Given the rise of more physiological *in vitro* models that result in more complicated responses, this could be a first step to implement comparison of metrics across the field. Finally, standardizing motility metric outcomes could help bridge the gap between 2D, 3D *in vitro* systems and their translation to *in vivo* physiology.

5.5 Conclusions

Current challenges in the field of cellular motility and invasion within biomaterial-based systems, including diversity of assays, metrics, and analyses, limit the translation of results across platforms and impede correlation between 2D, 3D and *in vivo*. Here, we summarize the most commonly used metrics to quantify cell motility, and describe the interrelation between these different motility measurements, the important differences in assays and reporting techniques used across the literature and describe the potential contribution of *in vitro* predictions to *in vivo* outcomes. To our surprise, we found cell invasion in 3D is negatively correlated with invasion in a glioblastoma model *in vivo*. Given the variability we saw in reporting in the literature, and the inability to predict 3D or *in vivo* invasion from simpler 2D assays, we suggest that standardized metrics are needed. We recommend the use of effect size as a possible avenue that allows direct comparison between two different groups independent on dimensionality or stimulus. Given the rise of more physiological *in vitro* models that result in more complicated responses, this could be a first step to implement comparison of metrics across the field. Finally, standardizing motility metric outcomes could help bridge the gap between 2D, 3D *in vitro* systems and their translation to *in vivo* physiology.

CHAPTER 6

APPLICABILITY OF DRUG RESPONSE METRICS FOR CANCER STUDIES USING BIOMATERIALS

6.1 Introduction

Bioengineers have also built more complex models of the tumor microenvironment (TME) in which to study cell-cell interactions, mechanisms of cancer growth and metastasis, and to test new therapies by modulating additional parameters in biomaterials. These models allow researchers to culture cells in conditions that include features of the *in vivo* TME implicated in regulating cancer progression, such as the extracellular matrix (ECM) stiffness[30, 223, 224], integrin binding to the ECM, immune and stromal cells[225], growth factor and cytokine deposits[226], and a 3D geometry more representative of the TME than traditional tissue culture polystyrene (TCPS)[227]. These biomaterials could be particularly useful for drug screening applications to make better predictions of efficacy, offering better translation to preclinical models and clinical trials. However, it can be challenging to compare drug response reports across different platforms in the current literature in part as a result of inconsistent reporting and use of drug response metrics[88], and vast differences in cell growth rates[89] across biomaterial designs.

As an attempt to address the large differences between cell growth rates across cell lines, Harner et al, [89] defined the GR_{50} (the concentration of a drug that reduces cell growth rate by half) as a new metric to account for cell line growth rate differences across drug response studies, with the aim to standardize current reports. However, additional parameters have also led to inconsistencies in results between studies, for example misinterpretation of drug response metrics or incorrect application of metrics in certain cases. As one high profile example, Haibe-Kains et al.,[88] reported inconsistencies between two large pharmacogenomic studies: the Cancer Genome Project (CGP) and the Cancer Cell line Encyclopedia (CCLE) where they compared the IC_{50} (the inhibition concentration of a drug where the response is reduced by half) and the area under the dose-response curve (AUC) for 15 drugs across 471 cell lines, and found very little correlation between the two studies (Spearman's rank correlation of 0.28 and 0.35 for IC_{50} and AUC, respectively).

To assess how these inconsistencies, translate to the implementation of biomaterials as drug screening platforms, we conducted a literature search to investigate how bioengineers have quantified drug response metrics in biomaterials. We found that often multiple drug response metrics are used, however, it was not clear in every study why certain reporting tools were used, and whether or not they were applied correctly. For instance, we found cases where an IC_{50} was reported, but the drug was not effective enough to inhibit growth of half the cell population. Thus, when analyzing the literature, we then wondered whether the implementation of a global, consistent analysis would reduce the disagreement of values reported. Would methods used to analyze drug responses in 2D culture also apply for 3D systems? In the case of co-culture systems, should a different approach be used to separate the responses from cancer cells and healthy cells in the TME? With this in mind, this study compares select cases in the literature, our own data for cell responses to drugs in and on biomaterials, metrics reported, and inconsistencies between studies. We attempt to clarify the definitions of drug response measurements used in the field and presents examples in which these measurements can and cannot be applied. We conclude with a "decision tree" that could help guide what metrics to use when working with biomaterial systems.

6.2 Results and Discussion

6.2.1 Definitions of Drug Response Metrics

Drug response assays evaluate the impact of a drug on a population of cells over a range of concentrations. For simplicity, we will define the number of cells at the start of the assay readout, or the 'initial value' of the cells as y_0 (fig. 6.1a). Unfortunately, many studies do not report y_0, which prevents some metrics from being reported, as we discussed later in this section. The cells are then incubated with drug for a defined period of time (typically 24-72 hours), and cell viability is measured (y_{final}). Cells are also incubated with a small amount of the vehicle in which the drug was dissolved (often DMSO or water), serving as a control (y_{ctrl}).

a

E_{max}: The maximum level of growth inhibition or cell death possible with the drug

Area under curve (AUC): The area under the curve fitted to the drug-response data

Metric	The drug concentration which...	The drug concentration where...
IC_{50}	reduces population to half of the control value	$(Population) = 0.5 \times y_{ctrl}$
GI_{50}	reduces total cell growth by 50%	$(Population) = \frac{(y_{ctrl} - y_0)}{2} + y_0$
GR_{50}	cell growth rate by 50%	$(Population) = 2^{log_2(y_{GI50}/y_0)/\ (y_{GI50}/y_0)} - 1$
EC_{50}	achieves half of the effect defined by E_{max}	$(Population) = \frac{(y_{ctrl} - E_{max})}{2} + E_{max}$

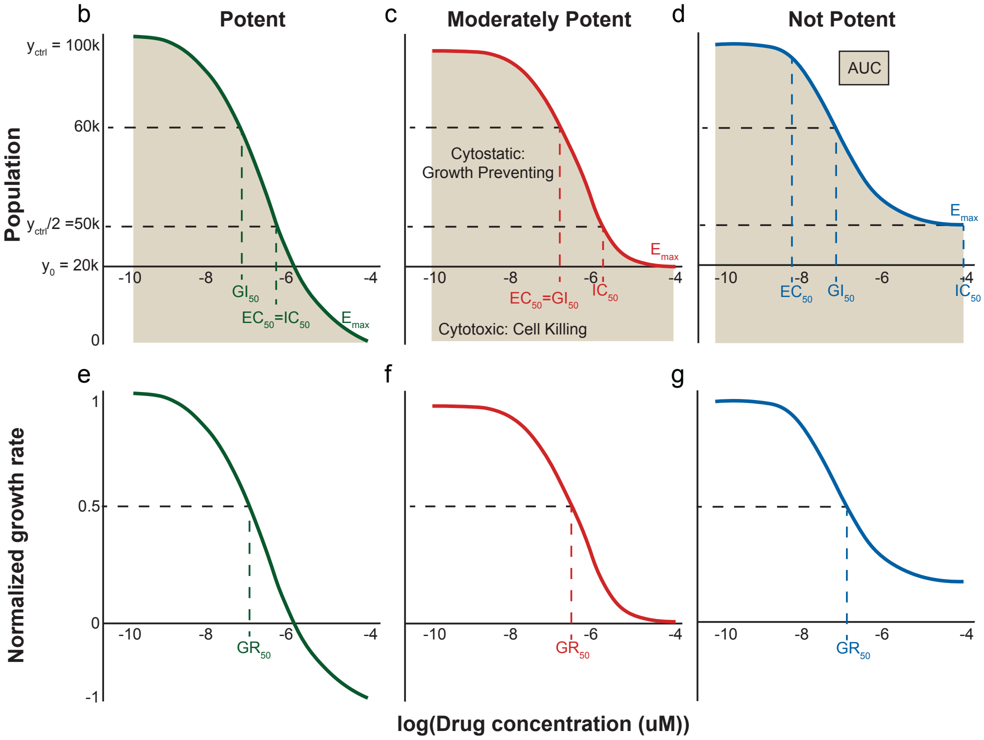

Figure 6.1: Definitions and examples of drug response metrics. a) Definitions of drug response metrics. The IC_{50} represents the drug concentration where the response is reduced by half. The EC_{50} represents the concentration of a drug that gives half-maximal response. The GI_{50} represents the concentration of a drug that reduces total cell growth by 50%. The GR_{50} represents the concentration of a drug that reduces cell growth rate by 50%. The E_{max} represents the fraction of viable cells at the highest drug concentration (maximal response), and the AUC represents the area under the dose–response curve. b) and e) The y-axis shows the cell count (top plots) and normalized growth rate (bottom plots). Drugs are considered “cytotoxic” if viability is reduced below the initial value (y_0), and “cytostatic” if viability is above the initial value, but below the control value (y_{ctrl}). Left curves (“Less potent”) show a drug which reduces viability by 50% at maximum dose, (IC_{50} is the maximum dose). c) and f) Middle curves (“Moderately potent”) show a drug which completely inhibits growth, but is not cytotoxic (E_{max} = initial viability). d) and g) Right curves (“Potent”) show a drug which is 100% cytotoxic (E_{max} = 0). Note that in these special cases some of the other metrics are also equal to each other, which are labeled on the plot.

A drug is considered cytostatic if it slows or completely prevents growth of cells[228]. In other words, if the measured cell viability is between y_0 and y_{ctrl}, that drug is said to be cytostatic at that concentration. Cytotoxic means that the drug reduces the cell number below the initial cell count ($y_{final}<y_0$). Note that when y_0 is not measured, a true drug cytotoxicity cannot be reported.

There are six typical metrics used to report the effect of a drug on a cell culture: IC_{50}, EC_{50}, GI_{50}, GR_{50}, E_{max}, and AUC (fig. 6.1a). Figure 6.1 gives definitions of these metrics, with three hypothetical drug response curves with varying degrees of "potency." A "potent" drug is 100% cytotoxic, a "moderately potent" drug achieves 100% growth inhibition but no net cell death, and a "less potent" drug reduces cell growth by 50% (fig. 6.1b-g). Drug potency can also be evaluated by the curve response class classifier (CRC), as described by Inglese et al.[229] The CRC metric helps group the efficacy of cell and drug combinations to reveal if a particular combination is fully cytotoxic or cytostatic, and can be valuable in cases where a full dose response curve is not obtained. Furthermore, these classifications aid in determining promising cases to select for future screening studies.

The IC_{50} and E_{max} metrics do not consider the initial population (y_0), nor the number of cell divisions during the length of the assay, which was a motivating factor for Hafner et al.,[89] to define the GR_{50}. Only the GI_{50} and GR_{50} take y_0 into consideration. GI_{50} is the dose that inhibits the growth of cells by 50%, and GR_{50} represents inhibition of the growth rate, not total growth, of the cell culture. The initial cell population, y_0, can vary between type of assay, cell type, or length of assay. To account for this variation, GI_{50} and GR_{50} are represented as data normalized with respect to the initial values (fig. 6.1e-g).

Although the '50' in IC_{50}, EC_{50}, GI_{50}, and GR_{50} metrics signifies a 50% inhibition, they can be used with values other than 50 to indicate different effects, e.g. IC_{90}[230, 231]. Negative values can be used for the cytotoxic regime ($y_{final}<y_0$), although these do not come from the formal definitions of GI or GR. In this case, GI_{-10} would be the concentration where the cells are reduced 10% from the initial value ($y_{final} = 0.9 \times y_0$), and GI_{-100} would be the concentration which kills all the cells. In the Figure 5.1 example, 0-100 is defined over the range of $20k \leq y \leq 100k$, while -100-0 is defined over the range of $0 \leq y \leq 20k$. IC_{-n} or EC_{-n} values are not possible since these metrics do not consider initial values.

The E_{max} and AUC metrics represent the maximum and cumulative effects of the drug, respectively. E_{max} is the fraction of viable cells at the highest drug concentration tested in the experiment, and AUC is the area under the viability curve for a cell population over the tested drug concentration range. Although neither of these metrics make any explicit assumption about growth kinetics, they still depend on the concentration range, experiment duration, and cell growth rate, which means that their reported values cannot be compared with other studies in most cases. For example, work by Fallahi-Sichani et al. [232] found AUC to be a robust response metric when the goal was to compare a single drug across identical cell lines. However, these need to be exposed to identical dose ranges, and preferentially at an intermediate concentration. E_{max} can be used with multiple drugs and concentration ranges but is more informative at high doses[232]. Particularly in the case of E_{max}, Fallahi-Sichani and colleagues' work highlighted it as a parameter that yielded high variation independent of cell proliferation rate. Yet, this study was unable to conclude what drug metric parameter best describes a drug response without considering drug concentration.

The IC_{50} is the most commonly reported drug response metric[233], and therefore it is important to highlight cases in which it is used with an incorrect definition. For instance, the IC_{50} should not be considered a measure of cell death[228]. As one example, in a case when the control value is more than 200% of the initial value ($y_{ctrl} > 2 \times y_0$, as can be seen in the examples given in fig. 6.1b-d), the IC_{50} will result in a "cytostatic" dose, but the cells are still growing, be it at a reduced rate. Second, in a case where a reduction in half the population is not reached, (such as In [234-236]) the IC_{50} cannot be appropriately calculated, and instead the EC_{50} is the more appropriate metric to report. In other instances, in the literature, the EC_{50} and GI_{50} are confused with the IC_{50} [89]. However, the GI_{50} metric is a correction of the IC_{50}, since it takes into consideration the initial cell count (y_0) [237].

Through our analysis, we also found examples where authors report a GI_{50}, when it is actually an IC_{50} (they did not measure y_0)[238]. For example, the cell population could grow over the course of an experiment, while the measured population values could still be lower than the control. Therefore, the initial cell populations must be measured to know whether a drug is killing cells or

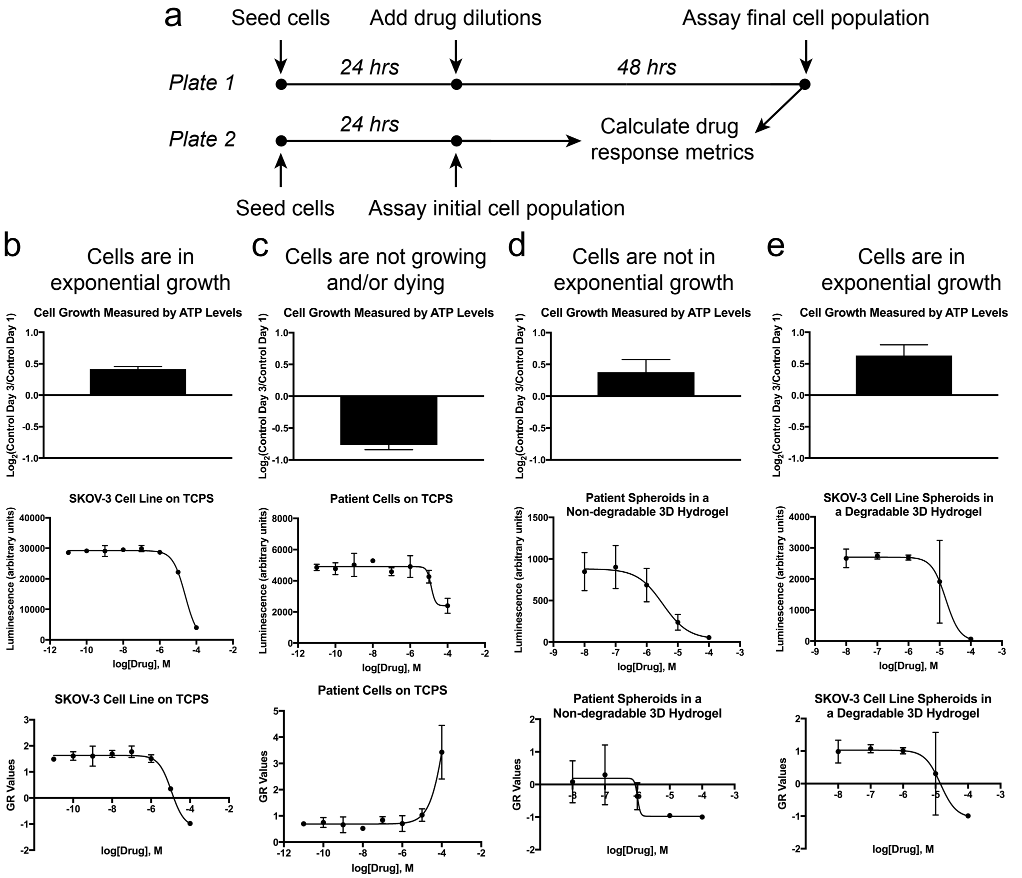

IC_{50}: 14.6 μM	IC_{50}: 13.2 μM	IC_{50}: 1.28 μM	IC_{50}: 12.1 μM
EC_{50}: 13.6 μM	EC_{50}: 29.8 μM	EC_{50}: 1.28 μM	EC_{50}: 12.0 μM
E_{max}: 0.153	E_{max}: 0.559	E_{max}: 0.0484	E_{max}: 0.0259
AUC: 1.01 a.u.*log[Drug], M	AUC: 1.08 a.u.*log[Drug], M	AUC: 0.511 a.u.*log[Drug], M	AUC: 0.812 a.u.*log[Drug], M
GR_{50}: 9.3 μM	GR_{50}: N/A	GR_{50}: N/A	GR_{50}: 9.11 μM

f

Curve Classification Criteria

Curve Class: 2a	Curve Class: 1a	Curve Class: 1b	Curve Class: 1b
Description: Incomplete curve	Description: Complete response	Description: Partial response	Description: Partial response
Efficacy: >80%	Efficacy: <80%	Efficacy: >80%	Efficacy: >80%
r^2: 0.891	r^2: 0.456	r^2: 0.766	r^2: 0.846
Asymptotes: 1	Asymptotes: 2	Asymptotes: 1	Asymptotes: 1
Inflection: Yes	Inflection: Yes	Inflection: Yes	Inflection: Yes

Figure 6.2: Application of drug response metrics to data from biomaterial drug screening. a) Schematic of typical experimental work flow for a drug response assay. Cells are seeded on a 2D tissue culture plastic surface, on a 2D biomaterial, or within a 3D biomaterial for drug dosing. Wells in a second plate are seeded with the same conditions as the drug dosing plate to measure GI_{50} or GR_{50} values. After 24 hours, drugs are added to the drug dosing plate and the second plate for initial values is assayed simultaneously for initial cell counts. The drug dosed plate is incubated for a period of time (e.g. 48 hours) and then assayed for the final cell response. The collected data is used to calculate drug response metrics. b) Cells grown on tissue culture plastic achieve sufficient growth to generate a traditional dose response curve, as well as a GR values curve to calculate a GR_{50}. c) An example of patient cells grown on tissue culture plastic that do not grow exponentially over the course of the dosing assay. This results in a curve for traditional drug response metrics, but a GR curve cannot be calculated. d) This is a case where cells grow over the course of the assay, but sufficient growth for calculating a GR_{50} measurement is not achieved because the resulting GR values are less than 0.5, which is the point where the GR_{50} is calculated. e) Cell line MCTS encapsulated in a degradable 3D hydrogel demonstrate enough growth to calculate a GR50 and other drug response metrics. f) Curve response classification descriptions for the data shown here. The cases presented here do not exactly correspond with the criteria

described by Inglese et al. (particularly r^2 values), but we categorized them to their nearest classification. Data gathered in collaboration with Dr. Elizabeth Brooks and Dr. Maria Gencoglu.

only slowing their growth. In addition, the IC_{50} is sometimes discussed in the context of growth inhibition[239], although it is not capable of measuring this. This highlights the importance of reporting the metric that is most appropriate for observed responses and experimental conditions, given the explanations stated above. Similarly measuring the initial cell population values (y_0) is indispensable as it would allow for GI_{50} and GR_{50} calculations (if cell growth of the control is achieved over the course of the assay). This is of particular importance when multiple cell lines or growth conditions are being tested, as these metrics will account for differences in growth rates.

The GR_{50} is very similar to GI_{50}, but is defined by reduction of the growth rate, not cell growth as the GI_{50}. Growth rate inhibition is calculated from initial and control values, and the fitting for the GR_{50} relies on the assumption that the cells are in exponential growth before application of the drug. GR_{50} is thus reported to be more robust than GI_{50} against variations in experimental protocols and conditions[89].

6.2.2 Applying drug response metrics to data obtained from biomaterial drug screening assays

Drug screening cells in biomaterials rather than on TCPS is increasingly popular due to the fact that more physiologically relevant features can be captured in biomaterials that may impact drug response. 2D[223, 240, 241] and 3D[91, 234, 242] biomaterial platforms have been developed to study cell behavior *in vitro*. Since it is widely accepted that cells grow at different rates in 2D and 3D biomaterial platforms[227], it is difficult to compare drug responses across these different environments without a GI_{50} or GR_{50}. Experiments to obtain these metrics require only minor adjustments to traditional drug screening protocols performed by seeding cells in an additional plate to measure initial population values (y_0) (fig. 6.2a). In particular, the GR_{50} has worked very well for over 4,000 combinations of breast cancer cell lines and drugs on TCPS[93], but work in 3D biomaterials systems has limited the use of the GR_{50}.[243]

Our own lab uses both 2D and 3D biomaterials in addition to TCPS for drug screening studies[86, 90], and we have adapted our experimental procedures to collect data for calculating GR metrics in addition to the other metrics depicted in figure 6.1. However, we have found that the GR_{50} cannot always be applied. As it has been previously reported[89, 93], it is necessary for the cells to achieve exponential growth over the course of the assay to use the GR_{50}. On TCPS, this is not an issue, as demonstrated by our data in figure 5.2b with SKOV-3 ovarian cancer cells dosed with Paclitaxel. In this case, the GR values span a -1 to 1 range, which results in a good curve fit to calculate a GR_{50}.

However, another important factor to consider in preclinical drug screening assays is the increasing use of patient-derived primary cells. This has become a hurdle as many primary cells grow more slowly or in some cases, not at all, making it impossible to calculate a GR_{50} value. In these cases, the calculated GR values remain well below 0.5, even at a control dose. Therefore, the formula for calculating GR values can be applied, but with growth rates that are too low they do not provide meaningful information. As illustrated by our own data of patient-derived cells, ovarian cancer cells from ascites dosed with Cisplatin on TCPS (fig. 6.2c), IC_{50} and EC_{50} values could be calculated, but growth was too low for a GR_{50} value, and could not be calculated. This serves as an example in which additional drug response metric parameters are necessary to understand the effect of drug dosing, given that these primary cells proliferated very slowly when grown in a 3D environment.

For example, work by Longati et al.[234] highlights how pluripotent stem cell (PSC) drug response differs on 2D vs. in 3D biomaterials. Although IC_{50} values were not reported in this work, we calculated the IC_{50} and EC_{50} from their published data and observed higher resistance in their PSC cells in 3D compared to 2D (Table C.1). Work from Ivanov et al. [91] performed drug response studies with neural stem cells (NSCs) and the UW228-3 glioblastoma cell line in 3D. They found that the NSC drug response was biphasic, but not for the human glioblastoma cell line (which showed more resistance in 3D). Here, two IC_{50} values were reported for the same curve in the case of primary cells, representing a situation where an IC_{50} (or GI/GR/EC_{50}) is inappropriate. In these cases, calculations of AUC or E_{max} would be more appropriate since they are not dependent on curve fitting (fig. 6.1b-d).

As demonstrated by our own experimental data (fig. 6.2d), culture of 3D patient-derived spheroids from ascites in a non-degradable 3D hydrogel exhibited a low growth rate over the course of the assay. Although a dose-response curve with Mafosfamide was generated from the data (fig. 6.2d), this does not mean that a valid GR_{50} value can be obtained. GR value curves need to pass through GR = 0.5 or they cannot have a reliable GR_{50} value, even if certain curve fitting software gives a value for these circumstances, as we demonstrate in figure 6.2d. Therefore, it would be good practice to only use the online GR calculator[89] to calculate GR metrics from raw data since this would ensure that true GR metrics are reported. There are cases of drug screening in 3D environments[243] where the GR metrics could be applied, but since growth is often slower in 3D than in 2D, the application of the GR calculations should be done carefully. In contrast to our dosing of ovarian cancer cells above, we demonstrate in figure 6.2e an example where we encapsulated SKOV-3 cells grown in multicellular tumor spheroids (MCTS) in a 3D hydrogel and dosed with Mafosfamide. In this case, the cell growth was high enough to calculate a GR_{50}. From our own work, we recommend reporting the GR_{50} when possible to best account for differences in growth rates between different cell sources. We also encourage others to provide all the raw data and drug response curves with their publications to allow others to compare published results with their own (Table C.2).

To further characterize the drug response in different material environments, we applied CRC metrics described by Inglese et al. [229] to our own data (fig. 6.2f). We found that the r^2 values that we obtained for the non-linear curve fits to the data were <0.9, which meant it was not possible to fit our results into these exactly defined classes according to the criteria set by Inglese *et al*. However, some of these drugs had >80% efficacy, and displayed drug response curve with one ('Partial'), two ('Complete'), or no asymptotes ('Incomplete'). We found that the 3D models, OCAS in a 3D non-degradable hydrogel and SKOV-3 MCTS in a degradable 3D hydrogel were in the same curve response class: 'Partial' even though their GR metrics were very different. Additionally, patient cells on TCPS had a ‘Complete’ response (class 1a), but it was not possible to calculate biologically meaningful GR metrics. Interestingly, at the range of concentrations that were tested the case of SKOV-3 cells on TCPS was classified with an ‘Incomplete’ response (class 2a), but all the traditional dose response and GR metrics could be calculated. These additional metrics could be helpful for eliminating cases for further study in biomaterials when there are no responses (class 4), but we do not show any examples of that in here. Characterization with CRC could be used as another method for grouping drug curves responses on biomaterials.

6.2.3 Evaluation of drug responses in biomaterials reported in literature

To compare IC_{50} values across studies, we mined data from 25 reports that performed drug screening with biomaterial systems, and that provided raw data that could be extracted and analyzed independently. We calculated the IC_{50}, EC_{50}, E_{max}, and AUC values and organized them by drug in Table C.1. We were not able to calculate GI_{50} and GR_{50}, because the initial population (y_0) and control (y_{ctrl}) values were not provided in these studies. Table C.1 shows a summary of the reported IC_{50} values from the literature and the drug response metrics calculated by us from their reported data. Table C.2 summarizes cases where the drug response curve did not reach 50% inhibition, meaning the IC_{50} was not reached. Table C.3 summarizes cases where the IC_{50} values reported in the literature did not agree with the values we calculated from reported data. We also applied the CRC metrics described by Inglese *et al.* to the data we extracted from the literature (Table C.1-3).

First, we found that for highly potent drug-cell line combinations, such as MCF7 with Paclitaxel or MDA-MB-231 with Epirubicin, IC_{50} values reported were on the same order of magnitude (Table C.1). In contrast, when a cell line was not particularly sensitive to the drug, like in the case of the MDA-MB-231 cell line to Paclitaxel or Docetaxel, and MCF7 treatment with Doxorubicin or Tamoxifen, IC_{50} values reported from different studies varied much more strongly. This variance appears to be more dependent on the potency of the drug than the platform in which the cells were treated. When drug sensitivity was moderate or low, wide ranges in IC_{50} values tended to be even more drastic in the 3D models compared to 2D.

Another finding in Table C.1 is that highly efficacious drugs had 'Complete' response curves, while less efficacious drugs had 'Partial' or 'Incomplete' curves. This is unsurprising, though there are some interesting observations: 1) all the drugs that failed to reach IC_{50} values had 'Incomplete' curves; 2) 'Incomplete' or 'Partial' response curves were mostly obtained in 2D models, while drugs tested in 3D models tended to display a 'Complete' response curve. Paclitaxel results with MDA-MB-231 are a good example of this. These results also illustrate the inadequacy of r^2. In Table C.2 we present 5 cases (out of 28 cases in Table C.1) where $r^2>0.9$, while the drug response curve had no asymptotes. So, it is unclear if Inglese et al's criteria applies here.

One of the major challenges we encountered during our literature search was that a limited number of studies published their drug response curves. Some publications did not report IC_{50} values for cases where the drug concentration did not kill half of the cell population (Table C.2). Unsurprisingly, these drug response curves were all 'Incomplete', with one exception. In most cases, there were too few points to even calculate an r^2 value from the nonlinear fit. In these cases, r^2 was reported as 'N.D.' (Non-determined).

Table C.3 illustrates cases in which the IC_{50} we independently calculated did not agree with the one reported. This was mostly the case for cell lines that were fairly drug insensitive, as evidenced by the 'Partial' response curves of these drugs. Despite the 'Partial' response curve, E_{max}, IC_{50}, and other metrics could be calculated for these drugs. This finding is significant, because it shows a pitfall of assessing drugs based on metrics without accounting for the drug response curve. The drugs in Table C.3 would seem efficacious based on their drug response metrics, although the drug response curve shows them to be insensitive to drugs. Finally, similarly to Table C.1, the drug response curves in Table C.3 have r^2 values of >0.9, but only one asymptote ('Partial'). This again shows that r^2 alone is not an adequate criterion for CRC classification.

The drug response metric values reported in Tables C.1-3 vary by study and may depend on the type/length of assay, biomaterial used, and/or analysis conducted. The most commonly used cell viability assays in our search included MTT assay, AlamarBlue (*i.e.* resazurin), Live/Dead staining, and CellTiter-Glo. These types of assays indirectly measure the cytostatic or cytotoxic effect of a drug, via metabolic activity, counting of dead cells, cell death, or ATP activity. There are additional complications with data reported in the literature. Many publications did not present enough data points for us to calculate IC_{50} and could not be included in the comparison. There were other published reports where no metrics were reported, which makes it impossible to relate them to other published data. Clearly, better standard practices should be adopted. We recommend that future publications explicitly define the metrics they use, for two reasons. First, clearly explaining the metrics used in an article would help others learn about drug response metrics, and it would also prevent them from misinterpreting results. Second, definitions of the metrics are dependent on the context. For example, in the articles we summarized, 'inhibition' in IC_{50} refers to the inhibition of cell viability. In other works, however, it may refer to the inhibition of cell growth, which should be called a GI_{50} and calculated accordingly.

Among the 30 studies we examined, 25 presented drug response curves from which IC_{50} values could be obtained. We used the WebPlotDigitizer Tool (https://automeris.io/WebPlotDigitizer) [244] to extract drug concentrations and cell viabilities from these curves. This data was analyzed in GraphPad Prism to calculate an IC_{50} using nonlinear regression with variable slope (4 parameter) and least squares fit method. From the data summarized in Tables C.1-3, we made comparisons between the 51 drug response curves and IC_{50} values reported in these studies. We found our results in agreement with 35 of these (69%), including 5 cases where neither we nor the original authors could obtain an IC_{50} value due to drug potencies being too low. In 16 cases (31%) IC_{50} values were significantly different between the value reported and our own calculation. These differences are possible because 1) we extracted the numerical data from plots in article figures, which may introduce error; 2) different researchers may have used different forms of nonlinear regression (e.g. least squares or robust fit methods for curve fitting, fixing the hill slope to the standard -1, or using variable slope); 3) other researchers may have chosen different methods (appropriate or not) to handle problems such as outliers and negative inhibition, including setting constraints on the maximum and minimum values, manually determining outliers, using software algorithms for automatic outlier detection, etc.; and 4) there could be cases where the IC_{50} could not be calculated due to the shape of the fitted curve, yet some data analysis software will attempt to calculate an IC_{50} that results in an unrealistic value.

6.2.4 Assessing drug response in multicellular culture systems

Coculturing cancer cells with stromal cells (e.g., cancer-associated fibroblasts, pericytes, or adipocytes) has been shown to drastically alter drug response, ranging from promoting drug resistance to increasing drug sensitivity[245-249]. Furthermore, multicellular cocultures may be more physiologically relevant than monocultures, either in 2D or 3D, as they can account for tissue level interactions. In fact, it was recently shown that basal-like and mesenchymal-like subclasses of breast cancer could be distinguished based on their expected drug sensitivities, but only when co-cultured with fibroblasts[246]. It is unclear how much complexity is required to accurately predict *in vivo* drug efficacy, but recreating aspects of the cellular TME is emerging as an important consideration due to the *in vivo* spatial heterogeneity[243]. Logsdon et al., found that MDA-MB-231 cells in mixed, 3D culture with fibroblasts were more resistant to 10 μM doxorubicin at low ratios of tumor to stromal cells (4:1) but equally affected by the drug at higher ratios (1:4)[245]. Shen at al., found similar results using a micro-patterned interface of tumor to stromal cells wherein MCF7 cell proliferation was inhibited by reversine at the interface but not in the bulk[250]. Expanding these data sets to evaluate a range of drug doses would provide insight into how dose response varies between the tumor bulk and regions of more diffuse invasion.

One challenge with co-cultures is the determination of drug response metrics for the discrete populations of cells. It is easiest to use cells expressing a reporter transgene or labeled with nontoxic dyes. Measurement of total fluorescence or bioluminescence then provides an estimate of the labeled cell number over the course of drug treatment[251, 252]. However, dead cells may remain within 3D models, so the use of total fluorescence readings in these systems may be inaccurate. More appropriate in 3D is to stain cells using a viability marker like propidium iodide or JC-1 and quantify cell viability and/or number using either confocal/multiphoton microscopy or flow cytometry[245, 246, 249]. These methods can be used to track the drug response of one cell type while ignoring other cell types or examine it for multiple cell types via multiplexing of different fluorophores. Coculture systems do require deciding which sample is more appropriate for calculating y_{ctrl}: a cancer cell only sample or a sample with all the cell types. Arguably, the respective untreated sample should be used for each treated sample to compensate for any effects of the stromal cells on cancer cell viability or growth rate. Additionally, the multiple centrifugation steps involved in harvesting and labeling cells for flow cytometry carry a risk of decreasing cell yield, such that it would be best to seed separate samples at the start of the study for determining an accurate y_0.

Physically separating stromal and tumor cells using either conditioned media or culture inserts can isolate effects, but several studies have shown that direct cell-cell contact may be a crucial component of stromal-derived effects on cancer cells[51, 250, 253]. In mixed cultures, the most common methods to assess cell viability, such as MTT Assay, AlamarBlue, and CellTiter-Glo, measure the entire population of cells such that isolating the effects on only the cancer cells is not feasible. For example, by using CellTiter-Glo Ngo and Harley reported an increase in the overall growth rate of glioblastoma-endothelial cell cocultures with increasing Temozolomide concentration, but it is unknown if both cell types contributed equally.

It is possible the cancer cells responded the same as in monoculture (growth rate inhibition) while endothelial cells increased their growth rate, or that only endothelial cells were affected and therefore protected the cancer cells. Separating the responses of different cell types may not always be a significant drawback, but the presence of stromal cells has potential to confound the results if overall survival apparently increases with drug treatment, as was reported by Yang et al., such that IC_{50} or EC_{50} would be impossible to calculate. Thus, it may be more appropriate in these multicellular cultures to calculate GR_{50} or GI_{50} to determine overall drug responses across conditions.

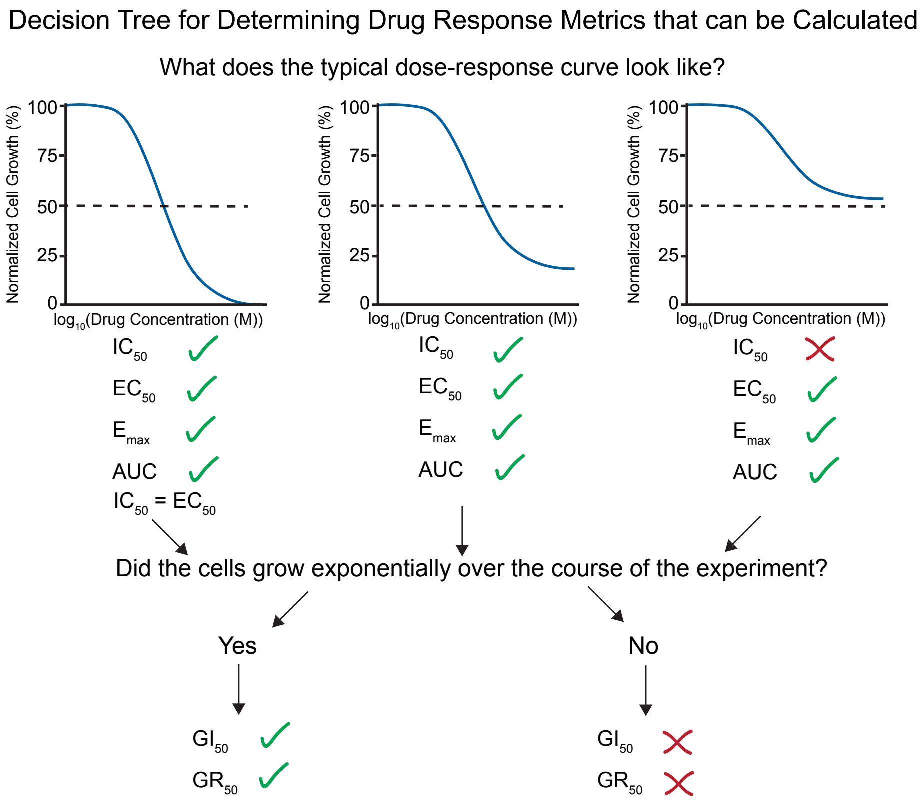

Figure 6.3: Decision tree for determining what drug response metrics can be calculated from drug response data. It is easiest to first look at a typical dose-response curve and calculate data from it. Then, depending on cell growth over the course of the assay, additional metrics may be calculated. In the first step, the criterion is whether the normalized cell growth decreased below 0.5, which is required for IC_{50} calculation. Criterion for second step is whether exponential growth was achieved during the experiment.

6.3 Materials and Methods

6.3.1 Cell Culture

All cell culture supplies were purchased from Thermo Fisher Scientific (Waltham, MA). The SKOV-3 cell line was purchased from American Type Culture Collection (ATCC, Manassas, VA) and the cells were grown in Roswell Park Memorial Institute (RPMI) medium, supplemented with 10% fetal bovine serum (FBS) and 1% penicillin/streptomycin (pen/strep).

6.3.2 Primary Ovarian Cancer Ascites Culture

Ascites samples were received from patients undergoing paracentesis at UMass Medical School (Worcester, MA), transported to UMass Amherst (Amherst, MA), and used immediately upon receipt. Samples were deidentified and were IRB exempt. Either single cells or ovarian ascites carcinoma spheroids (OCAS) were recovered from patient samples and treated as described previously. Single cells were seeded on tissue culture polystyrene (TCPS) and OCAS were encapsulated directly into 3D poly (ethylene glycol)-maleimide (PEG-MAL) hydrogels.

6.3.3 SKOV-3 multicellular tumor spheroids (MCTS)

Square pyramidal microwells (400 µm side-wall dimension) were fabricated as described previously. Briefly, master molds containing square-pyramidal pits were generated by anisotropic etching of 100 crystalline silicon in potassium hydroxide (KOH). Microwells were generated from poly(dimethylsiloxane) (PDMS) using a two-stage replica molding process of the master mold as described previously. Microwells were arranged in a square array with no space between adjacent wells and placed in 12-well plates. For cell seeding, microwell surfaces were UV sterilized for 30 minutes, pretreated with 5% Pluronic F-127 (Sigma-Aldrich, St. Louis, MO) for 30 minutes (2,465 x g, Eppendorf 5810R v3.3 centrifuge with A-4-62 rotor, Eppendorf, Hamburg, Germany), and then washed twice with sterile water. Cells were seeded at 1.00×10^4 cells/cm^2. After 24 hours, multicellular tumor spheroids (MCTS) were collected by shaking the plate gently to dislodge most of them, and gently aspirating medium and MCTS. MCTS solution was spun down at 400 rpm for 5 minutes. Medium was removed, and the MCTS were encapsulated in 3D PEG-MAL hydrogels. MCTS were handled using cut pipet tips to minimize shear stress.

6.3.4 3D PEG-MAL Hydrogel Platform

Patient OCAS were encapsulated into non-degradable 3D PEG-MAL hydrogels as described previously with minor modifications. The SKOV-3 MCTS were encapsulated into degradable 3D PEG-MAL hydrogels. The 3D RGD non-degradable hydrogel was prepared with a 20 kDa 4-arm PEG-MAL (Jenkem Technology, Plano, TX) at 10 wt % solution with 2 mM of cell adhesion peptide RGD (Genscript, Piscataway, NJ) and cross-linked at a 1:1 molar combination of the 1 kDa linear PEG-dithiol (Sigma-Aldrich). The 3D RGD degradable hydrogels were prepared in the same manner as the non-degradable hydrogel, plus cell-degradable cross-linker, Pan-matrix metalloproteinase (Pan-MMP, GCRDGPQGIWGQDRCG, Genscript). The final crosslinking concentration was 90 mM consisting of PDT (88 molar %) + Pan-MMP (12 molar %)**.** The hydrogels were synthesized by pipetting 1 µL of PDT or PDT/Pan-MMP solution onto the well surface, followed by pipetting 9 µL of the cell- containing PEG–MAL solution. MCTS and OCAS were transferred with cut pipet tips to minimize shear stress.

6.3.5 Drug Screening Assay

SKOV-3 cells were seeded in RPMI with 5% FBS and 1% pen/strep at 6,250 cell/cm^2 on TCPS. Primary ovarian single cancer cells were seeded in RPMI with 10% FBS at the same density, also on TCPS. OCAS were collected and encapsulated in 3D RGD hydrogel upon receipt. Drugs were added after 24 hours in the same type of medium that the cells were seeded in and the cells were incubated with drugs for 48 hours. Paclitaxel (MP Biomedicals, Santa Ana, CA), Cisplatin (Tocris Bioscience, United Kingdom), and Mafosfamide (Niomech, Germany), were added in 10-fold serial dilutions at concentrations of 1x10^{-5} to 1x10^2 µM, and dimethyl sulfoxide (DMSO, Sigma-Aldrich) was used as a vehicle control for all drugs. Cell viability was assayed at 24 hours post-cell seeding in a control plate and after 48 hours of drug incubation using the CellTiter-Glo luminescent viability assay (Promega, Madison, WI). Luminescence values were measured in a BioTek Synergy H1 plate reader (Winooski, VT).

6.3.6 GR$_{50}$ Metrics and Calculations

The data in figure 5.2 was analyzed using the online GR calculator, http://www.grcalculator.org/grcalculator/. We used the initial cell counts calculation method and Case A (multiple cell counts per row) for the input file format. “Replicate” was removed from the grouping variables list before the data was analyzed. In Table C.2, the material that the cells were tested in or on is listed under the “perturbation” heading. The IC$_{50}$ value for figure 5.2b was obtained using GraphPad prism v7.0c.

6.3.7 Inhibition Metrics Calculations from Published Data

Data from drug response curves were extracted with WebPlotDigitizer v4.1 from the published work cited in Tables C1-3. Re-plotted curves were used to calculate inhibition parameters IC$_{50}$, E$_{max}$, EC$_{50}$ and AUC with GraphPad prism v7.0d. Viability values were constrained to 0.00001 as a minimum for log calculations. Drug concentrations were expressed as log$_{10}$ of concentrations in μM. Viability data was then normalized, with the control set to 100%, and minimum set to 0%. Nonlinear regression with variable slope was used, with least squares fitting method. The IC_{50} was calculated from Prism dose-response inhibition analysis with variable slope of four parameters and following equation shown in figure 5.1. AUC was obtained from XY analysis in Prism. Additional parameters E_{max} and EC_{50} values were calculated following their respective equations shown in figure 5.1.

6.3.8 Curve Response Class (CRC) Classifier Analysis

Using guidelines described by Inglese et al.[229] we classified the drug response curves from our own data and the data that we analyzed from the literature. In some cases, the r^2 values that we observed for the non-linear fits to the equations were not greater than 0.9, which was criteria described by previously. However, the efficacy in these cases was greater than 80% and we observed dose response curves with two asymptotes. Since we observed dose responses (compounds were not inactive), we characterized the data presented here to the closest CRC that we could.

6.4 Conclusions

Drug screening in biomaterials could be particularly useful in making better predictions in the early stages of preclinical drug development. However, it can be challenging to compare drug responses across different platforms and conditions in the current literature. This is, in part, a result of inconsistent applications of drug response metrics, and differences in cell growth rates for cells cultured in different biomaterials. For this reason, we suggest the use of GI_{50} and GR_{50} to account for initial populations (y_0), and number of cell divisions during an assay, since cell growth highly impacts dose response. However, in instances when steady cell growth is not achieved, multiple drug response metrics could be applied (e.g. IC_{50}, EC_{50}, E_{max}, and AUC) to account for possible experimental variation. To aid researchers in determining what drug response metrics can be calculated from their data, we suggest the use of a decision tree (figure 6.3) based on the traditional drug response curve and cell growth rate data that are obtained for a drug response experiment.

First, visual inspection of a drug response curve will determine if an IC_{50} can be calculated if less than 50% of the control cell population is remaining at the highest drug concentration that was tested. If 100% cell death has been achieved, then the EC_{50} and IC_{50} will be equal. Furthermore, if the cells grew exponentially over the course of the drug screening assay, then the GI_{50} and GR_{50} metrics can be applied. We also encourage other research groups to incorporate raw data and drug response curves in their reports that will allow other researchers to gather additional data for their analyses. In the long term, this will lead to more accurate predictions early in the drug development pipeline of how likely a drug will be successful in a clinical setting.

CHAPTER 7

CONCLUSIONS AND FUTURE DIRECTIONS

7.1 Overall Conclusions

This dissertation presented the first hydrogel to culture human brain astrocytes that remained quiescent *in vitro* while demonstrating tight control on activation. Because of a wide variation in the brain modulus reported in the current literature, localized brain mechanics were explored via needle-induced cavitation rheology and volume-controlled cavity expansion in the brain for the first time. These techniques can be adopted for further exploration of the local mechanical properties of other materials. In order to expand on the brain specific ECM composition, proteomics was performed in four human cortex samples for healthy donors. This information was compiled in a throughout list of integrin-binding and MMP-degradable proteins. It was demonstrated that combining the brain properties found via mechanics and proteomics into a synthetic hydrogel as biochemical components with matched mechanical properties resulted in a hydrogel that can control astrocyte activation for the first time *in vitro*. The degree of activation was further explored based on hydrogel composition or induced via cytokine dosing. Finally, to aid with the implementation of biomaterials as *in vitro* platforms to predict *in vivo* physiology, the correlation between current 2D, 3D and *in vivo* studies of glioblastoma motility was explored, and how an effect size can help standardize comparison across labs and culture dimensions. An additional study highlighted the importance of adopting growth rate in drug metric responses and how these can be implemented in current biomaterial platforms. Overall, this work can help integrate biomaterials as models to predict *in vivo* physiology. This case study with a brain hydrogel system can be used as a platform to understand mechanistic studies of astrocytes activation.

7.2 Limitations and considerations for brain models

Tissues are very complex structures that possess a 3-dimensional geometry[227], an array of biochemical components[156] and in certain instances adopt different mechanical properties dependent on the state of disease[41]. Biomaterials have the capability to replicate these properties *in vitro*[254]. As the field moves towards the integration of more complex designs there are other parameters to consider[87]. However, one of the current challenges is the design of materials that remain simple and cost-effective while mimicking the complexity of the microenvironment of interest.

7.2.1 Viscoelastic and strain-stiffening deformation in synthetic hydrogels

Characterization of brain during deformation has shed light on its strain rate dependent deformation[255], and viscoelastic nature[100]. Others, including this work, have shown the strain stiffening nature of brain[100]. Similarly, others have also shown the anisotropy present in white matter which is not existent in gray matter[99]. Here we characterized brain properties and tuned the modulus of a synthetic hydrogel to successfully match the measured Young's modulus of brain (fig. 4.1). However, one of the limitations of fully synthetic systems is that their response to deformation is different from certain strain hardening tissues[33]. Other groups have aimed to replicate viscoelastic features of tissues using combinations of proteins[256] and synthetic polymers[33, 257, 258]. An interesting approach to modulate the chemical properties of hydrogels with MMP degradable sequences, recently introduced in work by Badeau et al.,[259], has used logic-gated biomaterials that undergo precise MMP degradation that subsequently trigger drug delivery responses. Given that degradable crosslinkers in the hydrogel presented in this work can be degraded by MMPs, it would be of interest to adopt a similar approach and explore additional groups at each end of the GCRD motif groups that upon degradation would allow for re-crosslinking of exposed groups. Further crosslinking by the new exposed groups could result in changes in the network and mechanical properties of the hydrogel. This would be of interest for future work addressing dynamic transitions into diseases where tissues increase in modulus over time due to the deposition of proteins by other cells while still retaining the MMP and integrin-binding functionality introduced in the brain hydrogel design (section 4.1)[31].

7.2.2 Integrating tissue vasculature in hydrogel to increase complexity

The brain consists of many compartments such as the frontal, parietal, temporal, occipital lobes and central gray matter structures[1]. Anatomically this organ can be further stratified into the cerebral cortex representing the outermost gray matter overlying white matter[1]. Various studies have characterized the brain extracellular space where the blood brain barrier (BBB), interstitial matrix and perineuronal nets compose the microarchitecture[5, 7, 8, 23]. Similarly, the vasculature of the brain plays an integral part in the flow of oxygen throughout, keeping toxins and serum at bay and promoting cell extravasation and invasion during disease and has been shown to be altered during neurodegenerative diseases. Yet, major challenges and limitations in replicating the brain ECM compartments and vasculature has been attributed to increase in cost, and major complexity of the system[66, 87].

While other work as focused on recreating the unique physiology of the BBB *in vitro* it has been excluded from this system[66, 87]. One of the reasons being current challenges in the design of microchannels in the elastic homogeneous hydrogel not remaining intact throughout. However, future optimization of the system should aim to incorporate a vasculature component. Additionally, because the brain is stratified into many compartments that make it a unique organ, characterization of proteins in other locations like the cerebellum, or the spinal fluid could be conducted with proteomics. Although, aiming to recreate a full brain organ *in vitro* is the ultimate challenge, others could aim to recreate key features of other brain regions as introduced here, and incorporate hydrogels side-by-side while changing the formulation to represent other compartments within the brain.

7.2.3 Expansion of other brain cell types in the brain hydrogel

The cerebral cortex incorporates neurons, astrocytes, microglia, oligodendrocytes and other vasculature related cell types making it a very complex organ with a large and diverse cell population[2, 260]. Aims to characterize the distinct population of cells in the brain have been mostly focused on neurons, and until recently have emerged on glial cells[2, 54]. The first modern description of reactive astrocyte occurred in 1970s after the discovery of the glial fibrillary acidic protein (GFAP)[261] and recent work, within the last 2-3 years, has aimed to expand on markers that are specific to astrocytes since work has shed light on the many different shades of astrocytes, microglia and neurons that compose the brain network[2, 54, 262]. Yet this work was focused on astrocyte culture due to their key role in inflammation and the imminent need for better models of their culture[263]. Although this work demonstrates tight control of astrocyte activation in the formulation of the brain hydrogel (section 4.1), other cell types in the brain should be explored by future work. Given that astrocytes were able to remain viable after 2 weeks in culture, it is expected other brain cell types will also be viable in the brain hydrogel.

7.2.4 Increasing knowledge of peptide sequences to be incorporated in the hydrogel

There is a wide array of proteins present in brain tissue[156]. Here we characterized the proteins in human brain and filtered them based on literature knowledge of sequences that are known to be interactive with cells. This can limit the scope of peptides that are incorporated into the hydrogel and hence the formulation. Because other work has shown other receptors like CD44 can have effects on astrocyte intracellular mechanisms[264], and similarly, other enzymes outside of matrix metalloproteinases can remodel the microenvironment, like for example cathepsins[265], additional parameters can be incorporated into the hydrogel if these are to be studied. Yet, a major challenge in the field is designing sufficiently complex yet simple *in vitro* models [266]. As additional moieties and biofunctionalities are incorporated into the hydrogel this can increase the cost of the system and make it more labor intensive which is a challenge to take into account in future tissue specific hydrogel designs.

7.3 Future directions

7.3.1 Brain hydrogel to study cell-ECM traumatic brain injury astrocyte activation

Reactive astrocytes play a key role in brain trauma and inflammation[46]. Radical changes in the central nervous system (CNS) have been shown to transform naïve astrocytes into reactive astrocytes that induce damage and can promote disease[45]. For example, work by Hara et al., [50] recently illustrated that interaction of astrocytes with collagen type I induces astrocyte scar formation via the integrin-N-cadherin pathway. Similarly, others have shown activated astrocytes in traumatic brain injury (TBI), induced by impact or cavitation[267], emerge soon after injury and accumulate at the site of injury as identified by staining with the intermediate filament marker

GFAP[157]. However, how impact or cavitation-induced injury elicit mechanistic responses of astrocytes or other CNS cells remains unexplored.

I propose the brain hydrogel presented in this work could be used as a platform to understand how cavitation-induced injury elicits astrocyte activation. The needle-induced cavitation rheology technique (section 2.1) used in this work for mechanical characterization of brain tissue allows for controlled local deformation *in situ*. Given that traumatic brain injury is expected to occur at very high strains[39], I propose this technique could be used to induce local injury in the brain hydrogel. Merging a precise controlled mechanical technique with a hydrogel that provides tight control of astrocyte activation could help bridge the gap of what intracellular signaling pathways are activated upon traumatic brain injury *in vitro.*

7.3.2 Brain hydrogel to understand astrocyte reactivity in cell-cell interactions during inflammation and brain trauma *in vitro*

Both microglia and astrocytes become reactive in concert during brain trauma and both play a role in neuroinflammation.[45, 63] Because of this, it has been a challenge to distinguish the role of both these cells *in vivo*[45]. Additionally, given that many key proteins are present in both cells, *in vivo* systems limit understanding cell-cell interactions and how external and internal cues elicit activation. For *in vitro* models, outside the challenge of no current model being able to replicate astrocyte reactivity, which has been addressed by this work, one major limitation in the field is that *in vitro* models that work for astrocytes usually do not work for microglia[45]. Hence, it has been very challenging to study microglia *in vitro* and how they might interact with astrocytes in a physiological and reactive setting. I propose the brain hydrogel presented in this work could be the first step to understand how reactive astrocytes influence microglia or if it is microglia that induces activation.

Similarly, recent work by Liddelow et al.,[55] shows that microglia induce reactive astrocytes produce a neurotoxin that affects neurons and oligodendrocytes that remains to be identified. Proteomics has proven to be a readily helpful tool in identifying proteins and molecules present in the extracellular compartment of tissue and *in vitro*[10]. I propose the brain hydrogel could be used as a platform to identify proteins and cytokines produced by reactive astrocytes. This would help shed light to what astrocyte-mediated signals induce injury to other CNS cells like neurons and oligodendrocytes.

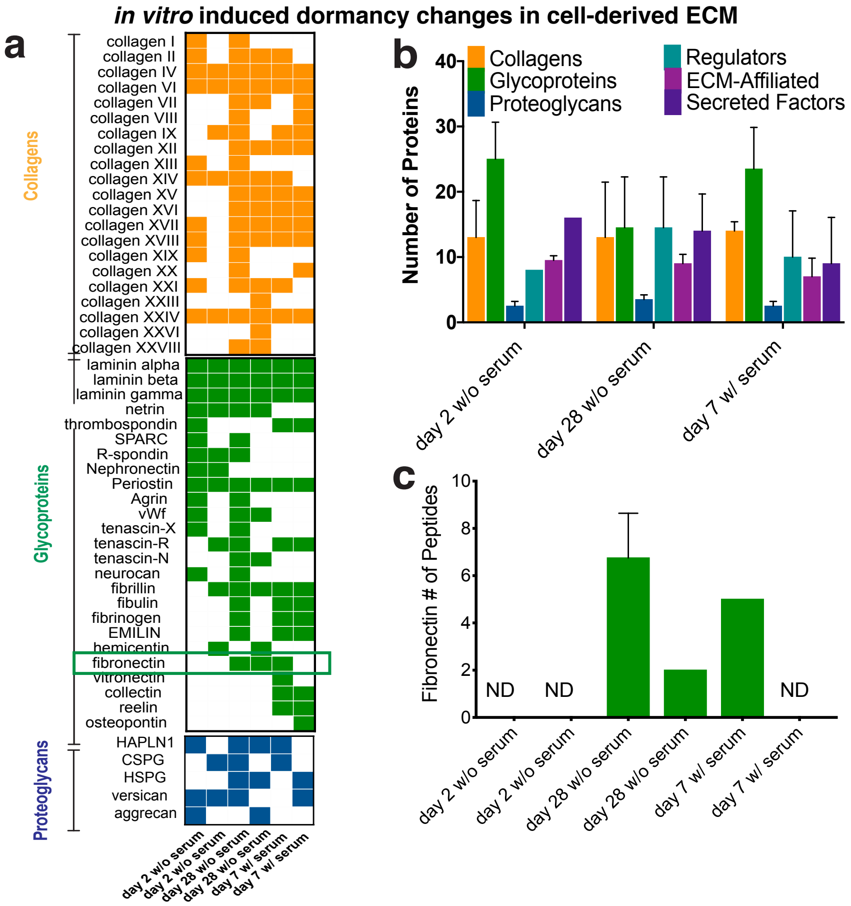

***in vitro* induced dormancy changes in cell-derived ECM**

Figure 7.1: Proteomics to identify ECM changes in disease. a) ECM proteins identified via proteomics workflow of breast cancer cells recovered after 2 days or 28 days of culture in serum free medium or 7 days of culture with 10% of serum containing media. Samples analyzed were prepared by Dr. Alyssa Schwartz and Dr. Christopher Hall. Heat map depicts ECM proteins present in all cell culture recovered conditions as collagens (orange), glycoproteins (green) and proteoglycans (blue). b) Distribution of core ECM proteins (collagens, glycoproteins and proteoglycans) and Matrisome associated proteins (Regulators (turquoise), ECM-affiliated (purple) and Secreted factors (dark purple) for samples of cell cultured recovered after 2 days, 28 days serum-free medium and 7 days with serum containing medium. Data shown is for two biological replicates per condition as mean and s.e.m. for number of proteins identified. c) Presence of cell-derived fibronectin for each of the cell culture conditions. The protein was only detected after 28 days of culture in serum free medium and one biological replicate of serum containing culture.

7.3.3 Implementation of Proteomics for characterization of ECM changes in development and in dormancy

Similarly, recent work has highlighted the ECM role in dormancy [30, 268]. Most of the relapses seen in metastatic cancers like breast and lung are due to underlying dormant cells that remain in the system even after the primary tumor has been eradicated[269]. Dormancy is hypothesized to be a result of early disseminated tumor cells (DTCs) to other secondary sites, which can undergo long-term latency and survival and finally result in overt metastasis[268, 270]. Recent work by Carlson et al.,[271] identified that DTCs are protected by the perivascular niche of the bone marrow microenvironment. Similarly, previous work in our lab[78] identified that cell secreted fibronectin, an ECM protein secreted by cells, mediates cell survival in an integrin mediated signaling. Proteomic tools that allow for the throughout characterization of the ECM components are indispensable in identifying the composition of these perivascular niches that allow for microenvironment mediated resistance. Implementation of proteomics as a workflow to characterize different time points during dormancy seems like a good avenue to test ECM driven hypotheses. Figure 7.1 shows preliminary data I gathered in collaboration with Dr. Alyssa Schwartz and Dr. Lauren Barney of the presence of fibronectin after long-term culture of serum deprived cells *in vitro* with the notion that they assemble fibronectin in order to survive. Proteomics identified the signature profile of ECM proteins and how these changes between serum dosed and serum deprived cultures. Assessing for the presence of fibronectin confirmed this protein was present after 28 days of serum deprived culture while not initially. This highlights how proteomics can be a useful tool to identify ECM changes during disease.

7.3.4 Expanding on tissue specific hydrogel design

Proteomic work by others has also illustrated the ECM diversity in tissues[10, 154]. Comparisons between lung and colon tissues ECM highlighted there are a subset of proteins unique to tissues and could give rise to the macroscopic differences that are observed in different organs.

We have extended our tissue specific hydrogel design to other tissues with information gathered by proteomics and designed hydrogels representing the thymus and omentum (fig. 7.2). We foresee the design of additional tissue specific hydrogels that can help pinpoint how tissues different set of ECM proteins regulate cell behavior in development and disease *in vitro*. Future work can expand of validation of these systems with the incorporation of tissue-specific cells.

7.3.5 Industrial applications of the brain hydrogel to identify neurodegenerative diseases and brain cancer targets

The fast, controllable and reproducible formulation of this brain hydrogel platform makes it an attractive system for high throughput applications (fig. 7.3). Currently, one of the major challenges in finding suitable targets for neurodegenerative diseases and other brain cancers is

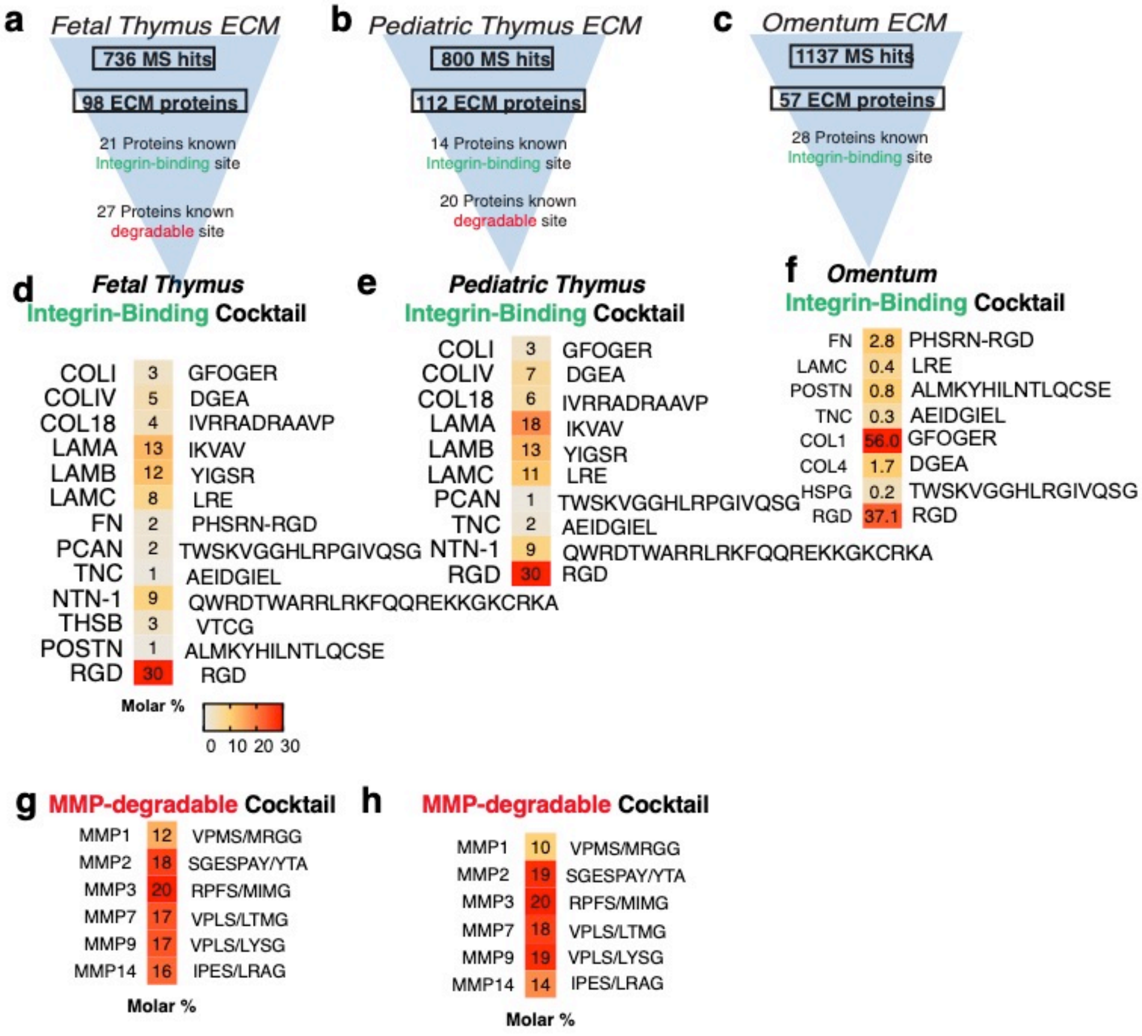

Figure 7.2: Expansion of tissue-specific ECM hydrogel designs. Workflow of the identification of integrin-binding proteins and MMP-degradable proteins from mass spectrometry data screened for ECM proteins for a) fetal thymus b) pediatric thymus and c) omentum tissue. Omentum mass spec data was gathered from the Naba et al., “Characterization of the Extracellular Matrix of Normal and Diseased Tissues Using Proteomics”. Heat map depicting molar composition of integrin-binding peptides for d) fetal- e) pediatric-thymus and f) omentum-specific hydrogels. Heatmap of MMP-degradable peptides for g) fetal and h) pediatric thymus hydrogels.

that there are no good models of the brain *in vitro*[66, 87, 272] and *in vivo* models show species differences[44, 62, 64]. For example, work has shed light on how some of the targets identified in the murine brain do not play a role in human brain disease progression and vice-versa[62, 64]. This can be one of the reasons why pre-clinical work has struggled at clinical stages.

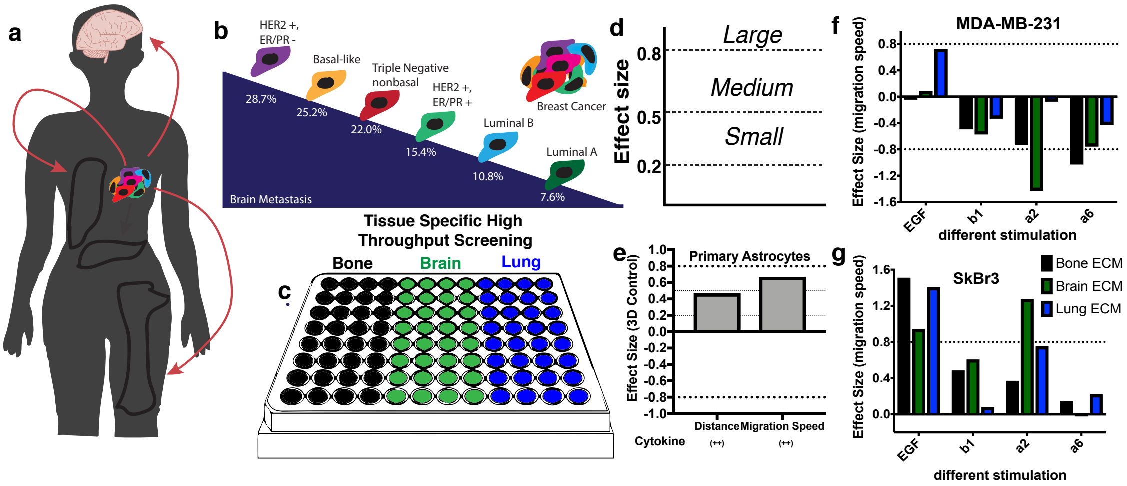

Figure 7.3: High throughput implementation of tissue-specific hydrogels. a) Breast cancer metastasizes to the brain, bone, lung and liver. b) Within the breast cancer sub-types each exhibits different degree of incidence of brain metastasis. c) Implementation of tissue specific high throughput screening could help understand preference to a specific ECM environment and test druggable targets. d) The use of an effect size could help compare results across different microenvironments based on a small (0.2<E<0.5), medium (0.5<E<0.8) or large (0.8>E) effect size response. e) example of effect size responses of astrocytes in the brain hydrogel after cytokine dosing and their effect on total distance migrated and migration speed as compared to control 3D brain hydrogel. f) example of effect size applied to data gathered from the Barney et al., “A cell-ECM screening method to predict breast cancer metastasis” for the breast cancer cell line MDA-MB-231 and g) SkBr3 after cell culture in 2D surfaces functionalized with bone-, brain- and lung-inspired ECM proteins and their effect size on migration speed after dosed with different stimulation (EGF, integrin beta1, alpha2 and alpha 6 inhibitors).

Recent work has shown that extracellular targets in the brain, as well as blocking certain cytokines of protein expression can help suppress disease[25, 51, 55, 273]. I propose this hydrogel model with unique human brain features could help bridge the gap between pre-clinical and clinical work in industry to find targets that are druggable. For example, astrocyte reactivity is dependent on the type of injury where to date there have been two phenotypes identified A1 and A2[54, 55]. A1 neuroinflammatory astrocytes upregulate many genes destructive to synapses and are suggested to be harmful[54-56]. Alternatively, ischemia-induced A2 astrocytes upregulate many neurotrophic factors that promote survival, growth of neurons, and have been suggested to be helpful.[57-59, 274] However, there are still questions whether there are more states of activation in human astrocytes similarly to how macrophages (another immune cell type) can be activated in different states. I propose the brain hydrogel as a platform to explore how inflammation triggered responses affect astrocytes mechanistically and screen their phenotype based on recent work by Liddelow et al., that showed the C3 marker could help identify between different states[55]. Additionally, I propose this hydrogel would allow for further understanding of the key intracellular signaling pathways that allow for polarization into an A1 or A2 phenotype.

Work by others has suggested that A1 astrocytes become reactive via the nuclear factor-κB (NF-κB) pathway since many inflammatory agents, such as cytokines, bacteria or viruses can activate it.[275, 276] Others have shown activation of this pathway in astrocytes during Alzheimer's disease and Hunting-ton's disease which provide evidence that NF-κB-activated-astrocytes might be harmful[56, 277, 278]. Similarly, others have suggested that A2 astrocytes become reactive via JAK-STAT3 pathway. This pathway in astrocytes is important during early brain development, since it helps to control astrogliogenesis and maturation[279, 280]. Studies have shown JAK-STAT3 in scar-forming astrocyte activation after injury[49, 60, 281]. Drugs that control Stat3 and NF-κB could have potential in modulating the activation state of reactive astrocytes into helpful or damaging cells to the CNS. I propose these mechanistic activations and potential drug targets can now be probed *in vitro.*

7.4 Materials and Methods

7.4.1 Proteomics sample preparation

Sample were ECM-enriched. The ECM-rich pellet was solubilized and reduced in 8M Urea, 100 mM of ammonium bicarbonate, and 10 mM dithiothreitol (DTT) (Fisher Scientific) for 30 minutes at pH 8 and 37C. Samples were alkylated with 25 mM iodoacetamide (Sigma) in the dark at room temperature for 30 minutes before the solution was quenched with 5mM DTT. Prior to cleavage the solution was diluted to 2M Urea with 100 mM ammonium bicarbonate at pH 8. Proteins were cleaved via trypsin (Thermo Scientific) and lys-C endoproteinase (Promega), at a ratio 1: 50 enzyme to protein overnight (12-16 hours) at 37C. Samples were cleaned and concentrated using a C18 column (Thermo Scientific). A reverse phase LC gradient was used to separate peptides prior to mass analysis. Mass Fusion Tribrid (Thermo Scientific). Peptides were aligned against the Matrisome using the Thermo Proteome Discoverer 1.41.14[10]. Parameters used trypsin as a protease, with 4 missed cleavage per peptide, a precursor mass tolerance of 10 ppm, and fragment tolerance of 0.6 Da.

7.4.2 Identifying integrin-binding and MMP-degradable proteins in Pediatric and Fetal Thymus

Manual data mining was used to identify 14 integrin-binding and 20 MMP-degradable proteins in pediatric thymus. For the fetal thymus 21 proteins were integrin-binding and 27 were MMP-degradable. This list was used to identify which proteins would be represented by integrin-binding or degradable peptide sequences. The proteins were relatively quantified with the peptide-spectrum match (PSM) from the mass spectrometry data and normalized to the molecular weight of the protein. The ratio was annotated for each protein and a relative percent abundance was obtained from the ratio of each protein over a sum of the total ratio identified per sample. This value was averaged across all the patient scores and was used to determine the percentage of each integrin-binding peptide and MMP-degradable crosslinker to use for proteins in the thymus ECM cocktail represented in supplementary tables 1 and 2, respectively.

7.4.3 Thymus mechanical characterization

The effective Young's modulus was measured using micro-indentation testing on a bulk thymus sample. A custom-built instrument was used as previously described[282]. Briefly, a flat cylindrical punch probe was indented into the samples at a fixed displacement rate of 10 um/s, for a maximum load of 1mN. The first 10% of the linear region of the force-indentation curves were analyzed using a Hertzian model modified by Shull et al. to account for dimensional confinement characterized by the ratio between the contact radius (a) and the sample height (h) to be between $0.5<a/h<2$ [283].

APPENDIX A

EXTRACELLULAR MATRIX OF THE HUMAN BRAIN CORTEX INTEGRIN-BINDING AND MMP-DEGRADABLE COMPONENTS

A.1: Proteomics of human brain cortex.

Human	**Protein**	**PSMs**	**Category**	**Division**
Donor 1	tenascin R precursor	25	ECM glycoprotein	Core Matrisome
	laminin subunit beta 2	42	ECM glycoprotein	Core Matrisome
	laminin subunit gamma 1	40	ECM glycoprotein	Core Matrisome
	fibrinogen beta chain isoform 1	10	ECM glycoprotein	Core Matrisome
	fibrinogen gamma chain	5	ECM glycoprotein	Core Matrisome
	oligodendrocyte myelin glycoprotein	8	ECM glycoprotein	Core Matrisome
	collagen alpha 1 (I) chain	48	Collagens	Core Matrisome
	collagen alpha 2 (IV) chain	29	Collagens	Core Matrisome
	collagen alpha 6 (VI) chain	62	Collagens	Core Matrisome
	collagen alpha 2(I)	18	Collagens	Core Matrisome
	versican	46	Proteoglycan	Core Matrisome
	neurocan core	29	Proteoglycan	Core Matrisome
	basement membrane specific heparan sulfate proteoglycan core	61	Proteoglycan	Core Matrisome
	neural cell adhesion molecule 1 isoform 2	32	ECM-affiliated Proteins	Matrisome-associated
	neurofascin isoform 4 precursor	37	ECM-affiliated Proteins	Matrisome-associated
	neural cell adhesion molecule L1 isoform 3	16	ECM-affiliated Proteins	Matrisome-associated
	annexin A2 isoform 1	15	ECM-affiliated Proteins	Matrisome-associated
	cathepsin D	11	ECM Regulators	Matrisome-associated
	Contactin-1 isoform 2 precursor	52	Other	Other
	contactin associated protein 1	24	Other	Other
	voltage dependent calcium channel subunit alpha 2 delta 1	27	Other	Other
	tetraspanin 7	3	Other	Other

	tubulointerstitial nephritis antigen like	10	Other	Other
Donor 2	**Protein**	**PSMs**	**Category**	**Division**
	laminin subunit beta 2	155	ECM glycoprotein	Core Matrisome
	laminin subunit gamma 1	164	ECM glycoprotein	Core Matrisome
	laminin subunit alpha 5 precursor	115	ECM glycoprotein	Core Matrisome
	fibrinogen beta chain isoform 1 preproprotein	38	ECM glycoprotein	Core Matrisome
	fibrinogen gamma chain isoform gamma A	19	ECM glycoprotein	Core Matrisome
	EMILIN 1	60	ECM glycoprotein	Core Matrisome
	tenascin R	48	ECM glycoprotein	Core Matrisome
	nidogen 1	49	ECM glycoprotein	Core Matrisome
	fibrinogen alpha chain isoform alpha E preproprotein	49	ECM glycoprotein	Core Matrisome
	fibrillin 1	82	ECM glycoprotein	Core Matrisome
	nidogen 2	60	ECM glycoprotein	Core Matrisome
	latent transforming growth factor beta binding protein 4	65	ECM glycoprotein	Core Matrisome
	laminin subunit beta 1	131	ECM glycoprotein	Core Matrisome
	fibronectin isoform 4 preproprotein	89	ECM glycoprotein	Core Matrisome
	elastin isoform d precursor	8	ECM glycoprotein	Core Matrisome
	thrombospondin type 1 domain containing protein 1 isoform 2	81	ECM glycoprotein	Core Matrisome
	sushi, nidogen and EGF like domain containing protein 1 precursor	86	ECM glycoprotein	Core Matrisome
	collagen alpha 1(I) chain	140	Collagens	Core Matrisome
	collagen alpha 2 (I) chain	64	Collagens	Core Matrisome
	collagen alpha 3 (VI) chain	199	Collagens	Core Matrisome
	collagen alpha 2 (IV) chain	110	Collagens	Core Matrisome
	collagen alpha 2 (VI) chain isoform 2C2	104	Collagens	Core Matrisome
	collagen alpha 1 (VI) chain precursor	48	Collagens	Core Matrisome
	collagen alpha 1 (XVIII) chain isoform 2	102	Collagens	Core Matrisome
	basement membrane specific heparan sulfate proteoglycan core protein	128	Proteoglycans	Core Matrisome
	biglycan preproprotein	27	Proteoglycans	Core Matrisome
	prolargin precursor	36	Proteoglycans	Core Matrisome

	annexin A2 isoform 2	69	ECM-affiliated Proteins	Matrisome-Associated
	neural cell adhesion molecule 1 isoform 2	49	ECM-affiliated Proteins	Matrisome-Associated
	annexin A1	44	ECM-affiliated Proteins	Matrisome-Associated
	neural cell adhesion molecule L1 isoform 3 precursor	57	ECM-affiliated Proteins	Matrisome-Associated
	A disintegrin and metalloproteinase with thrombospondin motifs 13	73	ECM Regulators	Matrisome-Associated
	protein glutamine gamma glutamyltransferase 2	28	ECM Regulators	Matrisome-Associated
	cathepsin D preproprotein	28	ECM Regulators	Matrisome-Associated
	tubulointerstitial nephritis antigen like	39	Other	Other
	phytanoyl CoA hydroxylase interacting protein	34	Other	Other
	contactin 1 isoform 1	135	Other	Other
	titin isoform N2-A	2644	Other	Other
	NSFL1 cofactor p47 isoform a	55	Other	Other
	CUB and sushi domain containing protein 2	103	Other	Other
	X ray repair cross complementing protein 6	50	Other	Other
	contactin associated protein 1	8	Other	Other
	integrin alpha D precursor	60	Other	Other
	SLIT and NTRK like protein 5 precursor	33	Other	Other
	phytanoyl CoA hydroxylase interacting protein like isoform 1	64	Other	Other
	complement component C1q receptor precursor	22	Other	Other
	myosin binding protein C cardiac type	101	Other	Other
	neurexin 1 beta isoform alpha 2 precursor	81	Other	Other
Donor 3	**Protein**	**PSMs**	**Category**	**Division**
	tenascin R	22	ECM glycoproteins	Core Matrisome
	oligodendrocyte myelin glycoprotein precursor	9	ECM glycoproteins	Core Matrisome
	collagen alpha 1(I) chain	62	Collagens	Core Matrisome
	collagen alpha 3 (VI) chain isoform 1	40	Collagens	Core Matrisome
	versican core protein isoform 1	55	Proteoglycans	Core Matrisome
	neurofascin isoform 4	28	ECM-affiliated Proteins	Matrisome-Associated
	neural cell adhesion molecule 1 isoform 2	29	ECM-affiliated Proteins	Matrisome-Associated
	fibroblast growth factor 11	28	Secreted Factors	Matrisome-Associated

	calcium activated chloride channel regulator 1	14	Other	Other
	kinesin like protein KIF21B	36	Other	Other
	tubulointerstitial nephritis antigen like	12	Other	Other
	SLIT and NTRK like protein 2	52	Other	Other
	mucin-2	25	Other	Other
	contactin associated protein 1	21	Other	Other
	contactin 1 isoform 2	44	Other	Other
Donor 4	**Protein**	**PSMs**	**Category**	**Division**
	laminin subunit beta 2	166	ECM glycoproteins	Core Matrisome
	laminin subunit alpha 5	150	ECM glycoproteins	Core Matrisome
	laminin subunit gamma 1	149	ECM glycoproteins	Core Matrisome
	tenascin R	93	ECM glycoproteins	Core Matrisome
	nidogen 1	73	ECM glycoproteins	Core Matrisome
	EMILIN 1	51	ECM glycoproteins	Core Matrisome
	elastin isoform d	8	ECM glycoproteins	Core Matrisome
	fibrillin 1	95	ECM glycoproteins	Core Matrisome
	nidogen 2	46	ECM glycoproteins	Core Matrisome
	fibronectin isoform 4 preproprotein	73	ECM glycoproteins	Core Matrisome
	laminin subunit alpha 4 isoform 2 precursor	147	ECM glycoproteins	Core Matrisome
	fibrinogen gamma chain isoform gamma A	16	ECM glycoproteins	Core Matrisome
	oligodendrocyte myelin glycoprotein precursor	39	ECM glycoproteins	Core Matrisome
	laminin subunit alpha 3 isoform 3	189	ECM glycoproteins	Core Matrisome
	tenascin X isoform 1	190	ECM glycoproteins	Core Matrisome
	laminin subunit alpha 2 isoform b	265	ECM glycoproteins	Core Matrisome
	von Willebrand factor A domain containing protein 1 isoform 1	18	ECM glycoproteins	Core Matrisome
	fibrinogen beta chain isoform 1 preproprotein	37	ECM glycoproteins	Core Matrisome
	agrin precursor	71	ECM glycoproteins	Core Matrisome
	fibrinogen alpha chain isoform alpha E preproprotein	58	ECM glycoproteins	Core Matrisome
	vitronectin precursor	21	ECM glycoproteins	Core Matrisome

von Willebrand factor preproprotein	134	ECM glycoproteins	Core Matrisome
laminin subunit beta 3	136	ECM glycoproteins	Core Matrisome
thrombospondin 1-precursor	43	ECM glycoproteins	Core Matrisome
collagen alpha 3 (VI) chain isoform 1	503	Collagens	Core Matrisome
collagen alpha 2 (I) chain	167	Collagens	Core Matrisome
colalgen alpha 2 (VI) chain isoform 2C2	183	Collagens	Core Matrisome
collagen alpha 1 (I) chain	194	Collagens	Core Matrisome
collagen alpha 1 (VI) chain	132	Collagens	Core Matrisome
collagen alpha 1 (XIV) chain	140	Collagens	Core Matrisome
collagen alpha 1 (XII) chain long isoform	266	Collagens	Core Matrisome
collagen alpha 2 (IV) chain preproprotein	171	Collagens	Core Matrisome
collagen alpha 1 (XVIII) chain isoform 3	66	Collagens	Core Matrisome
collagen alpha 1 (XXI) chain precursor	89	Collagens	Core Matrisome
collagen alpha 1 (XV) chain precursor	32	Collagens	Core Matrisome
collagen alpha 1(III) chain preproprotein	116	Collagens	Core Matrisome
collagen alpha 5 (IV) chain isoform 1	92	Collagens	Core Matrisome
basement membrane specific heparan sulfate proteoglycan core	218	Proteoglycans	Core Matrisome
biglycan preproprotein	87	Proteoglycans	Core Matrisome
versican core protein isoform 1	160	Proteoglycans	Core Matrisome
fibromodulin precursor	31	Proteoglycans	Core Matrisome
mimecan preproprotein	38	Proteoglycans	Core Matrisome
prolargin precursor	53	Proteoglycans	Core Matrisome
lumican precursor	14	Proteoglycans	Core Matrisome
neurocan core protein precursor	74	Proteoglycans	Core Matrisome
decorin isoform a preproprotein	12	Proteoglycans	Core Matrisome
brevican core protein isoform 1	40	Proteoglycans	Core Matrisome
annexin A6 isoform 1	86	ECM-affiliated Proteins	Matrisome-Associated
neural cell adhesion molecule 1 isoform 2	89	ECM-affiliated Proteins	Matrisome-Associated
galectin 1	21	ECM-affiliated Proteins	Matrisome-Associated
annexin A2 isoform 1	64	ECM-affiliated Proteins	Matrisome-Associated
neurofascin isoform 1	60	ECM-affiliated Proteins	Matrisome-Associated

neural cell adhesion molecule L1 isoform 3 precursor	34	ECM-affiliated Proteins	Matrisome-Associated
alpha tectorin precursor	87	ECM-affiliated Proteins	Matrisome-Associated
neuronal cell adhesion molecule isoform A precursor	50	ECM-affiliated Proteins	Matrisome-Associated
annexin A1	65	ECM-affiliated Proteins	Matrisome-Associated
neural cell adhesion molecule 2	49	ECM-affiliated Proteins	Matrisome-Associated
annexin A5	16	ECM-affiliated Proteins	Matrisome-Associated
annexin A8-like protein 2	38	ECM-affiliated Proteins	Matrisome-Associated
epithelial cell adhesion molecule precursor	56	ECM-affiliated Proteins	Matrisome-Associated
cathepsin D	46	ECM Regulators	Matrisome-Associated
protein glutamine gamma glutamyltransferase 2	39	ECM Regulators	Matrisome-Associated
disintegrin and metalloproteinase domain containing protein 23	74	ECM Regulators	Matrisome-Associated
coagulation factor XIII A chain precursor	28	ECM Regulators	Matrisome-Associated
inter-alpha-trypsin inhibitor heavy chain H5 isoform 3	78	ECM Regulators	Matrisome-Associated
prothrombin preprotein	26	ECM Regulators	Matrisome-Associated
alpha 2 macroglobulin like protein 1	78	ECM Regulators	Matrisome-Associated
protein S100-A13	13	Secreted Factors	Matrisome-Associated
transforming growth factor beta induced protein ig-H3 precursor	56	Secreted Factors	Matrisome-Associated
protein S100 A1	5	Secreted Factors	Matrisome-Associated
secreted frizzled related protein 5	11	Secreted Factors	Matrisome-Associated
fibroblast growth factor 11	45	Secreted Factors	Matrisome-Associated
protogenin precursor	79	Other	Other
fibronectin type III domain containing protein 1	145	Other	Other
midline 1	60	Other	Other
probable G-protein coupled receptor 110 isoform 1	69	Other	Other
X-ray repair cross-complementing protein 5	80	Other	Other
protocadherin Fat 1	178	Other	Other
target of Nesh SH3 precursor	58	Other	Other
brother of CDO precursor	33	Other	Other

tubulointerstitial nephritis antigen like	52	Other	Other
myomesin 2	231	Other	Other
leucine rich repeat containing protein 8D	82	Other	Other
fibronectin type III and SPRY domain containing protein 1	53	Other	Other
killer cell lectin like receptor subfamily B member 1	10	Other	Other
integrin beta 1 isoform 1A precursor	43	Other	Other
cation-independent mannose 6 phosphate receptor precursor	149	Other	Other
contactin associated protein like 2 precursor	51	Other	Other
X-ray repair cross-complementing protein 6	43	Other	Other
copine 5	33	Other	Other
phytanoyl CoA hydroxylase interacting protein	16	Other	Other
complement component C1q receptor precursor	36	Other	Other
26S proteasome nonATPase regulatory subunit 4	17	Other	Other
filamin C isoform b	251	Other	Other
filaggrin	199	Other	Other
neurexin 1 beta isoform alpha 2 precursor	66	Other	Other
leucine rich repeat transmembrane protein FLRT2 precursor	22	Other	Other
leucine rich repeat LGI family member 2	43	Other	Other
alpha 2 HS glycoprotein	15	Other	Other
general transcription factor IIH, polypeptide 2B	33	Other	Other
mucin 16	376	Other	Other
contactin 6 precursor	93	Other	Other
interleukin 27 receptor subunit alpha	24	Other	Other
leucine rich repeat and fibronectin type III domain containing protein 3	27	Other	Other
pappalysin 1 preproprotein	58	Other	Other
roundabout homolog 3 precursor	111	Other	Other
receptor type tyrosine protein phosphatase beta isoform a	182	Other	Other
signal peptide, CUB and EGF like domain containing protein 2 isoform 1	115	Other	Other
leucine rich repeat serine/threonine protein kinase 2	160	Other	Other
contactin 1 isoform 1	152	Other	Other
titin isofrom N2-A	3400	Other	Other

voltage dependent calcium channel subunit alpha 2 delta 1	95	Other	Other
WD repeat containing protein 33 isoform 1	238	Other	Other
contactin associated protein 1	47	Other	Other
leucine rich repeat containing protein 8B	48	Other	Other

A.2: Human Cortex protein scores from the Protein Atlas

(E)-endothelial cells, (G)-Glia, (N)-neurons, (NP)-Neuropil

Protein	(E)	(G)	(N)	(NP)	Average	RNA (RPKM)	Category
LAMC2	0	3	1	1	1.25	0.10	glycoprotein
POSTN	0	3	3	0	1.5	0.30	glycoprotein
FGB	3	0	2	1	1.5	0.10	glycoprotein
SPARC	2	0	0	3	1.25	57.80	glycoprotein
LAMA2	3	0	0	0	0.75	1.70	glycoprotein
LAMB2	3	0	1	2	1.5	8.40	glycoprotein
NID2	3	0	1	1	1.25	0.50	glycoprotein
VWF	3	0	0	0	0.75	7.80	glycoprotein
PSAP	1	2	3	0	1.5	358.30	glycoprotein
TNXB	0	2	3	2	1.75	1.80	glycoprotein
AGRN	2	1	3	0	1.5	21.60	glycoprotein
VWA2	2	2	3	1	2	0.30	glycoprotein
GPC3	1	2	3	1	1.75	0.20	glycoprotein
GPC4	0	1	3	2	1.5	2.20	glycoprotein
NFASC	1	0	1	3	1.25	13.40	glycoprotein
TNN	0	0	2	3	1.25	0.00	glycoprotein
NRP2	3	2	0	0	1.25	1.40	glycoprotein
THBS3	2	1	3	1	1.75	6.30	glycoprotein
LAMA1	2	0	1	2	1.25	0.70	glycoprotein
LAMB3	0	0	1	2	0.75	2.00	glycoprotein
THBS2	0	1	2	2	1.25	3.00	glycoprotein
THBS1	2	0	0	0	0.5	0.90	glycoprotein
FN1	2	0	0	0	0.5	9.80	glycoprotein
VTN	2	1	2	0	1.25	1.90	glycoprotein
TNR	0	0	0	2	0.5	13.90	glycoprotein
FBLN1	2	0	1	2	1.25	3.30	glycoprotein
ANGPT1	1	1	2	1	1.25	0.40	glycoprotein
CD59	2	0	0	1	0.75	88.10	glycoprotein
ENG	2	0	0	0	0.5	10.70	glycoprotein

STC1	0	0	0	2	0.5	1.30	glycoprotein
CD55	0	0	0	2	0.5	3.20	glycoprotein
FBLN7	0	2	2	2	1.5	2.10	glycoprotein
VWA7	0	2	0	0	0.5	4.10	glycoprotein
LAMB4	1	0	0	1	0.5	0.00	glycoprotein
TNC	0	0	0	2	0.5	0.70	glycoprotein
DAG1	1	0	0	0	0.25	10.40	glycoprotein
AFM	0	0	1	0	0.25	0.00	glycoprotein
VWA1	1	1	1	0	0.75	8.10	glycoprotein
VWC2	1	0	1	0	0.5	1.30	glycoprotein
LAMA4	1	0	0	0	0.25	2.00	glycoprotein
FBN3	1	0	0	0	0.25	0.20	glycoprotein
HSPG2	1	0	1	1	0.75	0.70	glycoprotein
LAMC1	2	0	0	0	0.5	2.70	glycoprotein
COL4A2	3	0	0	0	0.75	3.70	collagen
COL21A1	2	2	3	2	2.25	0.70	collagen
COL23A1	0	2	3	0	1.25	2.90	collagen
COL4A1	2	0	1	0	0.75	2.20	collagen
COL1A1	0	2	2	0	1	0.80	collagen
COL15A1	2	0	0	0	0.5	0.30	collagen
COL8A1	2	0	0	0	0.5	0.10	collagen
COL6A2	1	2	2	2	1.75	4.70	collagen
COL12A1	0	0	2	1	0.75	1.70	collagen
COL15A1	2	0	0	0	0.5	0.30	collagen
COL1A2	2	2	2	1	1.75	2.50	collagen
COL8A2	2	0	0	0	0.5	0.20	collagen
COL6A6	1	0	0	2	0.75	0.00	collagen
COL9A3	0	1	2	1	1	10.00	collagen
COL25A1	2	0	0	1	0.75	0.10	collagen
COL22A1	0	1	2	0	0.75	0.40	collagen
COL18A1	1	1	0	1	0.75	5.00	collagen
COL5A1	1	0	1	0	0.5	1.20	collagen
COL5A3	0	0	0	1	0.25	22.70	collagen
COL19a1	0	0	1	1	0.5	0.10	collagen
COL4A3	0	0	0	0	0	0.50	collagen
COL6A2	3	0	0	0	0.75	4.70	collagen
COL12A1	0	0	2	1	0.75	1.70	collagen
CSPG4	1	0	3	2	1.5	4.00	proteoglycan
BCAN	1	1	2	3	1.75	53.10	proteoglycan
SDC3	1	2	1	1	1.25	38.30	proteoglycan

SDC2	2	2	2	2	2	11.00	proteoglycan
LUM	0	0	0	2	0.5	0.50	proteoglycan
VCAN	2	0	1	2	1.25	2.80	proteoglycan
HAPLN2	0	0	0	2	0.5	25.20	proteoglycan
GPC6	2	1	2	1	1.5	0.40	proteoglycan
SDC2	2	2	2	2	2	11.00	proteoglycan
PRG4	0	0	0	2	0.5	0.00	proteoglycan
SDC3	1	2	1	1	1.25	38.30	proteoglycan
SDC4	1	1	1	0	0.75	30.00	proteoglycan
OGN	0	0	0	1	0.25	1.20	proteoglycan
NCAN	0	0	0	2	0.5	31.80	proteoglycan
ACAN	2	0	0	0	0.5	0.20	proteoglycan
DCN	1	0	0	0	0.25	5.60	proteoglycan
FBLN2	0	0	1	0	0.25	1.80	proteoglycan
HPSE	0	2	3	0	1.25	0.30	ECM regulator
PPT1	1	3	3	2	2.25	41.00	ECM regulator
CNP	0	2	0	3	1.25	51.10	ECM regulator
ADAMTS4	0	1	3	2	1.5	2.10	ECM regulator
ADAM9	1	0	3	2	1.5	5.50	ECM regulator
TIMP3	0	1	3	1	1.25	25.90	ECM regulator
ADAMTS18	1	1	3	2	1.75	0.20	ECM regulator
ADAMTSL4	0	2	3	2	1.75	0.80	ECM regulator
ADAMTSL5	2	2	3	3	2.5	0.60	ECM regulator
ADAMTS10	1	1	3	1	1.5	8.40	ECM regulator
SOD1	1	2	1	1	1.25	151.20	ECM regulator
SERPINA3	2	0	0	0	0.5		ECM regulator
SERPINH1	2	0	0	0	0.5	7.10	ECM regulator
NCSTN	0	1	2	0	0.75	11.20	ECM regulator
PLAT	2	0	0	0	0.5	5.00	ECM regulator
PRDX4	2	1	2	0	1.25	5.20	ECM regulator
ADAM17	2	1	2	2	1.75	2.80	ECM regulator
ARSA	1	2	2	0	1.25	11.50	ECM regulator
ADAMTS3	2	2	2	2	2	0.70	ECM regulator
ADAMTS20	0	1	1	2	1	0.00	ECM regulator
ADAMTS2	2	1	2	2	1.75	0.60	ECM regulator
PLAU	0	0	0	2	0.5	0.40	ECM regulator
ADAM15	1	1	2	1	1.25	12.40	ECM regulator
ADAMTS8	2	0	0	0	0.5	4.70	ECM regulator
ADAM8	0	0	2	0	0.5	1.50	ECM regulator
ADAMTS12	0	0	2	1	0.75	0.00	ECM regulator

ADAM23	2	1	2	0	1.25	17.00	ECM regulator
ADAMTSL3	2	0	1	0	0.75	0.30	ECM regulator
SERPINC1	0	0	0	1	0.25	0.10	ECM regulator
ADAMTS13	0	1	1	1	0.75	4.20	ECM regulator
TGFBR3	0	1	1	0	0.5	1.70	ECM regulator
EDN1	0	1	1	0	0.5	5.60	ECM regulator
ENTPD5	0	1	1	0	0.5	0.60	ECM regulator
TIMP2	0	0	1	0	0.25	39.70	ECM regulator
ADAMTS5	0	0	1	0	0.25	0.10	ECM regulator
ADAMTS14	0	1	0	0	0.25	1.30	ECM regulator
ADAM10	1	0	0	0	0.25	6.10	ECM regulator
ADAMTS13	0	1	1	1	0.75	4.20	ECM regulator
ADAMTS9	0	0	0	1	0.25	1.60	ECM regulator
PLAUR	0	0	0	1	0.25	1.20	ECM regulator
MMP2	3	0	0	0	0.75	0.70	ECM regulator
MMP3	0	3	3	1	1.75	0.00	ECM regulator
MMP7	0	0	1	0	0.25	0.00	ECM regulator
MMP9	1	0	0	0	0.25	0.30	ECM regulator
MMP10	1	1	1	1	1	0.00	ECM regulator
MMP14	2	0	1	0	0.75	1.90	ECM regulator
MMP15	1	1	2	2	1.5	3.10	ECM regulator
MMP16	1	2	1	0	1	1.80	ECM regulator
MMP25	0	1	1	2	1	0.60	ECM regulator
MATN2	1	2	1	3	1.75	2.80	ECM-affiliated protein
LGALS8	0	2	1	2	1.25	3.40	ECM-affiliated protein
LGALS1	2	1	1	1	1.25	119.50	ECM-affiliated protein
ICAM1	2	0	0	0	0.5	3.30	ECM-affiliated
LGALS3BP	1	0	0	0	0.25	13.80	ECM-affiliated
FRAS1	1	0	0	1	0.5	1.10	ECM-affiliated
TGFA	2	3	2	0	1.75	1.80	Secreted factors
VEGFA	1	0	2	1	1	13.00	Secreted factors
FGF1	2	0	0	0	0.5	33.90	Secreted factors
FGFR3	2	2	2	2	2	49.70	Secreted factors
MIF	1	0	2	1	1	0.00	Secreted factors
CX3CL1	1	1	2	1	1.25	22.90	Secreted factors
WISP2	0	0	1	1	0.5	0.20	Secreted factors
F8	1	0	1	1	0.75	2.50	Secreted factors
CXCL8	0	0	0	1	0.25	1.50	Secreted factors
NTN1	0	0	0	2	0.5	1.40	Secreted factors

A.3: Integrin-binding proteins of the human brain cortex via proteomics.

Protein	Peptide Sequence	Peptide Reference	Integrin	integrin references
NID1/ entactin	RGD	284	a5b1	285
VWF		286	avb3, aIIbB2	286
VTN			avb3	
FBN1		287	avb3	287
COL6A1		288	a1b1, a10b1	288
COL6A3				
COL6A2				
FGA		289	a5b1	289
FGB				
NFASC		290	b1	290
FN	PHSRN-RGDS	291	a5b1	291
COL1A1	GFOGERGVQ, DGEA	292	a1b1	293
COL1A2				
COL4A1	GLOGEN	292	a1b1	292
COL4A2				
COL4A1	FYFDLR	294	a2b1	294
COL4A2		294		
COL1A2	DGEA	295	a2b1	295
LAMB2	YIGSR	296	a6b1	
LAMC1	LRE	297	a3b1	298
LAMA5	IKVAV	299		
FGG	GWTVFQKRLDGS	300	avb3	300
Perlecan	TWSKVGGHLRPGIVQSG	301	b1	302
COL18A1	IVRRADRAAVP	303	b1 (a3b1)	303
ELN	GRKRK	304	avb3	304
FGA	GPR	305	axb2	305
COL18A1			a1b1	306
NID1/entactin			a3b1	307
Perlecan			avb3	308

A.4: MMP-degradable proteins via Proteomics.

Protein	MMP cleavage	# Samples	Cleavage Reference
dMAG	MMP2	3	309
COL1A1	MMP-2 (GPQG*IAGQRGVVGL)	4	310
COL1A2	MMP2 (GPQG*LLGAhypGFLGL)	3	
COL4A1	MMP2	4	311
COL4A2	MMP2	4	
COL6A1	MMP2	2	312
COL6A2	MMP2	2	
COL6A3	MMP2	3	
COL18A1	MMP2	3	313
LAMC	MMP2	4	314
LAMC2	MMP2 (TAAA-LTSC)	4	315
NFASC	MMP2	3	
NCAN	MMP2	2	
ELN	MMP2	2	311
VTN	MMP2	2	316
fibrillin-1	MMP2	2	317
LGALS1	MMP2	2	318
dMAG	MMP7	3	309
FN	MMP7	2	319
TNR	MMP7	4	320
AGRN	MMP7 (IST*FRA)	3	321
PCAN	MMP7	3	322
VCAN	MMP7	4	319
NID1	MMP7 (GLU34-LEU35) (GLY275-LEU276) (ALA637-LEU638) (CYS747-ILE746)	2	
ELN	MMP7	2	311
VTN	MMP7	2	316
dMAG	MMP9	3	309
COL6A1	MMP9	2	312
COL6A2	MMP9	2	
COL6A3	MMP9	3	
COL18A1	MMP9 (YVH-LRP) (SLA-HTH)	3	313
vWf	MMP9	3	323
NTN-1	MMP9	2	324
NID1	MMP9	2	325
ELN	MMP9	2	311
VTN	MMP9	2	316

Fibrillin	MMP9	2	317
COL1A1	MMP1 (GL*AGQRGIVGL*)	4	326
COL1A2	MMP1 (GL*AGQRGIVGL*)	3	
TNR	MMP1	4	320
AGRN	MMP1 (EQH*IRS)	3	321
COL1A1	MMP-8 (GPQG-IAQG)	4	311
TNR	MMP8	4	320
vWf	MMP8	3	323
COL1A1	MMP13 (GPQG-IAQG)	4	311
COL18A1	MMP13 (YVH-LRP) (SLA-HTH)	3	313
FN	MMP13	2	327
TNR	MMP13	4	320
FGA	MMP-13 (HKYKAXEH) (VKDHXSKH) (LVAXRGAH)	2	328
FGB	MMP-13 (HKYKAXEH) (VKDHXSKH) (LVAXRGAH)	3	
FGG	MMP-13 (HKYKAXEH) (VKDHXSKH) (LVAXRGAH)	3	
Fibrillin	MMP13	2	317
COL18A1	MMP3 (YVH-LRP) (SLA-HTH)	3	313
FN	MMP3	2	325
TNR	MMP3	4	320
AGRN	MMP3 (PHT* MLN)	3	321
PCAN	MMP3	3	325
NID1	MMP3	2	
VTN	MMP3	2	316
COL18A1	MMP12 (YVH-LRP) (SLA-HTH)	3	313
FGA	MMP-12 (HKYKAEEHT) (YKAEEHTV) (LTRNGPL) (LVALRGAH) (LRGAHPY)	2	328
ELN	MMP12	2	311
Fibrillin	MMP12	2	317
COL18A1	MMP20 (YVH-LRP) (SLA-HTH)	3	313
COL18A1	MMP14	3	
LAMA5	MMP14	2	329
LAMB	MMP14	3	
LAMC	MMP14	4	
FN	MMP14	2	327
TNR	MMP14	4	320
PCAN	MMP14	3	325
FGA	MMP-14 (LTRNGPL) (LVALRGA)	2	328
FGG	MMP-14 (LTRNGPL) (LVALRGA)	3	
NID1	MMP14	2	325

LGALS1	MMP14	2	330
TNR	MT2-MMP	4	320
TNR	MMP19	4	
NID1	MMP19	2	331

A.5: Integrin-binding proteins found via Protein Atlas.

Protein	Gene	Peptide	Integrin	Expression	Reference
COL I	*COL1A1*	DGEA	α1β1	1	295
	COL1A2			1.75	
COL IV	*COL4A1*	FYDLR	α2β1	0.75	294
	COL4A2			0.75	
LAMA	*LAMA2*	IKVAK	α4β1	0.75	299
	LAMA5			0.125	
LAMB	*LAMB2*	YIGSR	α6β1	1.5	296
	LAMB4			0.5	
LAMC	*LAMC1*	LRE	α3β1	0.5	297
	LAMC2			1.25	
POSTN	*POSTN*	ALMKYHILNTLQCSE	αXβ2	1.5	332
THSB	*THSB3*	VTCG	CD36,	1.75	333
COL XVIII	*COL18A1*	IVRRADRAAVP	α3β1	0.5	303
TN	*TNC*	AEGDIEL	α9β1	0.5	334
THSB	*THBS2*	RGD	α5β1	1.25	335
NFASC	*NFASC*		α5β1	1.25	290
FBN	*FBN1*		αVβ3	0.25	287
VTN	*VTN*		αVβ3	0.75	336
VWF	*VWF*		αVβ3	0.75	286
TNX	*TNXB*		α5β1	1.75	337
COL VI	*COL6A2*		α1β1,α7β1, α10β1	0.75	338
	COL6A6			0.75	

A.6: MMP-degradable proteins found via Protein Atlas.

Protein	Expression	Cleaved	Reference
THSB1	0.5	MMP2	339
POSTN	1.5	MMP2	340
BCAN	1.75	MMP-2(HPSA-FSEA)	320
Laminin	1.25	MMP2	
VCAN	1.25	MMP-2 (PPEA-LRGI)	315
ACAN	0.5	MMP2 (IPEN-FFGV)	
COL1A1	1	MMP2 (GPQG-IAGQ)	
COL1A2	1	MMP2 (GPQG-LLGA)	
decorin	0.25	MMP2 (DAAS-LLGL)	
LGALS3	0.25	MMP2 (PPGA-YHGA)	
LAMC2	1.25	MMP2 (TAAA-LTSC)	
SPARC	0.75	MMP2 (HPVG-LLAR)	
NCAN	0.5	MMP2	
COL18A1	0.75	MMP2	313
ELN	0.75	MMP2	311
COL4A1	0.75	MMP2	325
COL4A2	0.75	MMP2 (PPG-FLG)	
COL6A2	1.75	MMP2	312
COL6A6	0.75	MMP2	
NFASC	1.25	MMP2	
VTN	1.25	MMP2	316
LGALS1	1.25	MMP2 (ACGLVA)	318
fibrillin-1	0	MMP2	317
AVERAGE	0.91304348		
POSTN	1.5	MMP3	325
BCAN	1.75	MMP3	320
Laminin	1.25	MMP3	
ACAN	0.5	MMP3	325
COL1A1	1	MMP3	
COL1A2	1	MMP3	
NCAN	0.5	MMP-3 (IVAM-LRAP)	315
COL18A1	0.75	MMP3 (YVH-LRP) (SLA-HTH)	313
PERLECAN	0.75	MMP3	325
COL4A1	0.75	MMP3	
COL4A2	0.75	MMP3	
VTN	1.25	MMP3	321
TNXB	1.75	MMP3	325

FN1	0.5	MMP3	
TNC	0.5	MMP3	
AGRN	1.5	MMP3 (PHT* MLN)	321
AVERAGE	1		
POSTN	1.5	MMP9	325
Laminin	1.25	MMP9	320
ACAN	0.5	MMP9	325
LGALS3	0.25	MMP9	341
COL18A1	0.75	MMP9 (YVH-LRP) (SLA-HTH)	313
ELN	0.75	MMP9	311
COL6A2	1.75	MMP9	312
VWF	0.75	MMP9	323
VTN	1.25	MMP9	316
TNXB	1.75	MMP9	325
TNC	0.5	MMP9	
COL3A1	0	MMP9 (PGQLQG)	
fibrillin-1	0	MMP9	317
netrin-1	0.5	MMP9	
AVERAGE	0.82142857		
POSTN	1.5	MMP14	325
ACAN	0.5	MMP14	
COL18A1	0.75	MMP14	313
PERLECAN	0.75	MMP14	325
TNXB	1.75	MMP14	
FN1	0.5	MMP14	327
LGALS1	1.25	MMP14	330
TNC	0.5	MMP14	325
AVERAGE	0.9375		
BCAN	1.75	MMP7 (ALA360-PHE361)	320
Laminin	1.25	MMP7	
ACAN	0.5	MMP7 (ASN341-PHE342)	319
Decorin	0.25	MMP7 (ASP1-GLU2)	
SPARC	0.75	MMP7 (GLU20-VAL21) (GLN37-PHE38)	
COL18A1	0.75	MMP7 (VVQLHD)	325
COL18A1	0.75	MMP7 (GLN1276-LEU1277)	319
PERLECAN	0.75	MMP7	322
ELN	0.75	MMP7	311
COL4A2	0.75	MMP7	319
VTN	1.25	MMP7	316
VCAN	1.25	MMP7	319

TNC	0.5	MMP7 (LEU155-ASP156)	
AGRN	1.5	MMP7 (IST*FRA)	321
FBLN1	1.25	MMP7	342
FBLN2	0.25	MMP7 (ARG378-PHE379) (SER553-LEU554)	
syndecan-1	0	MMP7	319

A.7: Design of Synthetic Brain ECM.

Peptide	**Sequence**	**Atlas**	**MS**	**Average**	**% in Brain hydrogel**
POSTN	ALMKYHILNTLQCSE	10%	0%	4.8%	5%
COL18	IVRRADRAAVP	2%	7%	4.1%	4%
LAMA	IKVAV	5%	0%	2.4%	2%
LAMB	YIGSR	14%	10%	12.4%	12%
COLI	DGEA	14%	37%	25.6%	26%
COLIV	FYFDLR	2%	13%	7.5%	8%
FGB	RGD	43%	33%	37.7%	38%
NFASC					
NID2					
COL6A6					
TNXB					
FBLN					
THSB2					
THSB3	VTCG	8%	0%	4.0%	4%
TNC	AEIDGIEL	3%	0%	1.6%	2%
	Total	100%	100%	100.0%	100.0%
MMP2	IPVS-LRSG	20%	20%	20.1%	20%
MMP3	RPFS-MIMG	22%	20%	21.1%	21%
MMP7	VPLS-LTMG	19%	20%	19.3%	19%
MMP9	VPLS-LYSG	18%	21%	19.6%	20%
MMP14	IPES-LRAG	21%	19%	19.9%	20%
	Total			100.0%	100.0%

APPENDIX B

VARIATION IN MOTILITY ASSAY PARAMETERS IN THE CURRENT LITERATURE

B.1: Common metrics used in the literature to determine tumor cell motility.

Metric	Measurement	Description	Units	Frequency of use
% Migrating	Cell count	Number of cells moving, usually assessed by a baseline distance	%	
% Invasion	Cell count	Number of cells that have crossed a boundary	%, fold change	9
Persistence	Fitted parameter	Time at which a cell is moving in one direction before switching	time	4
MSD	X, Y, time	Measure of deviation of cell w.r.t. its initial position	μm^2	1
Chemotactic Index	X and Y coordinates	Net distance / total distance	0-1	
Net Distance	X and Y coordinates	Shortest distance between the initial and final position of the cell	μm	
Total Distance	X and Y coordinates	Total distance traveled by the cell	μm	
Speed	X, Y, time	Distance traveled by cell per unit of time	μm/min	12
Velocity	X, Y, time	Displacement of cell per unit of time (vector)	μm/min	

B.2: Concentration of basement membrane extract (i.e. Matrigel) used in tissue culture insert invasion assay experiments.

Cell line	BME Concentration	Reference
MDA-MB-231	not specified	343
MDA-MB-231		344
MDA-MB-231		
MCF7	50 μg/ml	345
SKBR3	not specified	346
SUM149		343
HMECs		
PC3	50 μg/ml	347
DU-145		
MDA-MB-231	0.2umol	348
T-47D		
Hs578T	not specified	349
MCF10A		
BT549		344

B.3: Tissue culture inserts used in assays with tumor cells.

Cell line	Pore size (μm)	Material of membrane	Reference
MDA-MB-231	8	polycarbonate	343
MDA-MB-231	8		344
MDA-MB-231	8		
MCF7	0.8	polyethylene terephthalate	350
SKBR3	ND	ND	346
SUM149	8	polycarbonate	343
HMECs	8		
PC3	8		347
DU-145	8		
MDA-MB-231	8	polyethylene terephthalate	348
T-47D	8		
Hs578T	8	polycarbonate	349
MCF10A	8		
BT549	8		344

B.4: Cell seeding and invasion metric data for tissue culture insert tumor cell invasion assays from the literature.

Cell line	Initial cells seeded	Invasion Data Format	Reported Invasion Value	Ref
MDA-MB-231	125,000 cells	Cell Per Field	147.8 cell per field	343
MDA-MB-231	250,000 cells	Invasion Value	89 invasion value	351
MDA-MB-231	50,000 cells/well	Number of invaded cells	1381.49 invaded cells	344
MDA-MB-231	50,000 cells/well		434.78 invaded cells	344
MDA-MB-231	200,000/ml cells	Fold Change	2.45 fold	350
MCF7	100,000 cells	Percentage Invasive Cells	4.70%	345
SKBR3	150,000 cells	Number of invaded cells	30.28 of invasive cells	346
MDA-MB-435	200,000/ml cells	Fold Change	1.95 fold	350
SUM149	125,000 cells	Cell Per Field	20 cell per field	343
HMECs	125,000 cells		52.44 cell per field	343
PC3	50000 cells		96.3 cell per field	347
DU-145	50000 cells		81.91 cell per field	347
MCF7	100000 cells	image only cannot quantify		352
MDA-MB-435	100000 cells	image only cannot quantify		352
MDA-MB-231	40,000 cells	cell per field	85.1 transmembrane cells	348
T-47D	40,000 cells	cell per field	8.97 transmembrane cells	348
Hs578T	50,000 cells	cell number	16744 cell number	349
MCF10A	50,000 cells	cell number	2590 cell number	349
BT549	50,000 cells/well	average cell per field	1249 average cell # per field	344

B.5: Assay readout for tissue culture insert invasion assays.

Cell line	Endpoint (hours)	Reference
MDA-MB-231	24	343
MDA-MB-231	24	344
MDA-MB-231	24	344
MCF7	12	345
SKBR3	48	346
SUM149	24	343
HMECs	24	343
PC3	18	347
DU-145	18	347
MDA-MB-231	48	348
T-47D	48	348
Hs578T	48	349
MCF10A	48	349
BT549	24	344

B.6: Tissue culture insert migration assay readout.

Cell line	Experiment time	Analysis method for readout	Ref.
MCF7	18 h	staining with 0.5% crystal violet avg. migrated cells bound per field	352
MCF7	0h, 12h, 36h	stained and counted	345
MDA-MB-231	24 h	stained with Diff-Quick staining set and counted	343
MDA-MB-231	48 hours	fixed 4% PFA, stained hematoxylin and eosin, counted	348
MDA-MB-231	24-48hrs	fixed 10% formalin, stained 0.05% crystal violet. Distance migration from spheroid center	344
MDA-MB-231	24 hours	fixed methanol, stained crytal violet.	350
MDA-MB-435	18 h	staining with 0.5% crystal violet avg. migrated cells bound per field	352
MDA-MB-435	24 hours	fixed methanol, stained crytal violet.	350
MDA-MB-453		stained and counted	345
SKBR3	24 hours	fixed methanol, stained 4 g/L crystal violet	346
BT549	24-48hrs	fixed 10% formalin, stained 0.05% crystal violet. Distance migration from spheroid center	344
SUM149	24 h	stained with Diff-Quick staining set and counted	343
HMECs	24 h	stained with Diff-Quick staining set and counted	343
T-47D	48 hours	fixed 4% PFA, stained hematoxylin and eosin, counted	348
Hs578T	48 hours	trypzinization and cell number counted	349
MCF10A	48 hours	trypzinization and cell number counted	349
PC-3	0h, 6h, 24h, 48h	%cell migration = [1-(scratch area at Tx (Hrs)/scratch area at T0]	347
DU-145	0h, 24h, 48h, 72h	%cell migration = [1-(scratch area at Tx (Hrs)/scratch area at T0]	347

B.7: Type of medium used in tissue culture insert invasion assays in lower chamber.

Cell line	Medium used with supplements in bottom chamber	Ref.
MCF7	fibroblast conditioned medium, 50ug/ml ascorbic acid serum free DMEM (lower chamber)	352
MCF7	lower chamber 500uL 10% FCS-DMEM	345
MDA-MB-231	bottom chambers 750 ul serum free medium	348
MDA-MB-231	RPMI 10% FBS	351
MDA-MB-231	FBS and fibronectin in lower chamber	344
MDA-MB-231	RPMI1640 20% FBS	350
MDA-MB-435	fibroblast conditioned medium, 50ug/ml ascorbic acid serum free DME	352
MDA-MB-435	RPMI1640 20% FBS	350
MDA-MB-453	lower chamber 500uL 10% FCS-DMEM	345
SKBR3	500 uL RPMI 1640, 10% serum bottom	346
BT549	FBS and fibronectin in lower chamber	344
Hs578T	complete medium with 10% FBS (750 μl)	349
MCF10A	complete medium with 10% FBS (750 μl)	349
T-47D	bottom chambers 750 μl serum free medium	348
PC-3	0.8ml serum free medium with 25ug/ml fibronectin	347
DU-145	0.8ml serum free medium with 25ug/ml fibronectin	347

APPENDIX C

VARIATION IN DRUG RESPONSE METRICS REPORTED IN THE LITERATURE FOR SAME CELL LINES

C.1: Range IC50 per drug and cell line combination.

Drug	Cell line	Format	Reported IC50	Calculated						Group
				IC50	Emax (growth inhibition)	AUC	EC50	R^2	Curve	
Paclitaxel	MCF7	2D	0.003 uM	0.003 uM	78% @ 11 uM	224.70	0.004 uM	0.97	Partial	353
		2D	3.2-8.3 uM	0.009 uM	71% @ 0.2 uM	156.40	0.006 uM	0.95	Incomplete	354
		2D	-	10.9 nM	55% @ 500nM	385.2	18nM	0.96	Partial	355
		3D GFR Matrigel	0.006 uM	0.005 uM	34% @ 191 uM	452.20	0.008 uM	0.97	Partial	353
		3D PEG-Heparin	-	2.81nM	37% @ 500nM	381.9	2.33nM	0.91	Complete	355
	MDA-MB-231	2D	0.004 uM	0.002 uM	97% @ 50 uM	139.60	0.004 uM	0.98	Partial	353
		2D	-	17.97 nM	45% @ 500nM	418.8	13.59nM	0.86	Partial	355
		2D	7.5 uM	4.6 uM	97% @ 25uM	2.375	5.26 uM	0.89	Incomplete	356
		3D GFR Matrigel	0.03 uM	0.03 uM	74% @ 199 uM	335.70	0.04 uM	1.00	Complete	353
		3D PEG-Heparin	-	4.41nM	37% @ 500nM	411.9	7.31nM	0.94	Complete	355
		3D fibroin Silk	50uM	50.3uM	58% @ 60uM	3.326	25uM	0.98	Incomplete	356
Doxorubicin	MCF7	2D	0.23 uM	0.3 uM	100% @ 112 uM	340.60	0.3 uM	0.98	Complete	239
		2D	0.84uM	0.88uM	99% @ 117uM	249.6	0.66uM	1.00	Incomplete	357
		3D GFR matrigel	Could not be calculated	14.2 uM	100% @ 239 uM	457.60	8.8 uM	1.00	Partial	239
		3D Matrigel	EC50=12 uM	not reached	41% @ 4uM	237.3	1.76uM	1.00	Incomplete	358
		3D agarose	70uM	32.79 ug/mL (60uM)	79% @ 115uM	294.8	19uM	1.00	Partial	357
Tamoxifen	MCF7	2D	7.74 uM	7.11 uM	80% @ 100uM	81.47	4.9uM	1.00	Partial	359
		2D	14.0uM	7.443uM	99% @ 807uM	163.6	14.49uM	0.97	Complete	360
		3D	20.62 uM	21uM	58% @ 90uM	126.4	14.4uM	0.99	Complete	359
		3D pNG cryogel	45.6uM	45.09uM	95% @ 800uM	224.9	38.5uM	0.99	Complete	360

		3D polynippam spheroids	72.6uM	71.35uM	88% @ 80uM	235.9	39uM	0.99	Complete	
Epirubicin	MDA-MB-231	2D	0.05 uM	0.04 uM	100% @ 1.1 uM	204.30	0.03 uM	0.97	Partial	353
		2D	0.6uM	0.49uM	85% @ 10uM	287.7	0.41uM	1.00	Partial	361
		3D GFR Matrigel	0.58 uM	0.5 uM	100% @ 52 uM	282.20	0.3 uM	0.99	Complete	353
		3D spheroid	0.6uM	0.317uM	70% @ 10uM	285.3	0.28uM	1.00	Partial	
Docetaxel	MDA-MB-231	2D	0.2uM	0.065uM	73% @ 10uM	247.4	0.05uM	1.00	Partial	361
		2D	31.4uM	35uM	93% 123uM	297.9	25.12uM	0.96	Incomplete	362
		3D	10uM	not reached	29% @ 0.1uM	312.4	could not determine	0.88	Incomplete	361

C.2: Examples where IC50 was not reached (drug concentration did not kill half of the cells).

Drug	Cell line	Format	Reported	Calculated						Ref
				IC50	Emax (growth inhibition)	AUC	EC50	R²	Curve	
Doxorubicin	MCF7	3D	EC50=12uM		41% @ 4uM	237.3	1.76uM	0.99	Incomplete	358
Methotrexate	JIMT1	2D	IC50 not reported	Drug did not kill half of the cells (IC50 not reached)	30% @ 20uM	406.80	0.02 uM	ND.	Incomplete	
Helenine	JIMT1	2D	IC50 not reported		11% @ 20 uM	511.70	2.0 uM	N.D.	Incomplete	
API-2	JIMT1	2D	IC50 not reported		17% @ 20 uM	398.70	11.1 uM	N.D.	Incomplete	363
								N.D.	Incomplete	
Gemcitabine	BXPC3	3D	showed resistance, No IC50		6% @ 500nM	255.2	230nM	N.D.	Incomplete	
Gemcitabine	Capan-1	3D	showed resistance, No IC50		25% @ 500 nM	231.4	63 nM	1.00	Partial	234
Docetaxel	MDA-MB-231	3D	IC50=10uM		29% @ 0.1uM	312.4	could not determine	0.88	Incomplete	361

C.3: IC50 reported in a publication differed from that calculated by our lab independently.

Drug	Cell line	Format	Reported	Calculated						Ref
				IC50	Emax	AUC	EC50	R^2	Curve	
Paclitaxel	SPCA-1	3D	IC50=2.97 uM	7.9uM	84% @ 8.5uM	19.7	7.75uM	0.99	Incomplete	364
	786-0	2D	38.0-51.3 uM	782 uM	62% @ 0.1 uM	212.20	0.04 uM	0.97	Partial	
	SW620	2D	2.6-3.6 uM	0.006 uM	100% @ 0.2 uM	128.70	0.006 uM	0.95	Partial	
	HT29	2D	2.8-4.7 uM	0.003 uM	100% @ 0.2 uM	119.20	0.003 uM	0.96	Partial	
	HeLa	2D	2.3-7.4 uM	0.02 uM	98% @ 0.1 uM	372.00	0.008 uM	0.99	Partial	
	SY5Y	2D	1.7-2.0 uM	0.006 uM	94% @ 0.1 uM	377.10	0.005 uM	0.99	Partial	
	PC3	2D	12.9-13.0 uM	0.03 uM	100% @ 0.2 uM	159.90	0.02 uM	0.99	Partial	354
Doxorubicin	HEPG2 (co-cultured with LX-2)	3D	50.4 uM	24.5 uM	69% @ 1957 uM	341.20	17.6 uM	0.99	Partial	
Doxorubicin	HEPG2 (co-cultured with LX-2)	2D	33.1 uM	228.7 uM	99% @ 213 uM	421.90	27.4 uM	0.89	Partial	
Doxorubicin + 0.1 uM calcipotriol	HEPG2 (co-cultured with LX-2)	3D	6.9 uM	3.92 uM	76% @ 1660 uM	317.10	5.89 uM	0.92	Partial	
Doxorubicin + 0.1 uM calcipotriol	HEPG2 (co-cultured with LX-2)	2D	43.7 uM	624.8 uM	96% @ 225 uM	388.40	42.7 uM	0.96	Partial	365
Epirubicin	MCF7	3D	0.5 uM	9.1 uM	98% @ 196 uM	406.30	3.8 uM	0.96	Partial	353

BIBLIOGRAPHY

1. Fuster, J. M., Prefrontal cortex. In *Comparative neuroscience and neurobiology*, Springer: 1988; pp 107-109.

2. Allen, N. J.; Barres, B. A., Neuroscience: glia—more than just brain glue. *Nature* **2009,** *457* (7230), 675-677.

3. Marín, O.; Rubenstein, J. L., Cell migration in the forebrain. *Annual review of neuroscience* **2003,** *26* (1), 441-483.

4. Freeman, M. R., Specification and morphogenesis of astrocytes. *Science* **2010,** *330* (6005), 774-778.

5. Novak, U.; Kaye, A. H., Extracellular matrix and the brain: components and function. *Journal of clinical neuroscience* **2000,** *7* (4), 280-290.

6. Zimmermann, D. R.; Dours-Zimmermann, M. T., Extracellular matrix of the central nervous system: from neglect to challenge. *Histochemistry and cell biology* **2008,** *130* (4), 635-653.

7. Dityatev, A.; Seidenbecher, C. I.; Schachner, M., Compartmentalization from the outside: the extracellular matrix and functional microdomains in the brain. *Trends in neurosciences* **2010,** *33* (11), 503-512.

8. Galtrey, C. M.; Kwok, J. C.; Carulli, D.; Rhodes, K. E.; Fawcett, J. W., Distribution and synthesis of extracellular matrix proteoglycans, hyaluronan, link proteins and tenascin-R in the rat spinal cord. *European Journal of Neuroscience* **2008,** *27* (6), 1373-1390.

9. Oberheim, N. A.; Goldman, S. A.; Nedergaard, M., Heterogeneity of astrocytic form and function. *Astrocytes: Methods and Protocols* **2012**, 23-45.

10. Naba, A.; Pearce, O. M. T.; Del Rosario, A.; Ma, D.; Ding, H.; Rajeeve, V.; Cutillas, P. R.; Balkwill, F. R.; Hynes, R. O., Characterization of the extracellular matrix of normal and diseased tissues using proteomics. *Journal of proteome research* **2017,** *16* (8), 3083-3091.

11. Ragelle, H.; Naba, A.; Larson, B. L.; Zhou, F.; Prijić, M.; Whittaker, C. A.; Del Rosario, A.; Langer, R.; Hynes, R. O.; Anderson, D. G., Comprehensive proteomic characterization of stem cell-derived extracellular matrices. *Biomaterials* **2017,** *128*, 147-159.

12. Naba, A.; Clauser, K. R.; Ding, H.; Whittaker, C. A.; Carr, S. A.; Hynes, R. O., The extracellular matrix: tools and insights for the “omics” era. *Matrix Biology* **2016,** *49*, 10-24.

13. Humphrey, J. D.; Dufresne, E. R.; Schwartz, M. A., Mechanotransduction and extracellular matrix homeostasis. *Nature reviews Molecular cell biology* **2014,** *15* (12).

14. Alberts, B.; Johnson, A.; Lewis, J.; Raff, M.; Roberts, K.; Walter, P., Integrins. **2002**.

15. Barczyk, M.; Carracedo, S.; Gullberg, D., Integrins. *Cell and tissue research* **2010,** *339* (1), 269.

16. Ruoslahti, E., RGD and other recognition sequences for integrins. *Annual Review of Cell and Developmental Biology* **1996,** *12* (1), 697-715.

17. Takada, Y.; Ye, X.; Simon, S., The integrins. *Genome biology* **2007,** *8* (5), 215.

18. Sternlicht, M. D.; Werb, Z., How matrix metalloproteinases regulate cell behavior. *Annual review of cell and developmental biology* **2001,** *17* (1), 463-516.

19. Barnes, J. M.; Przybyla, L.; Weaver, V. M., Tissue mechanics regulate brain development, homeostasis and disease. *Journal Cell Science* **2017,** *130* (1), 71-82.

20. Franz, C. M.; Jones, G. E.; Ridley, A. J., Cell migration in development and disease. *Developmental cell* **2002,** *2* (2), 153-158.

21. Reyes, C. D.; García, A. J., α2β1 integrin-specific collagen-mimetic surfaces supporting osteoblastic differentiation. *Journal of Biomedical Materials Research Part A: An Official Journal of The Society for Biomaterials, The Japanese Society for Biomaterials, and The Australian Society for Biomaterials and the Korean Society for Biomaterials* **2004,** *69* (4), 591-600.

22. Franze, K.; Janmey, P. A.; Guck, J., Mechanics in neuronal development and repair. *Annual Review of Biomedical Engineering* **2013,** *15*, 227-51.

23. Kwok, J. C.; Dick, G.; Wang, D.; Fawcett, J. W., Extracellular matrix and perineuronal nets in CNS repair. *Developmental neurobiology* **2011,** *71* (11), 1073-1089.

24. Valiente, M.; Obenauf, A. C.; Jin, X.; Chen, Q.; Zhang, X. H.-F.; Lee, D. J.; Chaft, J. E.; Kris, M. G.; Huse, J. T.; Brogi, E., Serpins promote cancer cell survival and vascular co-option in brain metastasis. *Cell* **2014,** *156* (5), 1002-1016.

25. Sarkar, S.; Mirzaei, R.; Zemp, F. J.; Wei, W.; Senger, D. L.; Robbins, S. M.; Yong, V. W., Activation of NOTCH signaling by tenascin-C promotes growth of human brain tumor-initiating cells. *Cancer Research* **2017,** *77* (12), 3231-3243.

26. Venkatesh, H. S.; Tam, L. T.; Woo, P. J.; Nagaraja, S.; Gillespe, S. M.; Lennon, J.; Ni, J.; Duveau, D. Y.; Morris, P. J.; Zhao, J. J., Targeting neuronal activity-regulated neuroligin-3 dependency for high-grade glioma therapy. *bioRxiv* **2017**, 153122.

27. Venkatesh, H. S.; Johung, T. B.; Caretti, V.; Noll, A.; Tang, Y.; Nagaraja, S.; Gibson, E. M.; Mount, C. W.; Polepalli, J.; Mitra, S. S., Neuronal activity promotes glioma growth through neuroligin-3 secretion. *Cell* **2015,** *161* (4), 803-816.

28. Gordon, R.; Brodland, G. W., The cytoskeletal mechanics of brain morphogenesis. *Cell biophysics* **1987,** *11* (1), 177-238.

29. Tyler, W. J., The mechanobiology of brain function. *Nature Reviews Neuroscience* **2012,** *13* (12), 867-78.

30. Lu, P.; Weaver, V. M.; Werb, Z., The extracellular matrix: a dynamic niche in cancer progression. *Journal of Cell Biology* **2012,** *196* (4), 395-406.

31. Pogoda, K.; Chin, L.; Georges, P. C.; Byfield, F. J.; Bucki, R.; Kim, R.; Weaver, M.; Wells, R. G.; Marcinkiewicz, C.; Janmey, P. A., Compression stiffening of brain and its effect on mechanosensing by glioma cells. *New Journal of Physics* **2014,** *16*, 075002.

32. Cheng, S.; Clarke, E. C.; Bilston, L. E., Rheological properties of the tissues of the central nervous system: a review. *Medical Engineering Physics* **2008,** *30* (10), 1318-37.

33. Peyton, S. R.; Gencoglu, M. F.; Galarza, S.; Schwartz, A. D., Biomaterials in Mechano-oncology: Means to Tune Materials to Study Cancer. In *Biomechanics in Oncology*, Springer: 2018; pp 253-287.

34. Samuel, M. S.; Lopez, J. I.; McGhee, E. J.; Croft, D. R.; Strachan, D.; Timpson, P.; Munro, J.; Schröder, E.; Zhou, J.; Brunton, V. G., Actomyosin-mediated cellular tension drives increased tissue stiffness and β-catenin activation to induce epidermal hyperplasia and tumor growth. *Cancer cell* **2011,** *19* (6), 776-791.

35. Faouzi, S.; Le Bail, B.; Neaud, V.; Boussarie, L.; Saric, J.; Bioulac-Sage, P.; Balabaud, C.; Rosenbaum, J., Myofibroblasts are responsible for collagen synthesis in the stroma of human hepatocellular carcinoma: an in vivo and in vitro study. *Journal of hepatology* **1999,** *30* (2), 275-284.

36. Seo, B. R.; Bhardwaj, P.; Choi, S.; Gonzalez, J.; Eguiluz, R. C. A.; Wang, K.; Mohanan, S.; Morris, P. G.; Du, B.; Zhou, X. K., Obesity-dependent changes in interstitial ECM mechanics promote breast tumorigenesis. *Science translational medicine* **2015,** *7* (301), 301ra130-301ra130.

37. Acerbi, I.; Cassereau, L.; Dean, I.; Shi, Q.; Au, A.; Park, C.; Chen, Y. Y.; Liphardt, J.; Hwang, E. S.; Weaver, V. M., Human breast cancer invasion and aggression correlates with ECM stiffening and immune cell infiltration. *Integrative Biology* **2015,** *7* (10), 1120-1134.

38. Murphy, M. C.; Huston, J., 3rd; Jack, C. R., Jr.; Glaser, K. J.; Manduca, A.; Felmlee, J. P.; Ehman, R. L., Decreased brain stiffness in Alzheimer's disease determined by magnetic resonance elastography. *Journal Magnetic Resonance Imaging* **2011,** *34* (3), 494-8.

39. Shafieian, M.; Darvish, K. K.; Stone, J. R., Changes to the viscoelastic properties of brain tissue after traumatic axonal injury. *Journal Biomechanics* **2009,** *42* (13), 2136-42.

40. Alfasi, A. M.; Shulyakov, A. V.; Del Bigio, M. R., Intracranial biomechanics following cortical contusion in live rats. *Journal Neurosurgery* **2013,** *119* (5), 1255-62.

41. Jamin, Y.; Boult, J. K. R.; Li, J.; Popov, S.; Garteiser, P.; Ulloa, J. L.; Cummings, C.; Box, G.; Eccles, S. A.; Jones, C.; Waterton, J. C.; Bamber, J. C.; Sinkus, R.; Robinson, S. P., Exploring the biomechanical properties of brain malignancies and their pathologic determinants in vivo with magnetic resonance elastography. *Cancer Research* **2015,** *75* (7), 1216-1224.

42. Lu, Y. B.; Franze, K.; Seifert, G.; Steinhauser, C.; Kirchhoff, F.; Wolburg, H.; Guck, J.; Janmey, P.; Wei, E. Q.; Kas, J.; Reichenbach, A., Viscoelastic properties of individual glial cells and neurons in the CNS. *Proc Natl Acad Sci U S A* **2006,** *103* (47), 17759-64.

43. Chatelin, S.; Constantinesco, A.; Willinger, R., Fifty years of brain tissue mechanical testing: from in vitro to in vivo investigations. *Biorheology* **2010,** *47* (5-6), 255-76.

44. Oberheim, N. A.; Takano, T.; Han, X.; He, W.; Lin, J. H.; Wang, F.; Xu, Q.; Wyatt, J. D.; Pilcher, W.; Ojemann, J. G., Uniquely hominid features of adult human astrocytes. *Journal of Neuroscience* **2009,** *29* (10), 3276-3287.

45. Liddelow, S. A.; Barres, B. A., Reactive astrocytes: production, function, and therapeutic potential. *Immunity* **2017,** *46* (6), 957-967.

46. Farina, C.; Aloisi, F.; Meinl, E., Astrocytes are active players in cerebral innate immunity. *Trends in immunology* **2007,** *28* (3), 138-145.

47. Sofroniew, M. V., Molecular dissection of reactive astrogliosis and glial scar formation. *Trends in neurosciences* **2009,** *32* (12), 638-647.

48. Sosunov, A. A.; Guilfoyle, E.; Wu, X.; McKhann, G. M.; Goldman, J. E., Phenotypic conversions of "protoplasmic" to "reactive" astrocytes in Alexander disease. *Journal of Neuroscience* **2013,** *33* (17), 7439-7450.

49. Ceyzeriat, K.; Abjean, L.; Carrillo-de Sauvage, M.-A.; Haim, L. B.; Escartin, C., The complex STATes of astrocyte reactivity: How are they controlled by the JAK–STAT3 pathway? *Neuroscience* **2016,** *330*, 205-218.

50. Hara, M.; Kobayakawa, K.; Ohkawa, Y.; Kumamaru, H.; Yokota, K.; Saito, T.; Kijima, K.; Yoshizaki, S.; Harimaya, K.; Nakashima, Y., Interaction of reactive astrocytes with type I collagen induces astrocytic scar formation through the integrin–N-cadherin pathway after spinal cord injury. *Nature medicine* **2017,** *23* (7), 818.

51. Chen, Q.; Boire, A.; Jin, X.; Valiente, M.; Er, E. E.; Lopez-Soto, A.; Jacob, L.; Patwa, R.; Shah, H.; Xu, K., Carcinoma-astrocyte gap junctions promote brain metastasis by cGAMP transfer. *Nature* **2016,** *533* (7604), 493.

52. Lorger, M.; Felding-Habermann, B., Capturing changes in the brain microenvironment during initial steps of breast cancer brain metastasis. *The American journal of pathology* **2010,** *176* (6), 2958-2971.

53. Kienast, Y.; Von Baumgarten, L.; Fuhrmann, M.; Klinkert, W. E. F.; Goldbrunner, R.; Herms, J.; Winkler, F., Real-time imaging reveals the single steps of brain metastasis formation. *Nature medicine* **2010,** *16* (1), 116.

54. Zamanian, J. L.; Xu, L.; Foo, L. C.; Nouri, N.; Zhou, L.; Giffard, R. G.; Barres, B. A., Genomic analysis of reactive astrogliosis. *Journal of neuroscience* **2012,** *32* (18), 6391-6410.

55. Liddelow, S. A.; Guttenplan, K. A.; Clarke, L. E.; Bennett, F. C.; Bohlen, C. J.; Schirmer, L.; Bennett, M. L.; Münch, A. E.; Chung, W.-S.; Peterson, T. C., Neurotoxic reactive astrocytes are induced by activated microglia. *Nature* **2017,** *541* (7638), 481.

56. Lian, H.; Yang, L.; Cole, A.; Sun, L.; Chiang, A. C. A.; Fowler, S. W.; Shim, D. J.; Rodriguez-Rivera, J.; Taglialatela, G.; Jankowsky, J. L., NFκB-activated astroglial release of complement C3 compromises neuronal morphology and function associated with Alzheimer's disease. *Neuron* **2015,** *85* (1), 101-115.

57. Gao, Q.; Li, Y.; Chopp, M., Bone marrow stromal cells increase astrocyte survival via upregulation of phosphoinositide 3-kinase/threonine protein kinase and mitogen-activated protein kinase kinase/extracellular signal-regulated kinase pathways and stimulate astrocyte trophic factor gene expression after anaerobic insult. *Neuroscience* **2005,** *136* (1), 123-134.

58. Zador, Z.; Stiver, S.; Wang, V.; Manley, G. T., Role of aquaporin-4 in cerebral edema and stroke. In *Aquaporins*, Springer: 2009; pp 159-170.

59. Hayakawa, K.; Pham, L.-D. D.; Arai, K.; Lo, E. H., Reactive astrocytes promote adhesive interactions between brain endothelium and endothelial progenitor cells via HMGB1 and beta-2 integrin signaling. *Stem cell research* **2014,** *12* (2), 531-538.

60. Anderson, M. A.; Burda, J. E.; Ren, Y.; Ao, Y.; O'Shea, T. M.; Kawaguchi, R.; Coppola, G.; Khakh, B. S.; Deming, T. J.; Sofroniew, M. V., Astrocyte scar formation aids central nervous system axon regeneration. *Nature* **2016,** *532* (7598), 195.

61. Valiente, M.; Ahluwalia, M. S.; Boire, A.; Brastianos, P. K.; Goldberg, S. B.; Lee, E. Q.; Le Rhun, E.; Preusser, M.; Winkler, F.; Soffietti, R., The evolving landscape of brain metastasis. *Trends in cancer* **2018,** *4* (3), 176-196.

62. Bos, P. D.; Nguyen, D. X.; Massagué, J., Modeling metastasis in the mouse. *Current opinion in pharmacology* **2010,** *10* (5), 571-577.

63. Blazquez, R.; Wlochowitz, D.; Wolff, A.; Seitz, S.; Wachter, A.; Perera-Bel, J.; Bleckmann, A.; Beißbarth, T.; Salinas, G.; Riemenschneider, M. J., PI3K: A master regulator of brain metastasis-promoting macrophages/microglia. *Glia* **2018,** *66* (11), 2438-2455.

64. Daphu, I.; Sundstrøm, T.; Horn, S.; Huszthy, P. C.; Niclou, S. P.; Sakariassen, P. Ø.; Immervoll, H.; Miletic, H.; Bjerkvig, R.; Thorsen, F., In vivo animal models for studying brain metastasis: value and limitations. *Clinical & experimental metastasis* **2013,** *30* (5), 695-710.

65. Zhuang, P.; Sun, A. X.; An, J.; Chua, C. K.; Chew, S. Y., 3D neural tissue models: From spheroids to bioprinting. *Biomaterials* **2018,** *154*, 113-133.

66. Hopkins, A. M.; DeSimone, E.; Chwalek, K.; Kaplan, D. L., 3D in vitro modeling of the central nervous system. *Progress in neurobiology* **2015,** *125*, 1-25.

67. Sloan, S. A.; Darmanis, S.; Huber, N.; Khan, T. A.; Birey, F.; Caneda, C.; Reimer, R.; Quake, S. R.; Barres, B. A.; Paşca, S. P., Human astrocyte maturation captured in 3D cerebral cortical spheroids derived from pluripotent stem cells. *Neuron* **2017,** *95* (4), 779-790.

68. Paşca, A. M.; Sloan, S. A.; Clarke, L. E.; Tian, Y.; Makinson, C. D.; Huber, N.; Kim, C. H.; Park, J.-Y.; O'Rourke, N. A.; Nguyen, K. D.; Smith, S. J.; Huguenard, J. R.; Geschwind, D. H.; Barres, B. A.; Paşca, S. P., Functional cortical neurons and astrocytes from human pluripotent stem cells in 3D culture. *Nature methods* **2015,** *12* (7), 671.

69. Paşca, S. P., Building three-dimensional human brain organoids. *Nature Neuroscience* **2018**.

70. Dezonne, R. S.; Sartore, R. C.; Nascimento, J. M.; Saia-Cereda, V. M.; Romão, L. F.; Alves-Leon, S. V.; De Souza, J. M.; Martins-de-Souza, D.; Rehen, S. K.; Gomes, F. C. A., Derivation of functional human astrocytes from cerebral organoids. *Scientific reports* **2017,** *7*, 45091.

71. Hsiao, T. W.; Tresco, P. A.; Hlady, V., Astrocytes alignment and reactivity on collagen hydrogels patterned with ECM proteins. *Biomaterials* **2015,** *39*, 124-130.

72. Ananthanarayanan, B.; Kim, Y.; Kumar, S., Elucidating the mechanobiology of malignant brain tumors using a brain matrix-mimetic hyaluronic acid hydrogel platform. *Biomaterials* **2011,** *32* (31), 7913-7923.

73. Khaing, Z. Z.; Milman, B. D.; Vanscoy, J. E.; Seidlits, S. K.; Grill, R. J.; Schmidt, C. E., High molecular weight hyaluronic acid limits astrocyte activation and scar formation after spinal cord injury. *Journal of Neural Engineering* **2011,** *8* (4), 046033.

74. Thompson, R. E.; Pardieck, J.; Smith, L.; Kenny, P.; Crawford, L.; Shoichet, M.; Sakiyama-Elbert, S., Effect of hyaluronic acid hydrogels containing astrocyte-derived extracellular matrix and/or V2a interneurons on histologic outcomes following spinal cord injury. *Biomaterials* **2018,** *162*, 208-223.

75. Placone, A. L.; McGuiggan, P. M.; Bergles, D. E.; Guerrero-Cazares, H.; Quiñones-Hinojosa, A.; Searson, P. C., Human astrocytes develop physiological morphology and remain quiescent in a novel 3D matrix. *Biomaterials* **2015,** *42*, 134-143.

76. Puschmann, T. B.; Zandén, C.; De Pablo, Y.; Kirchhoff, F.; Pekna, M.; Liu, J.; Pekny, M., Bioactive 3D cell culture system minimizes cellular stress and maintains the in vivo-like morphological complexity of astroglial cells. *Glia* **2013,** *61* (3), 432-440.

77. Johnson, K. M.; Milner, R.; Crocker, S. J., Extracellular matrix composition determines astrocyte responses to mechanical and inflammatory stimuli. *Neuroscience letters* **2015,** *600*, 104-109.

78. Barney, L., Extracellular Matrix Control of Breast Cancer Metastasis and Dormancy. **2016**.

79. DeForest, C. A.; Anseth, K. S., Advances in bioactive hydrogels to probe and direct cell fate. *Annual review of chemical and biomolecular engineering* **2012,** *3*, 421-444.

80. Celikkaya, H.; Cosacak, M. I.; Papadimitriou, C.; Popova, S.; Bhattarai, P.; Biswas, S. N.; Siddiqui, T.; Wistorf, S.; Nevado-Alcalde, I.; Naumann, L., GATA3 Promotes the Neural Progenitor State but Not Neurogenesis in 3D Traumatic Injury Model of Primary Human Cortical Astrocytes. *Frontiers in cellular neuroscience* **2019,** *13*.

81. Papadimitriou, C.; Celikkaya, H.; Cosacak, M. I.; Mashkaryan, V.; Bray, L.; Bhattarai, P.; Brandt, K.; Hollak, H.; Chen, X.; He, S., 3D culture method for Alzheimer's disease modeling reveals interleukin-4 rescues Aβ42-induced loss of human neural stem cell plasticity. *Developmental cell* **2018,** *46* (1), 85-101.

82. Seidlits, S. K.; Liang, J.; Bierman, R. D.; Sohrabi, A.; Karam, J.; Holley, S. M.; Cepeda, C.; Walthers, C. M., Peptide-modified, hyaluronic acid-based hydrogels as a 3D culture platform for neural stem/progenitor cell engineering. *Journal of Biomedical Materials Research Part A* **2019,** *107* (4), 704-718.

83. Puschmann, T. B.; Zandén, C.; Lebkuechner, I.; Philippot, C.; de Pablo, Y.; Liu, J.; Pekny, M., HB-EGF affects astrocyte morphology, proliferation, differentiation, and the expression of intermediate filament proteins. *Journal of neurochemistry* **2014,** *128* (6), 878-889.

84. Rao, S. S.; DeJesus, J.; Short, A. R.; Otero, J. J.; Sarkar, A.; Winter, J. O., Glioblastoma behaviors in three-dimensional collagen-hyaluronan composite hydrogels. *ACS applied materials & interfaces* **2013,** *5* (19), 9276-9284.

85. Priego, N.; Zhu, L.; Monteiro, C.; Mulders, M.; Wasilewski, D.; Bindeman, W.; Doglio, L.; Martínez, L.; Martínez-Saez, E.; y Cajal, S. R., STAT3 labels a subpopulation of reactive astrocytes required for brain metastasis. *Nature medicine* **2018,** *24* (7), 1024.

86. Schwartz, A. D.; Barney, L. E.; Jansen, L. E.; Nguyen, T. V.; Hall, C. L.; Meyer, A. S.; Peyton, S. R., A biomaterial screening approach reveals microenvironmental mechanisms of drug resistance. *Integrative Biology* **2017,** *9* (12), 912-924.

87. Zhuang, P.; Sun, A. X.; An, J.; Chua, C. K.; Chew, S. Y., 3D neural tissue models: From spheroids to bioprinting. *Biomaterials* **2018,** *154*, 113-133 %@ 0142-9612.

88. Haibe-Kains, B.; El-Hachem, N.; Birkbak, N. J.; Jin, A. C.; Beck, A. H.; Aerts, H. J. W. L.; Quackenbush, J., Inconsistency in large pharmacogenomic studies. *Nature* **2013,** *504* (7480), 389.

89. Hafner, M.; Niepel, M.; Chung, M.; Sorger, P. K., Growth rate inhibition metrics correct for confounders in measuring sensitivity to cancer drugs. *Nature methods* **2016,** *13* (6), 521.

90. Gencoglu, M. F.; Barney, L. E.; Hall, C. L.; Brooks, E. A.; Schwartz, A. D.; Corbett, D. C.; Stevens, K. R.; Peyton, S. R., Comparative study of multicellular tumor spheroid formation methods and implications for drug screening. *ACS Biomaterials Science & Engineering* **2018,** *4* (2), 410-420.

91. Ivanov, D. P.; Parker, T. L.; Walker, D. A.; Alexander, C.; Ashford, M. B.; Gellert, P. R.; Garnett, M. C., Multiplexing spheroid volume, resazurin and acid phosphatase viability assays for high-throughput screening of tumour spheroids and stem cell neurospheres. *PloS one* **2014,** *9* (8), e103817.

92. Jansen, L. E.; Negrón-Piñeiro, L. J.; Galarza, S.; Peyton, S. R., Control of thiol-maleimide reaction kinetics in PEG hydrogel networks. *Acta biomaterialia* **2018,** *70*, 120-128.

93. Hafner, M.; Heiser, L. M.; Williams, E. H.; Niepel, M.; Wang, N. J.; Korkola, J. E.; Gray, J. W.; Sorger, P. K., Quantification of sensitivity and resistance of breast cancer cell lines to anti-cancer drugs using GR metrics. *Scientific Data* **2017,** *4*, 170166.

94. Maher, J. M.; Markey, J. C.; Ebert-May, D., The other half of the story: effect size analysis in quantitative research. *CBE—Life Sciences Education* **2013,** *12* (3), 345-351.

95. Amrhein, V.; Greenland, S.; McShane, B., Scientists rise up against statistical significance. Nature: 2019; Vol. 567, pp 305-307.

96. Blanchard, G. B.; Adams, R. J., Measuring the multi-scale integration of mechanical forces during morphogenesis. *Current opinion in genetics & development* **2011,** *21* (5), 653-663.

97. Klein, C.; Hain, E. G.; Braun, J.; Riek, K.; Mueller, S.; Steiner, B.; Sack, I., Enhanced adult neurogenesis increases brain stiffness: in vivo magnetic resonance elastography in a mouse model of dopamine depletion. *PloS one* **2014,** *9* (3), e92582.

98. Hrapko, M.; van Dommelen, J. A.; Peters, G. W.; Wismans, J. S., Characterisation of the mechanical behaviour of brain tissue in compression and shear. *Biorheology* **2008,** *45* (6), 663-76.

99. Prange, M. T.; Margulies, S. S., Regional, directional, and age-dependent properties of the brain undergoing large deformation. *Journal of Biomechanical Engineering* **2002,** *124* (2), 244-52.

100. Franceschini, G.; Bigoni, D.; Regitnig, P.; Holzapfel, G. A., Brain tissue deforms similarly to filled elastomers and follows consolidation theory. *Journal of the Mechanics and Physics of Solids* **2006,** *54* (12), 2592-2620.

101. Chen, F.; Zhou, J.; Li, Y.; Wang, Y.; Li, L.; Yue, H., Mechanical Properties of Porcine Brain Tissue in the Coronal Plane: Interregional Variations of the Corona Radiata. *Annals of Biomedical Engineering* **2015,** *43* (12), 2903-10.

102. Lee, S. J.; King, M. A.; Sun, J.; Xie, H. K.; Subhash, G.; Sarntinoranont, M., Measurement of viscoelastic properties in multiple anatomical regions of acute rat brain tissue slices. *Journal of the Mechanical Behavior of Biomedical Materials* **2014,** *29*, 213-24.

103. van Dommelen, J. A.; van der Sande, T. P.; Hrapko, M.; Peters, G. W., Mechanical properties of brain tissue by indentation: interregional variation. *Journal of the Mechanical Behavior of Biomedical Materials* **2010,** *3* (2), 158-66.

104. Elkin, B. S.; Ilankova, A.; Morrison, I. I. I. B., Dynamic, Regional Mechanical Properties of the Porcine Brain: Indentation in the Coronal Plane. *Journal of Biomechanical Engineering* **2011,** *133* (7), 071009-071009-7.

105. Budday, S.; Sommer, G.; Haybaeck, J.; Steinmann, P.; Holzapfel, G. A.; Kuhl, E., Rheological characterization of human brain tissue. *Acta Biomaterialia* **2017**.

106. Nicolle, S.; Lounis, M.; Willinger, R.; Palierne, J. F., Shear linear behavior of brain tissue over a large frequency range. *Biorheology* **2005,** *42* (3), 209-23.

107. Hrapko, M.; van Dommelen, J. A.; Peters, G. W.; Wismans, J. S., The mechanical behaviour of brain tissue: large strain response and constitutive modelling. *Biorheology* **2006,** *43* (5), 623-36.

108. Cheng, S.; Bilston, L. E., Unconfined compression of white matter. *Journal of Biomechanics* **2007,** *40* (1), 117-24.

109. Miller, K.; Chinzei, K.; Orssengo, G.; Bednarz, P., Mechanical properties of brain tissue in-vivo: experiment and computer simulation. *Journal of biomechanics* **2000,** *33* (11), 1369-1376.

110. Gefen, A.; Margulies, S. S., Are in vivo and in situ brain tissues mechanically similar? *Journal of Biomechanics* **2004,** *37* (9), 1339-52.

111. Budday, S.; Nay, R.; de Rooij, R.; Steinmann, P.; Wyrobek, T.; Ovaert, T. C.; Kuhl, E., Mechanical properties of gray and white matter brain tissue by indentation. *Journal of the mechanical behavior of biomedical materials* **2015,** *46*, 318-30.

112. Elkin, B. S.; Azeloglu, E. U.; Costa, K. D.; Morrison, B., 3rd, Mechanical heterogeneity of the rat hippocampus measured by atomic force microscope indentation. *Journal of Neurotrauma* **2007,** *24* (5), 812-22.

113. Canovic, E. P.; Qing, B.; Mijailovic, A. S.; Jagielska, A.; Whitfield, M. J.; Kelly, E.; Turner, D.; Sahin, M.; Van Vliet, K. J., Characterizing Multiscale Mechanical Properties of Brain Tissue Using Atomic Force Microscopy, Impact Indentation, and Rheometry. *Journal of Visualized Experiments* **2016,** (115).

114. Zimberlin, J. A.; McManus, J. J.; Crosby, A. J., Cavitation rheology of the vitreous: mechanical properties of biological tissue. *Soft Matter* **2010,** *6* (15), 3632-3635.

115. Kundu, S.; Crosby, A. J., Cavitation and fracture behavior of polyacrylamide hydrogels. *Soft Matter* **2009,** *5* (20), 3963-3968.

116. Cui, J.; Lee, C. H.; Delbos, A.; McManus, J. J.; Crosby, A. J., Cavitation rheology of the eye lens. *Soft Matter* **2011,** *7* (17), 7827-7831.

117. Jansen, L. E.; Birch, N. P.; Schiffman, J. D.; Crosby, A. J.; Peyton, S. R., Mechanics of intact bone marrow. *Journal of the mechanical behavior of biomedical materials* **2015,** *50*, 299-307.

118. Polio, S. R.; Kundu, A. N.; Dougan, C. E.; Birch, N. P.; Aurian-Blajeni, D. E.; Schiffman, J. D.; Crosby, A. J.; Peyton, S. R., Cross-platform mechanical characterization of lung tissue. *PloS one* **2018,** *13* (10), e0204765.

119. Chin, M. S.; Freniere, B. B.; Fakhouri, S.; Harris, J. E.; Lalikos, J. F.; Crosby, A. J., Cavitation rheology as a potential method for in vivo assessment of skin biomechanics. *Plastic Reconstruction Surgery* **2013,** *131* (2), 303e-305e.

120. Raayai-Ardakani, S.; Chen, Z.; Earl, D. R.; Cohen, T., Volume-controlled cavity expansion for probing of local elastic properties in soft materials. *Soft matter* **2019,** *15* (3), 381-392.

121. Garo, A.; Hrapko, M.; van Dommelen, J. A.; Peters, G. W., Towards a reliable characterisation of the mechanical behaviour of brain tissue: The effects of post-mortem time and sample preparation. *Biorheology* **2007,** *44* (1), 51-8.

122. Hrapko, M.; van Dommelen, J. A.; Peters, G. W.; Wismans, J. S., The influence of test conditions on characterization of the mechanical properties of brain tissue. *Journal of Biomechanical Engineering* **2008,** *130* (3), 031003.

123. Rashid, B.; Destrade, M.; Gilchrist, M. D., Temperature effects on brain tissue in compression. *Journal of the Mechanical Behavior of Biomedical Materials* **2012,** *14*, 113-118.

124. McElhaney, J. H.; Melvin, J. W.; Roberts, V. L.; Portnoy, H. D., Dynamic Characteristics of the Tissues of the Head. In *Perspectives in Biomedical Engineering: Proceedings of a Symposium organised in association with the Biological Engineering Society and held in the University of Strathclyde, Glasgow, June 1972*, Palgrave Macmillan UK: London, 1973; pp 215-222.

125. Rashid, B.; Destrade, M.; Gilchrist, M. D., Mechanical characterization of brain tissue in compression at dynamic strain rates. *Journal of the Mechanical Behavior of Biomedical Materials* **2012,** *10*, 23-38.

126. Banerjee, A.; Arha, M.; Choudhary, S.; Ashton, R. S.; Bhatia, S. R.; Schaffer, D. V.; Kane, R. S., The influence of hydrogel modulus on the proliferation and differentiation of encapsulated neural stem cells. *Biomaterials* **2009,** *30* (27), 4695-4699.

127. Elkin, B. S.; Morrison, B., Viscoelastic properties of the P17 and adult rat brain from indentation in the coronal plane. *Journal of Biomechanical Engineering* **2013,** *135* (11), 114507.

128. Qian, L.; Zhao, H.; Guo, Y.; Li, Y.; Zhou, M.; Yang, L.; Wang, Z.; Sun, Y., Influence of strain rate on indentation response of porcine brain. *Journal of the mechanical behavior of biomedical materials* **2018,** *82*, 210-217.

129. Meurens, F.; Summerfield, A.; Nauwynck, H.; Saif, L.; Gerdts, V., The pig: a model for human infectious diseases. *Trends in microbiology* **2012,** *20* (1), 50-57.

130. Hutchens, S. B.; Crosby, A. J., Soft-solid deformation mechanics at the tip of an embedded needle. *Soft Matter* **2014,** *10* (20), 3679-84.

131. Jansen, L. E.; Birch, N. P.; Schiffman, J. D.; Crosby, A. J.; Peyton, S. R., Mechanics of intact bone marrow. *J Mech Behav Biomed Mater* **2015,** *50*, 299-307.

132. Hutchens, S. B.; Fakhouri, S.; Crosby, A. J., Elastic cavitation and fracture via injection. *Soft Matter* **2016,** *12* (9), 2557-2566.

133. Zimberlin, J. A.; Sanabria-DeLong, N.; Tew, G. N.; Crosby, A. J., Cavitation rheology for soft materials. *Soft Matter* **2007,** *3* (6), 763-767.

134. Murphy, M. C.; Huston, J., 3rd; Jack, C. R., Jr.; Glaser, K. J.; Manduca, A.; Felmlee, J. P.; Ehman, R. L., Decreased brain stiffness in Alzheimer's disease determined by magnetic resonance elastography. *J Magn Reson Imaging* **2011,** *34* (3), 494-8.

135. Prange, M. T.; Margulies, S. S., Regional, directional, and age-dependent properties of the brain undergoing large deformation. *J Biomech Eng* **2002,** *124* (2), 244-52.

136. Chen, F.; Zhou, J.; Li, Y.; Wang, Y.; Li, L.; Yue, H., Mechanical Properties of Porcine Brain Tissue in the Coronal Plane: Interregional Variations of the Corona Radiata. *Ann Biomed Eng* **2015,** *43* (12), 2903-10.

137. Lee, S. J.; King, M. A.; Sun, J.; Xie, H. K.; Subhash, G.; Sarntinoranont, M., Measurement of viscoelastic properties in multiple anatomical regions of acute rat brain tissue slices. *J Mech Behav Biomed Mater* **2014,** *29*, 213-24.

138. van Dommelen, J. A.; van der Sande, T. P.; Hrapko, M.; Peters, G. W., Mechanical properties of brain tissue by indentation: interregional variation. *J Mech Behav Biomed Mater* **2010,** *3* (2), 158-66.

139. Budday, S.; Sommer, G.; Haybaeck, J.; Steinmann, P.; Holzapfel, G. A.; Kuhl, E., Rheological characterization of human brain tissue. *Acta Biomater* **2017**.

140. Rashid, B.; Destrade, M.; Gilchrist, M. D., Mechanical characterization of brain tissue in simple shear at dynamic strain rates. *Journal of the mechanical behavior of biomedical materials* **2013,** *28*, 71-85 %@ 1751-6161.

141. MacManus, D. B.; Pierrat, B.; Murphy, J. G.; Gilchrist, M. D., Dynamic mechanical properties of murine brain tissue using micro-indentation. *Journal of biomechanics* **2015,** *48* (12), 3213-3218.

142. Chin, M. S.; Freniere, B. B.; Fakhouri, S.; Harris, J. E.; Lalikos, J. F.; Crosby, A. J., Cavitation rheology as a potential method for in vivo assessment of skin biomechanics. *Plast Reconstr Surg* **2013,** *131* (2), 303e-305e.

143. Franze, K.; Janmey, P. A.; Guck, J., Mechanics in neuronal development and repair. *Annu Rev Biomed Eng* **2013,** *15*, 227-51.

144. MacManus, D. B.; Pierrat, B.; Murphy, J. G.; Gilchrist, M. D., Region and species dependent mechanical properties of adolescent and young adult brain tissue. *Scientific reports* **2017,** *7* (1), 13729.

145. Velardi, F.; Fraternali, F.; Angelillo, M., Anisotropic constitutive equations and experimental tensile behavior of brain tissue. *Biomech Model Mechanobiol* **2006,** *5* (1), 53-61.

146. Green, M. A.; Bilston, L. E.; Sinkus, R., In vivo brain viscoelastic properties measured by magnetic resonance elastography. *NMR in Biomedicine: An International Journal Devoted to the Development and Application of Magnetic Resonance In vivo* **2008,** *21* (7), 755-64.

147. MacManus, D. B.; Pierrat, B.; Murphy, J. G.; Gilchrist, M. D., A viscoelastic analysis of the P56 mouse brain under large-deformation dynamic indentation. *Acta biomaterialia* **2017,** *48*, 309-318 %@ 1742-7061.

148. Darvish, K. K.; Crandall, J. R., Nonlinear viscoelastic effects in oscillatory shear deformation of brain tissue. *Med Eng Phys* **2001,** *23* (9), 633-45.

149. Rashid, B.; Destrade, M.; Gilchrist, M. D., Influence of preservation temperature on the measured mechanical properties of brain tissue. *Journal of Biomechanics* **2013,** *46* (7), 1276-1281.

150. Zhang, J.; Yoganandan, N.; Pintar, F. A.; Guan, Y.; Shender, B.; Paskoff, G.; Laud, P., Effects of tissue preservation temperature on high strain-rate material properties of brain. *J Biomech* **2011,** *44* (3), 391-6.

151. Miller, K.; Chinzei, K., Mechanical properties of brain tissue in tension. *J Biomech* **2002,** *35* (4), 483-90.

152. Zhang, W.; Liu, L.-f.; Xiong, Y.-j.; Liu, Y.-f.; Yu, S.-b.; Wu, C.-w.; Guo, W., Effect of in vitro storage duration on measured mechanical properties of brain tissue. *Scientific reports* **2018,** *8* (1), 1247.

153. Reyes, C. D.; García, A. J., α2β1 integrin-specific collagen-mimetic surfaces supporting osteoblastic differentiation. *Journal of Biomedical Materials Research Part A: An Official Journal of The Society for Biomaterials, The Japanese Society for Biomaterials, and The Australian Society for Biomaterials and the Korean Society for Biomaterials* **2004,** *69* (4), 591-600 %@ 1549-3296.

154. Naba, A.; Clauser, K. R.; Hynes, R. O., Enrichment of extracellular matrix proteins from tissues and digestion into peptides for mass spectrometry analysis. *Journal of visualized experiments: JoVE* **2015,** (101).

155. Swanson, L. W., *Comparison of the Human and Rat Central Nervous System: Major Divisions and Cortical Areas*. Elsevier Science: 1995.

156. Uhlén, M.; Fagerberg, L.; Hallström, B. M.; Lindskog, C.; Oksvold, P.; Mardinoglu, A.; Sivertsson, Å.; Kampf, C.; Sjöstedt, E.; Asplund, A., Tissue-based map of the human proteome. *Science* **2015,** *347* (6220), 1260419.

157. Okada, S.; Hara, M.; Kobayakawa, K.; Matsumoto, Y.; Nakashima, Y., Astrocyte reactivity and astrogliosis after spinal cord injury. *Neuroscience research* **2018,** *126*, 39-43 %@ 0168-0102.

158. Calvo, J.; Carbonell, A.; Boya, J., Co-expression of glial fabrillary acidic protein and vimentin in reactive astrocytes following brain injury in rats. *Brain research* **1991,** *566* (1), 333-336.

159. Kim, S.-J.; Kim, J.-S.; Park, E. S.; Lee, J.-S.; Lin, Q.; Langley, R. R.; Maya, M.; He, J.; Kim, S.-W.; Weihua, Z., Astrocytes upregulate survival genes in tumor cells and induce protection from chemotherapy. *Neoplasia* **2011,** *13* (3), 286-298.

160. Shumakovich, M. A.; Mencio, C. P.; Siglin, J. S.; Moriarty, R. A.; Geller, H. M.; Stroka, K. M., Astrocytes from the brain microenvironment alter migration and morphology of metastatic breast cancer cells. *The FASEB Journal* **2017**, 5049-5067.

161. Struve, J.; Maher, P. C.; Li, Y. q.; Kinney, S.; Fehlings, M. G.; Kuntz Iv, C.; Sherman, L. S., Disruption of the hyaluronan-based extracellular matrix in spinal cord promotes astrocyte proliferation. *Glia* **2005,** *52* (1), 16-24.

162. Summers, L.; Kangwantas, K.; Nguyen, L.; Kielty, C.; Pinteaux, E., Adhesion to the extracellular matrix is required for interleukin-1 beta actions leading to reactive phenotype in rat astrocytes. *Molecular and Cellular Neuroscience* **2010,** *44* (3), 272-281.

163. Peng, H.; Ong, Y. M.; Shah, W. A.; Holland, P. C.; Carbonetto, S., Integrins regulate centrosome integrity and astrocyte polarization following a wound. *Developmental neurobiology* **2013,** *73* (5), 333-353.

164. Zaidel-Bar, R.; Geiger, B., The switchable integrin adhesome. *Journal of Cell Science* **2010,** *123* (9), 1385-1388.

165. Raeber, G. P.; Lutolf, M. P.; Hubbell, J. A., Molecularly engineered PEG hydrogels: a novel model system for proteolytically mediated cell migration. *Biophysical journal* **2005,** *89* (2), 1374-1388.

166. Patterson, J.; Hubbell, J. A., Enhanced proteolytic degradation of molecularly engineered PEG hydrogels in response to MMP-1 and MMP-2. *Biomaterials* **2010,** *31* (30), 7836-7845.

167. Phelps, E. A.; Enemchukwu, N. O.; Fiore, V. F.; Sy, J. C.; Murthy, N.; Sulchek, T. A.; Barker, T. H.; García, A. J., Maleimide cross-linked bioactive PEG hydrogel exhibits improved reaction kinetics and cross-linking for cell encapsulation and in-situ delivery. *Advanced Materials* **2012,** *24* (1), 64-2.

168. Palomares, L. A.; Estrada-Moncada, S.; Ramírez, O. T., Production of recombinant proteins. In *Recombinant gene expression*, Springer: 2004; pp 15-51.

169. Ohtsubo, K.; Marth, J. D., Glycosylation in cellular mechanisms of health and disease. *Cell* **2006,** *126* (5), 855-867.

170. Solá, R. J.; Griebenow, K. A. I., Effects of glycosylation on the stability of protein pharmaceuticals. *Journal of pharmaceutical sciences* **2009,** *98* (4), 1223-1245.

171. Schein, C. H., Production of soluble recombinant proteins in bacteria. *Bio/technology* **1989,** *7* (11), 1141.

172. Lisowska, E., The role of glycosylation in protein antigenic properties. *Cellular and Molecular Life Sciences CMLS* **2002,** *59* (3), 445-455.

173. Shental-Bechor, D.; Levy, Y., Effect of glycosylation on protein folding: a close look at thermodynamic stabilization. *Proceedings of the National Academy of Sciences* **2008,** *105* (24), 8256-8261.

174. Wong, S. C.; Zhang, L.; Proefke, S. A.; Matherly, L. H., Effects of the loss of capacity for N-glycosylation on the transport activity and cellular localization of the human reduced folate carrier. *Biochimica et Biophysica Acta (BBA)-Biomembranes* **1998,** *1375* (1-2), 6-12.

175. Seitz, O., Glycopeptide synthesis and the effects of glycosylation on protein structure and activity. *ChemBioChem* **2000,** *1* (4), 214-246.

176. Gentzsch, M.; Tanner, W., Protein-O-glycosylation in yeast: protein-specific mannosyltransferases. *Glycobiology* **1997,** *7* (4), 481-486.

177. Hu, H.; Li, J.; Gagen, C. S.; Gray, N. W.; Zhang, Z.; Qi, Y.; Zhang, P., Conditional knockout of protein O-mannosyltransferase 2 reveals tissue-specific roles of O-mannosyl glycosylation in brain development. *Journal of Comparative Neurology* **2011,** *519* (7), 1320-1337.

178. Raju, T. S.; Briggs, J. B.; Borge, S. M.; Jones, A. J. S., Species-specific variation in glycosylation of IgG: evidence for the species-specific sialylation and branch-specific galactosylation and importance for engineering recombinant glycoprotein therapeutics. *Glycobiology* **2000,** *10* (5), 477-486.

179. Trewavas, A., Post-translational modification of proteins by phosphorylation. *Annual Review of Plant Physiology* **1976,** *27* (1), 349-374.

180. Aletta, J. M.; Cimato, T. R.; Ettinger, M. J., Protein methylation: a signal event in post-translational modification. *Trends in biochemical sciences* **1998,** *23* (3), 89-91.

181. Zhang, X.; Li, F.; Lu, X.-W.; Liu, C.-F., Protein C-terminal modification through thioacid/azide amidation. *Bioconjugate chemistry* **2009,** *20* (2), 197-200.

182. Mann, M.; Jensen, O. N., Proteomic analysis of post-translational modifications. *Nature biotechnology* **2003,** *21* (3), 255.

183. Baneyx, F.; Mujacic, M., Recombinant protein folding and misfolding in Escherichia coli. *Nature biotechnology* **2004,** *22* (11), 1399.

184. Choi, J. H.; Lee, S., Secretory and extracellular production of recombinant proteins using Escherichia coli. *Applied microbiology and biotechnology* **2004,** *64* (5), 625-635.

185. Jonasson, P.; Liljeqvist, S.; Nygren, P. A.; Ståhl, S., Genetic design for facilitated production and recovery of recombinant proteins in Escherichia coli. *Biotechnology and applied biochemistry* **2002,** *35* (2), 91-105.

186. Cruz-Acuña, R.; Quirós, M.; Farkas, A. E.; Dedhia, P. H.; Huang, S.; Siuda, D.; García-Hernández, V.; Miller, A. J.; Spence, J. R.; Nusrat, A., Synthetic hydrogels for human intestinal organoid generation and colonic wound repair. *Nature cell biology* **2017,** *19* (11), 1326.

187. Chandrasekaran, S.; Guo, N.-h.; Rodrigues, R. G.; Kaiser, J.; Roberts, D. D., Pro-adhesive and chemotactic activities of thrombospondin-1 for breast carcinoma cells are mediated by α3β1 integrin and regulated by insulin-like growth factor-1 and CD98. *Journal of Biological Chemistry* **1999,** *274* (16), 11408-11416.

188. Lichtner, R. B.; Howlett, A. R.; Lerch, M.; Xuan, J.-A.; Brink, J.; Langton-Webster, B.; Schneider, M. R., Negative Cooperativity between α3β1and α2β1Integrins in Human Mammary Carcinoma MDA MB 231 Cells. *Experimental cell research* **1998,** *240* (2), 368-376.

189. Li, S.; Nih, L. R.; Bachman, H.; Fei, P.; Li, Y.; Nam, E.; Dimatteo, R.; Carmichael, S. T.; Barker, T. H.; Segura, T., Hydrogels with precisely controlled integrin activation dictate vascular patterning and permeability. *Nature materials* **2017,** *16* (9), 953.

190. Renault-Mihara, F.; Okada, S.; Shibata, S.; Nakamura, M.; Toyama, Y.; Okano, H., Spinal cord injury: emerging beneficial role of reactive astrocytes' migration. *The international journal of biochemistry & cell biology* **2008,** *40* (9), 1649-1653.

191. Etienne-Manneville, S.; Hall, A., Integrin-mediated activation of Cdc42 controls cell polarity in migrating astrocytes through PKCζ. *Cell* **2001,** *106* (4), 489-498.

192. Pedron, S.; Becka, E.; Harley, B. A. C., Regulation of glioma cell phenotype in 3D matrices by hyaluronic acid. *Biomaterials* **2013,** *34* (30), 7408-7417.

193. Rayahin, J. E.; Buhrman, J. S.; Zhang, Y.; Koh, T. J.; Gemeinhart, R. A., High and low molecular weight hyaluronic acid differentially influence macrophage activation. *ACS biomaterials science & engineering* **2015,** *1.7*, 481-493.

194. Zhu, M.; Lerum, M. Z.; Chen, W., How to prepare reproducible, homogeneous, and hydrolytically stable aminosilane-derived layers on silica. *Langmuir* **2011,** *28* (1), 416-423.

195. Carmeliet, P.; Jain, R. K., Angiogenesis in cancer and other diseases. *Nature* **2000,** *407* (6801), 249.

196. Hanahan, D.; Weinberg, R. A., The hallmarks of cancer. *cell* **2000,** *100* (1), 57-70.

197. Hanahan, D.; Weinberg, R. A., Hallmarks of cancer: the next generation. *cell* **2011,** *144* (5), 646-674.

198. Northcott, P. A., Cancer: Keeping it real to kill glioblastoma. *Nature* **2017,** *547* (7663), 291.

199. Steeg, P. S., Targeting metastasis. *Nature reviews cancer* **2016,** *16* (4), 201.

200. Sheetz, M. P.; Felsenfeld, D. P.; Galbraith, C. G., Cell migration: regulation of force on extracellular-matrix-integrin complexes. *Trends in cell biology* **1998,** *8* (2), 51-54.

201. Lo, C.-M.; Wang, H.-B.; Dembo, M.; Wang, Y.-l., Cell movement is guided by the rigidity of the substrate. *Biophysical journal* **2000,** *79* (1), 144-152.

202. Charras, G.; Sahai, E., Physical influences of the extracellular environment on cell migration. *Nature Reviews Molecular cell biology* **2014,** *15* (12), 813.

203. West, J. L.; Hubbell, J. A., Polymeric biomaterials with degradation sites for proteases involved in cell migration. *Macromolecules* **1999,** *32* (1), 241-244.

204. Lutolf, M. P.; Hubbell, J. A., Synthetic biomaterials as instructive extracellular microenvironments for morphogenesis in tissue engineering. *Nature biotechnology* **2005,** *23* (1), 47.

205. Gobin, A. S.; West, J. L., Cell migration through defined, synthetic ECM analogs. *The FASEB Journal* **2002,** *16* (7), 751-753.

206. Peyton, S. R.; Putnam, A. J., Extracellular matrix rigidity governs smooth muscle cell motility in a biphasic fashion. *Journal of cellular physiology* **2005,** *204* (1), 198-209.

207. Peyton, S. R.; Raub, C. B.; Keschrumrus, V. P.; Putnam, A. J., The use of poly (ethylene glycol) hydrogels to investigate the impact of ECM chemistry and mechanics on smooth muscle cells. *Biomaterials* **2006,** *27* (28), 4881-4893.

208. Hirata, E.; Girotti, M. R.; Viros, A.; Hooper, S.; Spencer-Dene, B.; Matsuda, M.; Larkin, J.; Marais, R.; Sahai, E., Intravital imaging reveals how BRAF inhibition generates drug-tolerant microenvironments with high integrin β1/FAK signaling. *Cancer cell* **2015,** *27* (4), 574-588.

209. Benjamin, D. C.; Hynes, R. O., Intravital imaging of metastasis in adult Zebrafish. *BMC cancer* **2017,** *17* (1), 660.

210. Decaestecker, C.; Debeir, O.; Van Ham, P.; Kiss, R., Can anti-migratory drugs be screened in vitro? A review of 2D and 3D assays for the quantitative analysis of cell migration. *Medicinal research reviews* **2007,** *27* (2), 149-176.

211. Ridley, A. J.; Schwartz, M. A.; Burridge, K.; Firtel, R. A.; Ginsberg, M. H.; Borisy, G.; Parsons, J. T.; Horwitz, A. R., Cell migration: integrating signals from front to back. *Science* **2003,** *302* (5651), 1704-1709.

212. Kingsmore, K. M.; Logsdon, D. K.; Floyd, D. H.; Peirce, S. M.; Purow, B. W.; Munson, J. M., Interstitial flow differentially increases patient-derived glioblastoma stem cell invasion via CXCR4, CXCL12, and CD44-mediated mechanisms. *Integrative Biology* **2016,** *8* (12), 1246-1260.

213. Cornelison, R. C.; Brennan, C. E.; Kingsmore, K. M.; Munson, J. M., Convective forces increase CXCR4-dependent glioblastoma cell invasion in GL261 murine model. *Scientific reports* **2018,** *8* (1), 17057.

214. Barney, L. E.; Jansen, L. E.; Peyton, S. R.; Dandley, E. C.; Reich, N. G.; Mercurio, A. M., A cell–ECM screening method to predict breast cancer metastasis. *Integrative Biology* **2014,** *7* (2), 198-212.

215. Lee, J.; Kotliarova, S.; Kotliarov, Y.; Li, A.; Su, Q.; Donin, N. M.; Pastorino, S.; Purow, B. W.; Christopher, N.; Zhang, W., Tumor stem cells derived from glioblastomas cultured in bFGF and EGF more closely mirror the phenotype and genotype of primary tumors than do serum-cultured cell lines. *Cancer cell* **2006,** *9* (5), 391-403.

216. Munson, J. M.; Bellamkonda, R. V.; Swartz, M. A., Interstitial flow in a 3D microenvironment increases glioma invasion by a CXCR4-dependent mechanism. *Cancer research* **2013,** *73* (5), 1536-1546.

217. Hughes, C. S.; Postovit, L. M.; Lajoie, G. A., Matrigel: a complex protein mixture required for optimal growth of cell culture. *Proteomics* **2010,** *10* (9), 1886-1890.

218. Meyer, A. S.; Hughes-Alford, S. K.; Kay, J. E.; Castillo, A.; Wells, A.; Gertler, F. B.; Lauffenburger, D. A., 2D protrusion but not motility predicts growth factor-induced cancer cell migration in 3D collagen. *The Journal of Cell Biology* **2012,** *197* (6), 721-9.

219. Fraley, S. I.; Feng, Y.; Krishnamurthy, R.; Kim, D.-H.; Celedon, A.; Longmore, G. D.; Wirtz, D., A distinctive role for focal adhesion proteins in three-dimensional cell motility. *Nature cell biology* **2010,** *12* (6), 598.

220. Balzer, E. M.; Tong, Z.; Paul, C. D.; Hung, W.-C.; Stroka, K. M.; Boggs, A. E.; Martin, S. S.; Konstantopoulos, K., Physical confinement alters tumor cell adhesion and migration phenotypes. *The FASEB Journal* **2012,** *26* (10), 4045-4056.

221. Stroka, K. M.; Jiang, H.; Chen, S.-H.; Tong, Z.; Wirtz, D.; Sun, S. X.; Konstantopoulos, K., Water permeation drives tumor cell migration in confined microenvironments. *Cell* **2014,** *157* (3), 611-623.

222. Peyton, S. R.; Kalcioglu, Z. I.; Cohen, J. C.; Runkle, A. P.; Van Vliet, K. J.; Lauffenburger, D. A.; Griffith, L. G., Marrow-Derived stem cell motility in 3D synthetic scaffold is governed by geometry along with adhesivity and stiffness. *Biotechnology and bioengineering* **2011,** *108* (5), 1181-1193.

223. Nguyen, T. V.; Sleiman, M.; Moriarty, T.; Herrick, W. G.; Peyton, S. R., Sorafenib resistance and JNK signaling in carcinoma during extracellular matrix stiffening. *Biomaterials* **2014,** *35* (22), 5749-5759.

224. Pickup, M. W.; Mouw, J. K.; Weaver, V. M., The extracellular matrix modulates the hallmarks of cancer. *EMBO reports* **2014,** *15* (12), 1243-1253.

225. Coussens, L. M.; Werb, Z., Inflammation and cancer. *Nature* **2002,** *420* (6917), 860.

226. Brizzi, M. F.; Tarone, G.; Defilippi, P., Extracellular matrix, integrins, and growth factors as tailors of the stem cell niche. *Current opinion in cell biology* **2012,** *24* (5), 645-651.

227. Baker, B. M.; Chen, C. S., Deconstructing the third dimension–how 3D culture microenvironments alter cellular cues. *Journal of Cell Science* **2012,** *125* (13), 3015-3024.

228. Gillies, R. J.; Didier, N.; Denton, M., Determination of cell number in monolayer cultures. *Analytical biochemistry* **1986,** *159* (1), 109-113.

229. Inglese, J.; Auld, D. S.; Jadhav, A.; Johnson, R. L.; Simeonov, A.; Yasgar, A.; Zheng, W.; Austin, C. P., Quantitative high-throughput screening: a titration-based approach that efficiently identifies biological activities in large chemical libraries. *Proceedings of the National Academy of Sciences* **2006,** *103* (31), 11473-11478.

230. Marques, J.; Vilanova, E.; Mourão, P. A. S.; Fernàndez-Busquets, X., Marine organism sulfated polysaccharides exhibiting significant antimalarial activity and inhibition of red blood cell invasion by Plasmodium. *Scientific reports* **2016,** *6*, 24368.

231. Bulysheva, A. A.; Bowlin, G. L.; Petrova, S. P.; Yeudall, W. A., Enhanced chemoresistance of squamous carcinoma cells grown in 3D cryogenic electrospun scaffolds. *Biomedical Materials* **2013,** *8* (5), 055009.

232. Fallahi-Sichani, M.; Honarnejad, S.; Heiser, L. M.; Gray, J. W.; Sorger, P. K., Metrics other than potency reveal systematic variation in responses to cancer drugs. *Nature chemical biology* **2013,** *9* (11), 708.

233. Sebaugh, J. L., Guidelines for accurate EC50/IC50 estimation. *Pharmaceutical statistics* **2011,** *10* (2), 128-134.

234. Longati, P.; Jia, X.; Eimer, J.; Wagman, A.; Witt, M.-R.; Rehnmark, S.; Verbeke, C.; Toftgård, R.; Löhr, M.; Heuchel, R. L., 3D pancreatic carcinoma spheroids induce a matrix-rich, chemoresistant phenotype offering a better model for drug testing. *BMC Cancer* **2013,** *13* (1), 95.

235. Hongisto, V.; Jernström, S.; Fey, V.; Mpindi, J.-P.; Sahlberg, K. K.; Kallioniemi, O.; Perälä, M. J. P. o., High-throughput 3D screening reveals differences in drug sensitivities between culture models of JIMT1 breast cancer cells. **2013,** *8* (10), e77232.

236. Phan, N.; Hong, J. J.; Tofig, B.; Mapua, M.; Huang, J.; Memarzadeh, S.; Damoiseaux, R.; Soragni, A., A simple high-throughput approach to identify actionable drug responses in patient-derived tumor organoids. **2017**.

237. Monks, A.; Scudiero, D.; Skehan, P.; Shoemaker, R.; Paull, K.; Vistica, D.; Hose, C.; Langley, J.; Cronise, P.; Vaigro-Wolff, A., Feasibility of a high-flux anticancer drug screen using a diverse panel of cultured human tumor cell lines. *JNCI: Journal of the National Cancer Institute* **1991,** *83* (11), 757-766.

238. Vinci, M.; Gowan, S.; Boxall, F.; Patterson, L.; Zimmermann, M.; Lomas, C.; Mendiola, M.; Hardisson, D.; Eccles, S. A. J. B. b., Advances in establishment and analysis of three-dimensional tumor spheroid-based functional assays for target validation and drug evaluation. **2012,** *10* (1), 29.

239. Lovitt, C. J.; Shelper, T. B.; Avery, V. M., Doxorubicin resistance in breast cancer cells is mediated by extracellular matrix proteins. *BMC Cancer* **2018,** *18* (1), 41.

240. Zustiak, S.; Nossal, R.; Sackett, D. L. J. B. a. b., Multiwell stiffness assay for the study of cell responsiveness to cytotoxic drugs. **2014,** *111* (2), 396-403.

241. Mih, J. D.; Sharif, A. S.; Liu, F.; Marinkovic, A.; Symer, M. M.; Tschumperlin, D. J., A multiwell platform for studying stiffness-dependent cell biology. *PloS one* **2011,** *6* (5), e19929.

242. Lovitt, C. J.; Shelper, T. B.; Avery, V. M., Evaluation of chemotherapeutics in a three-dimensional breast cancer model. *Journal of Cancer Research and Clinical Oncology* **2015,** *141* (5), 951-959.

243. Ngo, M. T.; Harley, B. A., Perivascular signals alter global gene expression profile of glioblastoma and response to temozolomide in a gelatin hydrogel. *Biomaterials* **2018**.

244. Drevon, D.; Fursa, S. R.; Malcolm, A. L., Intercoder reliability and validity of WebPlotDigitizer in extracting graphed data. *Behavior Modification* **2017,** *41* (2), 323-339.

245. Logsdon, D. K.; Beeghly, G. F.; Munson, J. M., Chemoprotection Across the Tumor Border: Cancer Cell Response to Doxorubicin Depends on Stromal Fibroblast Ratios and Interstitial Therapeutic Transport. *Cellular and Molecular Bioengineering* **2017,** *10* (5), 463-481.

246. Landry, B. D.; Leete, T.; Richards, R.; Cruz-Gordillo, P.; Schwartz, H. R.; Honeywell, M. E.; Ren, G.; Schwartz, A. D.; Peyton, S. R.; Lee, M. J., Tumor-stroma interactions differentially alter drug sensitivity based on the origin of stromal cells. *Molecular systems biology* **2018,** *14* (8), e8322.

247. Cardenas, C.; Montagna, M. K.; Pitruzzello, M.; Lima, E.; Mor, G.; Alvero, A. B., Adipocyte microenvironment promotes Bcl xl expression and confers chemoresistance in ovarian cancer cells. *Apoptosis* **2017,** *22* (4), 558-569.

248. Duong, M. N.; Cleret, A.; Matera, E.-L.; Chettab, K.; Mathé, D.; Valsesia-Wittmann, S.; Clémenceau, B.; Dumontet, C., Adipose cells promote resistance of breast cancer cells to trastuzumab-mediated antibody-dependent cellular cytotoxicity. *Breast Cancer Research* **2015,** *17* (1), 57.

249. Harris, A. R.; Yuan, J. X.; Munson, J. M. J. M., Assessing multiparametric drug response in tissue engineered tumor microenvironment models. *Methods* **2018,** *134*, 20-31.

250. Shen, K.; Luk, S.; Hicks, D. F.; Elman, J. S.; Bohr, S.; Iwamoto, Y.; Murray, R.; Pena, K.; Wang, F.; Seker, E., Resolving cancer–stroma interfacial signalling and interventions with micropatterned tumour–stromal assays. *Nature communications* **2014,** *5*, 5662.

251. Yang, N.; Yan, T.; Zhu, H.; Liang, X.; Leiss, L.; Sakariassen, P. Ø.; Skaftnesmo, K. O.; Huang, B.; Costea, D. E.; Enger, P. Ø., A co-culture model with brain tumor-specific bioluminescence demonstrates astrocyte-induced drug resistance in glioblastoma. *Journal of translational medicine* **2014,** *12* (1), 278.

252. Goliwas, K. F.; Richter, J. R.; Pruitt, H. C.; Araysi, L. M.; Anderson, N. R.; Samant, R. S.; Lobo-Ruppert, S. M.; Berry, J. L.; Frost, A. R., Methods to evaluate cell growth, viability, and response to treatment in a tissue engineered breast cancer model. *Scientific reports* **2017,** *7* (1), 14167.

253. Borovski, T.; Verhoeff, J. J. C.; ten Cate, R.; Cameron, K.; de Vries, N. A.; van Tellingen, O.; Richel, D. J.; van Furth, W. R.; Medema, J. P.; Sprick, M. R., Tumor microvasculature supports proliferation and expansion of glioma-propagating cells. *International journal of cancer* **2009,** *125* (5), 1222-1230.

254. Tibbitt, M. W.; Anseth, K. S., Hydrogels as extracellular matrix mimics for 3D cell culture. *Biotechnology and bioengineering* **2009,** *103* (4), 655-663 %@ 0006-3592.

255. Qian, L.; Zhao, H.; Guo, Y.; Li, Y.; Zhou, M.; Yang, L.; Wang, Z.; Sun, Y., Influence of strain rate on indentation response of porcine brain. *Journal of the mechanical behavior of biomedical materials* **2018,** *82*, 210-217 %@ 1751-6161.

256. Nam, S.; Hu, K. H.; Butte, M. J.; Chaudhuri, O., Strain-enhanced stress relaxation impacts nonlinear elasticity in collagen gels. *Proceedings of the National Academy of Sciences* **2016,** *113* (20), 5492-5497.

257. Calhoun, M.; Bentil, S. A.; Elliott, E.; Otero, J. J.; Winter, J. O.; Dupaix, R. B., Beyond Linear Elastic Modulus: Viscoelastic Models for Brain and Brain Mimetic Hydrogels. *ACS Biomaterials Science & Engineering* **2019**.

258. Chaudhuri, O.; Gu, L.; Klumpers, D.; Darnell, M.; Bencherif, S. A.; Weaver, J. C.; Huebsch, N.; Lee, H.-p.; Lippens, E.; Duda, G. N., Hydrogels with tunable stress relaxation regulate stem cell fate and activity. *Nature materials* **2016,** *15* (3), 326-334.

259. Badeau, B. A.; Comerford, M. P.; Arakawa, C. K.; Shadish, J. A.; DeForest, C. A., Engineered modular biomaterial logic gates for environmentally triggered therapeutic delivery. *Nature chemistry* **2018,** *10* (3), 251.

260. Zhang, Y.; Chen, K.; Sloan, S. A.; Bennett, M. L.; Scholze, A. R.; O'Keeffe, S.; Phatnani, H. P.; Guarnieri, P.; Caneda, C.; Ruderisch, N., An RNA-sequencing transcriptome and splicing

database of glia, neurons, and vascular cells of the cerebral cortex. *Journal of Neuroscience* **2014,** *34* (36), 11929-11947.

261. Eng, L. F.; Vanderhaeghen, J. J.; Bignami, A.; Gerstl, B., An acidic protein isolated from fibrous astrocytes. *Brain research* **1971,** *28* (2), 351-354.

262. Brioschi, S.; Peng, V.; Colonna, M., Fifty Shades of Microglia. *Trends in neurosciences* **2019**.

263. Placone, A. L.; Quiñones-Hinojosa, A.; Searson, P. C., The role of astrocytes in the progression of brain cancer: complicating the picture of the tumor microenvironment. *Tumor Biology* **2016,** *37* (1), 61-69.

264. Dzwonek, J.; Wilczynski, G. M., CD44: molecular interactions, signaling and functions in the nervous system. *Frontiers in cellular neuroscience* **2015,** *9*.

265. Sevenich, L.; Bowman, R. L.; Mason, S. D.; Quail, D. F.; Rapaport, F.; Elie, B. T.; Brogi, E.; Brastianos, P. K.; Hahn, W. C.; Holsinger, L. J., Analysis of tumor-and stroma-supplied proteolytic networks reveals a brain metastasis-promoting role for cathepsin S. *Nature cell biology* **2014,** *16* (9), 876.

266. Kyburz, K. K. A., Synthetic Mimics of the Extracellular Matrix: How Simple is Complex Enough? Annals of Biomedical Engineering, 2015; Vol. 43, pp 489-500.

267. Wrede, A. H.; Shah, A.; McNamara, M. C.; Montazami, R.; Hashemi, N. N., Controlled positioning of microbubbles and induced cavitation using a dual-frequency transducer and microfiber adhesion techniques. *Ultrasonics sonochemistry* **2018,** *43*, 114-119.

268. Goddard, E. T.; Bozic, I.; Riddell, S. R.; Ghajar, C. M., Dormant tumour cells, their niches and the influence of immunity. *Nature cell biology* **2018,** *20* (11), 1240.

269. Ghajar, C. M.; Peinado, H.; Mori, H.; Matei, I. R.; Evason, K. J.; Brazier, H.; Almeida, D.; Koller, A.; Hajjar, K. A.; Stainier, D. Y. R., The perivascular niche regulates breast tumour dormancy. *Nature cell biology* **2013,** *15* (7), 807.

270. Ghajar, C. M., Metastasis prevention by targeting the dormant niche. *Nature Reviews Cancer* **2015,** *15* (4), 238.

271. Carlson, P.; Dasgupta, A.; Grzelak, C. A.; Kim, J.; Barrett, A.; Coleman, I. M.; Shor, R. E.; Goddard, E. T.; Dai, J.; Schweitzer, E. M., Targeting the perivascular niche sensitizes disseminated tumour cells to chemotherapy. *Nature cell biology* **2019,** *21* (2), 238.

272. Weigelt, B.; Ghajar, C. M.; Bissell, M. J., The need for complex 3D culture models to unravel novel pathways and identify accurate biomarkers in breast cancer. *Advanced drug delivery reviews* **2014,** *69*, 42-51.

273. Zhang, L.; Zhang, S.; Yao, J.; Lowery, F. J.; Zhang, Q.; Huang, W.-C.; Li, P.; Li, M.; Wang, X.; Zhang, C., Microenvironment-induced PTEN loss by exosomal microRNA primes brain metastasis outgrowth. *Nature* **2015,** *527* (7576), 100.

274. Anderson, M. J.; Swanson, K. A.; Waxman, S. G.; Eng, L. F., Glial fibrillary acidic protein in regenerating teleost spinal cord. *Journal of Histochemistry & Cytochemistry* **1984,** *32* (10), 1099-1106.

275. Gilmore, T. D., Introduction to NF-κB: players, pathways, perspectives. *Oncogene* **2006,** *25* (51), 6680.

276. Kaltschmidt, B.; Kaltschmidt, C., NF-κB in the nervous system. *Cold Spring Harbor perspectives in biology* **2009,** *1* (3), a001271.

277. Carrero, I.; Gonzalo, M. R.; Martin, B.; Sanz-Anquela, J. M.; Arevalo-Serrano, J.; Gonzalo-Ruiz, A., Oligomers of beta-amyloid protein (Aβ1-42) induce the activation of cyclooxygenase-2 in astrocytes via an interaction with interleukin-1beta, tumour necrosis factor-alpha, and a nuclear factor kappa-B mechanism in the rat brain. *Experimental neurology* **2012,** *236* (2), 215-227.

278. Hsiao, H.-Y.; Chen, Y.-C.; Chen, H.-M.; Tu, P.-H.; Chern, Y., A critical role of astrocyte-mediated nuclear factor-κB-dependent inflammation in Huntington's disease. *Human molecular genetics* **2013,** *22* (9), 1826-1842.

279. He, F.; Ge, W.; Martinowich, K.; Becker-Catania, S.; Coskun, V.; Zhu, W.; Wu, H.; Castro, D.; Guillemot, F.; Fan, G., A positive autoregulatory loop of Jak-STAT signaling controls the onset of astrogliogenesis. *Nature neuroscience* **2005,** *8* (5), 616.

280. Kanski, R.; van Strien, M. E.; van Tijn, P.; Hol, E. M., A star is born: new insights into the mechanism of astrogenesis. *Cellular and molecular life sciences* **2014,** *71* (3), 433-447.

281. Herrmann, J. E.; Imura, T.; Song, B.; Qi, J.; Ao, Y.; Nguyen, T. K.; Korsak, R. A.; Takeda, K.; Akira, S.; Sofroniew, M. V., STAT3 is a critical regulator of astrogliosis and scar formation after spinal cord injury. *Journal of Neuroscience* **2008,** *28* (28), 7231-7243.

282. Chan, E. P.; Smith, E. J.; Hayward, R. C.; Crosby, A. J., Surface Wrinkles for Smart Adhesion. *Advanced Materials* **2008,** *20* (4), 711-716.

283. Shull, K. R.; Ahn, D.; Chen, W. L.; Flanigan, C. M.; Crosby, A. J., Axisymmetric adhesion tests of soft materials. *Macromolecular Chemistry and Physics* **1998,** *199* (4), 489-511.

284. Mann, K.; Deutzmann, R.; Aumailley, M.; Timpl, R.; Raimondi, L.; Yamada, Y.; Pan, T.; Conway, D.; Chu, M., Amino acid sequence of mouse nidogen, a multidomain basement membrane protein with binding activity for laminin, collagen IV and cells. *The EMBO Journal* **1989,** *8* (1), 65.

285. Kohfeldt, E.; Sasaki, T.; Göhring, W.; Timpl, R., Nidogen-2: a new basement membrane protein with diverse binding properties. *Journal of molecular biology* **1998,** *282* (1), 99-109.

286. Beacham, D. A.; Wise, R. J.; Turci, S. M.; Handin, R. I., Selective inactivation of the Arg-Gly-Asp-Ser (RGDS) binding site in von Willebrand factor by site-directed mutagenesis. *Journal of Biological Chemistry* **1992,** *267* (5), 3409-3415.

287. Sakamoto, H.; Broekelmann, T.; Cheresh, D. A.; Ramirez, F.; Rosenbloom, J.; Mecham, R. P., Cell-type specific recognition of RGD-and non-RGD-containing cell binding domains in fibrillin-1. *Journal of Biological Chemistry* **1996,** *271* (9), 4916-4922.

288. Tulla, M.; Pentikäinen, O. T.; Viitasalo, T.; Käpylä, J.; Impola, U.; Nykvist, P.; Nissinen, L.; Johnson, M. S.; Heino, J., Selective binding of collagen subtypes by integrin α1I, α2I, and α10I domains. *Journal of Biological Chemistry* **2001,** *276* (51), 48206-48212.

289. Suehiro, K.; Mizuguchi, J.; Nishiyama, K.; Iwanaga, S.; Farrell, D. H.; Ohtaki, S., Fibrinogen binds to integrin α5β1 via the carboxyl-terminal RGD site of the Aα-chain. *The Journal of Biochemistry* **2000,** *128* (4), 705-710.

290. Koticha, D.; Babiarz, J.; Kane-Goldsmith, N.; Jacob, J.; Raju, K.; Grumet, M., Cell adhesion and neurite outgrowth are promoted by neurofascin NF155 and inhibited by NF186. *Molecular and Cellular Neuroscience* **2005,** *30* (1), 137-148.

291. Aota, S.-i.; Nomizu, M.; Yamada, K. M., The short amino acid sequence Pro-His-Ser-Arg-Asn in human fibronectin enhances cell-adhesive function. *Journal of Biological Chemistry* **1994,** *269* (40), 24756-24761.

292. Hamaia, S. W.; Pugh, N.; Raynal, N.; Némoz, B.; Stone, R.; Gullberg, D.; Bihan, D.; Farndale, R. W., Mapping of potent and specific binding motifs, GLOGEN and GVOGEA, for integrin α1β1 using collagen toolkits II and III. *Journal of Biological Chemistry* **2012,** *287* (31), 26019-26028.

293. Xu, Y.; Gurusiddappa, S.; Rich, R. L.; Owens, R. T.; Keene, D. R.; Mayne, R.; Höök, A.; Höök, M., Multiple binding sites in collagen type I for the integrins α1β1 and α2β1. *Journal of Biological Chemistry* **2000,** *275* (50), 38981-38989.

294. Underwood, P. A.; Bennett, F. A.; Kirkpatrick, A.; Bean, P. A.; Moss, B. A., Evidence for the location of a binding sequence for the α2β1 integrin of endothelial cells, in the β1 subunit of laminin. *Biochemical Journal* **1995,** *309* (3), 765-771.

295. Staatz, W.; Fok, K.; Zutter, M.; Adams, S.; Rodriguez, B.; Santoro, S., Identification of a tetrapeptide recognition sequence for the alpha 2 beta 1 integrin in collagen. *Journal of Biological Chemistry* **1991,** *266* (12), 7363-7367.

296. Graf, J.; Ogle, R. C.; Robey, F. A.; Sasaki, M.; Martin, G. R.; Yamada, Y.; Kleinman, H. K., A pentapeptide from the laminin B1 chain mediates cell adhesion and binds to 67000 laminin receptor. *Biochemistry* **1987,** *26* (22), 6896-6900.

297. Hunter, D. D.; Cashman, N.; Morris-Valero, R.; Bulock, J. W.; Adams, S. P.; Sanes, J. R., An LRE (leucine-arginine-glutamate)-dependent mechanism for adhesion of neurons to S-laminin. *Journal of Neuroscience* **1991,** *11* (12), 3960-3971.

298. Gehlsen, K. R.; Dickerson, K.; Argraves, W. S.; Engvall, E.; Ruoslahti, E., Subunit structure of a laminin-binding integrin and localization of its binding site on laminin. *Journal of Biological Chemistry* **1989,** *264* (32), 19034-19038.

299. Tashiro, K.-i.; Sephel, G. C.; Weeks, B.; Sasaki, M.; Martin, G. R.; Kleinman, H. K.; Yamada, Y., A synthetic peptide containing the IKVAV sequence from the A chain of laminin mediates cell attachment, migration, and neurite outgrowth. *Journal of Biological Chemistry* **1989,** *264* (27), 16174-16182.

300. Yokoyama, K.; Erickson, H. P.; Ikeda, Y.; Takada, Y., Identification of amino acid sequences in fibrinogen γ-chain and tenascin C C-terminal domains critical for binding to integrin αvβ3. *Journal of Biological Chemistry* **2000,** *275* (22), 16891-16898.

301. Farach-Carson, M. C.; Brown, A. J.; Lynam, M.; Safran, J. B.; Carson, D. D., A novel peptide sequence in perlecan domain IV supports cell adhesion, spreading and FAK activation. *Matrix Biology* **2008,** *27* (2), 150-160.

302. Brown, J. C.; Sasaki, T.; Göhring, W.; Yamada, Y.; Timpl, R., The C-terminal domain V of perlecan promotes β1 integrin-mediated cell adhesion, binds heparin, nidogen and fibulin-2 and can be modified by glycosaminoglycans. *European journal of biochemistry* **1997,** *250* (1), 39-46.

303. Wickström, S. A.; Alitalo, K.; Keski-Oja, J., An endostatin-derived peptide interacts with integrins and regulates actin cytoskeleton and migration of endothelial cells. *Journal of Biological Chemistry* **2004,** *279* (19), 20178-20185.

304. Rodgers, U. R.; Weiss, A. S., Integrin αvβ3 binds a unique non-RGD site near the C-terminus of human tropoelastin. *Biochimie* **2004,** *86* (3), 173-178.

305. Plow, E. F.; Haas, T. A.; Zhang, L.; Loftus, J.; Smith, J. W., Ligand binding to integrins. *Journal of Biological Chemistry* **2000,** *275* (29), 21785-21788.

306. Ortega, N.; Werb, Z., New functional roles for non-collagenous domains of basement membrane collagens. *Journal of cell science* **2002,** *115* (22), 4201-4214.

307. Dedhar, S.; Jewell, K.; Rojiani, M.; Gray, V., The receptor for the basement membrane glycoprotein entactin is the integrin alpha 3/beta 1. *Journal of Biological Chemistry* **1992,** *267* (26), 18908-18914.

308. Hayashi, K.; Madri, J. A.; Yurchenco, P. D., Endothelial cells interact with the core protein of basement membrane perlecan through beta 1 and beta 3 integrins: an adhesion modulated by glycosaminoglycan. *The Journal of cell biology* **1992,** *119* (4), 945-959.

309. Milward, E.; Kim, K. J.; Szklarczyk, A.; Nguyen, T.; Melli, G.; Nayak, M.; Deshpande, D.; Fitzsimmons, C.; Hoke, A.; Kerr, D., Cleavage of myelin associated glycoprotein by matrix metalloproteinases. *Journal of neuroimmunology* **2008,** *193* (1-2), 140-148.

310. Aimes, R. T.; Quigley, J. P., Matrix Metalloproteinase-2 Is an Interstitial Collagenase Inhibitor-Free Enzyme Catalyzes the Cleavage of Collagen Fibrils and Soluble Native Type I Collagen Generating the Specific ¾-and ¼-Length Fragments. *Journal of Biological Chemistry* **1995,** *270* (11), 5872-5876.

311. Van Doren, S. R., Matrix metalloproteinase interactions with collagen and elastin. *Matrix Biology* **2015,** *44*, 224-231.

312. Veidal, S. S.; Karsdal, M. A.; Vassiliadis, E.; Nawrocki, A.; Larsen, M. R.; Nguyen, Q. H. T.; Hägglund, P.; Luo, Y.; Zheng, Q.; Vainer, B., MMP mediated degradation of type VI collagen is highly associated with liver fibrosis–identification and validation of a novel biochemical marker assay. *PloS one* **2011,** *6* (9), e24753.

313. Ferreras, M.; Felbor, U.; Lenhard, T.; Olsen, B. R.; Delaissé, J.-M., Generation and degradation of human endostatin proteins by various proteinases. *FEBS letters* **2000,** *486* (3), 247-251.

314. Giannelli, G., Falk-Marzillier J, Schiraldi O, Stetler-Stevenson WG, Quaranta V. *Induction of cell migration by matrix metalloprotease-2 cleavage of laminin-5. Science* **1997,** *277*, 225-228.

315. Turk, B. E.; Huang, L. L.; Piro, E. T.; Cantley, L. C., Determination of protease cleavage site motifs using mixture-based oriented peptide libraries. *Nature biotechnology* **2001,** *19* (7), 661.

316. Imai, K.; Shikata, H.; Okada, Y., Degradation of vitronectin by matrix metalloproteinases-1,-2,-3,-7 and-9. *FEBS letters* **1995,** *369* (2-3), 249-251.

317. Ashworth, J. L.; Hindson, V. J.; Cunliffe, S.; Murphy, G.; Shuttleworth, C. A.; Kielty, C. M., Characterisation of matrix metalloproteinase cleavage sites in fibrillin. *International Journal of Experimental Pathology* **2000,** *81* (1), A2.

318. Dean, R. A.; Overall, C. M., Proteomics discovery of metalloproteinase substrates in the cellular context by iTRAQ™ labeling reveals a diverse MMP-2 substrate degradome. *Molecular & Cellular Proteomics* **2007,** *6* (4), 611-623.

319. Barrett, A. J.; Woessner, J. F.; Rawlings, N. D., *Handbook of proteolytic enzymes*. Elsevier: 2012; Vol. 1.

320. Ethell, I. M.; Ethell, D. W., Matrix metalloproteinases in brain development and remodeling: synaptic functions and targets. *Journal of neuroscience research* **2007,** *85* (13), 2813-2823.

321. Patel, T. R.; Butler, G.; McFarlane, A.; Xie, I.; Overall, C. M.; Stetefeld, J., Site specific cleavage mediated by MMPs regulates function of agrin. *PloS one* **2012,** *7* (9), e43669.

322. Yu, W.-H.; Woessner, J. F., Heparan sulfate proteoglycans as extracellular docking molecules for matrilysin (matrix metalloproteinase 7). *Journal of Biological Chemistry* **2000,** *275* (6), 4183-4191.

323. Wohner, N.; Kovács, A.; Machovich, R.; Kolev, K., Modulation of the von Willebrand factor-dependent platelet adhesion through alternative proteolytic pathways. *Thrombosis research* **2012,** *129* (4), e41-e46.

324. Miloudi, K.; Binet, F.; Wilson, A.; Cerani, A.; Oubaha, M.; Menard, C.; Henriques, S.; Mawambo, G.; Dejda, A.; Nguyen, P. T., Truncated netrin-1 contributes to pathological vascular permeability in diabetic retinopathy. *The Journal of clinical investigation* **2016,** *126* (8), 3006-3022

325. Stegemann, C.; Didangelos, A.; Barallobre-Barreiro, J.; Langley, S. R.; Mandal, K.; Jahangiri, M.; Mayr, M., Proteomic identification of matrix metalloproteinase substrates in the human vasculature. *Circulation: Cardiovascular Genetics* **2013,** *6* (1), 106-117.

326. Manka, S. W.; Carafoli, F.; Visse, R.; Bihan, D.; Raynal, N.; Farndale, R. W.; Murphy, G.; Enghild, J. J.; Hohenester, E.; Nagase, H., Structural insights into triple-helical collagen cleavage by matrix metalloproteinase 1. *Proceedings of the National Academy of Sciences* **2012,** *109* (31), 12461-12466.

327. Zhang, X.; Chen, C. T.; Bhargava, M.; Torzilli, P. A., A comparative study of fibronectin cleavage by MMP-1,-3,-13, and-14. *Cartilage* **2012,** *3* (3), 267-277.

328. Hiller, O.; Lichte, A.; Oberpichler, A.; Kocourek, A.; Tschesche, H., Matrix metalloproteinases collagenase-2, macrophage elastase, collagenase-3, and membrane type 1-matrix metalloproteinase impair clotting by degradation of fibrinogen and factor XII. *Journal of Biological Chemistry* **2000,** *275* (42), 33008-33013.

329. Bair, E. L.; Chen, M. L.; McDaniel, K.; Sekiguchi, K.; Cress, A. E.; Nagle, R. B.; Bowden, G. T., Membrane type 1 matrix metalloprotease cleaves laminin-10 and promotes prostate cancer cell migration. *Neoplasia* **2005,** *7* (4), 380-389.

330. Butler, G. S.; Dean, R. A.; Tam, E. M.; Overall, C. M., Pharmacoproteomics of a metalloproteinase hydroxamate inhibitor in breast cancer cells: dynamics of membrane type 1 matrix metalloproteinase-mediated membrane protein shedding. *Molecular and cellular biology* **2008,** *28* (15), 4896-4914.

331. Titz, B.; Dietrich, S.; Sadowski, T.; Beck, C.; Petersen, A.; Sedlacek, R., Activity of MMP-19 inhibits capillary-like formation due to processing of nidogen-1. *Cellular and Molecular Life Sciences CMLS* **2004,** *61* (14), 1826-1833.

332. Orecchia, P.; Conte, R.; Balza, E.; Castellani, P.; Borsi, L.; Zardi, L.; Mingari, M. C.; Carnemolla, B., Identification of a novel cell binding site of periostin involved in tumour growth. *European journal of cancer* **2011,** *47* (14), 2221-2229.

333. Prater, C. A.; Plotkin, J.; Jaye, D.; Frazier, W. A., The properdin-like type I repeats of human thrombospondin contain a cell attachment site. *The Journal of Cell Biology* **1991,** *112* (5), 1031-1040.

334. Yokosaki, Y.; Palmer, E. L.; Prieto, A. L.; Crossin, K. L.; Bourdon, M. A.; Pytela, R.; Sheppard, D., The integrin alpha 9 beta 1 mediates cell attachment to a non-RGD site in the third fibronectin type III repeat of tenascin. *Journal of Biological Chemistry* **1994,** *269* (43), 26691-26696.

335. Lawler, J.; Weinstein, R.; Hynes, R. O., Cell attachment to thrombospondin: the role of ARG-GLY-ASP, calcium, and integrin receptors. *The Journal of Cell Biology* **1988,** *107* (6), 2351-2361.

336. Felding-Habermann, B., Integrin adhesion receptors in tumor metastasis. *Clinical & experimental metastasis* **2003,** *20* (3), 203-213.

337. Elefteriou, F.; Exposito, J. Y.; Garrone, R.; Lethias, C., Cell adhesion to tenascin-X. *The FEBS Journal* **1999,** *263* (3), 840-848.

338. Aumailley, M.; Mann, K.; von der Mark, H.; Timpl, R., Cell attachment properties of collagen type VI and Arg-Gly-Asp dependent binding to its α2 (VI) and α3 (VI) chains. *Experimental cell research* **1989,** *181* (2), 463-474.

339. Bein, K.; Simons, M., Thrombospondin Type 1 Repeats Interact with Matrix Metalloproteinase 2 Regulation of Metalloproteinase activity. *Journal of Biological Chemistry* **2000,** *275* (41), 32167-32173.

340. Watanabe, T.; Yasue, A.; Fujihara, S.; Tanaka, E., PERIOSTIN regulates MMP-2 expression via the αvβ3 integrin/ERK pathway in human periodontal ligament cells. *Archives of oral biology* **2012,** *57* (1), 52-59.

341. Nangia-Makker, P.; Raz, T.; Tait, L.; Hogan, V.; Fridman, R.; Raz, A., Galectin-3 cleavage: a novel surrogate marker for matrix metalloproteinase activity in growing breast cancers. *Cancer research* **2007,** *67* (24), 11760-11768.

342. Sasaki, T.; Mann, K.; Murphy, G.; Chu, M. L.; Timpl, R., Different susceptibilities of fibulin-1 and fibulin-2 to cleavage by matrix metalloproteinases and other tissue proteases. *European journal of biochemistry* **1996,** *240* (2), 427-434.

343. Ma, L.; Teruya-Feldstein, J.; Weinberg, R. A., Tumour invasion and metastasis initiated by microRNA-10b in breast cancer. *Nature* **2007,** *449* (7163), 682.

344. Taliaferro-Smith, L.; Oberlick, E.; Liu, T.; McGlothen, T.; Alcaide, T.; Tobin, R.; Donnelly, S.; Commander, R.; Kline, E.; Nagaraju, G. P., FAK activation is required for IGF1R-mediated regulation of EMT, migration, and invasion in mesenchymal triple negative breast cancer cells. *Oncotarget* **2015,** *6* (7), 4757.

345. Cheng, G. Z.; Chan, J.; Wang, Q.; Zhang, W.; Sun, C. D.; Wang, L.-H., Twist transcriptionally up-regulates AKT2 in breast cancer cells leading to increased migration, invasion, and resistance to paclitaxel. *Cancer research* **2007,** *67* (5), 1979-1987.

346. Shi, S.-J.; Wang, L.-J.; Yu, B.; Li, Y.-H.; Jin, Y.; Bai, X.-Z., LncRNA-ATB promotes trastuzumab resistance and invasion-metastasis cascade in breast cancer. *Oncotarget* **2015,** *6* (13), 11652.

347. Rabbani, S. A.; Ateeq, B.; Arakelian, A.; Valentino, M. L.; Shaw, D. E.; Dauffenbach, L. M.; Kerfoot, C. A.; Mazar, A. P., An anti-urokinase plasminogen activator receptor antibody (ATN-658) blocks prostate cancer invasion, migration, growth, and experimental skeletal metastasis in vitro and in vivo. *Neoplasia* **2010,** *12* (10), 778-788.

348. Wang, L.; Zhou, X.; Zhou, T.; Ma, D.; Chen, S.; Zhi, X.; Yin, L.; Shao, Z.; Ou, Z.; Zhou, P., Ecto-5′-nucleotidase promotes invasion, migration and adhesion of human breast cancer cells. *Journal of cancer research and clinical oncology* **2008,** *134* (3), 365-372.

349. Chan, S. W.; Lim, C. J.; Guo, K.; Ng, C. P.; Lee, I.; Hunziker, W.; Zeng, Q.; Hong, W., A role for TAZ in migration, invasion, and tumorigenesis of breast cancer cells. *Cancer research* **2008,** *68* (8), 2592-2598.

350. Chen, L.-l.; Zhang, Z.-j.; Yi, Z.-b.; Li, J.-j., MicroRNA-211-5p suppresses tumour cell proliferation, invasion, migration and metastasis in triple-negative breast cancer by directly targeting SETBP1. *British journal of cancer* **2017,** *117* (1), 78.

351. Bhatia, M.; McGrath, K. L.; Di Trapani, G.; Charoentong, P.; Shah, F.; King, M. M.; Clarke, F. M.; Tonissen, K. F., The thioredoxin system in breast cancer cell invasion and migration. *Redox biology* **2016,** *8*, 68-78.

352. Hazan, R. B.; Phillips, G. R.; Qiao, R. F.; Norton, L.; Aaronson, S. A., Exogenous expression of N-cadherin in breast cancer cells induces cell migration, invasion, and metastasis. *The Journal of cell biology* **2000,** *148* (4), 779-790 %@ 0021-9525.

353. Lovitt, C. J.; Shelper, T. B.; Avery, V. M., Evaluation of chemotherapeutics in a three-dimensional breast cancer model. *J Cancer Res Clin Oncol* **2015,** *141* (5), 951-959.

354. Zustiak, S.; Nossal, R.; Sackett, D. L., Multiwell stiffness assay for the study of cell responsiveness to cytotoxic drugs. *Biotechnology and bioengineering* **2014,** *111* (2), 396-403.

355. Bray, L. J.; Binner, M.; Holzheu, A.; Friedrichs, J.; Freudenberg, U.; Hutmacher, D. W.; Werner, C., Multi-parametric hydrogels support 3D in vitro bioengineered microenvironment models of tumour angiogenesis. *Biomaterials* **2015,** *53*, 609-620.

356. Talukdar, S.; Kundu, S. C., A Non-Mulberry Silk Fibroin Protein Based 3D In Vitro Tumor Model for Evaluation of Anticancer Drug Activity. *Adv. Funct. Mater.* **2012,** *22* (22), 4778-4788.

357. Gong, X.; Lin, C.; Cheng, J.; Su, J.; Zhao, H.; Liu, T.; Wen, X.; Zhao, P., Generation of multicellular tumor spheroids with microwell-based agarose scaffolds for drug testing. *PLoS One* **2015,** *10* (6), e0130348.

358. Phan, N.; Tofig, B.; Huang, J.; Memarzadeh, S.; Damoiseaux, R.; Soragni, A., Miniring approach for high-throughput drug screenings in 3D tumor models. *bioRxiv* **2017**, 138412.

359. Ho, W. Y.; Yeap, S. K.; Ho, C. L.; Rahim, R. A.; Alitheen, N. B., Development of multicellular tumor spheroid (MCTS) culture from breast cancer cell and a high throughput screening method using the MTT assay. *PLoS One* **2012,** *7* (9), e44640.

360. Sarkar, J.; Kumar, A., Thermo-responsive polymer aided spheroid culture in cryogel based platform for high throughput drug screening. *Analyst* **2016,** *141* (8), 2553-2567.

361. Clémence, D.; Robin, D.; Pierre, D.; Corinne, A.; Claire, S.; Christelle, B.; Emmanuelle, M.; Frédérique, P.-L.; Bamdad, M., Development and cytotoxic response of two proliferative MDA-MB-231 and non-proliferative SUM1315 three-dimensional cell culture models of triple-negative basal-like breast cancer cell lines. *Oncotarget* **2017,** *8* (56), 95316.

362. Ma, W.-Y.; Hsiung, L.-C.; Wang, C.-H.; Chiang, C.-L.; Lin, C.-H.; Huang, C.-S.; Wo, A. M., A novel 96well-formatted micro-gap plate enabling drug response profiling on primary tumour samples. *Sci. Rep.* **2015,** *5*, 9656.

363. Hongisto, V.; Jernström, S.; Fey, V.; Mpindi, J.-P.; Sahlberg, K. K.; Kallioniemi, O.; Perälä, M., High-throughput 3D screening reveals differences in drug sensitivities between culture models of JIMT1 breast cancer cells. *PLoS One* **2013,** *8* (10), e77232.

364. Xu, Z.; Gao, Y.; Hao, Y.; Li, E.; Wang, Y.; Zhang, J.; Wang, W.; Gao, Z.; Wang, Q., Application of a microfluidic chip-based 3D co-culture to test drug sensitivity for individualized treatment of lung cancer. *Biomaterials* **2013,** *34* (16), 4109-4117.

365. Zhu, L.; Fan, X.; Wang, B.; Liu, L.; Yan, X.; Zhou, L.; Zeng, Y.; Poznansky, M. C.; Wang, L.; Chen, H., Biomechanically primed liver microtumor array as a high-throughput mechanopharmacological screening platform for stroma-reprogrammed combinatorial therapy. *Biomaterials* **2017,** *124*, 12-24.